



HAL
open science

Time-lapse (4D) seismic interpretation methodologies based on kriging analysis: application to the Senlac (onshoreCanada) and Marlim (offshore Brazil) heavy oilfields

Carlos Eduardo Borges de Salles Abreu

► **To cite this version:**

Carlos Eduardo Borges de Salles Abreu. Time-lapse (4D) seismic interpretation methodologies based on kriging analysis: application to the Senlac (onshoreCanada) and Marlim (offshore Brazil) heavy oilfields. Earth Sciences. Institut National Polytechnique de Lorraine, 2008. English. NNT : 2008INPL012N . tel-01753028

HAL Id: tel-01753028

<https://hal.univ-lorraine.fr/tel-01753028>

Submitted on 29 Mar 2018

HAL is a multi-disciplinary open access archive for the deposit and dissemination of scientific research documents, whether they are published or not. The documents may come from teaching and research institutions in France or abroad, or from public or private research centers.

L'archive ouverte pluridisciplinaire **HAL**, est destinée au dépôt et à la diffusion de documents scientifiques de niveau recherche, publiés ou non, émanant des établissements d'enseignement et de recherche français ou étrangers, des laboratoires publics ou privés.



AVERTISSEMENT

Ce document est le fruit d'un long travail approuvé par le jury de soutenance et mis à disposition de l'ensemble de la communauté universitaire élargie.

Il est soumis à la propriété intellectuelle de l'auteur. Ceci implique une obligation de citation et de référencement lors de l'utilisation de ce document.

D'autre part, toute contrefaçon, plagiat, reproduction illicite encourt une poursuite pénale.

Contact : ddoc-theses-contact@univ-lorraine.fr

LIENS

Code de la Propriété Intellectuelle. articles L 122. 4

Code de la Propriété Intellectuelle. articles L 335.2- L 335.10

http://www.cfcopies.com/V2/leg/leg_droi.php

<http://www.culture.gouv.fr/culture/infos-pratiques/droits/protection.htm>

***Time-lapse (4D) seismic interpretation methodologies
based on kriging analysis: application to the Senlac
(onshore Canada) and Marlim (offshore Brazil) heavy
oilfields***

THÈSE

présentée et soutenue publiquement le 7 mars 2008
pour l'obtention du

**Doctorat de l'Institut National Polytechnique de Lorraine
Spécialité Géosciences**

Par

Carlos Eduardo BORGES DE SALLES ABREU

Composition du jury

Rapporteurs : Richard SINDING LARSEN
Jean-Paul CHILÈS

Examineurs: Nathalie LUCET
Frédérique FOURNIER
Luc SANDJIVY

Directeur: Jean-Jacques ROYER

Invité : Paulo JOHANN

Acknowledgements

First of all, I would like to express my deep gratitude to my thesis director, M. Jean-Jacques Royer, for his continuous support and patience during this three and half years working together. All his pertinent comments and suggestions, framed on his outstanding intellectual rigour, have helped to guide and much enrich this work.

I am also very grateful to Nathalie Lucet, my responsible at the Institut Français du Pétrole, for all the opportunities we have had to discuss together. Thanks a lot, Nathalie! I am also indebted with Philippe Nivlet and Frederique Fournier, for their patience and continuous help, comments and corrections.

I also thank Mr. Richard Sinding-Larsen and Mr. Jean-Paul Chiles, that have accepted to revise my thesis and to be part of the jury. My thanks also go to Mr. Luc Sandjivy and M. Paulo Johann, for his observations and comments as members of the jury. Special thanks to Caroline Joseph, for her patience on helping me to wrap the final presentation up.

I am very grateful to all colleagues from the Geophysical Department from IFP, researchers and doctoral students, and as well as the administrative staff, for the warm welcome and collaboration. Christine Le Cleach did a great job on helping me with the MS Word problems.

My thanks to Encana, for the use of the data concerning the Senlac Field. I am also grateful with PETROBRAS to support me in my PhD project, and to permit me to work with and publish the results from the Marlim Field. Thanks to all my colleagues from Petrobras, that helped me on providing data and other material, as well as for the valuable discussions and comments.

Finally, I would like to express my deep gratitude and love to my wife, Danielle, and to my kids, Daniel and Bruna, for their comprehension and patience with all those moments I had to stay absent during our stay in France. They have supported me during all the good and bad times, and we have learned a lot together.

Résumé

Une gestion optimale de réservoir implique désormais l'acquisition quasi systématique de données de sismique 3D répétée (données 4D). Il s'agit donc de répéter une acquisition sismique 3D au cours du temps, généralement avant (« base survey ») et ensuite au cours de la production (« monitor survey »). L'utilité de ce type de données a été démontrée, par comparaison d'images du réservoir au cours de la production. On peut ainsi prédire des événements indésirables, tels que des venues d'eau ou détecter des zones non drainées. Néanmoins, l'exploitation des données 4D est aujourd'hui limitée aux interprétations qualitatives. L'interprétation quantitative des données de sismique répétée est loin d'être opérationnelle, et les travaux élaborés au cours de cette thèse ont pour objectif d'améliorer ce type d'interprétation.

L'exploitation des mesures de sismique répétée repose sur le principe que les variations du signal sismique au cours du temps traduisent les variations de pressions, de température et de saturations du réservoir suite aux mécanismes de la production. Le corollaire est que les variations de la mesure sismique en dehors du réservoir devraient être quasi-nulles, ce qui n'est généralement pas vérifié du fait des variations des conditions expérimentales de l'acquisition (équipements et dispositifs, météo, etc.); ces variations ne peuvent être totalement corrigées par les opérations de traitement classiques spécifiques aux données 4D. Les paramètres clé du succès d'une campagne de sismique répétée reposent sur deux notions de base : la répétitivité et la détectabilité. La répétitivité est une mesure de la ressemblance entre deux campagnes sismiques en termes d'acquisition et de traitement sismiques. Il est évident que plus la répétitivité est grande, plus grandes sont les chances de détecter et quantifier des changements dans le réservoir au cours du temps. La détectabilité est liée à la facilité d'identifier des changements au cours du temps, associés à des variations en termes de saturation en fluides, pression et température. Ce paramètre dépend du réservoir lui-même, et également de la résolution sismique. Une combinaison optimale de répétitivité et de détectabilité permet d'assurer le succès d'une campagne de sismique 4D.

L'objectif de la thèse est de développer des méthodologies d'interprétation permettant de caractériser et d'exploiter au mieux les variations des traces sismiques au cours du temps calendaire. Ces méthodologies sont tout d'abord utilisées pour évaluer la répétitivité des campagnes sismiques, puis pour filtrer les données afin d'éliminer les bruits indésirables qui ne sont pas liés à la production et produire ainsi des données « nettoyées » dans lesquelles la signature 4D sera plus lisible.

Table of Content

CHAPTER 1 - RÉSUMÉ (EN FRANÇAIS).....	21
<i>1.1. Introduction</i>	21
<i>1.2. Techniques de filtrage géostatistique appliquées aux données de sismique répétée</i>	23
1.2.1. La méthode du Krigeage Factoriel.....	25
1.2.2. Comparaison entre le Krigeage Factoriel, l'Analyse Spectrale et Decomposition en Valeurs Singulieres.....	29
<i>1.3. Application du filtrage géostatistique au champ d'huiles lourdes de Senlac</i>	30
1.3.1. Description du jeu de données de Senlac.....	31
1.3.2. Méthode de récupération assistée SAGD.....	31
1.3.3. Données de sismique répétée.....	32
1.3.4. Description statistique des données.....	33
1.3.5. Krigeage Factoriel.....	34
1.3.6. Analyse en faciès sismiques.....	36
1.3.7. Effets time-lapse et la pression.....	41
<i>1.4. Application du filtrage géostatistique à un champ d'huiles lourdes, offshore Brazil : Champ de Marlim</i>	42
1.4.1. Le Bassin de Campos et la géologie du Champ de Marlim.....	44
CHAPTER 2 - INTRODUCTION.....	50
CHAPTER 3 - GEOSTATISTICAL FILTERING TECHNIQUES APPLIED TO TIME- LAPSE SEISMIC DATA.....	53
<i>3.1. Geostatistical Basis</i>	55
3.1.1. Random Variables.....	55
3.1.2. Random Functions.....	57
3.1.3. Expected Value.....	58
3.1.4. Variance.....	58
3.1.5. Linear properties of the Expected Value.....	59
3.1.6. Stationarity.....	60
3.1.7. Covariance.....	61
3.1.8. Variogram.....	62
<i>3.2. Geostatistical Estimation</i>	66
3.2.1. Simple Kriging.....	67
3.2.2. Ordinary Kriging.....	68
3.2.3. Kriging with a trend model: Universal Kriging.....	69
3.2.4. Cokriging.....	70
3.2.5. Factorial Kriging.....	71
3.2.6. Analogy between Factorial Kriging and Spectral Methods.....	77
3.2.7. Analogy between Factorial Kriging and Single Value Decomposition.....	81
<i>3.3. Conclusions</i>	84
CHAPTER 4 - APPLICATION OF THE GEOSTATISTICAL FILTERING ON THE SENAC HEAVY OILFIELD.....	86
<i>4.1. The Senlac dataset</i>	87
4.1.1. SAGD thermal recovery scheme.....	89

4.1.2.	Time-lapse seismic data	91
4.1.3.	Seismic data interpretation	93
4.2.	<i>Statistical Characterization of Senlac Seismic Datasets</i>	95
4.2.1.	Overall Data Statistical Description	96
4.2.2.	Statistics of the Non-Reservoir Zone	99
4.2.3.	Statistics of the Reservoir Zone	101
4.2.4.	Discussion on Statistical Analysis.....	105
4.3.	<i>Factorial kriging</i>	106
4.3.1.	Variogram and Cross-Variogram Maps	106
4.3.2.	Structural analysis	108
4.3.3.	Orthogonal factors estimation	115
4.3.4.	Seismic Data Reconstruction & Filtering.....	120
4.3.5.	Discussion on the inline non-stationarity	123
4.4.	<i>Seismic Facies Analysis</i>	130
4.4.1.	Description of the Methodology	130
4.4.2.	Seismic Facies Classification Results	136
4.4.3.	Seismic Facies Analysis: Conclusions	144
4.5.	<i>Modeling pore pressure effects on time-lapse seismic</i>	144
4.5.1.	Effects of steam injection on reservoir properties.....	145
4.5.2.	Theory: Pressure effects	149
4.5.3.	Pore pressure and confining pressure relationships: Differential and effective pressure	151
4.5.4.	Predicting pressure effects with the Hertz model.....	153
4.5.5.	Negative time-shifts and pore pressure: Modeling and results	154
4.5.6.	Scenarios S1 and S2: Pore pressure reduction	158
4.5.7.	Scenarios S3 to S5: Pore pressure increase	159
4.5.8.	Scenario S6: which pore pressure variation fits to the observed time-lapse measurements?	161
4.5.9.	Discussion	162
4.6.	<i>Conclusions</i>	168
CHAPTER 5 - MARLIM CASE		171
5.1.	<i>Presentation of the Marlim field</i>	172
5.1.1.	Campos Basin overview	172
5.1.2.	Geological setting	175
5.1.3.	Seismic Acquisition Parameters	177
5.1.4.	Seismic processing issues.....	180
5.1.5.	Seismic Interpretation	185
5.2.	<i>Geostatistical Analysis</i>	192
5.2.1.	Volumetric Analysis.....	193
5.2.2.	Flattening seismic volumes	199
5.2.3.	Statistical Analysis of the flattened data	202
5.2.4.	Grouping the amplitude time-slices	206
5.2.5.	Structural Analysis: Modelling the experimental variograms.....	230
5.2.6.	Factorial Cokriging Results.....	251
5.2.7.	Decomposing and filtering the short-range G4 structures	252
5.2.8.	Results from time-slices clustering	255
5.2.9.	Differences DifS05-S97	271
5.2.10.	Comparing Low and High Noise Level Zones.....	275
5.3.	<i>Conclusions</i>	290

CHAPTER 6 - GENERAL CONCLUSIONS AND FUTURE WORK.....	293
6.1. <i>Future work and perspectives</i>	298
BIBLIOGRAPHIC REFERENCES.....	300
ANNEX A	310
ANNEX B	318
ANNEX C	322

List of Figures

Figure 1-1 – Plan de position de SENLAC: Campagnes sismiques 4D et position des puits horizontaux SAGD (Li et al., 2001). La zone étudiée correspond au carré jaune.	33
Figure 1-2 - Classification simultanée sur les 3 volumes sismiques (Lucet et al., 2001).	38
Figure 1-3- Cartes de faciès sismiques (approche non supervisée) à 5 classes. Le rang du haut montre des cartes calculées à partir des données brutes et celui du bas à partir des données filtrées.	40
Figure 1-4 – Probabilité d'affectation pour les 5 classes.	40
Figure 1-5 - Plan de situation du Bassin de Campos, situé au sud-est Brésil. Cette carte montre la plus importante zone de production offshore Brésil exploitée par PETROBRAS.....	44
Figure 1-6 - Ligne sismique crossline XL 6073, extraite du volume S05, montrant les horizons interprétés. En noir, les principaux segments de la faille qui limite le réservoir à l'est et le nord-est. Des zones sismiques de mauvaise qualité dus à la présence d'obstacles représentés par le rectangle rouge.	45
Figure 1-7 Section sismique inline représentative du champ de Marlim. Les horizons RM2 et RM2' représentent les limites inférieure et supérieure de la fenêtre d'intérêt. Échelles verticales et horizontales en millisecondes (TWT), et m, respectivement.	46
Figure 1-8 - Section verticale crossline campagne S97, montrant l'intervalle temps correspondant au groupe réservoir Marlim (TS21 à TS36). Échelle verticale de temps en ms (TWT).	47
Figure 1-9 – Time-slices 25, correspondent au Réservoir Marlim. Partant de gauche vers la droite, on voit les cartes d'amplitude extraites des campagnes S05 et S97 et leur différence S05-S97.	47
Figure 1-10 - Variogrammes de S97 (top) et S05 (bas à droite) et variogrammes croisés S97xS05 (bas à gauche) pour le groupe NG3 (TS21-TS36).	49
Figure 3-1 – Schematic representation of the basic theoretical semivariograms, with their most relevant parameters: the range, or the maximum correlation distance; the sill, or the variance at h=0; and nugget-effect.	65
Figure 4-1 - Location of the heavy and extra-heavy oil sands occurrences in Alberta and Saskatchewan states, Canada. The red arrow locates the Senlac oil pool (modified from Dusseault, 2002).	88
Figure 4-2 – Stratigraphic column illustrating the primary oil sands and heavy oil occurrences in Alberta, Canada (from www.lloydminsterheavyoil.com).	89
Figure 4-3 – Steam Assisted Gravity Drainage (SAGD) scheme (from www.encana.com). ..	90
Figure 4-4 - SENLAC time-lapse seismic surveys and SAGD wells location (Li et al., 2001). The studied area is represented by the yellow box.	91
Figure 4-5 - Inline seismic sections from AMP90, AMP97 and AMP98 (from left to right). The main interpreted horizons used to define the Reservoir and the Non-Reservoir zones are indicated.	95
Figure 4-6 – Histograms of the three SENLAC seismic volumes.	97
Figure 4-7 – Cumulated histograms of the three SENLAC seismic volumes.	97
Figure 4-8 – QQ-Plots of the three SENLAC seismic volumes.	97
Figure 4-9 – Scatter plots. The linear regression is shown as a red line, whereas the continuous black represents the conditional expectation curve and the dotted curves the standard deviation around the conditional expectation.	98
Figure 4-10 – Histograms of the NON Reservoir zone.	100
Figure 4-11 – Cumulated histograms of the Non-Reservoir zone.	100
Figure 4-12 - QQ Plot of the Non-Reservoir Zone.	100

Figure 4-13 – Scatter plots of the Non-Reservoir zone. The linear regression is shown as a red line, whereas the continuous black line represents the conditional expectation curve, and the dotted curves the standard deviation around the conditional expectation.....	100
Figure 4-14 – Histograms of the SENLAC Reservoir Zone.	103
Figure 4-15 –Cumulated histograms of the SENLAC Reservoir Zone.....	103
Figure 4-16 – Q-Q plots of the Reservoir Zone.	103
Figure 4-17 – Scatter plots of the Reservoir Zone. The linear regression is shown as a red line, whereas the continuous black represents the conditional expectation curve and the dotted curves the standard deviation around the conditional expectation.....	104
Figure 4-18 – The same scatter from Fig. 3.4-13, where the colors represent the number of points at each plot position.....	104
Figure 4-19 – Variogram (first row) and cross-variogram (second row) maps for the non-reservoir (left) and reservoir (right) zones, for the three SENLAC seismic datasets AMP90, AMP97 and AMP98. Scale of variance values in squared seismic amplitude unities. All variograms and cross-variograms with maximum search distance equal to 20 lags (or 400m).	108
Figure 4-20 – Non-Reservoir Zone experimental variograms and cross-variograms (thin lines) and final nested modeled variograms and cross-variograms (thick lines), with inline and cross-line directions indicated by red and green colors, respectively. Horizontal scale in meters and vertical scale in squared amplitude values, with experimental variances: AMP98=1,73.e+8; AMP97=1,69.e+8; AMP90= 1,80.e+8; AMP97xAMP98=AMP97xAMP90=1,63.e+8; AMP98xAMP90=1,67.e+8.....	110
Figure 4-21 – Reservoir Zone experimental variograms and cross-variograms (thin lines) and final nested modeled variograms and cross-variograms (thick lines), with inline and cross-line directions indicated by red and green colors, respectively. Horizontal scale in meters and vertical scale in squared amplitude values, with experimental variances: AMP98=1,56.e+9; AMP97=1,62.e+9; AMP90= 1,39.e+9; AMP97xAMP98=1,56.e+9; AMP99xAMP90=1,44.e+9; AMP97xAMP90=1,46.e+9.....	112
Figure 4-22 –The 12 resulting orthogonal factors estimated from 4 structures and 3 input data on the Non-Reservoir Zone, corresponding to the 10 th horizon-slice (from top to bottom). Numbers (in %) correspond to the contribution of each factor to the total variance.	119
Figure 4-23 – The 12 resulting orthogonal factors estimated from 4 structures and 3 input data on the Reservoir Zone, corresponding to the reservoir top horizon-slice. Number (in %) correspond to the contribution of each factor to the total variance.....	119
Figure 4-24 – Raw (left) and filtered (right) maps of the Reservoir top from AMP90 dataset. The factors filtered out correspond to small range structures C0 and C1.	122
Figure 4-25 – AMP90 (left) and AMP97 (right), after filtering the factors corresponding to structures C0 and C1.	122
Figure 4-26 – Experimental variograms from Senlac Reservoir zone corresponding to AMP90, AMP97 and AMP98, from top to bottom, respectively. Red and green lines corresponding to the inline and crossline directions. The trend in the inline direction is modeled by an exponential function, corresponding to the blue line.....	125
Figure 4-27 - Experimental cross-variograms from Senlac Reservoir zone corresponding to AMP90xAMP97, AMP90xAMP98 and AMP97xAMP98, from top to bottom, respectively. Red and green lines corresponding to the inline and crossline directions. The trend in the inline direction is modeled by an exponential function, corresponding to the blue line.	126
Figure 4-28 - Senlac Reservoir zone experimental variograms and cross-variograms (thin lines), and final nested modeled variograms and cross-variograms (thick lines) after	

removing the drift in the inline direction. Inline and crossline directions are indicated by red and green lines, respectively.	128
Figure 4-29 – Final amplitude maps corresponding to the Senlac reservoir top, AMP90 dataset. On the right, filtered map before the inline trend removal (on the right) and after (on the left).	129
Figure 4-30 – Simultaneous trace classification scheme, using three seismic volumes (Lucet et al., 2001).	131
Figure 4-31 – Definition of the optimal number of modal classes for the raw data.	133
Figure 4-32 - Definition of the optimal number of modal classes for the filtered data.	133
Figure 4-33 - Optimal number of learning traces is achieved by keeping constant $K = 32$ and analysing the evolution of the number of traces assigned to each class.	135
Figure 4-34 – Supervised facies classification (Dequirez et al., 1995), showing the 4 seismic facies related to reservoir quality. The black square corresponds to the present studied area, and the black lines to the horizontal well pairs.	138
Figure 4-35- Resulting facies maps from Unsupervised Classification using 5 classes. Top row showing facies maps computed on the raw data, whereas bottom row on the filtered data.	139
Figure 4-36 – Probability of assignment maps for 5 classes. Top row showing facies maps computed on the raw data, whereas bottom row on the filtered data.	139
Figure 4-37 - Resulting facies maps from Unsupervised Classification using 9 classes. Top row showing facies maps computed on the raw data, whereas bottom row on the filtered data.	142
Figure 4-38– Probability of assignment maps for 9 classes. Top row showing facies maps computed on the raw data, whereas bottom row on the filtered data.	142
Figure 4-39 – Maps of class change (9 classes) from AMP90 to AMP97 (left) and from AMP90 to AMP98(right), for the raw datasets. White colors indicate no facies change.	143
Figure 4-40 – Maps of class change (9 classes) from AMP90 to AMP97 (left) and from AMP90 to AMP98 (right), for the filtered datasets. White colors indicate no facies change.	143
Figure 4-41 - Temperature effect on compressional and shear velocities in a heavy oil reservoir (after Wang, 2001).	147
Figure 4-42 - Schematic representation of main pressure effects with depth (modified from Bruce and Bowers, 2002).	151
Figure 4-43 - Seismic traces taken from five different locations in the Senlac seismic survey, where the reservoir top and bottom are indicated by blue and black markers, respectively. Traces with grey-to-black colors represent the base surveys S90, whereas the blue and red traces represent the monitor surveys S97 and S98, respectively.	156
Figure 4-44 – Well A used as input to the pore pressure modeling. Logs registered prior to the start of the oil production. Rectangle in red corresponding to the reservoir limits, with top defined by the TopDina marker at approximately 522 ms, and the bottom defined by the geological marker Paleo at 534 ms.	157
Figure 4-45 – Seismic traces resulting from pore pressure modeling. On the left, traces in red (S1) and orange (S2) corresponding to a pore pressure reduction (under pressure condition). On the right, traces S3 to S5 resulting from the over pressurization of the reservoir interval. The central trace on both sides corresponds to the raw trace.	161
Figure 4-46 – The same as in Figure 4-45, considering the scenario 6, corresponding to very low pore pressure.	162

Figure 4-47 – Environmental scanning electron microscope (ESEM) photomicrography taken from one SENLAC heavy oilfield sample, before (a) and after (b) washing the sample by using solvents to remove the oil derived cement (extracted from Rokosh et al., 2004).	167
Figure 5-1 - Location map of the most important producing offshore oilfields from Campos Basin, operated by PETROBRAS.	173
Figure 5-2- Schematic diagram showing the Marlim and South Marlim fields, and the oil and gas production facilities.	174
Figure 5-3 –Representative seismic section from Marlim Field, showing the most relevant sedimentary megasequences from the Campos Basin stratigraphy (from Bruhn, 1998). Seismic reflections that correspond to the reservoir and to the regional geological marker are indicated in the figure by MRL and Marker Bed Blue, respectively.	177
Figure 5-4- Amplitude map representing the Marlim reservoir with the external limits of the three seismic surveys.	180
Figure 5-5 - Matching filter resulting time-shifts, extracted from crossline PP' as shown in Figure 5-8, for different horizons: (a) W Marker, above the reservoir; (b) MRL Top reservoir top; (c) MRL Bottom reservoir bottom; and (d) Blue Marker.	183
Figure 5-6 – Cross-equalization processing sequence applied to the S97 and S05 seismic datasets. (modified from PETROBRAS internal report, 2006).	184
Figure 5-7 - Schematic representation of the seismic cell size before (red for S97 and blue for S97) and after the cross-equalization processing (green). In both S97 and S05 surveys the N123 direction coincides with the Inline direction.	185
Figure 5-8 - Cross-line seismic section (XL 6073) extracted from the S05 volume, showing the interpreted horizons. In black, the segments of the main fault that limits the reservoir to the east and the northeast. Bad seismic quality zones due to the presence of obstacles represented by a red rectangle	187
Figure 5-9 – Seabottom amplitude map, extracted from the S05 monitor survey. The white polygons represent the area of influence of the operational obstacles present at the time of the S05 acquisition campaign, and the impact on the final cross-equalized time-lapse data.	189
Figure 5-10 - Blue marker top reflector amplitude maps of the S05 monitor (left) and S97 base (right) surveys.	190
Figure 5-11 – Amplitude maps from Marlim top reflector, with S05 monitor survey data on the left and S97 base survey on the right. The black polygon represents the Marlim reservoir limits.	191
Figure 5-12 – Amplitude maps from Marlim bottom horizon, with S05 monitor (left) and S97 base (right) surveys.	191
Figure 5-13 – Vertical seismic amplitude section from the inline direction. From top to bottom, S05 monitor survey, S97 base survey, and the difference DifS05-S97 (vertical scale in ms and horizontal in m). The difference amplitude section shows events exhibiting a spatial continuity due to the non-optimality repeatability conditions between base and monitor surveys.	195
Figure 5-14 – Experimental variograms from Marlim field GQ area, showing the variability in the inline direction, coincident with the main dip direction. S05 and S97 surveys, corresponding to the blue and green lines, showing a similar behavior. S97_NW data (inred) where no matching filter was applied with higher variability.	197
Figure 5-15 - Same as Figure 5-14, for the Crossline direction, and orthogonal to the main dip direction.	197
Figure 5-16 – Same as Figure 5-14, along the vertical direction (time axis).	198

Figure 5-17 - Inline seismic section from the Marlim field. The RM2 and RM2' horizons represent the inferior and superior limits of the window of interest. Vertical and horizontal scales are in milliseconds (TWT) and meters, respectively.	200
Figure 5-18 – Flattened amplitude seismic S05 survey section using the RM2 horizon as reference bottom (vertical time scale in milliseconds (TWT)).	201
Figure 5-19 – Inline seismic profile (top) and the correspondent geological schematic section (bottom). The Blue Marker displays a good seismic signature, which is not observed in other important geological markers from the Campos Basin (from Bruhn, 1998).	202
Figure 5-20 – Average variance values computed for each time-slice. Green curve represents the variance difference (%) relative to S97 data. S05 variance values are smaller than S97 only between time-slices TS30 and TS44.	204
Figure 5-21 - Same as in Figure 5-20, for the mean amplitude values.	204
Figure 5-22 – Amplitude maps corresponding to the topmost (first row) and bottommost (second row) time-slices from Group G1. From left to right, the three columns correspond to the S05, S97 and difference Dif S05-S97 datasets.	211
Figure 5-23 - Histograms corresponding to the S05, S97 and difference Dif S05-S97 data values distributions, for time slices Group G1. No major differences observed in terms of amplitude distribution when comparing the two vintage histograms, but a higher concentration of null values and smaller variance of S97 data.	211
Figure 5-24 – Comparative quantile-quantile distribution plots for Group G1, corresponding to S05, S97 and DifS05-S97 data, from left to right.	211
Figure 5-25 – Same as in Figure 5-22, for Group G2. Inline oriented spatial structures are predominant in the centre of the time-slices, and are more pronounced in the Dif S05-S97 data.	214
Figure 5-26 – Same as in Figure 5-23, for Group G2.	214
Figure 5-27 – Same as in Figure 5-24, for Group G2.	214
Figure 5-28 - Same as in Figure 5-22, for Group G3.	215
Figure 5-29 - Same as in Figure 5-23, for Group G3.	216
Figure 5-30 - Same as in Figure 5-24, for Group G3.	216
Figure 5-31 - Same as in Figure 5-22, for Group G4, including the intermediary TS25 time-slice amplitude maps.	218
Figure 5-32 – Same as in Figure 5-23, for Group G4.	218
Figure 5-33 - Same as in Figure 5-24, for Group G4.	219
Figure 5-34 - Same as in Figure 5-31, for Group G5.	221
Figure 5-35 - Same as in Figure 5-23 for Group G5.	222
Figure 5-36 - Same as in Figure 5-24 for Group G5.	222
Figure 5-37 - Same as in Figure 5-31, for Group G6.	224
Figure 5-38 - Same as in Figure 5-23, for Group G6.	224
Figure 5-39 – Same as in Figure 5-24, for Group G6.	225
Figure 5-40- Same as in Figure 5-31, for Group G7. The bottommost time-slice (TS50) from G7 corresponds to the flattened Blue marker reference horizon.	227
Figure 5-41 - Same as in Figure 5-24, for Group G7.	228
Figure 5-42 - Same as in Figure 5-23, for Group G7.	228
Figure 5-43 – Structural modelling results for Group G1, corresponding to time-slices TS01-TS06. Thin and thick lines correspond, respectively, to the experimental and theoretical variograms, whereas green and red colours to the crossline and inline directions, respectively.	233
Figure 5-44 - Same as in Figure 5-43, for Group G2.	234
Figure 5-45 - Same as Figure 5-43, for Group G3.	236
Figure 5-46 – Same as in Figure 5-43, for Group G4.	238

Figure 5-47 - Main characteristic dimensions of the turbiditic lobe geometry interpreted from time-slice TS26, G4, supporting the modelled structures of the variograms and cross-variograms. The thick black line suggesting the lobe system limits, as interpreted from the reservoir top anomalies. Dashed line indicates the main depositional axis.	239
Figure 5-48 – Same as Figure 5-43 , for G5, corresponding to time-slices TS29-TS36.....	240
Figure 5-49 – Same as Figure 5-43 for Group G6.	241
Figure 5-50 – Same as Figure 5-43, for G7.....	243
Figure 5-51 - Structural correlation coefficients computed for all spatial structures in the inline direction. Correlation coefficients are plotted as a function of the structure range.	247
Figure 5-52 – The same as in Figure 5-51, for the crossline direction.....	247
Figure 5-53 – TS26 time-slice amplitude values corresponding to orthogonal factors F1 (left) and F2 (right).....	253
Figure 5-54 - Amplitude values for TS26 time-slice.	254
Figure 5-55 - Scatter diagram of factors F1 and F2 computed for all time-slices from group G4. No linear correlation is observed.....	255
Figure 5-56 – Scatter plots of Factor 1 (left) and Factor 2 (right) and the difference Dif S05-S97. Scatter plots are computed for all time-slices from Group G4.	255
Figure 5-57 – Crossline seismic section from S97 survey showing the time-interval from TS01 to TS12, above the Marlim reservoir. The interval between time-slices corresponds to one sampling interval, or 4ms, vertical exaggeration of approximately 10 times.	257
Figure 5-58 - Same as in Figure 41, for the inline direction. Vertical exaggeration of approximately 20 times.	257
Figure 5-59 – TS10 time-slice, amplitude map of S05 (left) and S97 (right) surveys.....	259
Figure 5-60 – Experimental (thin) and modelled (thick) cross-variograms computed on group NG1	260
Figure 5-61 - Same as in Figure 5-60, for NG2.	262
Figure 5-62 – Vertical crossline section from S97 survey showing the TS21 to TS36 time interval. This zone corresponds to the main Marlim reservoir zone. Vertical exaggeration of approximately 10 times and vertical time scale in ms (TWT).....	262
Figure 5-63 - Variograms of S97 (top) and S05 (bottom right) and cross-variogram S97xS05 (bottom left) for group NG3 (TS21-TS36) including all time-slices from the Marlim reservoir level.	264
Figure 5-64 – Same as Figure 5-63, for group NG4.	266
Figure 5-65 – Same as Figure 5-63, for group NG5.	268
Figure 5-66 - Structural correlation coefficients computed for all spatial structures in the inline direction, plotted as a function of the structure range.	270
Figure 5-67 – Same as Figure 5-66, for the crossline direction.	270
Figure 5-68 – Experimental (thin lines) and modeled (thick lines) variograms computed for the variable DifS05-S97, computed for each new group of time-slices from NG1 to NG5.	272
Figure 5-69 - Definition of the Noise Free (blue) and Noisy (red) areas. The black polygon represents the limits of the Marlim reservoir.	276
Figure 5-70 -Average amplitude (a) and variance (b) traces computed in Noise free area, where the horizontal axis corresponds to the time-slice numbering. Left vertical axis representing variance unities (squared amplitude values) and, on the right, difference of variance from S05 and S97 data, in percentage.	278
Figure 5-71 – The same as in Figure 5-70, computed in the noisy area.	279
Figure 5-72 - Amplitude time-slices from TS06 representing the Non-Reservoir interval. ..	280

Figure 5-73 – Experimental variograms and cross-variograms for S97 and S05 datasets, corresponding to the Non-reservoir zone from group NG1 (TS01-TS12). Noise Free area data on the left, and the Noisy area on the right.....	280
Figure 5-74 - Same variogram functions as in previous figure, highlighting the first 1,500m of range.	282
Figure 5-75 – Experimental (thin) and theoretical (thick) variograms and cross-variograms for group NG1 (TS01-TS12) corresponding to the Noisy area.	284
Figure 5-76 - Cross-variograms for S05 and S97, corresponding to group NG1 (TS01-TS12). These variograms and cross-variograms were computed with the same parameters, but considering different areas. On the left, data corresponding to the original area, whereas on the right it corresponds to the Noise Area.....	285
Figure 5-77 – Results after filtering the short range C1 structure of variable S05 from time-slice TS11 of group NG1. Raw data on the left and filtered on the right, with black polygon corresponding to the interpreted reservoir limits.	287
Figure 5-78 – Same as in Figure 5-77 Figure 5-77, for the S97 data.....	287
Figure 5-79 - Experimental variograms and cross-variograms for S97xS05 corresponding to group NG3(TS21-TS36), in the Marlim reservoir zone. Identical calculation parameters were used. Noise Free area graphs displayed on the left, while for the Noisy Area on the right.	288
Figure 5-80 – Amplitude map corresponding to time-slice 26 (TS26), from Marlim reservoir interval NG3. The map corresponds to the difference of raw data.	289
Figure 5-81 – As in Figure 5-81, but corresponding to the difference of the data S05 and S97 after filtering the short scale structure C1.	289
Figure 0-1 - Model of packing of spheres submitted to normal and tangential forces F and T (from Mavko et al., 1998).	320
Figure 0-1 – Variogram map computed for the Blue marker amplitude map horizon taken from S05 monitor survey.....	323
Figure 0-2 – Cross-variogram map computed for the Blue marker amplitude map horizon, considering both the S05 monitor survey and S97 base survey.	323
Figure 0-3 - Variogram map computed for the Blue marker amplitude map horizon taken from S97 base survey.	323
Figure 0-4 - Variogram map computed for MRL Top horizon amplitude map horizon taken from S05 monitor survey.....	324
Figure 0-5 - Cross-variogram map computed for MRL Top amplitude map horizon, considering both the S05 monitor survey and S97 base survey.....	324
Figure 0-6 - Variogram map computed for the MRL Top amplitude map horizon taken from S97 base survey.	324
Figure 0-7 - Variogram map computed for MRL Bottom horizon amplitude map horizon taken from S05 monitor survey.	325
Figure 0-8 – Cross-variogram map computed for MRL Bottom horizon amplitude map horizon taken from S05 monitor and S97 base survey.....	325
Figure 0-9 - Variogram map computed for the MRL Bottom amplitude map horizon taken from S97 base survey.	325

List of tables

Table 1-1 – Paramètres résultant de la modélisation structurale, groupe NG3. Entre parenthèses, la contribution (en pourcentage) de la variance dans les directions inline et crossline.	48
Table 4-1 – Senlac seismic field acquisition parameters (extracted from Li et al., 2001).	92
Table 4-2 - Univariate statistics from SENLAC seismic volumes.....	98
Table 4-3 - Univariate statistics from SENLAC seismic volumes.....	98
Table 4-4 - Correlation coefficients computed for the entire seismic data time interval.	98
Table 4-5 - Univariate statistics from SENLAC seismic volumes for the Non Reservoir Zone.....	101
Table 4-6 - Continued univariate statistics from SENLAC seismic volumes for the Non Reservoir Zone.	101
Table 4-7 - Correlation coefficient computed for the Non Reservoir Zone.....	101
Table 4-8– Univariate statistics from SENLAC seismic volumes for the Reservoir Zone.	104
Table 4-9 - Univariate statistics from SENLAC seismic volumes for the Reservoir Zone.	104
Table 4-10– Correlation coefficient computed for the reservoir zone data.....	105
Table 4-11– Final structural models and coregionalization matrices for the 4 (four) structures interpreted in the Non-Reservoir Zone.	109
Table 4-12 Reservoir Zone nested variograms and cross-variograms fitting parameters and the final coregionalization matrix.	111
Table 4-13– Structural correlation coefficients of the variance-covariance matrices in the Non-Reservoir Zone.	113
Table 4-14– Structures correlation coefficients from the variance-covariance matrices, in the Reservoir Zone.	113
Table 4-15- Non-Reservoir Zone diagonalization of the coregionalization matrix.	116
Table 4-16-Reservoir Zone diagonalization of the coregionalization matrix.....	116
Table 4-17– Contribution of each computed orthogonal factor for each structure in the Non Reservoir Zone.	117
Table 4-18– Contribution of each computed orthogonal factor for each structure in the Reservoir Zone.	117
Table 4-19 – Reservoir zone nested variograms and cross-variograms fitting parameters after removing the inline non-stationarity.	127
Table 4-20 – Pressure gradients as a function of fluid type or density.	150
Table 4-21 – Senlac main reservoir properties (from Edmunds and Suggett, 1995). ..	155
Table 4-22 – Initial reservoir pressure conditions, before SAGD steam injection.....	157
Table 4-23 – Main parameters used in the seismic modeling of the pore pressure effects. ($P_{conf}=16.8$ MPa).	157
Table 4-24 – The same as in Table 4-23, for the new scenario S6. Model S2 was kept as a reference.....	162
Table 4-25 – Elastic properties of the components of the different phases of the Senlac data, with V_p in m/s, ρ in kg/m^3 and $K + \frac{4}{3}\mu$ in Pa.....	165
Table 4-26 – Theoretical bounds of the effective properties computed for the cases after and before steam injection.....	165

Table 5-1 – Seismic acquisition parameters from seismic campaigns recorded in the Marlim field.....	179
Table 5-2 – Limits of the study area. In brackets, the original Marlim seismic dataset limits.....	194
Table 5-3 - Statistical description of flattened time-slices.....	205
Table 5-4 - Definition of time-slices groups.....	207
Table 5-5 - Statistical data computed for each group of time-slice, for S05 seismic campaign.....	229
Table 5-6 - Same as in Table 5-5, for the S97 campaign.....	230
Table 5-7- Resulting modelling parameters from structural analysis of Group G1. In brackets, the percentage of the total variance explained by each structure, in the inline and in the crossline direction, respectively.....	232
Table 5-8- Same as Table 5-7, for Group G2.....	234
Table 5-9 - Same as Table 5-8, for Group G3.....	236
Table 5-10 – Same as Table 5-7, for Group G4.....	238
Table 5-11 – Same as in Table 5-7, for Group G5.....	240
Table 5-12 – Same as Table 5-7, for Group G6.....	241
Table 5-13 – Same as Table 5-7, for Group G7.....	243
Table 5-14 - Summary of all correlation coefficients for all time-slice Groups G1 to G7.....	247
Table 5-15 – New time-slice clustering based on previous results, reducing to five the number of clusters.....	256
Table 5-16 – Main statistical parameters for all time-slice groups.....	256
Table 5-17- Resulting modelling parameters from structural analysis of Group NG1. In brackets, the percentage of the total variance explained by each structure, in the inline and in the crossline direction, respectively.....	259
Table 5-18 - Same as Table 5-17, for group NG2.....	261
Table 5-19 – Resulting structural modeling parameters for group NG3. In brackets, the variance contribution in the inline and crossline directions (in percentage).....	263
Table 5-20 – Same as in Table 5-17, for the Group NG4.....	267
Table 5-21 – Same as in.....	267
Table 4 -5-22 - Main structures identified on the volume of differences Dif_S05-S97. From top to bottom, parameters computed for all new groups of time-slices NG1 to NG5.....	273
Table 5-23 – Summary of the spatial features for the Noise free and Noisy zones.....	282
Table 5-24 – Resulting modelling parameters from structural analysis, NG1 in Noisy area.....	284
Table 5-25 – Resulting modelling parameters from structural analysis of the Noise Free area.....	288

Abstract

This thesis research aims at investigating seismic interpretation methodologies and techniques that will help to better characterize the time-lapse, or 4D, seismic signatures. These techniques and methodologies are used first to evaluate the time-lapse repeatability and then to filter out undesirable artifacts that are non-related to the production, while enhancing the 4D signature.

In Chapter 1, an expanded resume of the thesis, written in French, is presented. Chapter 2 introduces the problem under study and outlines the main objectives of the thesis. In Chapter 3, a theoretical review of the most relevant geostatistical concepts and methods is introduced. The Factorial Kriging technique, based on the concept of Kriging Analysis (Analyse Krigeante) developed by Matheron in 1982, is presented, and applications of this technique in different domains are described, including geochemistry, geophysics and image processing. Then, a theoretical comparison with conventional seismic data filtering techniques, such as the Single Value Decomposition and Spectral Analysis, is presented.

In Chapter 4, an application of the proposed Factorial Kriging filtering methodology to the Senlac heavy oilfield, Canada, is described. First, a description of the geology, of the enhanced oil recovery technique and of the time-lapse seismic data is provided. Secondly, a comprehensive statistical analysis of the seismic datasets is presented. The application of the Factorial Kriging methodology to filter out spatial structures that were characterized as related to the acquisition noise is described, as well as the obtained results. In this case, the Unsupervised Seismic Facies Classification technique was called upon to quantify the impact of the filtering technique. At the end of this chapter, a discussion of the effects of reservoir changes on seismic data is presented. As unexpected time-shift values were observed in the time-lapse seismic data from Senlac, the Hertz-Mindim geomechanical model was used to evaluate the velocity dependence on pressure. Additionally, compressional velocities were computed assuming different effective-medium theories to test for the effects of varying porosity, saturations and load-bearing mechanisms.

Chapter 5 is dedicated to the time-lapse study from Marlim Field, an offshore deepwater heavy oilfield submitted to water flooding to enhance oil recovery and for pressure maintenance. In this case, two seismic campaigns were shot at different calendar times, and the final seismic data was processed by a contractor following a cross-equalization procedure to minimize the acquisition discrepancies. An exhaustive geostatistical analyses was performed to better understand and discriminate between possible events associated to time-lapse effects, geology and different types of noise. In this particular case, the introduction of the volume of the difference between the time-elapsd volumes in the proposed geostatistical methodology helped to better understand the different time-lapse effects.

The final conclusions of the results obtained are summarized in Chapter 6, as well as perspectives for future work.

Chapter 1 - Résumé (en français)

1.1. Introduction

Une gestion optimale de réservoir implique désormais l'acquisition quasi systématique de données de sismique 3D répétée (données 4D). Il s'agit donc de répéter une acquisition sismique 3D au cours du temps, généralement avant (« base survey ») et ensuite au cours de la production (« monitor survey »). L'utilité de ce type de données a été démontrée, par comparaison d'images du réservoir au cours de la production. On peut ainsi prédire des événements indésirables, tels que des venues d'eau ou détecter des zones non drainées. Néanmoins, l'exploitation des données 4D est aujourd'hui limitée aux interprétations qualitatives. L'interprétation quantitative des données de sismique répétée est loin d'être opérationnelle, et les travaux élaborés au cours de cette thèse ont pour objectif d'améliorer ce type d'interprétation.

L'exploitation des mesures de sismique répétée repose sur le principe que les variations du signal sismique au cours du temps traduisent les variations de pressions, de température et de saturations du réservoir suite aux mécanismes de la production. Le corollaire est que les variations de la mesure sismique en dehors du réservoir devraient être quasi-nulles, ce qui n'est généralement pas vérifié du fait des variations des conditions expérimentales de l'acquisition (équipements et dispositifs, météo, etc.); ces variations ne peuvent être totalement corrigées par les opérations de traitement classiques spécifiques aux données 4D. Les paramètres clé du succès d'une campagne de sismique répétée reposent sur deux notions de base : la répétitivité et la détectabilité. La répétitivité est une mesure de la ressemblance entre deux campagnes sismiques en termes d'acquisition et de traitement sismiques. Il est évident que plus la répétitivité est grande, plus grandes sont les chances de détecter et quantifier des changements dans le réservoir au cours du temps. La détectabilité est liée à la facilité d'identifier des changements au cours du temps, associés à des variations en termes de saturation en fluides, pression et température. Ce paramètre dépend du réservoir lui-même, et également de la résolution sismique. Une combinaison optimale de répétitivité et de détectabilité permet d'assurer le succès d'une campagne de sismique 4D.

L'objectif de la thèse est de développer des méthodologies d'interprétation permettant de caractériser et d'exploiter au mieux les variations des traces sismiques au cours du temps calendaire. Ces méthodologies sont tout d'abord utilisées pour évaluer la répétitivité des campagnes sismiques, puis pour filtrer les données afin d'éliminer les bruits indésirables qui ne sont pas liés à la production et produire ainsi des données « nettoyées » dans lesquelles la signature 4D sera plus lisible.

Le Chapitre 3 présente une revue théorique des concepts et méthodes géostatistiques. La technique de Krigeage Factoriel, basée sur l'analyse krigeante développée par Matheron en 1982, est présentée, ainsi que des applications de cette méthode dans différents domaines tels que la géochimie, la géophysique et le traitement du signal. Une comparaison théorique entre cette dernière technique et des techniques plus couramment utilisées pour le filtrage des données sismiques telle que la décomposition en valeurs singulières ou l'analyse spectrale, est ensuite présentée.

Le Chapitre 4 décrit une application de la méthode de krigeage factoriel sur le jeu de données réelles de Senlac, champ d'huiles lourdes canadien. Après une description de la géologie et de la technique de récupération de l'huile lourde par injection de vapeur, une première analyse des données sismiques permet de les comparer en termes statistiques, et d'évaluer la répétitivité. Après analyse variographique des trois campagnes disponibles, la méthode de krigeage factoriel a été utilisée pour filtrer les structures spatiales identifiées comme du bruit lié à l'acquisition. Une technique d'analyse en termes de faciès sismiques, appliquée sur les données brutes et filtrées, a ensuite permis d'évaluer la qualité de ce filtrage. La dernière partie du chapitre est consacrée à l'étude de l'impact des changements des paramètres réservoir sur les traces sismiques. En particulier, plusieurs hypothèses ont été étudiées à l'aide de modèles géomécaniques ou de lois de mélanges, pour expliquer les décalages en temps négatifs observés entre la campagne de base et les campagnes suivantes.

Le Chapitre 5 présente les travaux réalisés sur un autre cas réel de sismique répétée, le champ de turbidites de Marlim situé en mer profonde, au large du Brésil dans le bassin de Campos. Dans ce cas la production est assurée à l'aide d'injection d'eau, afin de maintenir la pression dans le réservoir. Deux campagnes sismiques 3D ont été

acquises sur ce champ ; elles ont ensuite été retraitées en parallèle par un contracteur en appliquant en particulier une technique de cross égalisation permettant de minimiser les différences liées à l'acquisition. Une étude variographique détaillée a ensuite été conduite afin d'identifier les structures liées à la géologie, aux divers bruits (acquisition ou autres) et enfin à la signature 4D. Dans ce cas particulier, l'utilisation du cube des différences d'amplitude entre les campagnes sismiques a permis de mieux comprendre les effets 4D observés.

Les conclusions finales sont présentées dans le chapitre 6, ainsi que des perspectives de travaux futurs.

1.2. Techniques de filtrage géostatistique appliquées aux données de sismique répétée

La technologie utilisant l'enregistrement de données sismiques répétées au cours du temps - la sismique 4D - utilise des images 3D enregistrées à plusieurs reprises sur la même zone, à différents temps calendaires. En comparant ces données sismiques, cette technologie vise à fournir des informations qualitatives et quantitatives que permettront d'améliorer la description des propriétés du réservoir pétrolier, à la fois statique et dynamique, au cours de la production d'hydrocarbures.

La compréhension du chemin préférentiel des parcours des fluides injectés dans le réservoir – des puits injecteurs aux producteurs - et également, une quantification du volume total compris dans les zones du réservoir non balayées peuvent contribuer à (i) la redéfinition des stratégies de gestion du réservoir, en incluant par exemple des forages supplémentaires (ii) économiser les coûts de forages planifiés dans des zones balayées, et (iii) équilibrer de manière optimale les taux d'injection et de production dans le gisement.

Dans une situation supposée idéale, les variations - dues à la production d'hydrocarbures - observées dans les données sismiques répétées ne devraient être détectables qu'au niveau du réservoir. C'est dans cette zone uniquement que l'on devrait pouvoir observer des changements de la saturation fluide, de la pression et de la température, suite à l'implémentation des processus primaire, secondaire ou tertiaire de

récupération amélioré de pétrole , si l'on suppose une absence de fuites à partir du réservoir.

Toutefois, lorsque l'on compare les données 4D entre elles, on constate fréquemment que des différences non négligeables entre valeurs de l'amplitude sismique peuvent être observées en dehors du réservoir. Ces artefacts résultent souvent de différences dans les paramètres d'acquisition et de traitement sismique, ou de l'utilisation d'une technologie plus moderne ou tout simplement différente.

En fonction du rapport signal / bruit des données sismiques, ces artefacts peuvent compromettre l'objectif principal d'un projet de sismique 4D, en augmentant les incertitudes associées à l'interprétation finale en termes, par exemple, de variations de pression et de fluides au niveau du réservoir étudié. Ces effets, non liés à la production d'hydrocarbures, peuvent avoir différents types de source, et sont le plus souvent détectés, même dans des données de bonne qualité supposées reproductibles (Eiken, 2001; Calvert, 2005).

Lors de l'interprétation des données 4D, et en particulier lors qu'on cherche des modèles spatiaux de distribution des hydrocarbures dans les réservoirs, on se heurte au problème de la décomposition de la trace sismique comme réponse à toutes les composantes qui ont été combinées pour produire la réponse sismique moyenne enregistrée. Ce processus de lissage est le résultat de la propagation des ondes à travers le sous-sol, qui atteignent différentes couches géologiques avec des caractéristiques différentes, et à des échelles différentes - de l'échelle microscopiques de distribution de grains, jusqu'au faciès réservoir puis à son l'architecture elle-même-. Les évènements dynamiques observés sur les données 4D, liés à la bande passante, montrent des structures spatiales qui dépendent des paramètres pétrophysiques, mais aussi des hétérogénéités du réservoir.

La géostatistique comprend une série d'outils permettant de caractériser des structures spatiales. Une de ces techniques, développée par Georges Matheron dans son article de 1982 Pour Une Analyse Krigeante des Donnés Regionalisées, est connue sous le nom de Krigeage Factoriel. Cette méthode repose sur le principe qu'une variable régionalisée peut être décomposée en un jeu de fonctions orthogonales. Ces fonctions

orthogonales peuvent être interprétées à l'aide de leurs caractéristiques spatiales, et associées à des phénomènes tels que des structures géologiques, des effets dus à la production ou encore à des structures liées à des bruits d'acquisition ou de traitement sismiques.

Beaucoup d'autres techniques ont été développées pour filtrer spatialement du bruit. Il s'agit par exemple de l'Analyse en Composantes Principales Généralisée (ACPG) (Voutay, 2003) ou de l'Analyse Canonique Généralisée (ACG). D'autres techniques, telle que la décomposition en valeurs singulières, basée également sur l'analyse en composantes principales, et les techniques de filtrage dans le domaine fréquentiel utilisant des transformées de Fourier, sont couramment utilisées dans l'industrie pour entreprendre le même type d'analyse et de filtrage de données (Ma et Royer, 1987, 1988; Galli, 1987). L'inconvénient de ces méthodes est qu'elles ne se basent pas sur la variabilité spatiale des données, au contraire des techniques de Krigeage Factoriel.

Au cours des séquences de traitement sismique classique, des techniques de filtrage fréquentiel 1D, appliquées trace à trace, sont fréquemment utilisées et de même que pour les techniques ACPG ou ACG, la structure spatiale des données ne peut pas être respectée.

1.2.1. La méthode du Krigeage Factoriel

La technique de krigeage factoriel (FK), proposée à l'origine par Georges Matheron, a été largement utilisée dans de nombreux domaines des géosciences pour décomposer divers types d'image, et fournir des outils de filtrage à travers l'utilisation de décomposition en facteurs orthogonaux.

Parmi les autres applications, le FK a été utilisé pour : traiter des images de radar (Ma & Royer, 1987); analyser des champs de vitesses sismiques (Coléou, 1987; Sandjivy, 2001); égaliser des données de sismique répétée (Coléou, 2001); filtrer des cartes d'amplitude (Mundim et al., 2001), analyser des données magnétiques et gravimétriques (Galli, 1987; Gilles, 1988) et des analyses géochimiques (Goovaerts, 1995 et Sandjivy, 1987). Plus récemment, de nombreux articles ont présenté des études climatologiques utilisant la technique FK.

Les conventions suivantes pour les indices et les variables seront retenues dans les développements ultérieurs.

- \mathbf{u} : vecteur des coordonnées (x,y,z) ;
- $Z_i(\mathbf{u})$: variable aléatoire régionalisée (REV);
- i : indice des volumes des données sismiques
- p : indice des structures spatiales contenues dans les données
- k : nombre de variables orthogonales, ou facteurs, qui sont limitées, par définition, au nombre maximum de variables d'entrée
- $\Gamma_p^i(\mathbf{u})$: composantes spatiale à la suite de la décomposition de $Z_i(\mathbf{u})$
- $\gamma_p(h)$: variogrammes de base admissible des modèles liés a la même structure spatiale, avec comme contrainte que la somme de toutes les paliers doit être égale à 1
- B_p : matrice carrée symétrique, définie positive, des paliers des structures spatiales
- $m_i(\mathbf{u})$: valeur moyenne de $Z_i(\mathbf{u})$
- $Y_p^k(\mathbf{u})$: correspond à la k^{th} variable orthogonal, ou facteur résultant de la décomposition de la structure spatiale $\Gamma_p^i(\mathbf{u})$, avec les propriétés suivantes

$$\begin{cases} m = 0 \\ Var(Y_p^k) = 1 \\ Cov(Y_p^k, Y_p^{k'}) = \delta_{kk'} \end{cases} \quad (1)$$

- $\delta_{kk'}$ fonction delta de Kronecker

Le but de la technique de FK est de décomposer une variable aléatoire régionalisée, tels que l'amplitude de traces sismiques enregistrées dans un point donné, en une somme de deux termes, dont un non-stationnaire et l'autre stationnaire, représentant une combinaison linéaire des structures spatiales indépendantes. Ce modèle linéaire peut être décrit comme suit

$$Z_i(x, y, z) = m_i(x, y, z) + \sum_{p=1}^P \Gamma_p^i(x, y, z) \quad (2)$$

Si l'on considère N fonctions aléatoires intrinsèques $Z_i(\mathbf{u})$, on dit que ces fonctions suivent un modèle linéaire de co-régionalisation si leurs variogrammes simple et croisé peuvent être décrits comme une combinaison linéaire de modèles de variogrammes de base γ_p , tel que

$$\gamma_{Z_i, Z_j} = \sum_{p=1}^P B_p \gamma_p \quad (3)$$

La procédure d'estimation de Γ_p^i dépend des hypothèses de stationnarité choisies; différentes approches de krigeage pourront être utilisées, selon le comportement de m_i , telles que le krigeage ordinaire avec m_i inconnu; krigeage simple avec m_i constant ou krigeage simple avec m_i variable et représenté par une carte (krigeage avec dérive externe).

Ce modèle linéaire peut être écrit comme le montre l'équation (2). L'estimation de chaque structure spatiale est effectuée en résolvant le système de krigeage suivant

$$\Gamma_p^i(x, y, z) = \sum_{\alpha} \lambda_{\alpha} Z_i(x, y, z) \quad (4)$$

où les coefficients λ_{α} sont des poids utilisés pour tous les points voisins α du point à estimer.

Soit I le nombre de composantes spatiales. En introduisant les coefficients a_p^{ik} , l'équation (2.45) est reformulée comme suit:

$$\Gamma_p^i(x, y, z) = \sum_{k=1}^K a_p^{ik} Y_p^k(x, y, z) \quad \forall i = 1, \dots, I \quad (5)$$

où Y_p^1, \dots, Y_p^N sont des facteurs indépendants, orthogonaux, de moyenne nulle ($E(Y_p^i Y_p^j) = 0, \forall i \neq j$), de variance 1 ($E\{(Y_p^i)^2\} = 1$), et de variogramme γ_p .

Si l'on remplace (58) dans Eq. (55) et (1.2), on obtient:

$$Z_i(x, y, z) = m_i(x, y, z) + \sum_{p=1}^P \sum_{k=1}^K a_p^{ik} Y_p^k(x, y, z) \quad \forall i = 1, \dots, I \quad (6)$$

De la même manière, il est possible de réécrire les variogrammes simples et croisés de la façon suivante:

$$\gamma_{Z_i Z_j} = \sum_{p=1}^P \sum_{k=1}^K a_p^{ik} a_p^{jk} \gamma_p \quad (7)$$

En supposant l'indépendance des facteurs orthogonaux Y_p^1, \dots, Y_p^N et des structures spatiales $\Gamma_1^i, \dots, \Gamma_p^i$, la covariance est donnée par:

$$\text{Cov}(Y_p^k, Y_p^k) = \delta_{pp} \delta_{kk} \quad (8)$$

En introduisant le coefficient

$$b_p^{ij} = \sum_{k=1}^K a_p^{ik} a_p^{jk} \quad (9)$$

le variogramme (60) peut être réécrit comme une somme linéaire des variogrammes des facteurs orthogonaux Y_p de la façon suivante:

$$\gamma_{Z_i Z_j} = \sum_{p=1}^P b_p^{ij} \gamma_p \quad (10)$$

où b_p^{ij} est la matrice des paliers de la structure spatiale p . L'équation (10) établit la relation entre les composantes structurales et les variogrammes des facteurs orthogonaux.

Enfin, l'application de la technique de krigeage factoriel peut être réalisée en deux étapes, comme suit:

- **Décomposition des structures spatiales en facteurs orthogonaux**, par diagonalisation de la matrice de variance-covariance \mathbf{B}_p . Une valeur propre λ_p sera associée à chaque facteur orthogonal Y_p , et permettra de quantifier la quantité d'informations provenant des variables aléatoires portée par chaque facteur.
- **Estimation des facteurs orthogonaux Y_p** par cokrigeage des mesures expérimentales, résolution du système de cokrigeage pour chaque facteur.

Lors de la mise en œuvre de l'analyse krigéante dans le cas multivarié, il faut noter la difficulté supplémentaire provenant du nombre croissant de variogrammes simples et croisés qui à ajuster. Ce nombre est fonction de la quantité N_v de variables considérées, et est égal à $N_v(N_v + 1)/2$.

1.2.2. Comparaison entre le Krigeage Factoriel, l'Analyse Spectrale et Decomposition en Valeurs Singulieres

Dans le Chapitre 3 de cette thèse, une comparaison entre la méthode issue de l'analyse krigéante et de deux autres techniques de filtrage, la méthode spectrale et la décomposition en valeurs singulières, est présentée avec plus de détails.

Dans l'analyse krigéante, ou dans le filtrage factoriel (FK), le but est de décomposer un phénomène, qu'il soit stationnaire ou non, dans ses propres fréquences caractéristiques dévoilées par l'analyse structurale (Sandjivy, 1984). Une approche équivalente est proposée par l'analyse spectrale (SA), encore appelée analyse de Fourier. Cette méthode utilise la décomposition d'une fonction, dans ce cas une fonction continue et périodique, en une somme de fonctions sinusoïdales, chacune avec amplitude, nombre d'ondes et phase différents. Le spectre d'amplitude et de phase des données d'entrée sont dérivés de la transformée de Fourier. L'Analyse Spectrale consiste à estimer et interpréter un élément caractéristique d'un processus stationnaire appelé la densité spectrale, ou le spectre. Le spectre est une mesure de la contribution de chaque fréquence à la variance du phénomène. Il existe, donc une équivalence entre le variogramme utilisé en géostatistique et la densité spectrale de l'analyse spectrale, ainsi que la fonction d'autocorrélation de l'analyse en séries temporelles (Solow, 1984).

Ma et Royer (1987, 1988), discutent le comportement des fonctions de pondération dans le formalisme du krigeage factoriel, en comparant ce formalisme avec celui issu de l'analyse spectrale appliqué dans le domaine des fréquences. Ces auteurs montrent que les fonctions de pondération du krigeage factoriel sont similaires aux filtres classiques utilisés en traitement d'image, pour un même modèle de covariance, ou variogramme.

Une autre technique se basant sur la décomposition de la matrice de covariance des données est la décomposition en valeurs singulières, ou Singular Value Decomposition (SVD), utilisées dans de nombreuses applications dans le traitement des données sismiques pour le filtrage (Freire et al, 1988, Mari, 2005), ou bien encore dans l'analyse de courbure (Bergbauer et al., 2003).

La SVD technique vise à décomposer les données matrice de variance-covariance en une combinaison linéaire de vecteurs propres orthogonaux avec les valeurs propres correspondantes. La plus grande valeur propre, ou valeur singulière, correspond à la plus basse des fréquences. Grâce à cette propriété, elle peut être utilisée comme une technique de filtrage.

1.3. Application du filtrage géostatistique au champ d'huiles lourdes de Senlac

Ce chapitre est dédié à l'application de la méthode de krigeage factoriel sur des données sismiques 4D acquises sur un champ d'huiles lourdes du Canada, le champ de Senlac. Une méthode de récupération améliorée du pétrole basée sur la technique Steam Assisted Gravity Drainage (SAGD) a été mise en œuvre sur ce champ. La sismique 4D a été proposée pour suivre l'évolution de la chambre de vapeur.

Trois campagnes sismiques ont été enregistrées à différents moments à Senlac: (a) en 1990, une campagne sismique de base, considérée comme la donnée 4D de référence ; (b) en 1997, une première acquisition "monitoring", enregistré dix-huit mois après le début de l'injection de vapeur; et (c) en 1998, la deuxième acquisition monitoring, enregistrée six mois plus tard. Ces données sismiques ont été enregistrées avec des paramètres d'acquisition très différents, et les données sismiques ont été soigneusement traitées afin de réduire les plus fortes différences observées entre elles (Li et al., 2001). On appellera les trois données sismiques acquies en 1990, 1997 et 1998 comme AMP90, AMP97 et AMP98.

Tout d'abord, une caractérisation statistique des données sismiques 4D de Senlac a été mise en œuvre; elle a contribué à une meilleure compréhension et a permis une description de la variabilité spatiale et des corrélations observées entre les volumes sismiques. Deux fenêtres temporelles différentes ont été analysés: la zone du réservoir et une autre zone non-réservoir, où des effets dus à la production n'étaient pas attendus.

L'étape suivante était la mise en oeuvre de la méthode d'analyse krigéante; elle comprenait: l'analyse variographique; l'estimation des facteurs orthogonaux; le filtrage des composantes associées à des artefacts ou des bruit sismiques, et la reconstruction des données sismiques. Finalement, afin de quantifier l'impact de la technique de filtrage géostatistique sur l'interprétation finale des résultats, une interprétation en termes de faciès sismiques utilisant une technique non-supervisée a été menée sur les données brutes et filtrées.

La dernière partie débat de l'interprétation des décalages en temps observés entre campagne en termes de changement des paramètres, en particulier des variations de pression. Il a été observé que, par rapport aux données sismiques de référence de 1990, les données monitor de 97 et 98 montraient des décalages en temps négatifs (effet de pull-up) dans l'intervalle du réservoir. Ce résultat est en désaccord avec ce qui est attendu à partir des modèles théoriques ou expérimentaux décrivant l'effet de la température, et de la saturation en fluides, sur les vitesses de propagation. C'est pourquoi une attention particulière a été portée sur les effets de la pression.

1.3.1. Description du jeu de données de Senlac

Le champ de Senlac appartient à un pool d'huiles lourdes situé à proximité de la frontière Alberta-Saskatchewan, au Canada. Le réservoir correspond à des grès non consolidés, déposés dans un environnement fluvial, au Crétacé Inférieur (formation Dina). La partie inférieure du réservoir contient surtout des grès massifs. La partie supérieure du canal de dépôt montre une augmentation du contenu en argiles, et est souvent composée d'intercalations de sables et d'argiles (zone de transition).

Ces réservoirs sont à faible profondeur, à environ 730 m (équivalent à 700 ms en temps double), avec une épaisseur moyenne de 15 m. De bonnes perméabilités (5-10 D) et une porosité moyenne de 33% (Dequirez et al., 1995; Li et al., 2001) sont observées. Par contre, le pétrole en place est de fortes densité (13 ° API) et viscosité (5000 cP) en conditions réservoir, imposant donc de sérieuses limitations à une production primaire.

1.3.2. Méthode de récupération assistée SAGD

Du fait des fortes densité et porosité rencontrées sur ce champ, une méthode thermique de récupération assistée des hydrocarbures a été mise en place. La méthode

Seam Assisted Gravity Drainage (SAGD) a donc été adoptée pour le champ de Senlac, et, d'un point de vue géophysique, elle est l'une des méthodes les plus intéressantes pour mettre en oeuvre une surveillance sismique, du fait de la forte sensibilité des propriétés acoustiques aux changements de température et de fluides dans le réservoir. Plusieurs applications de monitoring sismique sur des champs pour lesquels ce type de récupération utilisant des effets thermiques est utilisé, sont décrites dans la littérature (Lumley, 1995, Zhang et coll., 2004).

Cette méthode SAGD est implémentée à l'aide de doublets de forage horizontaux situés dans le réservoir, pour lesquels le puits injecteur est situé quelques mètres au-dessus du puits producteur. La vapeur est injectée dans le puits du haut, créant une zone où la température est augmentée, et fluidifiant ainsi l'huile qui peut s'écouler par gravitation jusqu'au puits producteur.

1.3.3. Données de sismique répétée

Trois campagnes de sismique 3D ont été acquises à des époques différentes de la vie du champ, afin de mieux comprendre l'évolution de la chambre de vapeur. Les paramètres d'acquisition sont très différents d'une campagne à l'autre, non seulement pour les directions d'acquisition des lignes et leur espacement, mais également pour le type de source utilisée.

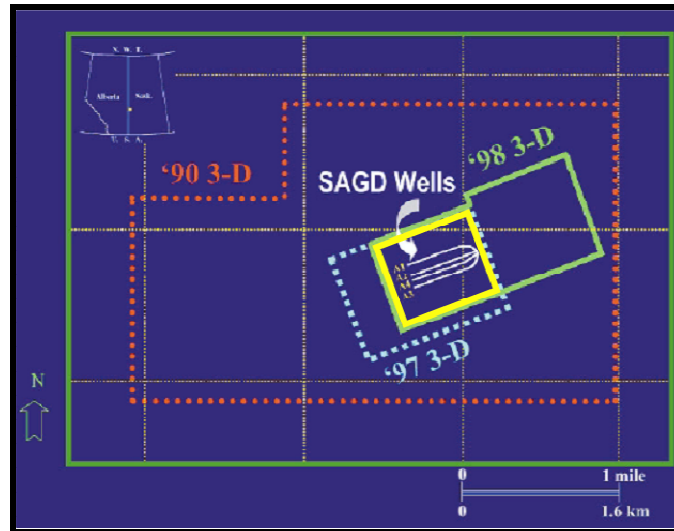


Figure 1-1 – Plan de position de SENLAC: Campagnes sismiques 4D et position des puits horizontaux SAGD (Li et al., 2001). La zone étudiée correspond au carré jaune.

Afin de compenser au mieux des différences d'acquisition entre les campagnes, un traitement 4D soigneux a été effectué par l'opérateur sur ces données sismiques, en se focalisant sur trois étapes importantes dans ce cas: le réalignement des données sur une grille commune, l'égalisation des amplitudes, et la cross-égalisation (Li et al., 2001).

1.3.4. Description statistique des données

L'objectif principal de cette phase de l'étude est d'explorer les caractéristiques des distributions de données, leur représentation statistique, ainsi que les relations entre les variables étudiées. Trois fenêtres temporelles différentes, extraites des trois campagnes sismiques, soit neuf fenêtres, ont été analysées .

La première fenêtre étudiée donne une description générale de l'ensemble des volumes sismiques, puisqu'elle couvre un grand intervalle de temps allant de 200ms à 1500ms, correspondant à 651 échantillons. Cette fenêtre sert de référence, à laquelle sont comparées deux autres fenêtres plus courtes : une en-dehors du réservoir et une dans le réservoir, qui correspondent, respectivement, à 49 et 12 échantillons. De cette analyse, on peut conclure que:

a) les données en amplitudes monitor AMPP97 et AMP98 montrent une distribution similaire, mais différent de la base AMP90, à la fois pour les zones non-réservoir et

réservoir. Ces différences peuvent peut-être s'expliquer par la géométrie d'acquisition assez proche pour AMP97 et AMP98, et différente pour AMP90 sur lesquelles une rotation de maillage ainsi qu'un "rebinning" ont dû être effectués.

b) Dans la zone non-réservoir, les valeurs d'amplitude sont représentées par une distribution normale, et sont assez proches de la distribution de l'ensemble des l'amplitude, comme indiqué dans le Paragraphe 3.2.1. Les trois distributions sont asymétriques, avec un biais négatif, et montrent une valeur modale proche de la valeur zéro en amplitude;

c) Une distribution bimodale caractérise les amplitudes de la zone du réservoir, ce qui peut s'expliquer par la taille de la fenêtre, beaucoup plus courte. Dans cette zone, une diminution globale de l'amplitude entre les données base et monitor peut être observée; cet effet peut être lié à la non-répétitivité, comme indiqué en (a), mais pourrait aussi être dû aux variations des propriétés acoustiques induites par l'exploitation du réservoir.

1.3.5. Krigeage Factoriel

Le principal objectif de ce travail est d'effectuer une caractérisation géostatistique pour identifier les structures sous-jacentes, présentes dans les données de sismique répétée. Ces structures pourront ensuite être interprétées en termes de géologie, de signal lié à la production, ou bien en termes de bruit qui pourront être filtrés après identification. Cette approche de caractérisation géostatistique semble également constituer un moyen pratique d'évaluer la qualité du traitement sismique de cross-égalisation, en fournissant des outils adéquats.

Les cartes de variogramme sont des outils très utiles pour évaluer la variabilité spatiale des variables aléatoires, pour déterminer leurs structures sous-jacentes et ainsi les principales directions de l'anisotropie.

Ces cartes de variogramme, calculées sur les amplitudes sismiques des trois cubes, dans les deux zones d'étude "réservoir" et "non-réservoir", montrent partout un comportement anisotrope, pour lequel les deux directions principales de continuité sont parallèles aux directions des lignes d'acquisition ("inline") ou perpendiculaires

(crossline). Dans la zone non-réservoir, la réponse anisotrope la plus complexe est observée pour les amplitudes AMP97.

Lorsque l'on compare les directions inline et crossline, l'analyse des cartes de variogramme sur la zone du réservoir révèle une anisotropie zonale, avec une plus grande continuité dans la direction crossline (V). Ces deux grandes orientations d'anisotropie sont également en accord avec l'axe principal de dépôt des chenaux fluviaux du réservoir Senlac, qui sont orientée E-NE/W-SW. Une plus forte variabilité est également observée dans la zone réservoir par rapport à la non-réservoir, d'un ou deux ordres de grandeur des valeurs de variance.

L'étape suivante est de modéliser les variogrammes en décomposant ceux-ci à l'aide de structures de base. Cette étape est fondamentale puisque c'est à partir de cette décomposition que l'interprétation de chaque structure, en termes de bruit indésirable ou au contraire d'évènement lié à la production, sera faite. Le choix des modèles est cependant tout à fait subjectif, et la décomposition obtenue n'est pas unique.

Dans cette étude, l'objectif était d'utiliser le moins de structures possible, afin d'éviter l'introduction d'un trop grand nombre de modèles difficilement interprétables sur plusieurs campagnes. Finalement, les variogrammes ont été décomposés en 4 structures, que ce soit dans la zone réservoir ou non réservoir, détaillées ci-dessous:

- Zone non-réservoir: deux structures sphériques de petit portée; une exponentielle de portée moyenne et une structure sphérique de grand portée.
- Zone réservoir: deux structures sphériques de petit portée, et deux autres exponentielles de portée moyenne, ont été identifiées. L'intervalle réservoir montre une variance largement plus grande que le non-réservoir; deux raisons physiques peuvent être avancées pour expliquer ces écarts : tout d'abord, les changements de faciès géologiques qui font augmenter le contraste des propriétés sismiques, et, dans une moindre mesure, les variations des propriétés sismiques suite à la mise en œuvre de la technologie SAGD

Après définition des variogrammes simples et croisés, les étapes suivantes sont:

(1) décomposer les structures spatiales en facteurs orthogonaux , par diagonalisation de la matrice de variance-covariance. La valeur propre associée à chaque facteur fournit une quantification de la quantité d'informations qui a été retenue dans chaque facteur de variables aléatoires,

(2) estimer les facteurs orthogonaux des mesures expérimentales, en résolvant le système de cokrigage pour chaque facteur.

Dans notre cas, on aura donc ($k=12$) douze facteurs orthogonaux estimés résultant de ($p=4$) quatre structures identifiées dans les trois ($i = 3$) cubes de données, dans les zones réservoir et non-réservoir.

Les Tableau 3-17 et 3-18 résumant les contributions à la variance totale de chaque facteur orthogonal, dans les zones non-réservoir et réservoir; on peut remarquer que:

les contributions des Facteurs 2 et 3 sont beaucoup plus élevées pour la zone non-réservoir que pour la zone réservoir;

les structures C1 et C2, de petite portée, (10x40 et 50x120m, respectivement) et anisotropie NE-SW, semblent liés à du bruit existant à la fois dans la zone non-réservoir et réservoir ;

les structures C3 et C4 sont de portée moyenne ou grande et peuvent refléter des informations géologiques redondantes dans les trois campagnes sismiques

1.3.6. Analyse en faciès sismiques

Disposant de deux jeux de données, l'un contenant les données brutes et l'autre les données filtrées, l'objectif est maintenant de quantifier l'impact du filtrage à l'aide d'une méthode d'interprétation telle que la classification en faciès sismiques.

Cette technique a pour but d'identifier et de regrouper ensemble, par "faciès sismique", les traces sismiques de forme similaire d'une population donnée. Elle permet la manipulation d'un grand nombre d'attributs sismiques, extraits à chaque trace sismique, pour les regrouper de façon pertinente afin d'être utilisés ensuite dans les

études de caractérisation de réservoir, ou de monitoring sismique comme dans le cas qui nous intéresse.

En fonction de la disponibilité des données et des objectifs de l'étude, deux types de mise en œuvre peuvent être utilisés: une classification non supervisée ou supervisée. Dans le premier cas, aucun a priori n'est introduit pour orienter le classement, alors que dans le deuxième cas, une information déduite par exemple des puits est introduite pour guider le classement. Dans cette étude de cas, la technique de classement de faciès sismique non supervisée est utilisée.

Description de la méthode

La méthode d'analyse en termes de faciès sismique non supervisée utilisée à l'IFP est une technique de classement qui comporte trois principales étapes: (i) l'estimation de la fonction de densité multivariée dans l'espace des attributs sismiques, (ii) la définition du nombre de modes naturels de la fonction densité, et (iii) l'analyse discriminante, permettant d'affecter chaque trace dans une classe, avec la probabilité d'affectation correspondante (Fournier, 2004).

Les volumes d'amplitudes sismiques, AMP90, AMP97 et AMP98, ont été filtrés en utilisant le krigeage factoriel présenté plus haut, en éliminant les composantes interprétées comme du bruit (C0 et C1). Ces versions filtrées, ainsi que les données brutes, ont servi de base à une classification en faciès sismiques. Dans les deux cas, douze (12) couches ont été extraites de l'intervalle de temps défini comme la zone du réservoir SENLAC, et ce sont ces douze attributs d'amplitude, obtenus pour chaque trace, qui ont servi de base à l'espace dans lequel la classification a été menée. Chaque trace sismique est donc représentée par un point dans cet espace.

Au lieu d'effectuer un classement des traces sismiques sur chaque cube séparément, une procédure de classement simultanée des traces des trois cubes (Lucet et al., 2001) a été utilisée, de manière à obtenir les mêmes classes pour les trois jeux de données, et rendre plus facile l'interprétation des distributions de faciès (Figure 1-2).

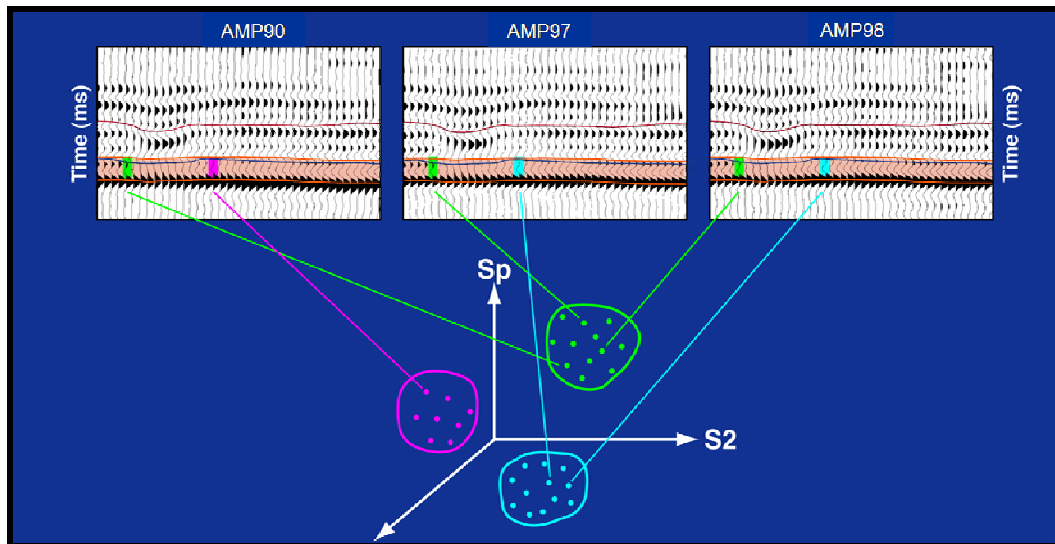


Figure 1-2 - Classification simultanée sur les 3 volumes sismiques (Lucet et al., 2001).

L'analyse en faciès sismiques réalisée sur les deux jeux de données, brutes et filtrées, a permis d'obtenir une classification à cinq ou bien à neuf classes. Ce sont des classes qui sont naturellement présentes dans les données. Nous présenterons ici les résultats obtenus dans le cas de cinq classes.

Dans les cartes ci-dessous, les puits horizontaux soumis à l'injection de vapeur pour la méthode SAGD sont représentés comme des lignes noires.

- **Interprétation des résultats pour les cartes à 5 faciès sismiques**

Les cartes de faciès correspondantes sont présentées sur le Figure 2 5; les résultats obtenus sur les données brutes sont sur la ligne du haut et sur les données filtrées sur la ligne du bas. Ces cartes suscitent quelques remarques:

- i. **Lissage des cartes filtrées**

- Les faciès sismiques montrent tous une distribution plus continue dans les cartes filtrées par rapport aux données brutes; on voit par exemple le faciès bleu être remplacé par le faciès gris dans le haut des cartes, menant ainsi à une plus grande continuité de ce faciès gris.
- La comparaison des cartes de probabilité d'attribution pour les 5 classes montre une très légère amélioration pour les données filtrées (Figure 6). Cette

probabilité était déjà très élevée ($> 0,95$) pour les données brutes, et ne pouvait guère être améliorée.

ii. Effets 4D

- Deux principales régions sont bien caractérisées à la fois sur les données brutes et filtrées, lorsqu'on étudie l'effet 4D: la zone nord-nord-ouest, comprenant les faciès 3, 4 et 5 ne change pas avec le temps; alors que la seconde région, dans la zone sud, où les faciès 1 et 2 sont dominants, change; il est important de noter que ces zones correspondent à peu près aux zones de bonne qualité de réservoir décrit par Dequirez et al. (1995);
- s'on compare les faciès 1 et 2 sur la carte de faciès filtrée, il est clair que le faciès 1 remplace le 2 entre AMP90 et AMP97, au centre de la carte. Cet effet - également observée dans les données brutes, pourrait être un effet lié à la production ;

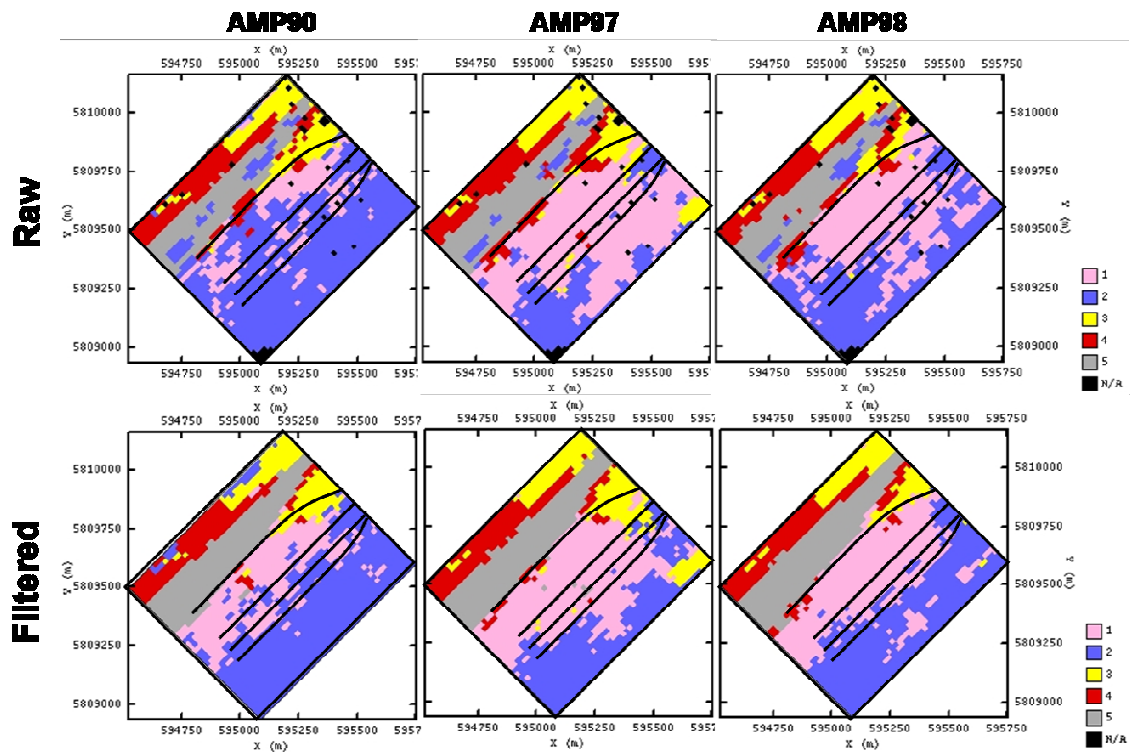


Figure 1-3- Cartes de faciès sismiques (approche non supervisée) à 5 classes. Le rang du haut montre des cartes calculées à partir des données brutes et celui du bas à partir des données filtrées. .

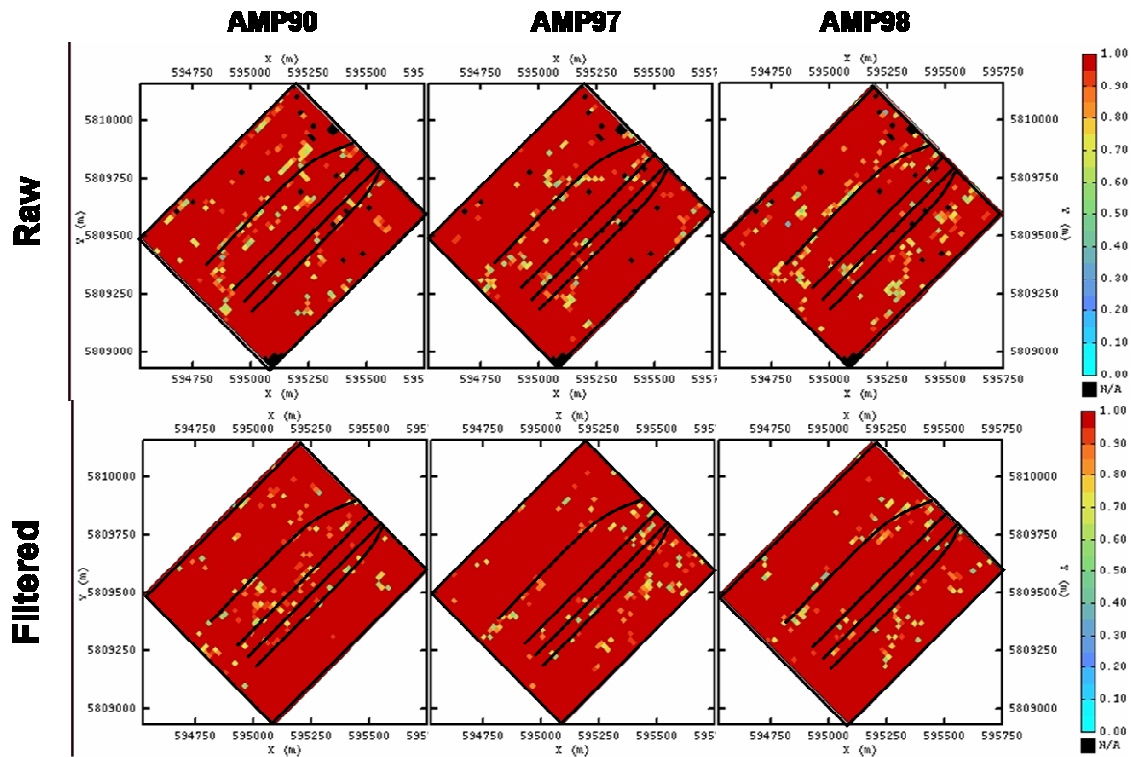


Figure 1-4 – Probabilité d'affectation pour les 5 classes.

1.3.7. Effets time-lapse et la pression

La dernière partie de ce chapitre débat de l'interprétation des décalages en temps observés entre campagne en termes de changement des paramètres, en particulier des variations de pression. Il a été observé que, par rapport aux données sismiques de référence de 1990, les données monitor de 97 et 98 montraient des décalages en temps négatifs (effet de pull-up) dans l'intervalle du réservoir. Ce résultat est en désaccord avec ce qui est attendu à partir des modèles théoriques ou expérimentaux décrivant l'effet de la température, et de la saturation en fluides, sur les vitesses de propagation. C'est pourquoi une attention particulière a été portée sur les effets de la pression.

Visant à fournir une base physique pour ces réponses anormales de décalages en temps, un modèle monodimensionnel simple, tenant compte de la dépendance entre vitesses et pression, a été mis en place. Ce modèle est issu de la proposition de Landro et Kvam (2002), elle-même basée sur la théorie de Hertz-Mindlin (Mindlin, 1949). Pour étayer les hypothèses de pression de réservoir, six scénarios de pression différents ont été étudiés, parmi lesquels cinq - de S1 à S5 - peuvent être considérés comme correspondant à des pressions normales. Pour aucun des cas étudiés, les variations de pression et par conséquent de vitesse, n'ont pu expliquer les différences de temps observés, de l'ordre de 2 ms; il faudrait une augmentation de vitesse de l'ordre de 24%.

Le sixième modèle montre qu'il faut dépressuriser le réservoir de 42 MPa par rapport à l'état initial de pression de 11,6 Mpa, pour obtenir cette augmentation de vitesse, ce qui est tout à fait irréaliste. Il semble donc que, en se basant sur la théorie de contact de Hertz-Mindlin, les différences de temps négatives observées dans les données sismiques 4D de Senlac ne peuvent pas être expliquée par une variation de pression.

Une hypothèse valable pour expliquer l'augmentation de la vitesse au cours de l'exploitation, peut être que les grès non consolidés et saturés par l'huile lourde ne se comportent pas comme un matériau rigide, mais plutôt comme un mélange de grains minéraux et d'huile lourde. Dans ce cas, ces grains ne sont pas en contact élastique, mais sont plutôt flottant dans le liquide. Cette hypothèse a été testée en utilisant des modèles de milieu effectif tels que les modèles de Voigt, Reuss, et Hill. Les résultats ont montré

que la vitesse sismique augmenterait dans l'intervalle réservoir, ce qui conduirait à des changements négatifs de temps en accord avec les observations. Une autre hypothèse explorée concerne la possible réduction de porosité liée à la production d'huile, qui devrait également conduire à une augmentation de la vitesse V_p , et donc à un décalage en temps négatif.

1.4. Application du filtrage géostatistique à un champ d'huiles lourdes, offshore Brazil : Champ de Marlim

La technique de Krigeage Factoriel (voir le Chapitre 3 pour la théorie) a été appliquée sur les données sismiques répétées du champ de Marlim, offshore Brazil. Situé en offshore profond, le champ de Marlim est un champ turbiditique à huiles lourdes situé dans le Bassin de Campos, le long de la partie Nord de l'Etat de Rio de Janeiro, côte sud Est du Brésil. Afin d'identifier, dans le réservoir, les effets dus à l'exploitation d'huile, deux campagnes sismiques time-lapse - données 4D - ont été acquises en 1997 et 2005. L'objectif de ces campagnes est d'évaluer l'efficacité du programme d'injection d'eau et de récupération améliorée du pétrole, et d'aider à mieux positionner les nouveaux puits de production/injection.

Les précédentes études de faisabilité de sismique 4D ont montré que la variation de vitesse acoustique attendue en réponse du remplacement de l'huile par de l'eau était de l'ordre de 7%. Ce contraste de vitesses est faible et correspond donc à une faible détectabilité de la signature 4D. De plus, au cours de l'enregistrement des données sismiques « monitor » de 2005, des obstacles opérationnels, telles que les plates-formes offshore, ont limité la mise en œuvre de l'acquisition sismique dans certaines zones du champ de Marlim. Afin de permettre une interprétation fiable - en termes de propriétés réservoir -, il est donc nécessaire de disposer d'un jeu de données le plus « propre » possible, dans lequel les événements bruités auront été filtrés.

Après une introduction sur les aspects géologiques et géophysiques, la méthodologie d'interprétation sismique adoptée dans ce travail est présentée. Une attention particulière est accordée au traitement sismique de cross-égalisation, mis en œuvre afin de réduire les différences attachées à l'acquisition sismique entre les données de base et monitor. Le troisième paragraphe montre que la signature sismique 4D peut être améliorée à

l'aide d'autres traitements géostatistiques qui minimisent les incertitudes sur les estimations des propriétés réservoir à partir de la sismique.

L'analyse géostatistique proposée a été appliquée sur une partie des données sismiques, sélectionnée dans la zone sud du champ de Marlim. La méthodologie de traitement géostatistique au cours de ce travail comporte quatre étapes:

- une procédure d'extraction des amplitudes sismiques, utilisant un marqueur stratigraphique régional comme référence, a permis de générer les volumes sismiques à traiter,

une analyse statistique et géostatistique a été effectuée le long de plans horizontaux parallèles à l'horizon de référence,

une procédure permettant de regrouper ensemble les plans présentant des caractéristiques structurelles et spatiales similaires; et

une étape d'Analyse Krigéante (Factorial coKriging), visant à éliminer, par filtrage, les structures spatiales indésirables et associées au bruit.

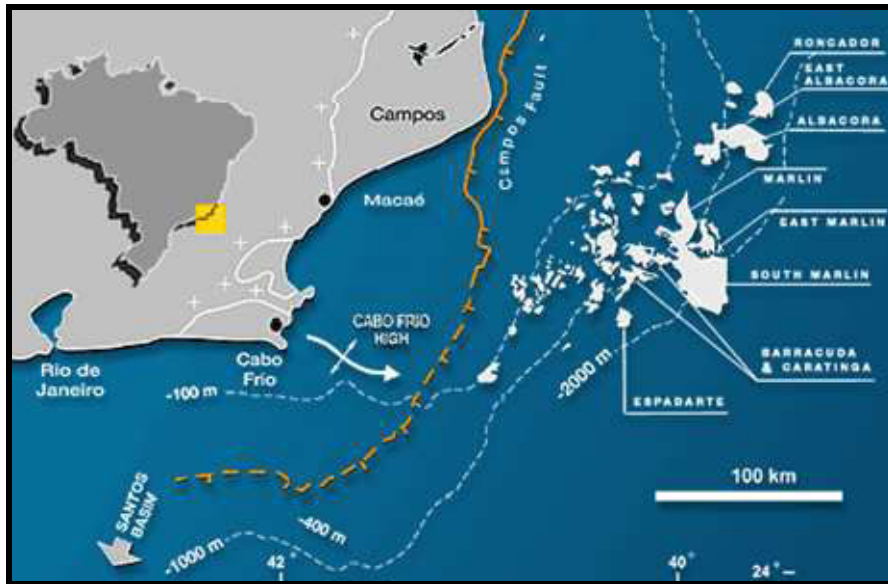


Figure 1-5 - Plan de situation du Bassin de Campos, situé au sud-est Brésil. Cette carte montre la plus importante zone de production offshore Brésil exploitée par PETROBRAS.

1.4.1. Le Bassin de Campos et la géologie du Champ de Marlim

Comprenant une surface sédimentaire d'environ 100,000 km², le Bassin de Campos est considéré, à ce jour, comme le plus important système de pétrole en eaux profondes de la plate-forme continentale brésilienne en termes de production et de réserves de pétrole, et l'un des plus grands du monde (Weimer, 2004). Ce bassin sédimentaire est situé entre la partie nord de Rio de Janeiro et le sud de l'Espírito Santo, et est limité vers le nord par le Vitoria haut, et vers le sud par le Cabo Frio haut, (cf Figure 1-5).

Le champ de Marlim a été découvert par le puit exploratoire RJS-219, foré en 1985 sous une profondeur d'eau de 850 m. Ce puit a traversé une épaisseur de 70 m de grès turbiditiques du réservoir de l'Oligocène/Miocène, saturés en huile de 20° API. Dans le champ, la viscosité de l'huile varie entre 4 et 8 cP, la pression de saturation est de 2,16 Mpa (22,00 kgf/cm²), en dessous de la pression initiale de 28,14 MPa (soit l'équivalent de 287,00 kgf/cm²). Les caractéristiques de permo-porosité sont excellentes et le sable est complètement non-consolidé. Le volume initial de l'huile en place (STOIP) est de STD 1,020 millions de m³ (6,416 millions STB). Le champ correspond à une surface de 165 km², le profondeur de couche de l'eau allant de 600 à 1100 m (Pinto et al., 2001).

Le champ de Marlim est classé comme un piège combiné stratigraphique et structural. Ce réservoir est limité aux côtés ouest, au nord et au sud par des pinch-out stratigraphiques, alors qu'une grande faille, résultant de l'halocinèse des séquences évaporitiques sous-jacentes, limite le réservoir à l'Est et au Nord-Est.

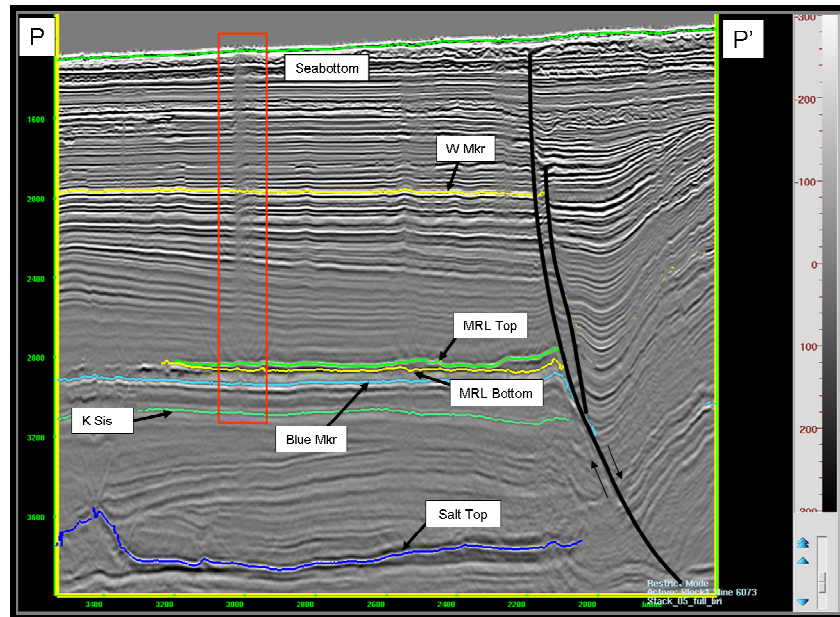


Figure 1-6 - Ligne sismique crossline XL 6073, extraite du volume S05, montrant les horizons interprétés. En noir, les principaux segments de la faille qui limite le réservoir à l'est et le nord-est. Des zones sismiques de mauvaise qualité dus à la présence d'obstacles représentés par le rectangle rouge.

Trois campagnes sismiques ont été acquises sur le champ de Marlim. La première campagne sismique 3D, enregistrée en 1986 juste après la découverte, avait pour but la délimitation de la géométrie externe du réservoir. La deuxième campagne sismique (97) a été acquise non seulement pour fournir une meilleure description de la géométrie externe des limites du réservoir, mais aussi pour mieux comprendre l'architecture interne de cette séquence turbiditique.

Couvrant une superficie de 1520 km², et englobant les champs de Marlim, Marlim Est et Marlim Sud, la campagne sismique 2005 a été acquise alors que 13 obstacles permanents (unités de production, plates-formes, etc) et 40 obstacles

temporaires (Johann et al., 2006) étaient présents sur la zone. L'objectif de cette campagne est principalement de contrôler les déplacements de fluides dans le réservoir correspondant donc à la réponse au régime /méthode de récupération des hydrocarbures, basé sur un mécanisme d'injection d'eau. (Pinto et al., 2001; Shecaira et al., 2002).

Une section sismique représentant la fenêtre de temps étudiée est présentée sur la Figure 1-7. Cette fenêtre est limitée par le marqueur régional RM2 en bas, et par un version décalée en temps de cet horizon, dénommé RM2', au sommet, de façon à définir une fenêtre de temps de 200ms entourant l'intervalle correspondant au réservoir Marlim. L'horizon RM2, correspondant au marker géologique Blue Marker, sera utilisé comme référence par la procédure d'horizontalisation.

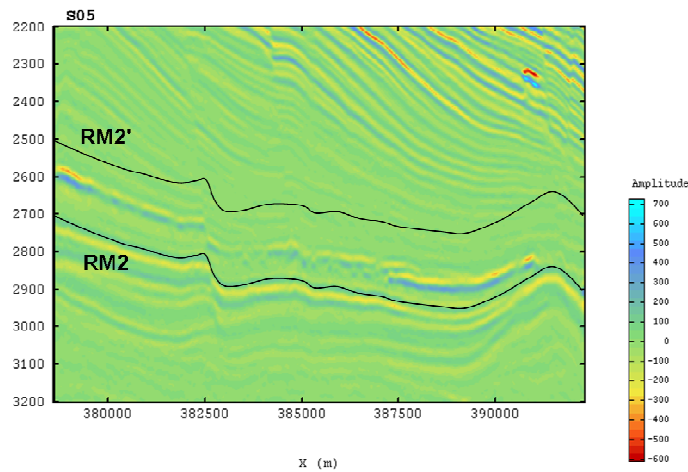


Figure 1-7 Section sismique inline représentative du champ de Marlim.
 Les horizons RM2 et RM2' représentent les limites inférieure et supérieure de la fenêtre d'intérêt.
 Échelles verticales et horizontales en millisecondes (TWT), et m, respectivement.

Analyse structurale

La fenêtre étudiée correspond à une épaisseur temps de 200ms, et donc à 50 « horizon slice », le pas d'échantillonnage étant de 4ms. Ces horizons sont numérotés de 1 à 50 en partant de l'horizon supérieur (TS1 à TS50). Une première analyse structurale a permis d'opérer des regroupements parmi ces horizons, et en particulier de définir le groupe NG3, composé de 17 tranches de temps de TS21 à TS36, qui représente

principalement le réservoir principal Marlim. Cet intervalle correspond donc à une épaisseur totale d'environ 60ms (TWT), comme indiqué dans la section en amplitude crossline de la Figure 1-8, extraite des données sismiques S97. Le toit du réservoir Marlim est associé à un maximum de valeur négative d'amplitude, en rouge, et la base du réservoir comme un valeur positive d'amplitude sismique, en bleu.

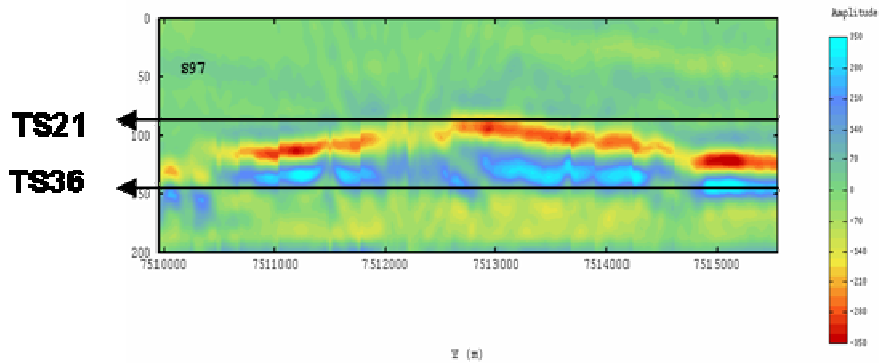


Figure 1-8 - Section verticale crossline campagne S97, montrant l'intervalle temps correspondant au groupe réservoir Marlim (TS21 à TS36). Échelle verticale de temps en ms (TWT).

Cet intervalle correspond au Réservoir Marlim; on constate que les variances des deux campagnes sont proches ($\sigma_{S05}^2 = 8178$ and $\sigma_{S97}^2 = 8261$), et plus fortes que dans les zones environnantes hors du réservoir, comme on le voit dans la Figure 1-8 et dans la Figure 1-9.

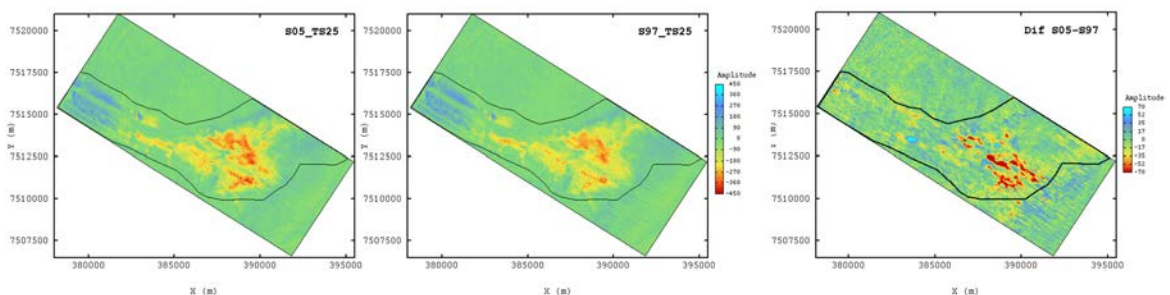


Figure 1-9 – Time-slices 25, correspondent au Réservoir Marlim. Partant de gauche vers la droite, on voit les cartes d'amplitude extraites des campagnes S05 et S97 et leur différence S05-S97.

L'analyse structurale de la zone Marlim a abouti à un assez bon résultat, où trois structures de base ont été utilisées pour ajuster les variogrammes imbriqués, comme le montre la Figure 5-63. Une petite structure sphérique, isotrope, avec une portée $a = 155\text{m}$, tout à fait compatible avec les précédentes interprétations, a été identifiée. Par

contre, sa contribution à la variation totale est faible, égale à 3% pour S05 et à 2% pour S97, avec un coefficient de corrélation linéaire réduit égal à 0,76.

L'analyse des cartes d'amplitudes correspondant à cet intervalle a montré que deux phénomènes de petite échelle pourraient éventuellement être associés aux petites structures:

- le premier, associé au bruit d'acquisition, correspond à des directions observées sur les groupes NG1 et NG2 (non réservoir), (cf Figure 1-9, carte des différences, à droite)
- les valeurs d'amplitudes plus fortes observées parallèlement à la direction inline, principalement dans la zone ouest du sous-volume, peuvent être associées aux réservoirs turbiditiques canalisés; ceux-ci sont principalement détectés dans les tranches supérieures de cet intervalle, et visibles dans les cartes d'amplitudes S05 et S97 dans la Figure 1-9, à gauche et au centre, respectivement;

Deux structures additionnelles, à grande échelle, ont été utilisées pour modéliser le variogramme expérimental: (a) une structure sphérique, parallèle à la ligne de direction des lignes de portée égale à 3,250 m, et (b) une troisième structure, anisotrope, de portée égale à 5,200 m et 2,780 m, dans les directions inline et crossline, respectivement, comme le montrent la Figure 1-10 et le Table 1-1.

Table 1-1 –Paramètres résultant de la modélisation structurale, groupe NG3. Entre parenthèses, la contribution (en pourcentage) de la variance dans les directions inline et crossline.

Structure		Ranges (m)		Sills			Correlation
		Inline	Crossline	S05	S97	S05xS97	
C ₁	Spherical	155	155	280 (3/4)	235 (2/3)	195 (2/3)	0.76
C ₂	Spherical	3250	N/A	3168 (30/-)	3490 (33/-)	3305 (32/-)	0.99
C ₃	Exponential	5200	2780	7030 (67/96)	6805 (65/97)	6825 (66/97)	0.99

Les données ont ensuite été filtrées par krigeage factoriel, en éliminant les structures de faible portée. Les résultats ont montré que l'effet 4D semblait avoir été touché par ce filtrage, ce qui n'est pas le but escompté puisque l'on cherche au contraire à préserver et à mettre en valeur cet effet 4D.

Une autre stratégie a alors été utilisée, se basant sur le cube des différences d'amplitudes entre les deux campagnes. En utilisant le même découpage en groupes que précédemment, l'analyse variographique a permis de distinguer une structure de courte portée (135m) visible sur les 5 groupes considérés. On montre que le filtrage de cette structure permet d'éliminer les bruits d'acquisition et d'obtenir des cartes de différences d'amplitudes dans lesquelles l'effet 4D est plus facilement interprétable.

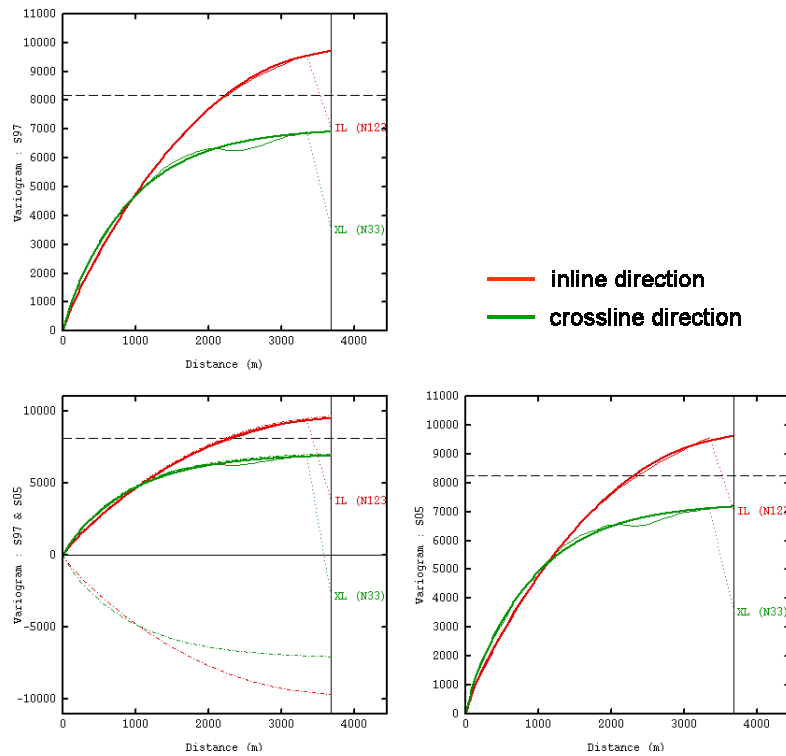


Figure 1-10 - Variogrammes de S97 (top) et S05 (bas à droite) et variogrammes croisés S97xS05 (bas à gauche) pour le groupe NG3 (TS21-TS36).

Chapter 2 - Introduction

Time-lapse seismic monitoring technology is becoming a conventional tool for monitoring and managing hydrocarbon reservoirs. The physical principle supporting this technology is simple, and is based on the recording of repeated seismic surveys over a hydrocarbon producing field at different calendar times. The hydrocarbon production determines changes in the reservoir properties due to fluid saturation, pressure, or temperature variations that could potentially be registered on the repeated seismic surveys.

This technology aims to provide qualitative and quantitative information to improve the reservoir description in terms of both static and dynamic properties during hydrocarbon production. Tracking the actual pathways of the fluids injected into the reservoir from the injector to the producer wells, and quantifying the total amount of upswept oil zones, helps with (i) redefining reservoir management strategies that include the positioning of well locations in infill programs, (ii) saving planned wells to be drilled in swept zones, and (iii) balancing injection and production rates.

Two key factors control the success of a time-lapse experiment: the seismic repeatability and the seismic detectability. Repeatability measures how similar two (or more) seismic surveys are in terms of seismic acquisition and processing parameters. The higher the repeatability, the more likely the time-lapse signal is to be identified and mapped. Detectability refers to the ability to identify changes within the reservoir due to the production effects, commonly associated with fluid saturation, pressure and temperature variations. This parameter is much dependent on both reservoir properties and seismic resolution. The combination of seismic repeatability and seismic detectability responds for the ability to map a time-lapse seismic signal within the reservoir.

When compared to other monitoring techniques, such as radioactive tracers or other methods based on well-log information, time-lapse seismic has the great advantage of being a unique volumetric monitoring technology, allowing to directly image dynamic reservoir processes in a true volumetric sense and give snapshots of the fluid fronts movements.

This thesis research aims at investigating seismic interpretation methodologies and techniques that will help to better characterize the time-lapse, or 4D, seismic signatures. These techniques and methodologies are used first to evaluate the time-lapse repeatability and then to filter out undesirable artifacts that are non-related to the production, while enhancing the 4D signature.

In Chapter 3, a theoretical review of the most relevant geostatistical concepts and methods is introduced. The Factorial Kriging technique, based on the concept of Kriging Analysis (Analyse Krigeante) developed by Matheron in 1982, is presented, and applications of this technique in different domains are described, including geochemistry, geophysics and image processing. Then, a theoretical comparison with conventional seismic data filtering techniques, such as the Single Value Decomposition and Spectral Analysis, is presented.

In Chapter 4, an application of the proposed Factorial Kriging filtering methodology to the Senlac heavy oilfield, Canada, is described. First, a description of the geology, of the enhanced oil recovery technique and of the time-lapse seismic data is provided. Secondly, a comprehensive statistical analysis of the seismic datasets is presented. The application of the Factorial Kriging methodology to filter out spatial structures that were characterized as related to the acquisition noise is described, as well as the obtained results. In this case, the Unsupervised Seismic Facies Classification technique was called upon to quantify the impact of the filtering technique. At the end of this chapter, a discussion of the effects of reservoir changes on seismic data is presented. As unexpected time-shift values were observed in the time-lapse seismic data from Senlac, the Hertz-Mindlin model was used to evaluate the velocity dependence on pressure. Additionally, compressional velocities were computed assuming different effective-medium theories to test for the effects of varying porosity, saturations and load-bearing mechanisms.

Chapter 5 is dedicated to the time-lapse study from Marlim Field, an offshore deepwater heavy oilfield submitted to water flooding to enhance oil recovery and for pressure maintenance. In this case, two seismic campaigns were shot at different calendar times, and the final seismic data was processed by a contractor following a cross-equalization procedure to minimize the acquisition discrepancies. An exhaustive geostatistical analyses was performed to better understand and discriminate between possible events associated to time-lapse effects, geology and different types of noise. In

this particular case, the introduction of the volume of the difference between the time-elapsed volumes in the proposed geostatistical methodology helped to better understand the different time-lapse effects.

The final conclusions of the results obtained are summarized in Chapter 6, as well as perspectives for future work.

Chapter 3 - Geostatistical Filtering Techniques Applied to Time-Lapse Seismic Data

Time-lapse seismic monitoring technology, or simply 4D seismics, uses time-lapse 3D images recorded repeatedly in the space at different calendar times. By comparing the resulting elapsed seismic data, this technology aims at providing qualitative and quantitative information to improve the reservoir description in terms of both static and dynamic properties during hydrocarbon production. Tracking the actual pathways of the fluids injected into the reservoir - from injector to the producer wells, and quantifying the total amount of unswept oil zones, helps with (i) redefining reservoir management strategies that include the positioning of well locations in infill programs, (ii) saving planned wells to be drilled in swept zones, and (iii) balancing injection and production rates.

Assuming an ideal situation, variations observed in time-lapse seismic data due to hydrocarbon production should only be detectable at the reservoir level. This subsurface region was the only one to undergo changes in fluid saturation, pressure and temperature, as a result of primary, secondary and/or tertiary recovery processes¹, under the hypothesis of no reservoir leakage.

However, when comparing these time-elapsed seismic volumes, one observes that they usually show non-negligible amplitude differences outside the reservoir level. These artifacts are mainly a result of different seismic acquisition and processing parameters and/or technologies used to produce the different seismic vintages. Depending on the signal to noise ratio, these artifacts may compromise the ultimate goal of a time-lapse seismic data (TLSD) study, by increasing the associated uncertainties of the final interpretation in terms of, for instance, pressure and fluid variations over the reservoir level. These non-related to the production artifacts may have different kinds of sources, and are detected even in highly repeatable seismic experiments (Eiken, 2001; Calvert, 2005).

During the interpretation of time-lapse seismic data, and particularly when looking for spatial patterns of hydrocarbon distribution within reservoirs, one faces the

problem of decomposing/splitting the seismic trace response into each of the several components that were combined to produce the average registered seismic response. This averaging process is a result of the wave propagation through the subsurface, reaching different geological features at distinct scales, from the microscopic grains distribution, through the reservoir facies up to the mesoscopic reservoir architectural elements. The hydrocarbon flow effects observed in seismic data depends on the final seismic bandwidth registered, and show a spatial structure that depends not only on petrophysical parameters but also on reservoir heterogeneities.

Geostatistics encompasses a set of tools that are suitable for characterizing such spatial structures. One particular geostatistical technique, that was proposed by George Matheron in the 1982's article *Pour Une Analyse Krigeante des Donnés Regionalisées*, is the factorial kriging technique (FK). FK relies on the principle that a regionalized variable can be decomposed into a set of orthogonal functions. These orthogonal functions will then be interpreted and, by comparing their spatial characteristics in terms of variability, will be associated to possible phenomena, such as geological structures, hydrocarbon production effects, or even to other structures not related to the production, such as seismic related noise due to acquisition or processing.

Many other tools were developed and are applied to spatial filters. Some are still under development, such as the General Principal Component Analyses (Voutay, 2003) or the General Canonical Analyses. Others, such as Single Value Decomposition, also based on the principal component approach, and frequency-filtering techniques based on the Fourier transforms, are currently used in the seismic industry to perform this sort of analysis and filter (Ma et Royer, 1987, 1988; Galli, 1987). These approaches, however, do not take into account the spatiality concept as assumed by the regionalized variables used in the FK. In the conventional seismic processing sequence, many one-dimensional frequency domain filtering techniques are applied in a trace-by-trace approach, and as previously noticed by GPCA and GCA, the data spatiality cannot, per construction, be considered.

¹ The oil industry also uses, in a confusing way, the terms Enhanced Oil Recovery (EOR) and Improved Oil Recovery (IOR) to designate all processes that are used to increase the recovery factor and are applied after the secondary recovery.

3.1. Geostatistical Basis

A brief description of the basic geostatistical concepts, methods and tools is provided in this introduction. These notes are important as a reminder to the most important concepts, and essential to better understand the Factorial Kriging methodology that will be later presented.

Geostatistics, as conceived by Matheron, is concerned with the study of all phenomena that fluctuate in space and/or in time, offering a collection of deterministic and statistical tools aimed at understanding and modeling spatial variability. These tools may be divided into two main categories: deterministic and stochastic (or geostatistics). The former essentially deals with all the developments around kriging, and is considered to be deterministic in the sense that it provides a single model as a result. The stochastic approach covers all techniques around the conditional simulation concept where a family of realizations of 1D, 2D or 3D models is generated (Dubrule, 2003). They are mainly used for quantifying uncertainties. In this work, the focus will be mainly on deterministic applications.

The following review is based on the developments found in Journel & Huijbreits (1978) and Deutsch & Journel (1998).

3.1.1. Random Variables

The basic paradigm of predictive statistics is to characterize any unsampled or unknown value z as a random variable (RV) Z , where the probability distribution of these models describes the uncertainty about the variable z . This random variable, that can assume a variety of outcome values according to a given probability distribution, is traditionally denoted by capital letters, as Z . On the other hand, the outcomes of this random variable are usually denoted by lower case letters, z , for instance.

The cumulative probability distribution function, cpdf, of a random variable Z is the function

$$F(z) = \text{Prob}(Z \leq z) \quad (11)$$

which completely describes the probability distribution of the RV Z .

The important concept of Regionalized Variables serves as the basis of Geostatistics. It was developed by George Matheron (1965), who stated that “Geostatistics are the application of the theory of the Regionalized Variables to the estimation of mineral deposits (with all that this implies)”. In this approach, a phenomenon is said to be regionalized if it is spread in the space and exhibits a certain spatial structure.

Despite being first introduced for ore mining deposits, the regionalization concept describes quite well most of the phenomena observed in other earth science fields, such as soil science, meteorology, etc. The regionalization concept is purely descriptive and does not carry any probabilistic interpretation. However, when used together with the Random Variable concept, the Regionalized Variable (RV) model stands for the basis of geostatistics.

The RV model Z is usually written as $Z(\mathbf{u})$, where \mathbf{u} represent the vector of coordinates of the sampled location. The sampled variable $Z(\mathbf{u})$ may represent continuous or categorical quantities that occur in nature. The continuous quantities may correspond, for instance, with acoustic or elastic impedance values, or other continuous attribute derived from seismic amplitude values; petrophysical measurements, such as permeabilities and porosities, etc. Geological properties, such as rock, facies or fluid types, are, on the other hand, considered as categorical values.

The cumulative distribution function (cdf) of a continuous RV is written as

$$F(\mathbf{u}; z) = \text{Prob}\{Z(\mathbf{u}) \leq z\} \quad (12)$$

and it fully characterizes the RV.

The same function can also be written for any categorical variable case, when the RV $Z(\mathbf{u})$ can take one of the K outcome values $k = 1, \dots, K$, in the form

$$F(\mathbf{u}; k | (K)) = \text{Prob}(Z(\mathbf{u}) = k) \quad (13)$$

In opposition to the continuous case, categorical variables do not follow any predefined order, so the probability distribution (13) is a cumulative probability density function rather than a cumulative distribution function.

The notation conditional to (n) is used when the cdf is made specific to a particular information set, e.g., n neighboring data values $Z(\mathbf{u}_\alpha) = z(\mathbf{u}_\alpha), \alpha = 1, \dots, n$, defining the conditional cumulative distribution function, or ccdf. For instance, in the continuous case, $F(\mathbf{u}, z | (n)) = Prob\{Z(\mathbf{u}) \leq z | (n)\}$.

In Geostatistics, most of the information related to an unsampled value $z(\mathbf{u})$ comes from sample values extracted in the neighboring locations \mathbf{u}' , whether defined on the same attribute z or on some related attribute y . Therefore, it is important to model the degree of correlation or dependence between any number of RV's $Z(\mathbf{u}_\alpha) = z(\mathbf{u}_\alpha), \alpha = 1, \dots, n$, and more generally $Z(\mathbf{u}_\alpha) = z(\mathbf{u}_\alpha), \alpha = 1, \dots, n$, $Y(\mathbf{u}'_\beta) = y(\mathbf{u}'_\beta), \beta = 1, \dots, n'$. The concept of random function, RF, allows such modeling and updating of prior cdf's into posterior ccdf's.

3.1.2. Random Functions

A random function is a set of RV's defined over some field of interest, such as $\{Z(\mathbf{u}), \mathbf{u} \in \text{study area}\}$ also denoted simply as $Z(\mathbf{u})$. Usually, the RF definition is restricted to RV's related to the same attribute, say z , hence another RF would be defined to model the spatial variability of a second attribute, say $\{Y(\mathbf{u}), \mathbf{u} \in \text{study area}\}$.

Just as a RV $Z(\mathbf{u})$ is characterized by its cdf (Eq. (12)), a RF $Z(\mathbf{u})$ is characterized by the set of all its K-variate cdf's for any number K and any choice of K locations, $\mathbf{u}_k, k = 1, \dots, K$

$$F(\mathbf{u}_1, \dots, \mathbf{u}_k; z_1, \dots, z_k) = Prob\{Z(\mathbf{u}_1) \leq z_1, \dots, Z(\mathbf{u}_k) \leq z_k\} \quad (14)$$

This multivariate cdf models the joint uncertainty about the K values $z(\mathbf{u}_1), \dots, z(\mathbf{u}_k)$, and may be conveniently characterized by its first moments, which correspond to the expected value and to the covariance.

3.1.3. Expected Value

The expected value is the probability-weighted sum of all possible occurrences of the RV Z . It is also called the mean of the variable Z , or the first order moment defined in the discrete case as

$$E\{Z\} = m = \sum_{i=1}^N p_i z_i \quad (15)$$

with $p_i \geq 0$, for all $i=1, \dots, N$ and where p_i are weights that $\sum_{i=1}^N p_i = 1$. In the case of equiprobable sampling, i.e., if each realization Z_i has the same degree of confidence, then p_i is equal to $\frac{1}{n}$.

In the continuous case, the expected value is defined under the condition of existence of the integrals, as

$$\begin{aligned} E\{Z\} &= m = \int_{-\infty}^{+\infty} z dF(z) = \int_{-\infty}^{+\infty} z f(z) dz \\ &= \lim_{K \rightarrow \infty} \sum_{k=1}^K z'_k [F(z_{k+1}) - F(z_k)] \\ &= \lim_{K \rightarrow \infty} \sum_{k=1}^K z'_k f(z_k) [(z_{k+1}) - (z_k)] \end{aligned} \quad (16)$$

with $z'_k \in]z_k, z_{k+1}]$, where $f(z) = F'(z) = \frac{dF}{dz} = \lim_{\Delta z \rightarrow 0} \frac{F(z + \Delta z) - F(z)}{\Delta z}$ is the probability density function (pdf), defined as the derivative of the cdf $F(z)$, when it exists.

3.1.4. Variance

The variance, or the second order moment of the RV Z , is defined as the expected squared deviation of Z from its mean

$$Var\{Z\} = \sigma_z^2 = E\{[Z - m]^2\} \geq 0 \quad (17)$$

and is expressed in the discrete case as

$$\text{Var}\{Z\} = \sum_{i=1}^N p_i (z_i - m)^2 \quad (18)$$

while in the continuous case - provided that the integrals converge, it is written as

$$\sigma_z^2 = \text{Var}\{Z\} = \int_{-\infty}^{+\infty} (z - m)^2 dF(z) = \int_{-\infty}^{+\infty} (z - m)^2 f(z) dz \quad (19)$$

3.1.5. Linear properties of the Expected Value

The expected value is a linear operator, in the sense that, as soon as it exists, the expected value of a linear combination of RVs $Z = \sum_k a_k Z_k$ is the linear combination of the expected value of these functions

$$m_z = E\{Z\} = E\left\{\sum_k a_k Z_k\right\} = \sum_k a_k E\{Z_k\} \quad (20)$$

whatever the RV's Z_k whether dependent or independent from each other, and whatever the constant a_k . By consequence, the variance may be expressed as

$$\begin{aligned} \text{Var } Z &= E\{[Z - m]^2\} = E\{[Z^2 - 2Zm + m^2]\} \\ &= E\{Z^2\} - 2mE\{Z\} + m^2 \\ &= E\{Z^2\} - m^2 \end{aligned} \quad (21)$$

The variance of a linear combination $Y = \sum_k a_k Z_k$ can be calculated as

$$\begin{aligned} \sigma_Y^2 &= E\{(Y - m_Y)^2\} = E\left[\sum_k a_k (Z_k - m_k)\right]^2 \\ &= \sum_k \sum_l a_k a_l E[(Z_k - m_k)(Z_l - m_l)] \\ &= \sum_k \sum_l a_k a_l \sigma_{Z_k Z_l} = \sum_k \sum_l a_k a_l r_{z_k z_l} \sigma_{Z_k} \sigma_{Z_l} \end{aligned} \quad (22)$$

where $r_{z_k z_l}$ is the correlation coefficient between the variables Z_k and Z_l , and σ_{Z_k} and σ_{Z_l} the standard deviation of Z_k and Z_l , respectively, and $\sigma_{Z_k Z_l}$ is the covariance between Z_k and Z_l .

3.1.6. Stationarity

A RF $\{Z(\mathbf{u}), \mathbf{u} \in A\}$ is said to be stationary within the field A if its multivariate cdf is invariant under any translation of the K coordinate vectors \mathbf{u}_k , that is

$$F(\mathbf{u}_1, \dots, \mathbf{u}_k; z_1, \dots, z_k) = F(\mathbf{u}_1 + \mathbf{l}, \dots, \mathbf{u}_k + \mathbf{l}; z_1, \dots, z_k), \forall \text{ translation vector } \mathbf{l} \quad (23)$$

The invariance over translation of the multivariate cdf entails invariance of any lower order cdf, including the univariate and bivariate cdf's, and invariance of their moments. It is important to notice that the stationarity is not a quality or a property of the data itself, but refers to a choice of the model used to describe the variable over the domain of interest.

As described by Chilès et al. (1999), when dealing with stationary random functions, three main models may to be considered regarding stationarity. They can be summarized as follows:

Strict stationarity, when the distributions are invariant under every arbitrary translation of the points by a vector \mathbf{h}

$$\Pr\{Z(\mathbf{u}_1) < z_1, \dots, Z(\mathbf{u}_k) < z_k\} = \Pr\{Z(\mathbf{u}_1 + \mathbf{h}) < z_1, \dots, Z(\mathbf{u}_k + \mathbf{h}) < z_k\} \quad (24)$$

And the phenomenon is said to be homogeneous or stationary in the space, as it repeats itself over the studied domain;

Second-order stationarity, also expressed as weak stationarity, or wide-sense stationarity, this hypothesis entails the invariance under translations of the first two moments of the random variable, when they exist, as follows

$$\begin{cases} E\{Z(\mathbf{u})\} = m \\ E\{[Z(\mathbf{u}) - m][Z(\mathbf{u} + \mathbf{h}) - m]\} = C(\mathbf{h}) \end{cases} \quad (25)$$

which means that the mean value of the distribution is constant and the covariance function does not depend on the location \mathbf{u} , but only on the separation vector \mathbf{h} .

Intrinsic hypothesis, a similar but less restrictive assumption in comparison to the Second-order stationarity, this model assumes the stationarity of the increments of $Z(\mathbf{u})$, say $Y_h(\mathbf{u}) = Z(\mathbf{u} + \mathbf{h}) - Z(\mathbf{u})$, and is characterized by the following relationships

$$\begin{cases} E\{Z(\mathbf{u} + \mathbf{h})\} = \langle a, \mathbf{h} \rangle \\ \text{Var}\{[Z(\mathbf{u} + \mathbf{h}) - Z(\mathbf{u})]\} = 2\gamma(\mathbf{h}) \end{cases} \quad (26)$$

where $\langle a, \mathbf{h} \rangle$ is the linear drift of the increment of $Z(\mathbf{u})$, the intrinsic random function.

3.1.7. Covariance

The covariance function $C(\mathbf{h})$ of the RF Z is defined considering the stationarity of its first two moments: the *mean* and the *covariance*

$$\begin{cases} E[Z(\mathbf{u})] = m, \forall \mathbf{u} \in D \\ E[Z(\mathbf{u})Z(\mathbf{u} + \mathbf{h})] - m^2 = C(\mathbf{h}), \forall \mathbf{u}, \mathbf{u} + \mathbf{h} \in D \end{cases} \quad (27)$$

And the covariance never exceeds the variance

$$|C(\mathbf{h})| \leq C(0) = \text{var}(Z(\mathbf{u})) \quad (28)$$

Two important properties of the covariance function are:

$$\text{Var}(Z, Y) = \text{Var}(Z) + \text{Var}(Y) + 2\text{Cov}(Z, Y) \quad (29)$$

and

$$\text{Cov}(Z, Y) = 0 \quad (30)$$

if Z and Y are uncorrelated.

The correlation function is defined as the ratio of the covariance at a lag \mathbf{h} and its value at the origin, as

$$\rho(\mathbf{h}) = \frac{C(\mathbf{h})}{C(0)} \quad (31)$$

and is limited from $-1 \leq \rho \leq 1$.

3.1.8. Variogram

An appropriate tool to describe spatial data continuity of a sampled dataset from $Z(\mathbf{u})$ is the experimental variogram. The variogram is computed as the squared differences of two different sample values taken over a distance h , where the vector distance h is referred to as the lag, in the geostatistical jargon. It depends on the distance but also on the direction. When bounded, the variogram function is equivalent to the covariance function.

The variogram is defined as the variance of the increments $[Z(\mathbf{u}) - Z(\mathbf{u} + \mathbf{h})]$. Then, for a stationary RF the variogram is expressed as

$$2\gamma(\mathbf{h}) = \text{Var}\{Z(\mathbf{u} + \mathbf{h}) - Z(\mathbf{u})\} \quad (32)$$

or in an equivalent way, as

$$\gamma(\mathbf{h}) = C(0) - C(\mathbf{h}) \quad (33)$$

where the term $C(\mathbf{h})$ is the stationary covariance and $C(0) = \text{Var}\{Z(\mathbf{u})\}$ is the stationary variance. Due to these properties, the variogram function was originally called *intrinsic dispersion function* (Rivoirard, 2003).

The variogram is equal to zero at the origin, where $\mathbf{h} = 0$, and $[Z(\mathbf{u}) - Z(\mathbf{u} + \mathbf{h})] = [Z(\mathbf{u}) - Z(\mathbf{u})] = 0$, then

$$\gamma(\mathbf{h}) = 0, \quad \mathbf{h} = 0 \quad (34)$$

It is a positive symmetrical function

$$\gamma(\mathbf{h}) \geq 0, \quad \forall \mathbf{h} > 0 \quad (35)$$

and also an even function

$$\gamma(\mathbf{h}) = \gamma(-\mathbf{h}) \quad (36)$$

In Figure 2.1, three important features of the variogram function are presented: *sill*, *range* and *nugget effect*:

Sill: this value corresponds to the plateau where the range is reached;

Range: the lag distance h from where the data variability reaches a plateau, and the data pairs become uncorrelated; and

Nugget-effect: the jump in variance from the position $h=0$ to the value of the variogram at extremely small distances, and is usually associated to the measurement errors.

The previous formulations presented only the discrete variograms that were computed for each lag distance h . To be able to use the variogram during the estimation procedure, some functions have been developed to allow the continuous representation of the spatial variability whichever h distance one is interested in. These functions must

obey mathematical constraints so that the resulting kriging equations are solvable (e.g., positive-definiteness between sample covariance matrices).

The most commonly used authorized (in the sense of positive-definite matrices) models are described as:

- **Spherical Model**, defined by an actual range a and a positive variance contribution c (or sill value c)

$$\gamma(h) = \begin{cases} c \left[1.5 \frac{h}{a} - 0.5 \left(\frac{h}{a} \right)^3 \right] & \text{if } h \leq a \\ c & \text{if } h \geq a \end{cases} \quad (37)$$

- **Exponential Model**, defined by an effective range a (integral range $a/3$) and positive variance contribution c (or sill value c)

$$\gamma(h) = \begin{cases} c \left[1 - \exp\left(-\frac{3h}{a}\right) \right] & \end{cases} \quad (38)$$

- **Gaussian Model**, defined by an effective range a (integral range $a/3$) and positive variance contribution c (or sill value c)

$$\gamma(h) = \begin{cases} c \left[1 - \exp\left(-\frac{3h^2}{a^2}\right) \right] & \end{cases} \quad (39)$$

- **Power Model** defined by a power $0 < \omega < 2$ and positive slope c

$$\gamma(h) = c.h^\omega \quad (40)$$

where the **Linear Model** is a particular case with $\omega = 1$;

- **Hole-effect Model**, defined by a length a to the first peak, associated to the size of the underlying cyclic features, and positive variance contribution c

$$\gamma(h) = c. \left[\text{sinc} \left(\frac{h}{a} \cdot \pi \right) \right] \quad (41)$$

A schematic representation of these six semi variogram basic models is presented in Figure 3-1.

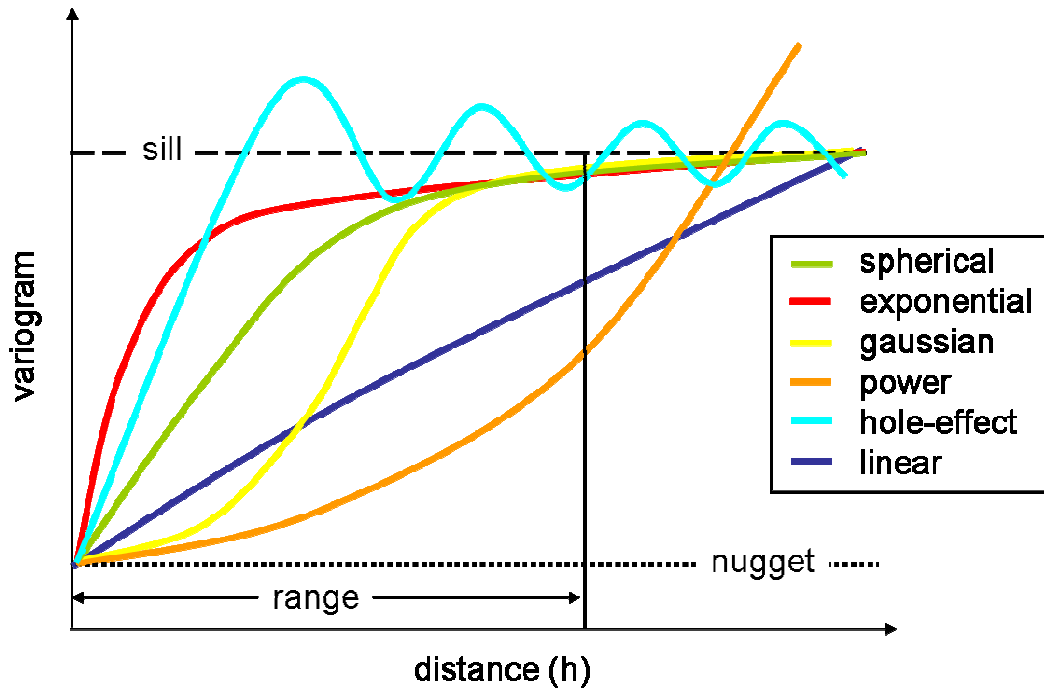


Figure 3-1 – Schematic representation of the basic theoretical semivariograms, with their most relevant parameters: the range, or the maximum correlation distance; the sill, or the variance at $h=0$; and nugget-effect.

3.2. Geostatistical Estimation

Geostatistics deals with regionalized variables that spread in space, and one of its most traditional applications is to provide tools to estimate a variable of interest at unsampled locations. It is a rather common situation in oil exploration and production, where the well locations are planned and drilled based on assumptions that are far from providing a regular sampling grid, but follow only the natural oil pathways within the reservoir. Even when dealing with regularly gridded sampling campaigns, as those resulting from the acquisition of dense tridimensional (3D) seismic data, the lack of seismic information due to, for instance, operational obstacles (wells, platforms, rigs, etc), may impose the use of some estimation technique to fill in seismic attribute maps at these unsampled locations.

Conceived by Georges Matheron in the 60's, the kriging technique encompasses a family of linear regression algorithms, known as *BLUE* estimator, an acronym for *Best Linear Unbiased Estimator*. It is considered to be the best estimator, as the algorithm searches to minimize the variance of the kriging error, usually constrained to be equal to zero.

The term Kriging was coined by geostatisticians to define this collection of generalized linear regression techniques for minimizing an estimation variance defined from an *a priori* model for a covariance (Deusch & Journel, 1998). The problem to be solved is: *how to estimate unsampled values* $z(\mathbf{u}_\alpha), \alpha = 1, \dots, n$.

This estimation technique is a linear regression method, based on a linear combination of the neighborhood samples to predict the unsampled value, assigning weights to each neighborhood samples. The so-called "kriging system" relates the covariance between the samples, or the data-to-data covariance, to the covariance between each sample and the location to be estimated, or the data-to-unknown and the unknown weights, as shown in Equation (43). Assuming that these covariance matrices are invertible, the kriging system weights are easily computed by inverting a linear system of equations involving the data covariance matrix. The first matrix accounts for the data redundancy, or said in a different way, the existence of clustering in the dataset,

assigning weights as a function of the statistical distance between the data. On the other hand, the data-to-unknown covariance matrix provides a weighting scheme that is similar to the one from inverse distance methods (Isaacs and Srivastava, 1989).

In the following, the three main classes of kriging estimators are presented. The difference between these three approaches concerns the stationarity assumption for the mean value $m = E\{Z(\mathbf{u})\}$ assumed for each model.

3.2.1. Simple Kriging

The Simple Kriging estimator assumes that the stationary mean $m(\mathbf{u})$ is known and constant throughout the studied area. It is written as:

$$Z_{SK}^*(\mathbf{u}) = \sum_{\alpha=1}^n \lambda_{\alpha}(\mathbf{u})Z(\mathbf{u}_{\alpha}) + \left(1 - \sum_{\alpha=1}^n \lambda_{\alpha}(\mathbf{u})\right)m \quad (42)$$

where $Z(\mathbf{u})$ is the *RV* model at location \mathbf{u} , the \mathbf{u}_{α} are the n data locations, $m(\mathbf{u}) = E\{Z(\mathbf{u})\}$ is the location-dependent mean value of *RV* $Z(\mathbf{u})$, and $Z_{SK}^*(\mathbf{u})$ is the simple kriging estimator.

The weights λ_{α} are determined to minimize the error or the estimated variance, and this minimization results in a set of normal equations

$$\sum_{\beta=1}^n \lambda_{\beta}(\mathbf{u})C(\mathbf{u}_{\beta} - \mathbf{u}_{\alpha}) = C(\mathbf{u} - \mathbf{u}_{\alpha}), \quad \forall \alpha = 1, \dots, n \quad (43)$$

where the indexes α and β specify the neighborhood locations to the point \mathbf{u} to be estimated.

The corresponding minimized kriging variance is written as

$$\sigma_{SK}^2 = C(0) - \sum_{\alpha=1}^n \lambda_{\alpha}(\mathbf{u}) C(\mathbf{u} - \mathbf{u}_{\alpha}) \geq 0 \quad (44)$$

3.2.2. Ordinary Kriging

Ordinary Kriging assumed that the local mean $m(\mathbf{u})$ is unknown and locally constant in the neighborhood of $z(\mathbf{u})$. Then, assuming an unbiased condition for the kriging estimator $Z_{OK}^*(\mathbf{u})$, in the sense that $E\{Z_{OK}^*(\mathbf{u})\} = E\{Z(\mathbf{u})\}$, a new constraint is imposed on the sum of the weights $\sum_{\alpha=1}^n \lambda_{\alpha}(\mathbf{u})$ which must be equal to 1. Ordinary Kriging can be viewed as a filter of the local mean compared to the SK estimator given by (42) because it requires that the kriging weights sum to 1. The resulting ordinary kriging (OK) estimator equations are given by:

$$Z_{OK}^*(\mathbf{u}) = \sum_{\alpha=1}^n \lambda_{\alpha}^{(OK)}(\mathbf{u}) Z(\mathbf{u}_{\alpha}) \quad (45)$$

After minimization the error variance $\sigma_{OK}^2(\mathbf{u}) = \text{Var}\{Z_{OK}^*(\mathbf{u}) - Z(\mathbf{u})\}$ under the constraint for unbiased errors, the following OK system must be solved:

$$\begin{cases} \sum_{\beta=1}^n \lambda_{\beta}^{(OK)}(\mathbf{u}) C(\mathbf{u}_{\beta} - \mathbf{u}_{\alpha}) + \mu(\mathbf{u}) = C(\mathbf{u} - \mathbf{u}_{\alpha}), \alpha = 1, \dots, n \\ \sum_{\alpha=1}^n \lambda_{\alpha}^{(OK)}(\mathbf{u}) = 1 \end{cases} \quad (46)$$

where $\lambda_{\alpha}^{(OK)}(\mathbf{u})$ are the OK weights, and $\mu(\mathbf{u})$ is the Lagrange parameter associated with the OK weight constraint. Thus, the OK estimator (46) is, in fact, a simple kriging of type (42), where the constant mean value m is replaced by the location-dependent estimate $m^*(\mathbf{u})$, and the OK estimator can be written as

$$\begin{aligned}
Z_{OK}^*(\mathbf{u}) &= \sum_{\alpha=1}^n \lambda_{\alpha}^{(OK)}(\mathbf{u}) Z(\mathbf{u}_{\alpha}) \\
&\equiv \sum_{\alpha=1}^n \lambda_{\alpha}^{(OK)}(\mathbf{u}) Z(\mathbf{u}_{\alpha}) + \left(1 - \sum_{\alpha=1}^n \lambda_{\alpha}(\mathbf{u})\right) m^*(\mathbf{u})
\end{aligned} \tag{47}$$

Due to its less restrictive assumptions in terms of the behavior of the mean – say knowledge and stationary hypothesis, the OK estimator procedure is usually preferred in comparison to the SK (Goovaerts, 1997; and Deutsch, 1998).

3.2.3. Kriging with a trend model: Universal Kriging

The term Universal Kriging is traditionally used to denote the kriging procedure with an *a priori* trend model. It considers an underlying RF model composed by a sum of a trend component $m(\mathbf{u})$ plus a residual $R(\mathbf{u})$

$$Z(\mathbf{u}) = m(\mathbf{u}) + R(\mathbf{u}) \tag{48}$$

The trend component $m(\mathbf{u})$ is usually modeled as a smoothly varying deterministic function of the coordinates \mathbf{u} (usually polynomial) whose unknown parameters are fitted from the sampled data

$$m(\mathbf{u}) = \sum_{k=0}^K a_k f_k(\mathbf{u}) \tag{49}$$

where the $f_k(\mathbf{u})$ are the known functions of the location coordinates and a_k are the unknown parameters. The universal kriging estimator equations are given by

$$Z_{KT}^*(\mathbf{u}) = \sum_{\alpha=1}^n \lambda_{\alpha}^{(KT)}(\mathbf{u}) Z(\mathbf{u}_{\alpha}) \tag{50}$$

and the universal kriging system by

$$\begin{cases} \sum_{\beta=1}^n \lambda_{\beta}^{(KT)}(\mathbf{u}) C_R(\mathbf{u}_{\beta} - \mathbf{u}_{\alpha}) + \sum_{k=0}^K \mu_k(\mathbf{u}) f_k(\mathbf{u}_{\alpha}) = C_R(\mathbf{u} - \mathbf{u}_{\alpha}) \\ \sum_{\beta=1}^n \lambda_{\beta}^{(KT)}(\mathbf{u}) f_k(\mathbf{u}_{\beta}) = f_k(\mathbf{u}) \end{cases} \tag{51}$$

where $\lambda_{\beta}^{(KT)}(\mathbf{u})$ are the kriging weights, and $\mu_k(\mathbf{u})$ the (K+1) Lagrange parameters associated with the (K+1) weight constraints.

3.2.4. Cokriging

In the case where more than one variable is available, and assuming that these variables are correlated, one can perform an estimation from one variable taking into account the behavior of the second variable.

The ordinary cokriging estimator of $Z(\mathbf{u})$, considering only a single secondary variable (Y), is written as

$$Z_{COK}^*(\mathbf{u}) = \sum_{\alpha_1=1}^{n_1} \lambda_{\alpha_1}(\mathbf{u}) Z(\mathbf{u}_{\alpha_1}) + \sum_{\alpha_2=1}^{n_2} \lambda'_{\alpha_2}(\mathbf{u}) Y(\mathbf{u}'_{\alpha_2}) \quad (52)$$

where the λ_{α_1} and λ'_{α_2} are the weights applied, respectively, to the n_1 z and n_2 y samples.

3.2.5. Factorial Kriging

One of the particular implementations of the geostatistical estimation technique is the Factorial Kriging. Originally proposed by George Matheron (1982) in his paper entitled *Pour Une Analyse Krigeante des Données Regionalisées*, the Factorial Kriging technique addresses the problem of decomposing a regionalized variable into a set of orthogonal random functions. Due to this feature, it has been extensively used in many geoscience areas to decompose any sort of images, and in providing tools to filter them through the resulting orthogonal factors.

Among other applications, FK has been used to filter: radar images (Ma & Royer, 1987); seismic velocity fields analyses (Coléou, 1987; Sandjivy, 2001); time-lapse seismic data equalization (Coléou, 2001); amplitude maps (Mundim et al., 2001), magnetic/gravimetric data analyses (Galli, 1987, Gilles, 1988) and geochemical analyses (Goovaerts, 1995 and Sandjivy, 1987). Numerous papers on FK applications for climatological studies have been presented in recent past years.

Galli et al. (1984) have compared the results obtained by applying the Factorial Kriging technique with those from classical Fourier analysis on magnetic data. In these analyses, the main goal is to distinguish the sources of the registered anomalous magnetic values that are summed up in the registered magnetic field. The anomalies may be associated to superficial or deep sources, and understanding and mapping the origin of these structures is of capital interest.

Sandjivy (1984) analyzed geochemical prospection data from different surveys, including a multivariate dataset from a granitic tin mineralization in Malaysia, and different types of geochemical data from a site located at Munster, France. The application of the Factorial Kriging technique enabled the discrimination of metal concentrations associated to the regional geochemical background from those local anomalies. Additionally, the technique also helped on distinguishing the primary sources associated to these anomalous values, as well as an accurate position of these primary sources.

Ma and Royer (1987) presented an alternative factorial kriging approach named *Local Kriging Analyses*, or, LKA, applied to image processing. They studied through several examples the effects of varying the stationary assumptions, the variogram model type, and the combinations of permissible nested variogram models. The authors also provide an analytical comparison between LKA and other image filtering techniques, particularly to those based on spectral analysis, showing the analogy between the two approaches and the advantages of the geostatistical filtering technique. Ma and Royer (1988) established a formal correspondence between the Factorial Kriging and the classical image processing techniques, showing that the FK weighting functions computed by this technique are similar to the classical filters, for a given covariance or semivariogram model. The authors considered both stationary and non-stationary hypotheses.

The robustness of the Factorial Kriging approach was evaluated by Bourgault (1994) by considering three different noise conditions: first, an uncorrelated noise; secondly, a heterocedastic noise – heterocedasticity means that the variance of the noise is a function of the signal values: the higher the signal, the higher the noise variance - but uncorrelated to the signal; and finally, a heterocedastic and correlated noise. The conclusions showed that the Factorial Kriging gave robust results even in the presence of heterocedastic noise, but restricted to those cases when the noise is not linearly correlated with the signal.

Arnaud et al. (2001) use the Analyse Krigeante or Kriging Analysis to evaluate a multivariate dataset composed of different pedological properties, aiming at identifying groups of sites with the same characteristics. This dataset was composed of 110 shallow soil measurements taken from a 6×6m sampling grid at different depths and from a set of six drilling cores, enabling the short range variability study. The authors explore three variables and adjust a co-joint structure by a linear model of coregionalization with three different permissible models: a nugget, an exponential and a power model, where the last two models present a geometrical anisotropy. By analyzing the resulting factors from Kriging Analysis, they show that the first factor estimated from the exponential structure is in good agreement with a qualitative map of pedological properties. This article provides a comprehensive description of the Kriging Analysis technique.

Coléou (2005) describes in the US PATENT number 2005/0209895, entitled “Method for Filtering Seismic Data, Particularly by Kriging”, a procedure to automatically filter seismic data. The author uses the formalism of Kriging Analysis presented by Matheron (1982), and proposes two methodologies to estimate the *common part* and the *orthogonal residues* from grids of different datasets. The first, referred to as an *automatic approach*, uses the experimental covariances and assumes a known cross-variogram model γ_{12} for the two maps, corresponding to the regionalized variables Z_1 and Z_2 , with samples taken from the same area at different calendar times (or from different attributes). So the estimate is determined, satisfying the equation

$$Z_{12}^*(x) = \sum_{\alpha=1}^N \lambda_{\alpha}^1 Z_{\alpha}^1 + \sum_{\alpha=1}^N \lambda_{\alpha}^2 Z_{\alpha}^2 \quad (53)$$

The weights applied in equation (53) are determined by inverting a cokriging equation, which is an estimate of the component that is common to both data series. The residual components are computed by subtracting the estimated common part of each input data.

The second proposed approach, referred to as a *semi-automatic filtering*, addresses the problem of filtering only one dataset, S_1 , and assumes that a model of covariance exists.

The FK methodology relies on the principle that the variograms $\gamma_1, \dots, \gamma_p$ (or the covariance function) from a regionalized variable Z_1, \dots, Z_n can be decomposed into a linear combination of a set of independent components or orthogonal functions. These orthogonal components of the RF could explain, at different scales, the variability observed in the variogram or in the covariance function from a REV. The simple or cross semivariograms are referred to as nested structures, as they result from a linear combination of basic structures.

Factorial kriging performed in a multivariate framework, deals *sensu stricto* with cokriging estimates. In this approach, the decomposition of a regionalized variable into a linear combination of orthogonal factors that will explain, at various scales, the

phenomena under study, is considered. In the time-lapse domain, these factors could be interpreted as: a *common geological* response; a *common acquisition noise* or even a *4D seismic response* due to production and injection.

In the subsequent developments, the following conventions for indexes and variables are used:

- \mathbf{u} : location vector with coordinates (x, y, z) ;
- $Z_i(\mathbf{u})$: regionalized random function (REV);
- i : index of input seismic data volumes
- p : index of spatial structures contained in the data
- \mathcal{K} : number of orthogonal variables, or factors, that are limited, per construction, to the maximum number of input variables
- $\Gamma_p^i(\mathbf{u})$: spatial components as a result of the decomposition of $Z_i(\mathbf{u})$
- $\gamma_p(h)$: permissible basic variograms models from spatial structure p , with the constraint that the sums of the all sills must be equal to 1
- B_p : symmetric definite-positive square matrix from the sills of the p spatial structures
- $m_i(\mathbf{u})$: average value of $Z_i(\mathbf{u})$
- $Y_p^k(\mathbf{u})$: corresponds to the k^{th} orthogonal variable, or *factor*, resulting from the decomposition of the spatial structure $\Gamma_p^i(\mathbf{u})$, with the following properties

$$\begin{cases} m = 0 \\ Var(Y_p^k) = 1 \\ Cov(Y_p^k, Y_p^{k'}) = \delta_{kk'} \end{cases} \quad (54)$$

- $\delta_{kk'}$ Kronecker delta function

The goal is to provide a way to decompose a REV, such as a seismic amplitude trace, into a sum of two terms: a *non-stationary* $m_i(x, y, z)$ and a *stationary* one representing a linear combination of independent spatial structures.

This linear model may be described as follows

$$Z_i(x, y, z) = m_i(x, y, z) + \sum_{p=1}^P \Gamma_p^i(x, y, z) \quad (55)$$

Considering N jointly intrinsic random functions $Z_i(x, y, z)$, it is said that these functions follow a linear model of co-regionalization if their simple and cross-variograms can be described as a linear combination of permissible variograms models γ_p , as

$$\gamma_{Z_i, Z_j} = \sum_{p=1}^P B_p \gamma_p \quad (56)$$

The estimation procedure of Γ_p^i depends on the stationary assumptions, and we may choose different kriging approaches, such as ordinary kriging with an unknown m_i ; simple kriging with constant m_i or simple kriging with a variable m_i , given as an input map (kriging with an *external drift*).

The estimation of each spatial structure is performed by solving the following kriging system

$$\Gamma_p^i(x, y, z) = \sum_{\alpha} \lambda_{\alpha} Z_i(x, y, z) \quad (57)$$

where λ_{α} are the weights to be used in all α neighbors of the point to be estimated.

Let I be the number of spatial components, and introducing the coefficient a_p^{ik} , Eq. (57) is rewritten as

$$\Gamma_p^i(x, y, z) = \sum_{k=1}^K a_p^{ik} Y_p^k(x, y, z) \quad \forall i = 1, \dots, I \quad (58)$$

where Y_p^1, \dots, Y_p^N are the mutually independent orthogonal kriging factors whose means are equal to 0 ($E(Y_p^i Y_p^j) = 0, \forall i \neq j$) and their variance to 1 ($E\{(Y_p^i)^2\} = 1$), and with variogram γ_p .

By replacing (58) in Eq. (55) and (1.2), it becomes

$$Z_i(x, y, z) = m_i(x, y, z) + \sum_{p=1}^P \sum_{\kappa=1}^K a_p^{i\kappa} Y_p^\kappa(x, y, z) \quad \forall i = 1, \dots, I \quad (59)$$

In the same way, it is possible to rewrite the variograms and cross-variograms as

$$\gamma_{Z_i Z_j} = \sum_{p=1}^P \sum_{\kappa=1}^K a_p^{i\kappa} a_p^{j\kappa} \gamma_p \quad (60)$$

Assuming the independence of the orthogonal factors Y_p^1, \dots, Y_p^N and of the spatial structures $\Gamma_1^i, \dots, \Gamma_p^i$, the covariance is given by

$$\text{Cov}(Y_p^k, Y_p^k) = \delta_{pp} \delta_{kk} \quad (61)$$

By introducing the coefficient

$$b_p^{ij} = \sum_{\kappa=1}^K a_p^{i\kappa} a_p^{j\kappa} \quad (62)$$

the variogram in (60) may be rewritten as a linear combination of the variograms of orthogonal factors Y_p as

$$\gamma_{Z_i Z_j} = \sum_{p=1}^P b_p^{ij} \gamma_p \quad (63)$$

where b_p^{ij} is the sill matrix of the spatial structure p . Equation (63) establishes the relationship between the structural components and the variograms of orthogonal factors.

Finally, the implementation of the factorial kriging technique can be performed in two-steps.

- **Decomposition of the spatial structures into orthogonal factors**, by diagonalizing the variance-covariance matrix \mathbf{B}_p . An eigenvalue λ_p will be associated to each orthogonal factor Y_p , and provides a quantification of the amount of information from the random variables was retained in each factor.
- **Estimation of the orthogonal factors Y_p by cokriging the experimental measurements**, and by solving the cokriging system for each factor.

When performing the multivariate factorial cokriging, an important point refers to the additional difficulties imposed by the increasing number of semivariograms and cross semivariograms to be adjusted, which is a function of the N_v variables considered in the problem at hand, and equal to $N_v(N_v + 1)/2$.

3.2.6. Analogy between Factorial Kriging and Spectral Methods

In the original paper where the Factorial Kriging concept was proposed, Matheron (1982) states that most of data analysis techniques available at that time shared a common feature: *none of the available tools could handle the spatial characteristics of a regionalized phenomena found in the geosciences domain*. He also noticed the difficulties found when applying spectral analysis techniques on data collected at irregular spacing, an usual situation in the mining or petroleum exploration.

In this section, a brief description of the formal link between the spectral analysis methods, which are conventionally used in seismic data processing and

analysis, and its equivalent in the geostatistical domain, is presented and discussed. Despite the increasing utilization of these techniques, mainly during the reservoir characterization phase in the oil industry, geostatistical techniques are still far from the point to be considered as a daily basic tool available for the geoscientists in charge of the seismic interpretation. A comprehensive theoretical discussion of the similarities and differences between geostatistics and spectral analysis may be found in Solow (1984).

In the Factorial Kriging Analysis, or simply *Factorial Kriging* approach (FK), the goal is to decompose a phenomenon, whether stationary or not, into its own different characteristic frequencies as show by the structural analysis (Sandjivy, 1984). The same idea is behind the Spectral Analysis (SA), or Fourier analysis method. It provides a decomposition of a function, in this case a periodic and continuous function, into a sum of sinusoidal functions, each with a different amplitude, wave number and phase. The amplitude and phase spectra of the input data are then derived from direct Fourier transform.

Spectral analysis consists of estimating and interpreting a characteristic feature of a stationary process called the *spectral density*, or the *spectrum*. The spectrum is a measure of the contribution to the variance of the process made at each frequency. Comparing FK with SA, an equivalence exists between the semivariogram used in geostatistics and the spectral density (or spectrum) of the spectral analysis; and the autocorrelation function from the time-series analysis (Solow, 1984).

Ma and Royer (1987, 1988) discuss the behavior of the weighting functions in the formalism of the Factorial Kriging, comparing this algorithm with the spectral analysis that works in the frequency domain. These authors show that the weighting functions from the Factorial Kriging are similar to the classical filters used in image processing, for a given model of covariance, or variogram.

Considering a second order stationary random function $Z(\mathbf{u})$, with mean $m = E\{Z(\mathbf{u})\}$, the Factorial Kriging approach consists of decomposing a stationary

random function into a sum of orthogonal and stationary centered random functions $Z_i(\mathbf{u})$, with

$$\begin{cases} Z(\mathbf{u}) - m = \sum_{i=1}^k Z_i(\mathbf{u}) \\ E\{Z_i(\mathbf{u})\} = 0 \\ Cov(Z_i(\mathbf{h}), Z_j(\mathbf{h})) = C_{ij}(\mathbf{h}) = 0 \quad \forall i \neq j \end{cases} \quad (64)$$

From the previous hypothesis, the auto covariance function $C_{ZZ}(h)$ of $Z(\mathbf{u})$ can be written as a linear combination of each individual auto covariance function $C_{ii}(h)$ of each component $Z_i(\mathbf{u})$

$$C_{ZZ}(h) = \sum_{i=1}^k C_{ii}(h) \quad (65)$$

where k is the number of components or models of covariance present in the nested structure. Considering the kriging approach as presented in paragraph 3.2.1, the linear estimator of the component $Z_i(\mathbf{u})$ at \mathbf{u}_α is

$$Z_i^*(\mathbf{u}) = \sum_{\alpha=1}^n \lambda_i^\alpha(\mathbf{u}) [Z(\mathbf{u}_\alpha) - m]; \quad \alpha \in V_\alpha \quad (66)$$

where n is the number of data points in the neighborhood α , and $\lambda_i^\alpha(\mathbf{u})$ is the weight to be assigned at every data $z(\mathbf{u})$ for the estimation of the i^{th} component.

Assuming the knowledge of the mean value, the kriging system provides the estimation of $Z_i(\mathbf{u})$ by computing, first, the weights $\lambda_i^\alpha(\mathbf{u})$, as follows

$$\sum_{\alpha=1}^n \lambda_i^\alpha C_{ZZ}^{\alpha\beta} = C_{ZZ}^{x\beta} \quad i = 1, \dots, k \quad (67)$$

Equation (67) is a generalization of the Wiener filter in the case where $Z_i(\mathbf{u})$ does not represent the whole function, but one of its components, regardless its origin, whether associated to signal or noise.

Rewriting equation (66) in a matrix form, it becomes

$$Z_i^*(\mathbf{u}) = \Lambda_i^t [\mathbf{Z} - m \cdot \mathbf{u}] \quad (68)$$

Where

Λ_i^t is the row vector of weights;

\mathbf{Z} is the column data vector; and

\mathbf{u} is an unit column vector of dimension equal to n ;

And equation (67) becomes

$$\mathbf{C}_{ZZ} \Lambda_i = \mathbf{C}_{Z_i Z} \quad (69)$$

With weights expressed as

$$\Lambda_i^t = \mathbf{C}_{Z_i Z}^t \mathbf{C}_{ZZ}^{-1} = \mathbf{C}_i^t \mathbf{C}_{ZZ}^{-1} \quad (70)$$

Where \mathbf{C}_{ZZ} is the Toeplitz matrix of the covariances of $Z(\mathbf{u})$ and $\mathbf{C}_{Z_i Z}$ is the vector of the cross-covariances between $Z_i(\mathbf{u})$ and $Z(\mathbf{u})$.

The Wiener-Khinchine theorem shows that the autocovariance function is the Fourier transform of the spectral density in one dimension. Then, by computing the Fourier transform of the weights, the frequency solution from equation (70) is found as follows (Ma and Royer, 1987)

$$\Gamma_i(\omega) = \frac{\Phi_{Z_i Z}(\omega)}{\Phi_{ZZ}(\omega)} = \frac{\Phi_{ii}(\omega)}{\Phi_{ZZ}(\omega)} \quad (71)$$

And the Fourier transform of the weight vector Λ_i' is defined as the ratio between the cross-spectrum between the RF $Z_i(\mathbf{u})$ and the auto-spectrum of $Z(\mathbf{u})$.

The estimation of the RF $Z_i(\mathbf{u})$ component by Factorial Kriging may be taken as a convolution process involving the kriging vector weights $\lambda_i^\alpha(\mathbf{u})$ and the raw data $Z(\mathbf{u})$. These vector weights may be considered as the transfer functions of the linear system.

Chilés et al. (1999) list a few practical limitations usually found in spectral methods that are not observed when performing geostatistical filtering by FK, such as:

- a complete and rectangular grid of data is required, therefore involving additional data interpolation and/or extrapolation. These operations could, a priori, potentially modify the spectral characteristics of the input irregular data;
- tapering and padding to make the input grid periodic; and
- smearing of local anomalies over all frequencies.

3.2.7. Analogy between Factorial Kriging and Single Value Decomposition

Another technique that explores the decomposition of the data covariance matrix is the Singular Value Decomposition (SVD), with many applications in the seismic processing domain to filter seismic data (Freire et al., 1988, Mari, 2006), or curvature analyses (Bergbauer et al., 2003).

The SVD technique aims at decomposing the data variance-covariance matrix into a linear combination of orthogonal eigenvectors and its corresponding eigenvalues. The largest eigenvalue, or singular value, corresponds to the lowest frequencies. Due to this property, it can be explored as a filtering technique.

The work presented by Freire et al. (1988), describes an application of the SVD algorithm on the decomposition of a VSP data. In this case, the goal was to discriminate and filter out different types of signal recorded in the wavefield. The matrix of data \mathbf{Z} , containing M traces, where each trace with N data points described as

$$\mathbf{Z} = \{z_{ij}\}, \quad i = 1, 2, \dots, M; \quad j = 1, 2, \dots, N; \quad (72)$$

may be decomposed by SVD as

$$\mathbf{Z} = \sum_{i=1}^r \sigma_i \mathbf{u}_i \mathbf{v}_i^T \quad (73)$$

where

T represents the transpose of the matrix;

r indicates the rank of the matrix \mathbf{Z} ;

\mathbf{u}_i is the eigenvector of the covariance matrix $\mathbf{Z}\mathbf{Z}^T$;

\mathbf{v}_i is the eigenvector of the covariance matrix $\mathbf{Z}^T\mathbf{Z}$; and

σ_i is the singular value of the matrix \mathbf{Z} , or the positive square roots of the eigenvalues of the covariance matrices $\mathbf{Z}\mathbf{Z}^T$ and $\mathbf{Z}^T\mathbf{Z}$;

Due to the positive definite nature of the covariance matrices $\mathbf{Z}\mathbf{Z}^T$ and $\mathbf{Z}^T\mathbf{Z}$, the corresponding eigenvalues are always real and positive.

The decomposition scheme proposed in equation 2.51 is similar to principal component analysis. The product $\mathbf{u}_i \mathbf{v}_i^T$ represents a matrix of unitary rank, which is called an *eigenimage* of the data matrix \mathbf{Z} . The magnitude of the corresponding singular value σ_i responds for the contribution of each eigenimage when reconstructing the original \mathbf{Z} data. Due to the orthogonality of the eigenvectors, these eigenimages form an orthogonal base for the representation of the matrix \mathbf{Z} .

Assuming that all M seismic traces are independent from each other – which is not a reasonable assumption when dealing with seismic data - then the matrix of data \mathbf{Z} is of full rank M , and all singular values σ_i are different from zero. In this case, the reconstruction of the original data \mathbf{Z} requires all computed eigenimages. The opposite case, when all the M trace vectors are linear dependent, the matrix \mathbf{Z} is of rank one and is represented only by the first eigenimage $\sigma_1 \mathbf{u}_1 \mathbf{v}_1^T$.

In the most general case, the linear dependence of the input data traces will control the amount of eigenimages necessary to correctly reconstruct the original data \mathbf{Z} . The correlation between the input traces is, therefore, the criteria used to reject or accept the seismic traces in a filtering procedure: a *band-pass* filtered image, for instance, results from the reconstruction where both the highly correlated and the highly non-correlated traces are rejected. On the other hand, a *low-pass* and a *high-pass* SVD images are obtained by rejecting, respectively, the highly correlated and the highly non-correlated traces.

Compared to the Factorial Kriging approach, the Single Value Decomposition presents the drawback of operating only on the variance-covariance matrix, as the factors, or eigenimages, are uncorrelated only at zero distance (Chiles et al., 1999). Actually, this particular point is one of the strengths of the Factorial cokriging methodology, where a separate PCA is performed for each p spatial component, for every sill matrix \mathbf{B}_p , enabling a scale-dependent analysis of the correlation structures among the considered variables. Additionally, the SVD technique works only on data regularly distributed in a grid, imposing an additional restriction.

3.3. Conclusions

In this chapter, a brief introduction of some important geostatistical concepts and techniques and formulations were presented and discussed, with the main focus on the Factorial Kriging (FK) technique and its applications.

A comparison of the Factorial Kriging technique with other conventional techniques, such as the Single Value Decomposition (SVD) and the Spectral Analysis, is presented. These tools are usually applied in the conventional seismic processing workflow to perform spatial data analysis and filtering, but both have limited impact when evaluating the variability as a scale-dependent phenomena. In the first case, it was show that the SVD operates only on the variance-covariance matrix of the available data, and that the resulting eigenimages are only independent at zero lag distances. The Spectral Analysis applications, on the other side, operates directly on the frequency domain, typically by implementations of the Fourier transforms. These applications are not constrained by any spatial structure, and performs a brute filtering .

One shortcoming of the Factorial Kriging technique – and of all estimation techniques applications based on the variogram - is the strong dependence on an arbitrary and subjective variogram interpretation, usually referred to as the structural analyses. The decomposition of the random function $Z(\mathbf{u})$ in a set of independent basic variogram functions is strongly dependent on the interpreters choice. As described in the text, some authors have explored the uncertainties associated to the variogram estimation parameters. If this decomposition is based solely on the z sample covariance, then it is an artifact of the model rather than a proof of the physical significance of the resulting orthogonal factors Y_p^k (Deutsch & Journel, 1998). Some approaches are based on the automatic extraction of the "common-part" provided by the experimental cross-covariance or cross-variogram, as the automatic extraction technique proposed by Coleou (2005). This author suggests that this robust common part extraction may bypass this characteristic, considered as a drawback of the Factorial Kriging technique. In this work, we will explore the possibility of adapting those models of covariance or variograms used in the FK to better characterize the underlying spatial structures from time-lapse seismic datasets.

Chapter 4 - Application of the Geostatistical Filtering on the Senlac heavy oilfield

In this chapter, a description of the implementation of the Factorial Kriging on a heavy oil reservoir is presented. This geostatistical estimation methodology enables the analysis and the decomposition of the spatial structures present in the multivariate time-lapse seismic dataset into its corresponding orthogonal factors.

First, a description of the geology and the enhanced oil recovery scheme adopted in the Senlac heavy oilfield is presented, followed by a description of the time-lapse seismic acquisition parameters and the seismic processing previously carried out by the contractor in the area.

Secondly, the statistical characterization of the three time-lapse seismic data volumes from Senlac is presented, that will help in describing the variability and the correlations observed among the volumes. Two different time-windows, corresponding to a reservoir zone and to a non-reservoir zone, where no production related effects are expected, are analyzed.

The following section involves the implementation of the Factorial Kriging analyses on the data, and includes: variographic analysis, orthogonal factors estimation, seismic data reconstruction, and filtering those components assumed to be associated to artifacts. An unsupervised seismic facies analysis classification on both raw and filtered seismic datasets is then performed, aiming at quantifying the impact of the geostatistical filtering technique on the interpretation results.

In the last paragraph, the theoretical dependence of the elastic parameters on the reservoir pressure is investigated and discussed. It was observed that, in the time-lapse seismic campaign data registered on the heavy oil Senlac reservoir, the monitor seismic data surveys exhibit negative time-shifts (or a pull-up) in the reservoir interval, when compared to the base survey. This result is in disagreement with what is expected from

theoretical models relating temperature and velocities, and the possible causes for this discrepancy are presented and discussed.

At the end, a conclusion is presented, including perspectives for future works.

4.1. The Senlac dataset

The SENLAC oil pool belongs to a heavy oil belt located close to the Alberta-Saskatchewan border in Canada, as shown in Figure 4-1. The oil production in this pool started in 1996, where the producing reservoir corresponds to unconsolidated sandstones deposited as fluvial channels of the Lower Cretaceous Dina Formation, overlying directly an erosional surface of Paleozoic carbonate rocks. Figure 4-2 presents a stratigraphic column of the SENLAC area.

The depositional environment of the Dina Formation is interpreted to be either a valley fill system or an estuary deposit. This formation is composed by a massive sandstone at the bottommost part, and fines upward. The upper portion of the channel deposit shows an increasing shale content, being often comprised of sand and shale interbeds ("transition zone"). The Dina channel is laterally offset by the Regional Dina Facies, which are composed of interbedded argillaceous sands and shales, not considered to be prospective. The source rocks are believed to be older shales or carbonate sequences.

These reservoirs occur at shallow depths, at approximately 730 m (equivalent to 700 ms of two-way-time), showing an average thickness of 15 m with good permeabilities (5-10 D) and average porosity of 33% (Dequirez et al., 1995; Li et al., 2001). Despite the good average petrophysical properties of the Senlac reservoir, the oil shows an API gravity of 13°API and a viscosity of 5000 cp (at reservoir conditions), imposing serious limitations to the primary oil production.

The high viscosity of these heavy oil reservoirs demanded additional efforts to improve their production performance by using enhanced recovery methods. Three major types of enhanced oil recovery operations are: chemical flooding (alkaline flooding or micellar-polymer flooding); miscible displacement (carbon dioxide [CO₂]

injection or hydrocarbon injection); and thermal recovery (steam flood or in-situ combustion). The optimal application of each type depends on many reservoir parameters, such as: reservoir temperature, pressure, depth, net pay, permeability, residual oil and water saturations, porosity and fluid properties such as oil API gravity and viscosity.

The thermal recovery scheme was adopted in the Senlac oil pool, and, from a geophysical point of view, it is one of the most interesting for seismic monitoring purposes, as acoustic seismic properties are much sensitive to density and velocity contrasts imposed by temperature effects and fluid changes. Many well succeeded applications of monitoring of thermal effects using time-lapse seismic are described in the literature (Lumley, 1995; Zhang et al., 2004)

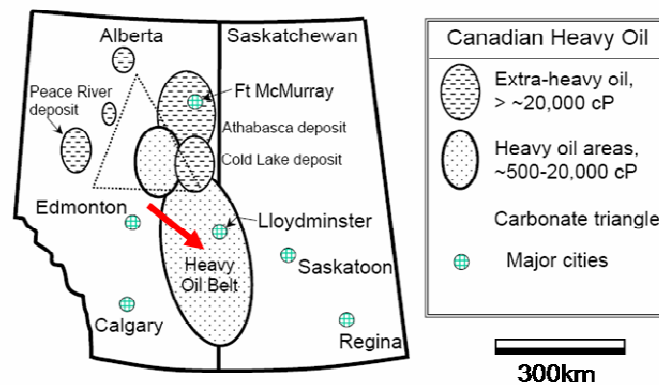


Figure 4-1 - Location of the heavy and extra-heavy oil sands occurrences in Alberta and Saskatchewan states, Canada. The red arrow locates the Senlac oil pool (modified from Dusseault, 2002).

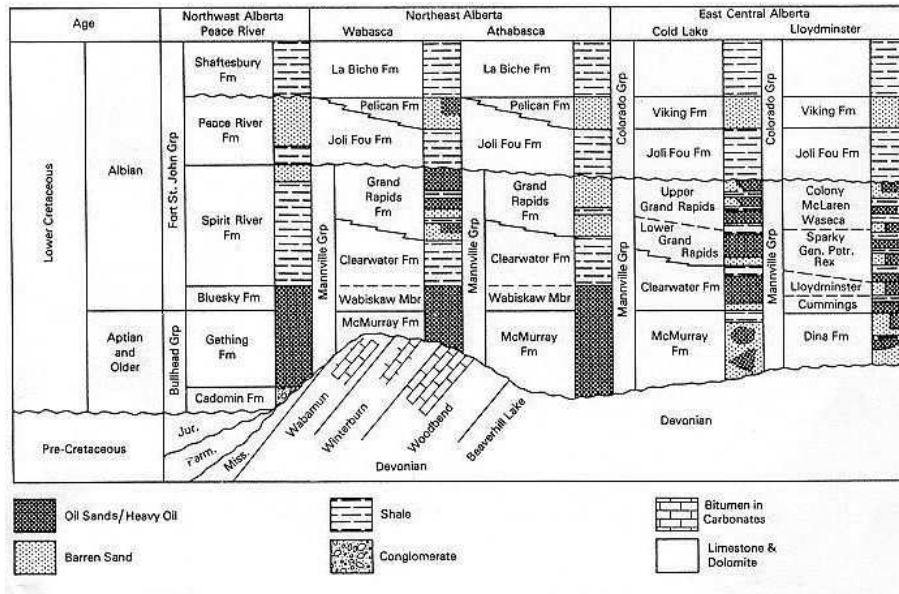


Figure 4-2 – Stratigraphic column illustrating the primary oil sands and heavy oil occurrences in Alberta, Canada (from www.lloydminsterheavyoil.com).

4.1.1. SAGD thermal recovery scheme

Due to the high density and viscosity (13° API and 5000 cp, at reservoir conditions) of the Senlac oil, a thermal recovery scheme was adopted to enhance the hydrocarbon production.

The selected thermal technique, known as Steam Assisted Gravity Drainage - SAGD, is implemented by drilling a pair of horizontal wells through the reservoir zone, where the injector well is placed a few meters above the producer. The former injects steam into the producing zone, creating a high-temperature steam chamber in the formation. The induced heat decreases the viscosity of the thick crude, allowing gravity to assist it to flow freely to the horizontal production well below, as shown in Figure 4-3.

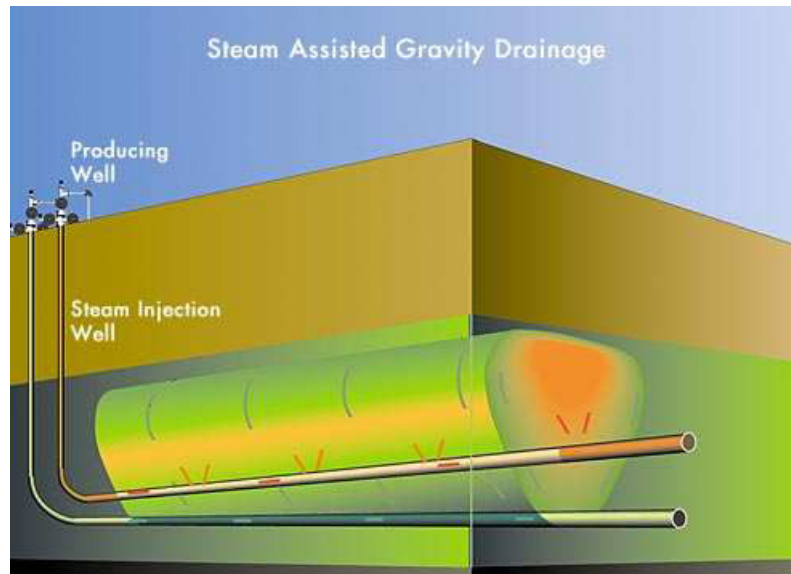


Figure 4-3 – Steam Assisted Gravity Drainage (SAGD) scheme (from www.encana.com).

4.1.2. Time-lapse seismic data

To better characterize the SAGD steam chamber evolution, its efficiency in terms of oil sweep, as well as to understand the effects of the reservoir heterogeneities on the distribution of the heated reservoir zones, a time-lapse seismic monitoring study was performed in the SENLAC pool. Three different seismic surveys have been acquired at different calendar times over the field. The map in Figure 4-4 shows the relative location of these three time-lapse seismic data.

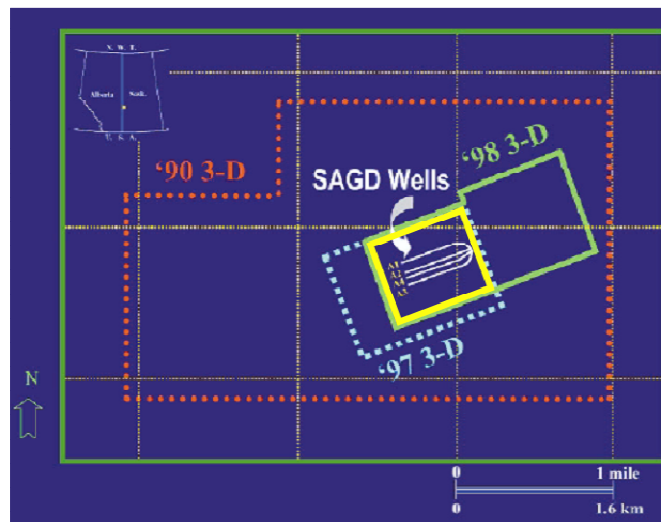


Figure 4-4 - SENLAC time-lapse seismic surveys and SAGD wells location (Li et al., 2001). The studied area is represented by the yellow box.

The first seismic survey was shot in 1990 for static reservoir characterization, and has been used as the reference or baseline survey, since it preceded the beginning of SENLAC oil production. Two other monitor seismic campaigns were shot in 1997 and 1998, respectively 18 and 24 months after the start of the steam injection. The maximum heating temperature, 260° C, was reached during this second monitor survey. The acquisition parameters for these three campaigns are listed in Table 4-1 below. In the following sections, the seismic datasets of 1990, 1997, and 1998 will be referred to as AMP90, AMP97, and AMP98, respectively.

Table 4-1 – Senlac seismic field acquisition parameters (extracted from Li et al., 2001).

Field parameters	Survey 1	Survey 2	Survey 3
Date	Winter 1990	Fall 1997	Spring 1998
Source type	Vibroseis 1 vibrator center on flag 8 sweeps, 6 seconds 18-144 Hz linear 6 dB/oct boost	Weight-drop Truckmount 16 pops per shot	Dynamite 1 Kg, single hole 6-m burial depth
Geophones	Geospace 14 Hz 12 over 2 m inline	SM-24 10 Hz 6 over 20 m inline	OYO 10 Hz 6 over 20 m inline
Recording equipment	I/O system I 360 channels max SEG-D format, FP gain 3(12)-180(75) Hz (dB/oct) notch out 9.0 s listen	I/O system II 728 channels max SEG-D format, FP gain 3(12)-207(298) Hz (dB/oct) 3/4 Nyquist min phase notch out	I/O system II 532 channels max SEG-D format, FP gain 3(12)-411(275) Hz (dB/oct) 3/4 Nyquist linear phase notch out
Record length	3.0 s @ 2ms	3.0 s @ 2 ms	3.0 s @ 1 ms
Source line spacing	180 m EW	160 m NE-SW	80 m NW-SE
Receiver line spacing	180 m NS	120 m NW-SE	80 m NW-SE
Source interval	60 m	40 m	80 m
Receiver interval	30m	20 m	40 m
Typical patch	8 lines × 45 stations 1260 m × 1320 m	13 lines × 56 stations 1440 m × 1100 m	19 lines × 28 stations 1440 m × 1080 m
Natural bin size	15 m × 30 m	10 m × 20 m	20 m × 40 m

It is worth mentioning the highly potential sources of non-repeatability observed in the seismic acquisition parameters listed in Table 4-1, where Survey 1, 2 and 3 accounts for AMP90, AMP97 and AMP98, respectively. From these parameters, at least three of them should be highlighted, as they were difficult to be properly handled during the seismic processing sequence:

- surveys shot at different calendar times, acquired at different times of the year: effects on source and receiver coupling and signatures;
- varying inline and cross-line directions, from base to the monitors: effects of seismic anisotropy;
- non-multiple bin sizes from base to monitors: re-binning issues

Other observed differences in the seismic acquisition parameters, such as the different geophone arrays and types, the difference on the number of available channels per shot, and different spread lengths used for each survey, will also contribute to reduce data repeatability.

To compensate for these major differences observed in seismic acquisition parameters, a careful cross-equalization seismic processing sequence was carried out by EnCana, the Senlac oilfield operator. This processing sequence aimed to minimize the observed acquisition discrepancies, yield the use of such data to seismic monitoring purposes. Three main processing steps were considered:

1. **Spatial realignment:** a pre-stack regridding was applied to set all three different surveys into a common grid, and the traces were reorganized in their new positions to form the new CDP gathers by using a 20x40m bin-size oriented with the azimuthal directions of the monitor surveys. A final post-stack interpolation transformation resized the final post-stack bin to 20x20m;
2. **Amplitude balancing:** aiming at preserving relative amplitudes, the following corrections / steps were performed: trace editing; noise filtering; off-set dependent spherical divergence gain corrections; inelastic attenuation correction; surface-consistent followed by single-trace zero-phase spiking deconvolution; and amplitude rescaling; and
3. **Cross-equalization:** using the AMP90 baseline line survey as the reference, the selected wavelet operator to cross-equalize the three different vintages used a long time window, from 250-1350ms (including the reservoir zone at approximately 710ms), and involved frequency content balancing, root-mean-square (RMS) energy equalization, time static corrections, and phase matching.

A detailed description of the seismic processing sequence can be found in Li et al. (2001).

4.1.3. Seismic data interpretation

A volumetric seismic interpretation has been performed in the seismic datasets, based on previous interpretation works and available seismic-to-well calibrations. Three

inline seismic sections corresponding to the AMP90, AMP97 and AMP98 seismic surveys are presented in Figure 4-5. In this figure, both the reservoir and non-reservoir zones are presented, where the main characteristics of the area, with very gentle dips, are observed. An inspection in these three cross-equalized inlines also shows that only small differences can be observed, as a result of the cross-equalization processing.

The Reservoir Zone has been limited on the top by the seismic horizon corresponding to the Lloydminster shale, a strong reflector corresponding to a trough, whereas on the bottom by the seismic horizon mapped as the reservoir base, corresponding to a peak, or a positive amplitude value. All horizons have been interpreted on the AMP90 seismic data, and used as a reference to extract all amplitude information from the AMP97 and AMP98 surveys.

The Non-Reservoir zone has been selected following two criteria: a) to be above and far enough from the reservoir zone to ensure no production-related effects; and b) to be able to interpret two seismic horizons with good lateral consistency. As shown in Figure 4-5, the top and bottom horizons defining the non-reservoir zone occur at approximately 445ms and 530ms of two-way-time (TWT).

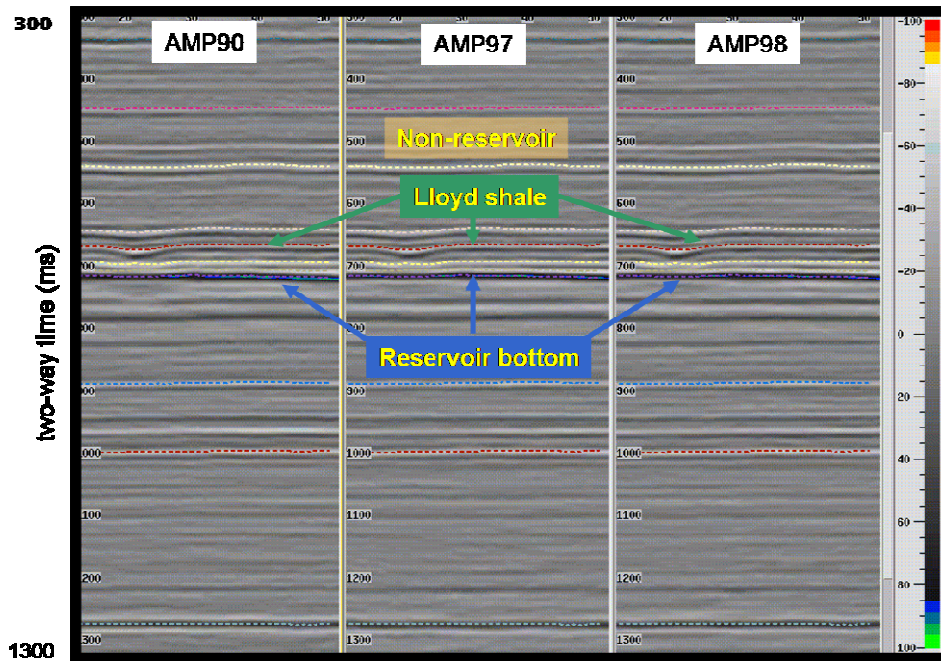


Figure 4-5 - Inline seismic sections from AMP90, AMP97 and AMP98 (from left to right). The main interpreted horizons used to define the Reservoir and the Non-Reservoir zones are indicated.

4.2. Statistical Characterization of Senlac Seismic Datasets

The main goal of this phase of the study is to explore the characteristics of the data distribution, its statistical representation, as well as the relationship between the studied variables, typically by using a set of graphical tools.

In this section, three different time windows of the three different seismic campaigns are analyzed. The first time window studied gives an overall description of the whole seismic volumes, covering a time interval ranging from 200ms to 1500ms, corresponding to 651 samples. This window is an important reference, allowing the comparison of the other two narrower windows studied: the Non-Reservoir and the Reservoir Zones, that correspond, respectively, to 49 and 12 samples.

4.2.1. Overall Data Statistical Description

The histograms and cumulated histograms from this big time interval are presented in Figure 4-6 and Figure 4-7. These histograms show a clear symmetric distribution, with a stronger peak close to zero amplitude, approaching a double exponential distribution, with a rapid decay to the tails. Skewness values are close to zero and positive kurtosis can be observed for all three volumes, as shown in Table 4-3. By analyzing this table and Table 4-2, where all main statistics are presented – minimum, maximum, mean, standard deviation, and variance values, the strong similarity among all three populations is remarkable. The variational coefficient –ratio between the standard deviation and the mean – are quite high, confirming that the mean values are close to zero, when compared to the range of the distribution.

The quantile-quantile plots (Q-Q plots) from Figure 4-8 show larger deviations from the normal behavior for high positive amplitude values; this could be associated with clipping at high amplitude values.

The scatter plots of the whole seismic volumes are presented in Figure 4-9, with a resume of the correlation coefficients in Table 4-4. A higher dispersion is observed in the scatter of AMP90xAMP97, that shows a coefficient of $\rho = 0,867$, increasing to 0,896 in the AMP90xAMP98. These smaller correlation coefficient values should actually be expected when one compares the acquisition design and parameters presented in Table 4-1 and Figure 4-4. Both AMP97 and AMP98 are quite similar in terms of acquisition parameters, as confirmed by the higher coefficient $\rho = 0.922$ and smaller dispersion presented in the AMP97xAMP98 scatter plots.

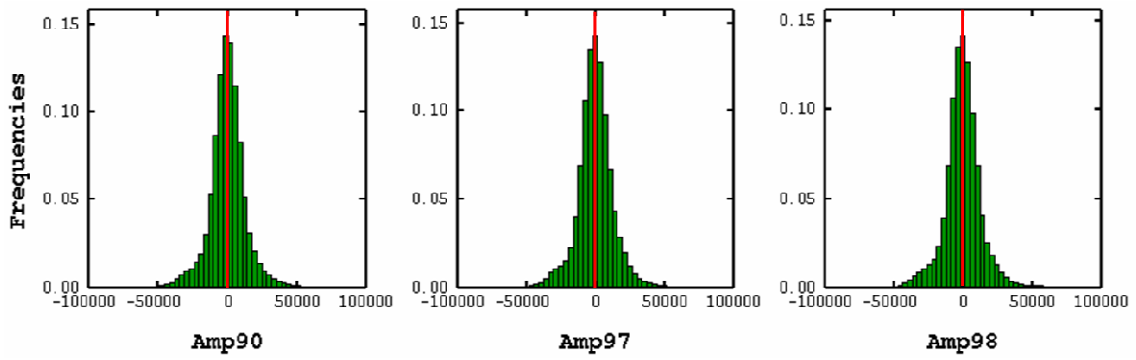


Figure 4-6 – Histograms of the three SENLAC seismic volumes.

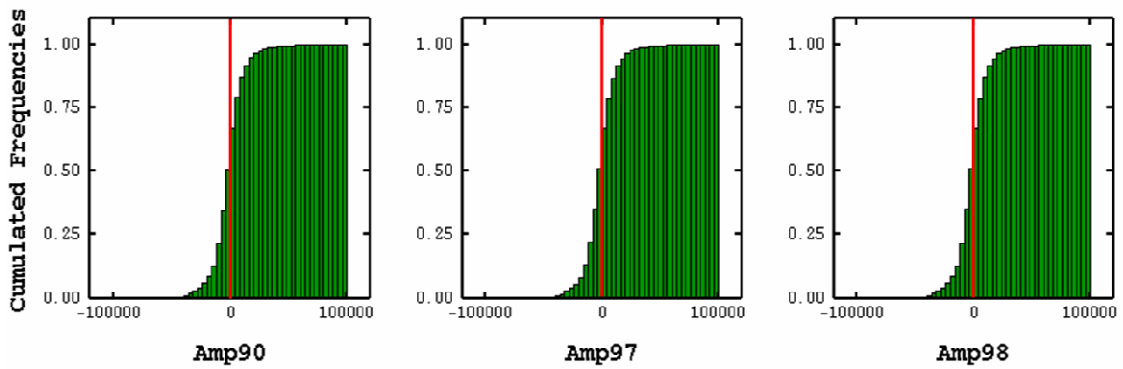


Figure 4-7 – Cumulated histograms of the three SENLAC seismic volumes.

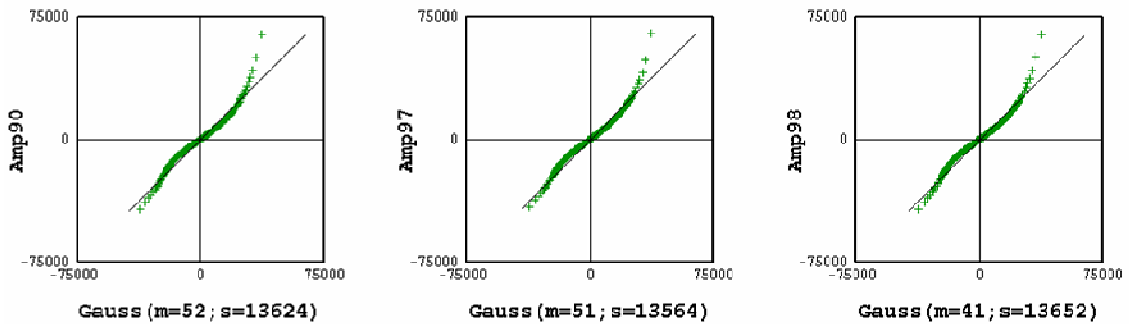


Figure 4-8 – QQ-Plots of the three SENLAC seismic volumes.

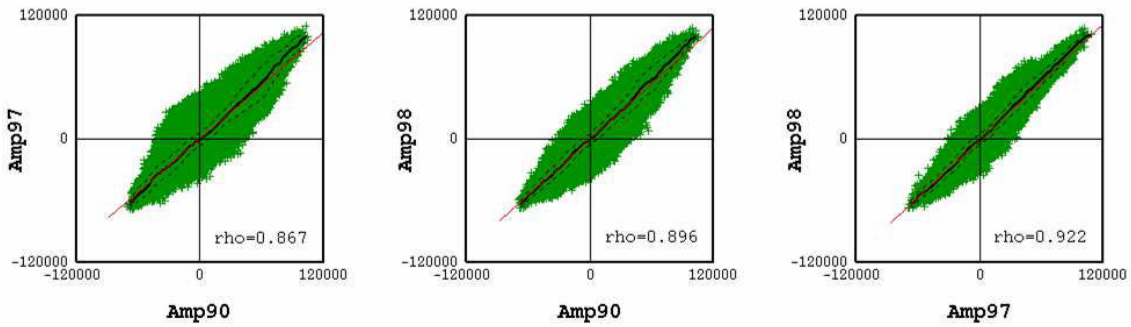


Figure 4-9 – Scatter plots. The linear regression is shown as a red line, whereas the continuous black represents the conditional expectation curve and the dotted curves the standard deviation around the conditional expectation.

Table 4-2 - Univariate statistics from SENLAC seismic volumes.

	Count	Minimum	Maximum	Mean	Standard Deviation	Variance (x10 ⁸)
AMP90	1204350	-69924	104991	52	13624	1,856
AMP97	1204350	-69240	107894	51	13564	1,840
AMP98	1204350	-67835	106000	41	13651	1,864

Table 4-3 - Univariate statistics from SENLAC seismic volumes.

	Variational Coefficient	Skewness	Kurtosis
AMP90	259,57	0,60	7,52
AMP97	267,73	0,66	7,69
AMP98	334,17	0,62	7,68

Table 4-4 - Correlation coefficients computed for the entire seismic data time interval.

	Correlation Coefficient		
	AMP90	AMP97	AMP98
AMP90	1	0.87	0.90
AMP97	0.87	1	0.92
AMP98	0.90	0.92	1

4.2.2. Statistics of the Non-Reservoir Zone

The Non-Reservoir zone has been described in Section 3.1.3 as a time-window constrained by top and bottom horizons at approximately 445ms and 530ms TWT.

The histograms and cumulated histograms for the Non-Reservoir zone are presented in Figure 4-10 and Figure 4-11, and show a strong peak close to 0 amplitude value, and are skewed to the negative amplitude side (left). The histograms of AMP97 and AMP98 suggest a bimodal distribution, whereas a three-mode distribution may be suggested to AMP90, and this shift from the normality is confirmed by the reduction of the kurtosis values, as shown in Table 4-6, compared to the whole dataset description.

Analysis of Table 4-5 confirms the results concerning data similarity presented in the previous paragraph. In the Non-Reservoir interval, despite the high correlation coefficients shown in Table 4-7 and almost the same behavior presented by the scatter plots of the three datasets (Figure 4-13), the data variances show a higher dispersion when compared to both the whole seismic interval and the Reservoir Zone, as may be observed in Table 4-5. The analysis of the quantile-quantile plots (Q-Q plots) also confirms the data similarity, with the three plots showing the same behavior, as seen in Table 4-8.

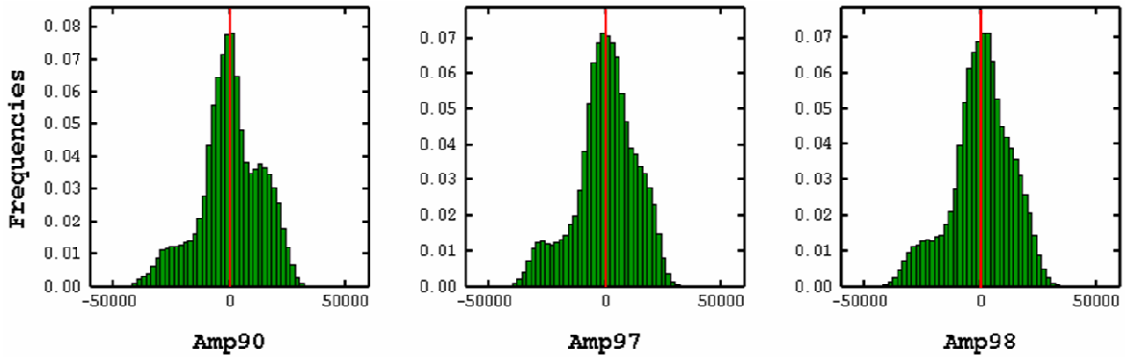


Figure 4-10 – Histograms of the NON Reservoir zone.

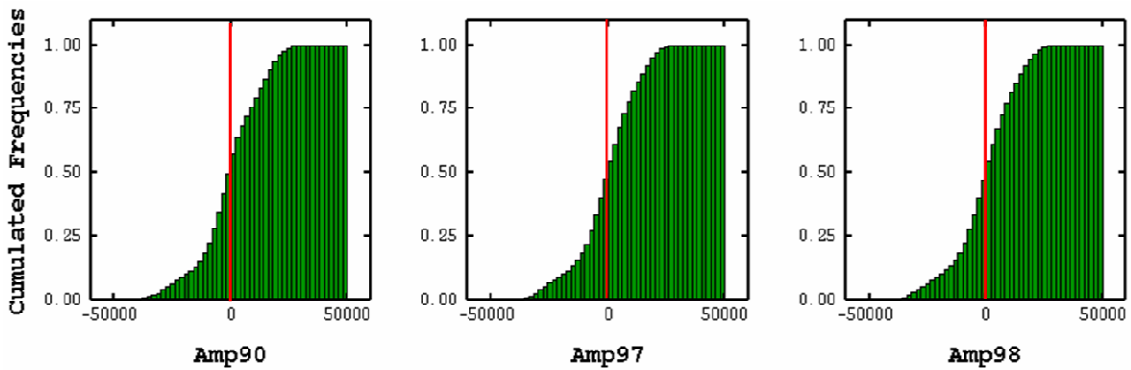


Figure 4-11 – Cumulated histograms of the Non-Reservoir zone.

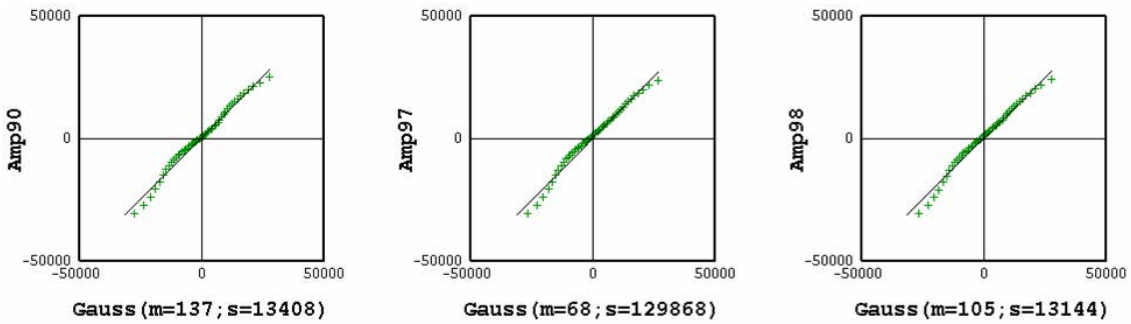


Figure 4-12 - QQ Plot of the Non-Reservoir Zone.

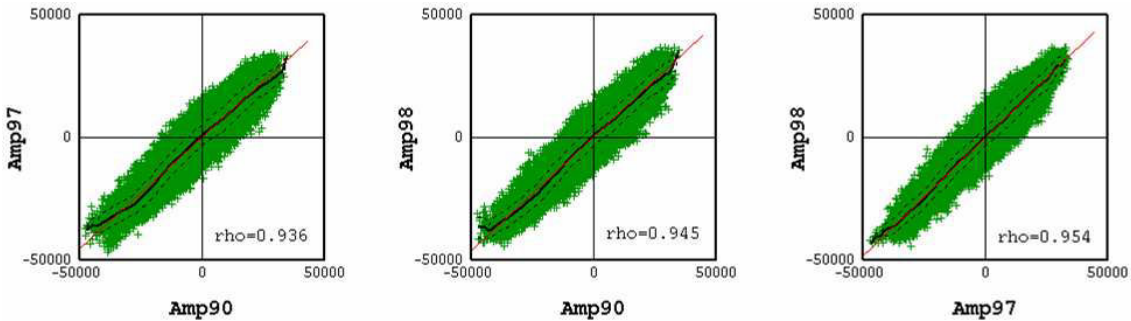


Figure 4-13 – Scatter plots of the Non-Reservoir zone. The linear regression is shown as a red line, whereas the continuous black line represents the conditional expectation curve, and the dotted curves the standard deviation around the conditional expectation.

Table 4-5 - Univariate statistics from SENLAC seismic volumes for the Non Reservoir Zone.

	Count	Minimum	Maximum	Mean	Standard Deviation	Variance (x10⁸)
AMP90	85491	-47409	34672	137	13408	1,798
AMP97	85491	-47258	33457	68	12986	1,686
AMP98	85491	-45086	35894	105	13144	1,728

Table 4-6 - Continued univariate statistics from SENLAC seismic volumes for the Non Reservoir Zone.

	Variational Coefficient	Skewness	Kurtosis
AMP90	97,71	-0,38	3,10
AMP97	191,51	-0,48	3,12
AMP98	125,58	-0,46	3,15

Table 4-7 - Correlation coefficient computed for the Non Reservoir Zone.

Correlation Coefficient			
	AMP90	AMP97	AMP98
AMP90	1	0,94	0,95
AMP97	0,94	1	0,95
AMP98	0,95	0,95	1

4.2.3. Statistics of the Reservoir Zone

Compared to the previous analysis of both the whole seismic interval and the Non-Reservoir zone, it is noticeable that the Reservoir Zone shows a much higher variability that is mainly related to the geology observed in this zone.

Defined in a shorter time window that comprises the producing sandstones and with an average time-thickness of 32ms, the Reservoir zone shows a characteristic bimodal histogram for the three analyzed datasets, as seen in Figure 4-14. This bimodality may be due to the wavelet response, with a stronger peak representing the negative amplitude values and a secondary positive peak. With very small skewness and kurtosis, as seen in Table 4-9, these zone showed the highest correlation coefficients –

all higher than 0,95, as seen in Table 4-10, with the AMP97 and AMP98 reaching 0,99. These higher correlation coefficients observed in the Reservoir zone, compared to the other ones studied, may suggest that a stronger processing effort in the cross-equalization step has been carried out.

A detailed inspection of Figure 4-18, which presents the scatter plots with a color code to represent the density of points per cell in the scatter, shows that a larger dispersion is observed between the positive amplitude values (ranging from approximately 20000 to 60000 units of amplitude) for both AMP90xAMP97 and AMP90xAMP98 plots. On the other hand, the AMP97xAMP98 scatterplot shows a much smaller dispersion. This response could be associated to the fact that these surveys were registered with coincident inline and crossline directions, or probably to the hydrocarbon production effect on the seismic amplitudes.

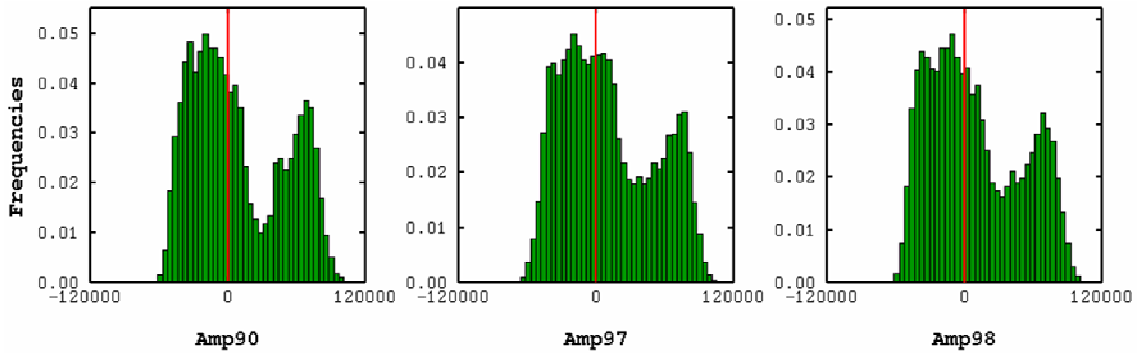


Figure 4-14 – Histograms of the SENLAC Reservoir Zone.

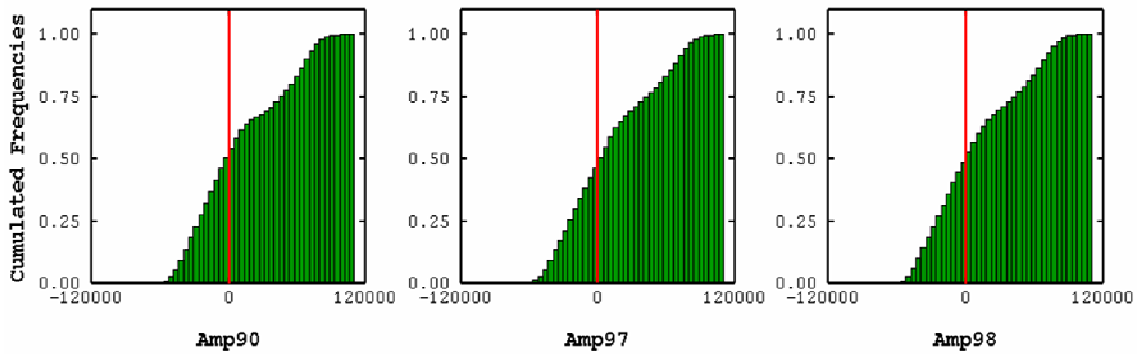


Figure 4-15 –Cumulated histograms of the SENLAC Reservoir Zone.

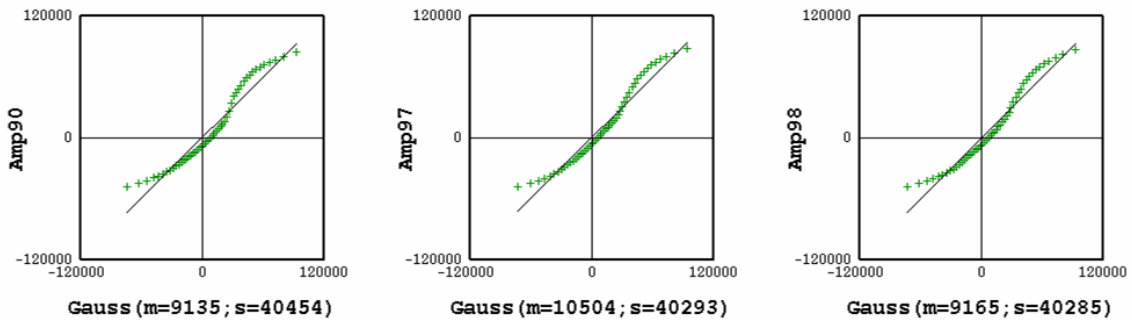


Figure 4-16 – Q-Q plots of the Reservoir Zone.

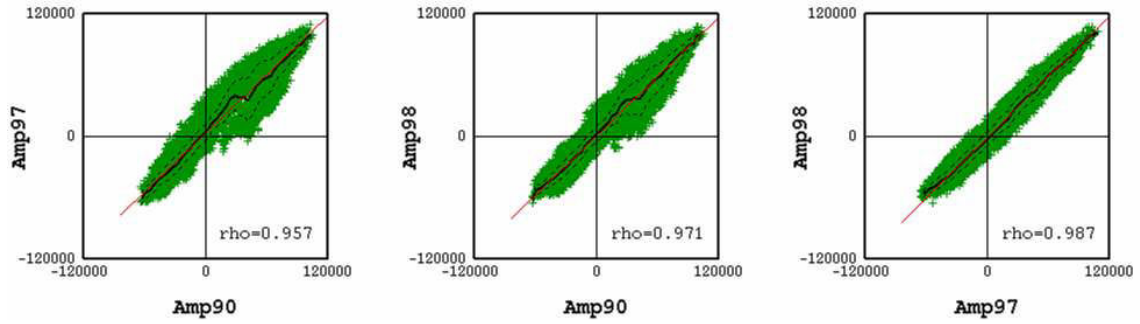


Figure 4-17 – Scatter plots of the Reservoir Zone. The linear regression is shown as a red line, whereas the continuous black represents the conditional expectation curve and the dotted curves the standard deviation around the conditional expectation.

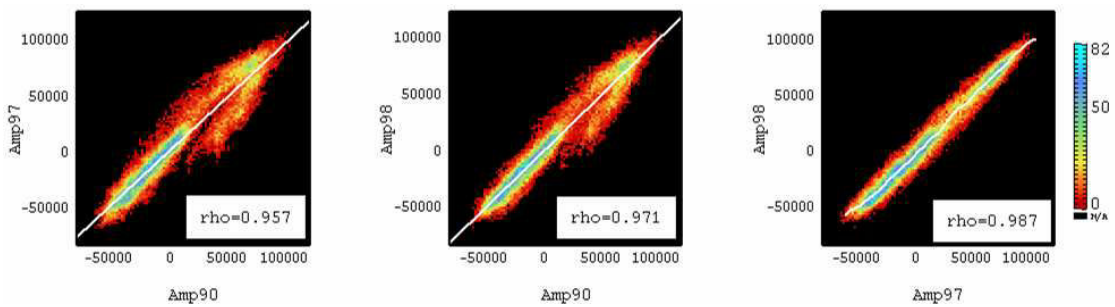


Figure 4-18 – The same scatter from Fig. 3.4-13, where the colors represent the number of points at each plot position.

Table 4-8– Univariate statistics from SENLAC seismic volumes for the Reservoir Zone.

	Count	Minimum	Maximum	Mean	Standard Deviation	Variance (x10 ⁸)
AMP90	25523	-63372	104991	9135	40454	16,365
AMP97	25523	-65575	107894	10504	40293	16,235
AMP98	25523	-66569	106000	9165	40284	16,228

Table 4-9 - Univariate statistics from SENLAC seismic volumes for the Reservoir Zone.

	Variational Coefficient	Skewness	Kurtosis
AMP90	4,4	0,39	1,87
AMP97	3,8	0,37	1,99
AMP98	4,4	0,40	1,97

Table 4-10– Correlation coefficient computed for the reservoir zone data.

Correlation Coefficient			
	AMP90	AMP97	AMP98
AMP90	1	0.96	0.97
AMP97	0.96	1	0.99
AMP98	0.97	0.99	1

4.2.4. Discussion on Statistical Analysis

From the previous analysis, it can be concluded that:

- a) The amplitude distribution behavior for AMP97 and AMP98 are similar, but differ from the AMP90 survey, for both Non-Reservoir and Reservoir zones, probably due to the closer acquisition geometry used in the AMP97 and AMP98 surveys; and to the grid rotation and rebinning imposed to AMP90 data;

- b) The amplitude values are closer to a normal distribution in the Non-reservoir Zone, as observed in the kurtosis values and the Q-Q plots from Table 3-6 and Figure 3-12,, and are much closer to the overall amplitude distribution as shown in paragraph 4.2.1. The three distributions are asymmetric, negatively skewed, and show a strong peak close to zero value amplitude;

- c) A bimodal distribution characterizes the amplitudes over the Reservoir Zone, possibly explained by the shorter window length. In this level, overall amplitude dimming with the elapsed-time can be observed. This effect may be related to non-repeatability, as stated in (a), but could also be due to acoustic properties variations induced by reservoir exploitation.

4.3. Factorial kriging

The main goal of this work, carried out using the Senlac seismic cross-equalized datasets, was to perform a geostatistical characterization to identify underlying structures contained in the dataset that could be interpreted in terms of geology, production-related signal, or noise, for further filtering and analysis. This interpretation was based on their structural behavior, and on the previous works carried out by Lucet and Fournier (2001) and Nivlet et al. (2001).

This geostatistical characterization approach also seems to be a convenient way to evaluate the cross-equalization procedure, providing tools to investigate the level of over or under cross-equalization applied in the datasets during the processing sequence.

4.3.1. Variogram and Cross-Variogram Maps

Variogram maps are useful tools to inspect the spatial variability of random variables and to determine their underlying structures and main directions of anisotropy.

The approach considered to compute the variogram and cross-variogram maps for each zone is the following:

- for the two zones, the data has been flattened, using, respectively, the base horizon of the Non-Reservoir zone and the top horizon of the Reservoir zone as the reference levels for the flattening procedure. It is important to stress that the choice of the top horizon as the reference for the flattening procedure seemed to be more convenient, as the reservoir bottom directly overlies an erosional surface corresponding to the top of the Paleozoic, which would compromise the facies classification and the final interpretation results;
- on the flattened volumes, and starting from the flattened horizon references, a vertical volume resampling has been performed, with the same time sampling interval as for the original data;

- omni-directional variograms and cross-variogram maps for each flattened slice have been computed, considering only the horizontal directions. The vertical variograms were not computed; and
- average horizontal omni-directional variogram and cross-variogram maps have been computed.

All variograms and cross-variograms have been computed using a 20m lag distance, following the original seismic grid dimensions. To avoid unbalanced points distribution and possible misinterpretations during the variograms modeling phase, a maximum lag distance of half the dimensions of the area studied has been considered, which represents approximately 20 lags. The horizontal variogram maps computed for the Non-Reservoir and for the Reservoir Zones are presented in Figure 4-19.

The variogram maps over the Non-Reservoir zone show an anisotropic behavior, with main continuity directions following both inline (U) and cross line (V) directions. These directions are also represented in the following graphs, by U (red) and V (green) arrows, respectively. A more complex response is observed in the AMP97 variogram map, showing a medium to long range behavior oriented to N15, bisecting the inline-crossline directions.

The analysis of the variogram maps over the Reservoir zone reveals a zonal anisotropy when comparing the inline and crossline directions, with a higher continuity in the cross-line (V) direction. These two main anisotropy directions are also in agreement with the main depositional axis of the fluvial channels of the Senlac reservoirs, oriented E-NE/W-SW. As seen before, a higher variability is also observed in the Reservoir zone compared to the Non-Reservoir, of one or two orders of magnitude in variance values.

Comparing the two window results, it seems obvious that the variability behavior is much more complex for the Non-Reservoir than for the Reservoir zone, possibly due to the more cautious processing applied to the latter.

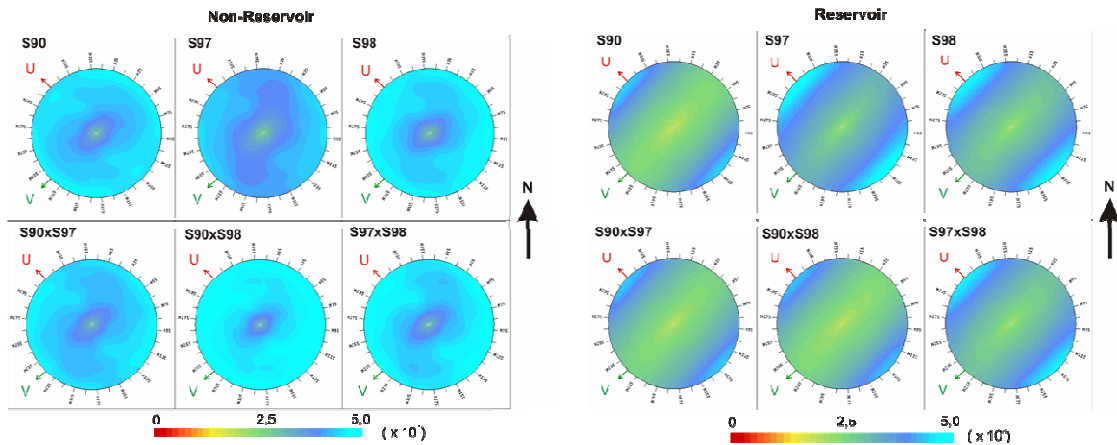


Figure 4-19 – Variogram (first row) and cross-variogram (second row) maps for the non-reservoir (left) and reservoir (right) zones, for the three SENLAC seismic datasets AMP90, AMP97 and AMP98. Scale of variance values in squared seismic amplitude unities. All variograms and cross-variograms with maximum search distance equal to 20 lags (or 400m).

4.3.2. Structural analysis

The experimental variograms and cross-variograms considered to model the spatial variability in both the Non-Reservoir and Reservoir zones, represent the average variogram and cross-variogram responses of forty nine horizontal horizons and twelve horizons, for the Non-Reservoir and Reservoir Zone respectively, that compose each seismic interval, as presented in section 3.2.

The strategy adopted to simultaneously fit the variograms and cross-variograms, following a Linear Model of coregionalization, involved: (i) testing and deciding the minimum numbers of basic structures and the hypothesis of anisotropy to be considered to better model the studied phenomena; (ii) fitting procedure, by modeling first the cross-variograms, and then each single variogram; and (iii) determining the variogram parameters - ranges and sills, adjusting the variance contribution for each component and for each direction.

a) Non-Reservoir Zone

In the Non-Reservoir interval, no significant trend was observed in the available experimental variograms and cross-variograms, for the investigated ranges. The decision as to which linear model of coregionalization to apply in this interval involved tests on the number of structures and ranges, and the best fit was achieved considering a nested model composed by 4 (four) basic structures: two spherical structures, a medium range exponential structure and a long range spherical, as shown in Table 4-11. In Figure 4-20, the experimental and modeled variograms and cross-variograms for the Non-Reservoir zone are presented.

Table 4-11– Final structural models and coregionalization matrices for the 4 (four) structures interpreted in the Non-Reservoir Zone.

Structure	Sill Matrix B_p ($\times 10^8$)
C1: Spherical Model, Isotropic <u>Practical ranges:</u> a = 10m (315°) a= 40m (225°)	$B_1 = \begin{pmatrix} 0,05 & 0,03 & 0,03 \\ 0,03 & 0,04 & 0,03 \\ 0,03 & 0,03 & 0,04 \end{pmatrix}$
C2: Spherical Model <u>Practical ranges:</u> a = 190m (315°) A= 70m (225°)	$B_2 = \begin{pmatrix} 0,07 & 0,05 & 0,05 \\ 0,05 & 0,05 & 0,04 \\ 0,05 & 0,04 & 0,07 \end{pmatrix}$
C3: Exponential Model <u>Practical ranges:</u> a = 220m (315°) a= 480m (225°)	$B_3 = \begin{pmatrix} 0,20 & 0,16 & 0,16 \\ 0,15 & 0,21 & 0,18 \\ 0,16 & 0,18 & 0,21 \end{pmatrix}$
C4: Spherical Model; Zonal anisotropy <u>Practical ranges:</u> a = 10000m (315°) a= 2500m (225°)	$B_4 = \begin{pmatrix} 0,03 & 0,03 & 0,07 \\ 0,03 & 0,08 & 0,06 \\ 0,07 & 0,06 & 0,14 \end{pmatrix}$

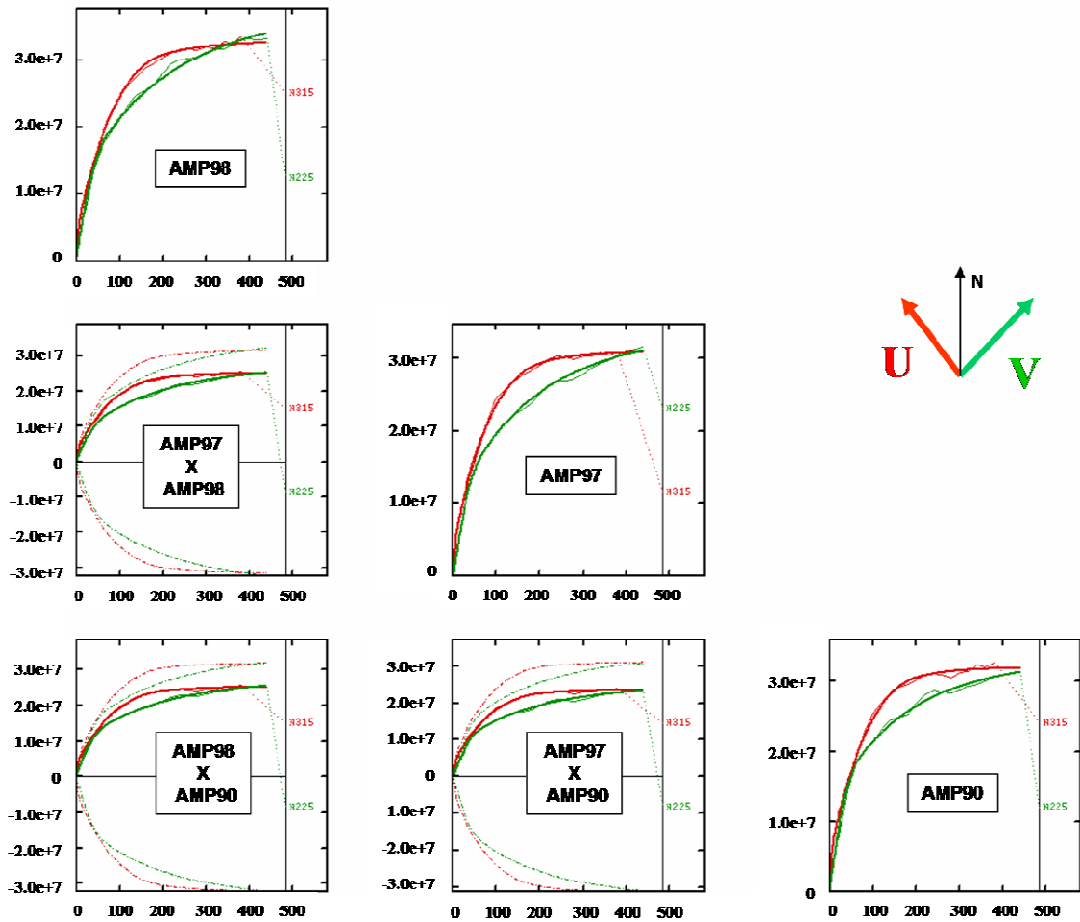


Figure 4-20 – Non-Reservoir Zone experimental variograms and cross-variograms (thin lines) and final nested modeled variograms and cross-variograms (thick lines), with inline and cross-line directions indicated by red and green colors, respectively. Horizontal scale in meters and vertical scale in squared amplitude values, with experimental variances: AMP98=1,73.e+8; AMP97=1,69.e+8; AMP90= 1,80.e+8; AMP97xAMP98=AMP97xAMP90=1,63.e+8; AMP98xAMP90=1,67.e+8.

b) Reservoir Zone

The same approach as described in the previous paragraph has been adopted to model the nested structure on the reservoir zone. As observed in Section 0, this interval shows higher variance values when compared to the Non-Reservoir, and two possible physical reasons are suggested to explain these anomalous variance values:

the higher lateral variability due to the lateral reservoir facies variation, imposing higher contrasts of seismic properties; and

to a lesser extent, seismic property variations as a result of the SAGD enhanced recovery scheme;

It is also worth mentioning that a trend is observed in the inline direction in the Reservoir Zone, as shown in Figure 4-21. However, the adopted modeling strategy disregarded, at this phase, this horizontal non-stationarity.

Table 4-12 Reservoir Zone nested variograms and cross-variograms fitting parameters and the final coregionalization matrix.

Structure	Sill Matrix B_p ($\times 10^8$)
C1: Spherical Model; Zonal Anisotropy <u>Practical range:</u> a = 10m (315°)	$B_1 = \begin{pmatrix} 0,04 & 0,06 & 0,07 \\ 0,06 & 0,09 & 0,10 \\ 0,07 & 0,10 & 0,12 \end{pmatrix}$
C2 : Spherical Model <u>Practical range:</u> a = 120m (315°) a= 50m (225°)	$B_2 = \begin{pmatrix} 0,11 & 0,14 & 0,14 \\ 0,14 & 0,17 & 0,17 \\ 0,14 & 0,17 & 0,17 \end{pmatrix}$
C3: Exponential Model; Zonal anisotropy <u>Practical range:</u> a = 240m (315°)	$B_3 = \begin{pmatrix} 1,49 & 1,46 & 1,34 \\ 1,46 & 1,82 & 1,56 \\ 1,34 & 1,56 & 1,60 \end{pmatrix}$
C4: Exponential Model; Zonal anisotropy <u>Practical range:</u> a= 250m (225°)	$B_4 = \begin{pmatrix} 0,77 & 0,70 & 0,69 \\ 0,70 & 0,97 & 0,80 \\ 0,69 & 0,80 & 0,89 \end{pmatrix}$

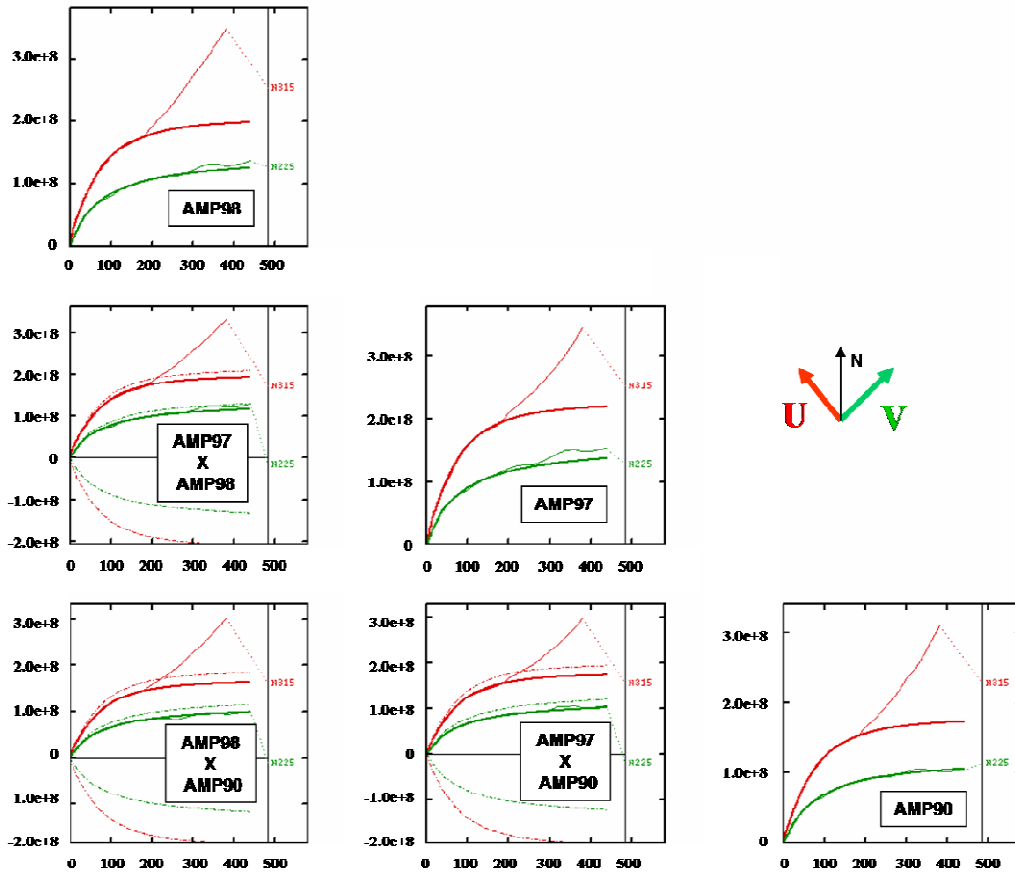


Figure 4-21 – Reservoir Zone experimental variograms and cross-variograms (thin lines) and final nested modeled variograms and cross-variograms (thick lines), with inline and cross-line directions indicated by red and green colors, respectively. Horizontal scale in meters and vertical scale in squared amplitude values, with experimental variances: AMP98=1,56.e+9; AMP97=1,62.e+9; AMP90= 1,39.e+9; AMP97xAMP98=1,56.e+9; AMP99xAMP90=1,44.e+9; AMP97xAMP90=1,46.e+9.

The nested variogram and cross-variogram models in the Reservoir zone, shown in Figure 4-21, have been modeled with four basic structures: two spherical structures were identified in the short range, and two medium range exponential ones. All the parameters defined for these nested structures are presented in Table 4-12.

c) Resume on Variogram and Cross-Variogram Fitting

The variogram fitting is a basic step for the description of the spatial structures, and has a strong impact on the final cokriging estimates. The choice of the authorized models, however, is quite subjective, and more than one solution to achieve the “best fit” can be found.

During this study, the focus was to use as minimum a number of structures as possible, as well to avoid introducing models that could not be physically corroborated.

Table 4-13– Structural correlation coefficients of the variance-covariance matrices in the Non-Reservoir Zone.

Correlation Matrix - Non-Reservoir Zone			
Structure	AMP90 x AMP97 ($\rho = 0,94$)	AMP90 x AMP98 ($\rho = 0,95$)	AMP97 x AMP98 ($\rho = 0,95$)
C1	0,78	0,80	0,68
C2	0,71	0,73	0,67
C3	0,77	0,80	0,86
C4	0,68	0,98	0,60

Table 4-14– Structures correlation coefficients from the variance-covariance matrices, in the Reservoir Zone.

Correlation Matrix - Reservoir Zone			
Structure	AMP90 x AMP97 ($\rho = 0,96$)	AMP90 x AMP98 ($\rho = 0,97$)	AMP97 x AMP98 ($\rho = 0,99$)
C1	1,00	1,00	1,00
C2	1,00	1,00	1,00
C3	0,88	0,87	0,91
C4	0,81	0,83	0,86

The analysis of the correlations between the seismic vintages from the variance-covariance matrices, computed for each structure, as shown in Table 4-13 and Table 4-14, indicates that:

- structures C1 and C2, with smaller ranges and NE-SW anisotropy mainly along inline direction, are slightly smaller, in the Non-Reservoir Zone, for AMP97xAMP98 (C1=0.68, C2=0.67) than for AMP90xAMP97 (C1=0.78,

C2=0.71) and AMP90xAMP98 (C1=0.80, C2=0.73), suggesting that these spatial structures may be interpreted as artifacts related to the bin resizing and regriding applied during the cross-equalization processing;

- the same structures C1 and C2, at the Reservoir Zone, show identical spatial correlations, equal to 1.00. This constant spatial correlation for both structures suggests that, at this zone, a stronger filtering effort might have been implemented to better attenuate these artifacts;
- structure C3, with medium ranges (220x480 and 240), shows similar spatial correlation for both Non-Reservoir and Reservoir zones, indicating a possible association of this structure to a common geological response that has been captured by all seismic vintages; and
- structure C4, with medium ranges and oriented in the cross-line direction in the Reservoir Zone, shows smaller values for AMP90xAMP97 and for AMP90xAMP98 (C4=0.81 and 0.83, respectively), and a higher value for AMP97xAMP98 (C4=0.86) , and could be associated to spatial effects related to the hydrocarbon production.

The variographic analysis performed over the Non-reservoir Zone has helped to better understand, explain and decompose the structures identified in the Reservoir zone, but it was not used quantitatively to filter out the noise in the Reservoir zone.

4.3.3. Orthogonal factors estimation

Now that the variograms and cross-variograms are already fitted and the linear model of coregionalization is defined for the studied area, the next step involves the orthogonal factors estimation by Factorial Kriging.

This estimation is performed in two-steps.

- **Decomposition of the spatial structures into orthogonal factors**, by diagonalizing the variance-covariance matrix \mathbf{B}_p . An eigenvalue λ_p^k will be associated to each orthogonal factor Y_p^k , with $p = 1, \dots, 4$ and $k = 1, \dots, 3$, and it provides a quantification of the amount of information that was retained in each factor from the random variables.
- **Estimation of the orthogonal factors** Y_p^k from the experimental measurements using a cokriging technique, by solving the cokriging system for each factor.

The diagonalization of the variance-covariance matrices (or sill matrices) B_p of the Non-reservoir and Reservoir zones, presented in Table 4-11 and Table 4-12, provides the resulting eigenvectors and eigenvalues matrices. These matrices, presented in Table 4-15 and Table 4-16, give all necessary information to compute the orthogonal factors from the input variables, or, in a similar way, to recompose the original input data from the computed orthogonal factors.

Each orthogonal factor Y_p^k is associated to only one positive eigenvalue λ_p^k from the variance-covariance matrix B_p , where the eigenvalues provide a measurement of the amount of information contained in each computed factor. A simple way to evaluate the relative importance of each computed factor is to rank the respective eigenvalues. In

Table 4-15 and Table 4-16, it can be noticed that these values are ranked in a decreasing way, from the first to the last row.

Table 4-15- Non-Reservoir Zone diagonalization of the coregionalization matrix.

Structure	Diagonalization – NON RESERVOIR Zone	
	Eigenvector Matrix	Eigenvalue Matrix (x10 ⁸)
C1 (Sph.)	$Q_1 = \begin{pmatrix} 0.6485 & 0.5442 & 0.5322 \\ 0.1064 & -0.7571 & 0.6446 \\ 0.7537 & -0.3614 & -0.5489 \end{pmatrix}$	$\Lambda_1 = \begin{pmatrix} 0,10 & 0 & 0 \\ & 0,01 & 0 \\ & & < 0,01 \end{pmatrix}$
C2 (Sph.)	$Q_2 = \begin{pmatrix} 0.6234 & 0.5015 & 0.5999 \\ -0.2612 & -0.5896 & 0.7643 \\ 0.7370 & -0.6332 & -0.2366 \end{pmatrix}$	$\Lambda_2 = \begin{pmatrix} 0,16 & 0 & 0 \\ & 0,02 & 0 \\ & & 0,02 \end{pmatrix}$
C3 (Exp.)	$Q_3 = \begin{pmatrix} 0.5496 & 0.5875 & 0.5939 \\ 0.8113 & -0.5449 & -0.2117 \\ -0.1992 & -0.5982 & 0.7762 \end{pmatrix}$	$\Lambda_3 = \begin{pmatrix} 0,54 & 0 & 0 \\ & 0,05 & 0 \\ & & 0,03 \end{pmatrix}$
C4 (Sph.)	$Q_4 = \begin{pmatrix} -0.3836 & -0.4725 & -0.7935 \\ 0.1194 & -0.8774 & 0.4647 \\ -0.9158 & 0.0835 & 0.3930 \end{pmatrix}$	$\Lambda_4 = \begin{pmatrix} 0,21 & 0 & 0 \\ & 0,04 & 0 \\ & & < 0,01 \end{pmatrix}$

Table 4-16-Reservoir Zone diagonalization of the coregionalization matrix.

Structure	Diagonalization – RESERVOIR Zone	
	Eigenvector Matrix	Eigenvalue Matrix (x10 ⁸)
C1 (Sph)	$Q_1 = \begin{pmatrix} 0.4214 & 0.6005 & 0.6796 \\ 0.6653 & -0.7140 & 0.2183 \\ -0.6163 & -0.3602 & 0.7003 \end{pmatrix}$	$\Lambda_1 = \begin{pmatrix} 0,25 & 0 & 0 \\ & < 0.01 & 0 \\ & & < 0.01 \end{pmatrix}$
C2 (Sph.)	$Q_2 = \begin{pmatrix} 0.4884 & 0.6182 & 0.6160 \\ 0.8674 & -0.2662 & -0.4205 \\ 0.0960 & -0.7396 & 0.6662 \end{pmatrix}$	$\Lambda_2 = \begin{pmatrix} 0,45 & 0 & 0 \\ & < 0.01 & 0 \\ & & < 0.01 \end{pmatrix}$
C3 (Exp.)	$Q_3 = \begin{pmatrix} 0.5426 & 0.6155 & 0.5716 \\ 0.8310 & -0.2945 & -0.4718 \\ 0.1220 & -0.7311 & 0.6713 \end{pmatrix}$	$\Lambda_3 = \begin{pmatrix} 4,55 & 0 & 0 \\ & 0.21 & 0 \\ & & 0.14 \end{pmatrix}$
C4 (Exp.)	$Q_4 = \begin{pmatrix} 0.5294 & 0.6126 & 0.5869 \\ 0.7989 & -0.5927 & -0.1020 \\ -0.2854 & -0.5229 & 0.8032 \end{pmatrix}$	$\Lambda_4 = \begin{pmatrix} 2,34 & 0 & 0 \\ & 0.16 & 0 \\ & & 0.12 \end{pmatrix}$

Table 4-17– Contribution of each computed orthogonal factor for each structure in the Non Reservoir Zone.

Non-Reservoir Zone				
	C1	C2	C3	C4
Y_p^1	84,11	80,6	87,34	84,17
Y_p^2	9,98	10,24	7,89	1,60
Y_p^3	5,91	9,16	4,77	0,23
Total	100,00	100,00	100,00	100,00

Table 4-18– Contribution of each computed orthogonal factor for each structure in the Reservoir Zone.

Reservoir Zone				
	C1	C2	C3	C4
Y_p^1	99,95	99,97	92,70	89,18
Y_p^2	0,04	0,03	4,35	6,15
Y_p^3	0,01	0,00	2,95	4,67
Total	100,00	100,00	100,00	100,00

The amount of information that belongs to each structure that can be explained by each factor (or the contribution of each factor to explain the total variance of each structure) is shown in Tables 3-17 (Non-Reservoir Zone) and 3-18 (Reservoir Zone). In this multivariate case, this analysis provides a comprehensive description of the importance of each resulting factor on explaining a part of the data variance.

Based on the analysis of the Factors contribution presented in Tables 3.17 and 3.18, it may be concluded that:

- Factors 2 and 3 contributions are much higher for the Non-Reservoir Zone than for the Reservoir Zone;
- Structures C1 and C2, with smaller ranges (10x40 and 50x120m, respectively) and NE-SW anisotropy mainly along inline direction, account for noise in both Reservoir and Non-Reservoir Zones, as can be interpreted by inspecting the resulting factors maps, in Figures 3.22 and 3.23. These structures are probably related to the bin resizing and regridding effects as a result of the seismic

processing sequence applied to minimize the discrepancies between the vintages (see paragraph 3.1.2);

- The contribution of Factors 2 and 3 for structures C1 and C2 are much higher in the Non-Reservoir than in the Reservoir Zone. A possible explanation for this behavior is that a stronger filtering effort was applied over the reservoir level to improve the noise filtering; and
- Structures C3 and C4, on the other hand, reflect medium to large range structures and reveal the redundant geological response contained in the seismic datasets and/or the exploitation effect.

The estimation procedure is performed by cokriging the input variables, and involves the definition of kriging strategy to be considered (depending on the data characteristics, such as: vertical and horizontal stationarity; heterotopic sampling; degree of correlation between co-estimated variables; etc) and the definition of the neighborhood for each structure to be estimated.

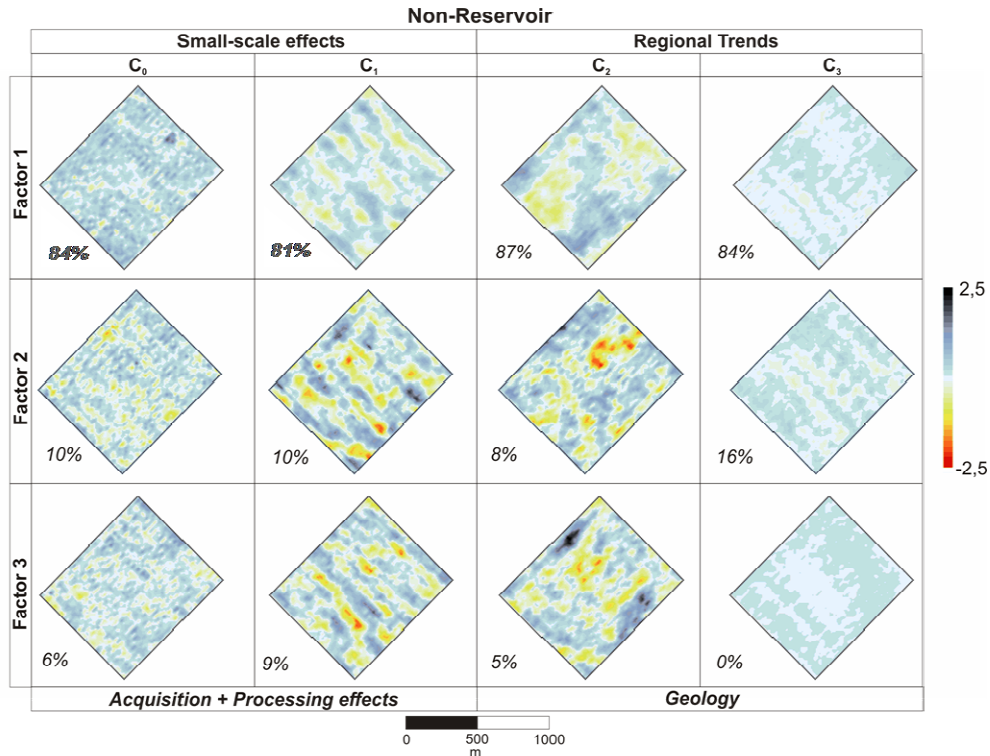


Figure 4-22 –The 12 resulting orthogonal factors estimated from 4 structures and 3 input data on the Non-Reservoir Zone, corresponding to the 10th horizon-slice (from top to bottom). Numbers (in %) correspond to the contribution of each factor to the total variance.

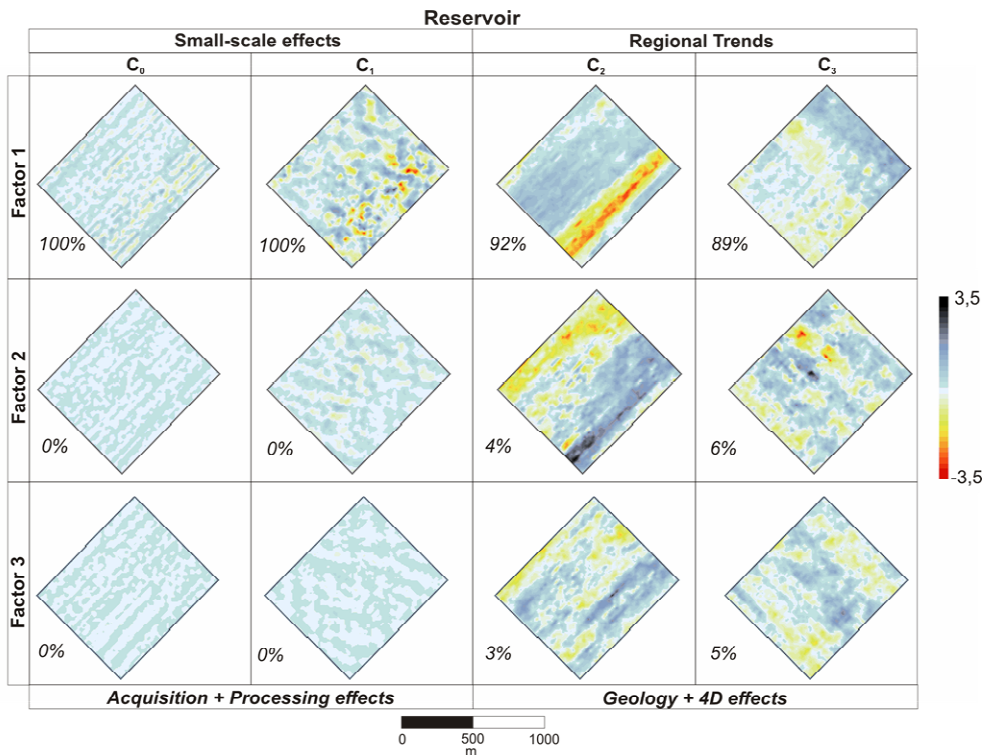


Figure 4-23 – The 12 resulting orthogonal factors estimated from 4 structures and 3 input data on the Reservoir Zone, corresponding to the reservoir top horizon-slice. Number (in %) correspond to the contribution of each factor to the total variance.

4.3.4. Seismic Data Reconstruction & Filtering

As previously described, one possible approach to cross-validate the variable decomposition into orthogonal factors is to recombine all estimated factors to retrieve the original input data. This step, called Data Reconstruction, uses a multi-linear regression technique, by computing the linear regression of a target variable – the input data - explained as a function of a set of explanatory variables – the estimated orthogonal factors - at each sample locations.

By performing a multilinear regression on the estimated factors, one can compute the weights to be assigned to each explanatory variable – the orthogonal factors estimated by Factorial Kriging - as well as the multi-linear regression error, or the distance between the true and the regressed value, for each sample in the investigated domain.

The final model equations to retrieve the original inputs from the computed orthogonal factors are:

$$\begin{aligned} Amp_{90} = & 99.F1C0 + 1440.F1C1 + 11120.F1C2 + 6448.F1C3 \\ & - 1349.F2C0 - 1348.F2C1 + 3516.F2C2 + 2346.F2C3 \\ & + 26085.F3C0 + 649.F3C1 + 497.F3C2 - 796.F3C3 \end{aligned} \quad (3.1)$$

$$\begin{aligned} Amp_{97} = & 291.F1C0 + 1860.F1C1 + 12585.F1C2 + 7621.F1C3 \\ & - 988.F2C0 - 344.F2C1 + 1286.F2C2 - 2177.F2C3 \\ & + 19497.F3C0 + 2551.F3C1 + 2367.F3C2 - 1570.F3C3 \end{aligned} \quad (3.2)$$

$$\begin{aligned} Amp_{98} = & 584.F1C0 + 1900.F1C1 + 11723.F1C2 + 7219.F1C3 \\ & - 438.F2C0 - 158.F2C1 - 1987.F2C2 - 475.F2C3 \\ & + 27235.F3C0 - 418.F3C1 + 2315.F3C2 + 2309.F3C3 \end{aligned} \quad (3.3)$$

By using this regression equation, one can easily filter out one or more components by introducing a null value weight on the factor(s) to be filtered. In this case study, the short range components C0 and C1 have been identified as noise and were filtered out.

Results of the component/factor filtering are shown in the amplitude maps of Figure 4-24 and in Figure 4-25, where the top of the reservoir is used as the reference horizon for the analysis. Figure 4-24 compares the raw and filtered AMP90 data, where factors corresponding to the structures C0 and C1 were filtered out. These structures are presented in Figure 4-23. Only the high spatial frequency features were taken out from the raw data, while preserving all medium to long range structures (mainly oriented NNE-SSW).

Figure 4-25 shows the filtered maps for AMP90 and AMP97 for the reservoir top horizon, where the C0 and C1 have been removed. These maps show that the medium and long ranges structures, common to both vintages, can be easily identified, assuring that the filtering applied on the data did not remove or change any structures other than the short range ones. It is also interesting to notice the anomalous amplitude values close to the center of the area in the AMP97 data, which could be associated to the production effect.

AMP90 reservoir top

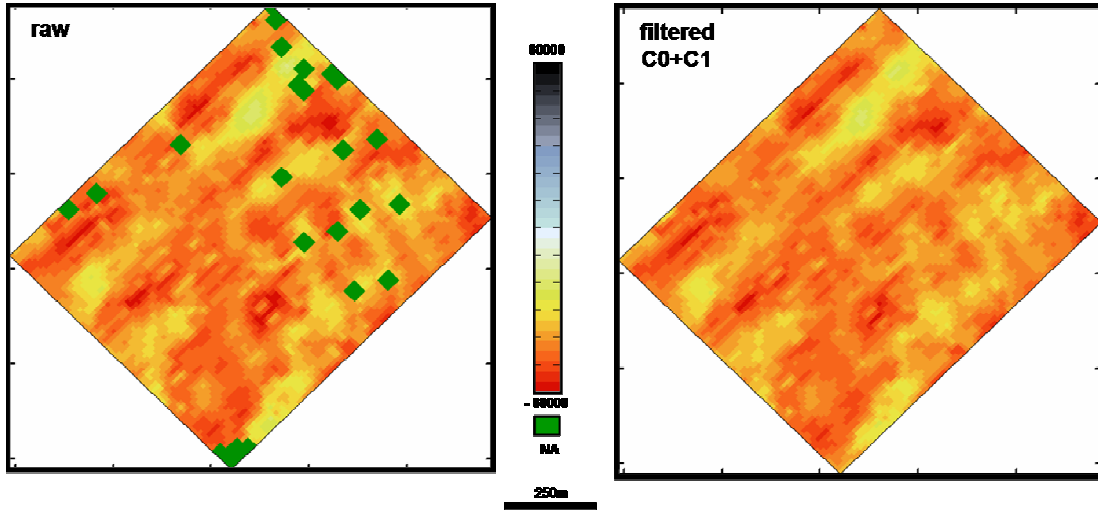


Figure 4-24 – Raw (left) and filtered (right) maps of the Reservoir top from AMP90 dataset. The factors filtered out correspond to small range structures C0 and C1.

AMP90 reservoir top

AMP97 reservoir top

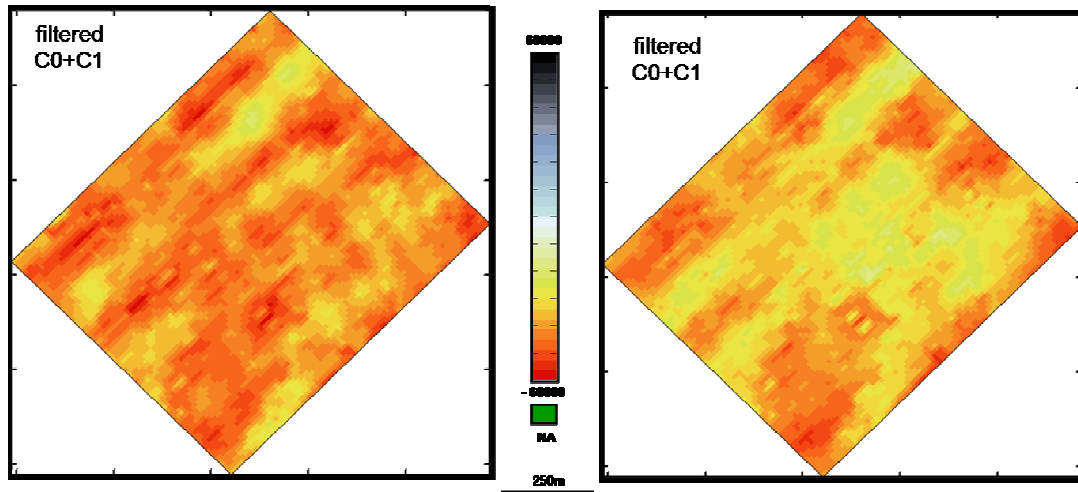


Figure 4-25 – AMP90 (left) and AMP97 (right), after filtering the factors corresponding to structures C0 and C1.

4.3.5. Discussion on the inline non-stationarity

In the previous analyses concerning the variables AMP90, AMP97 and AMP98 from the reservoir zone of the Senlac heavy oil field, as presented in paragraphs 4.3.1 to 4.3.3, the directions of maximum data variability were considered to be coincident with the inline and crossline directions, or parallel to the seismic grid. The experimental variograms and crossvariograms were then computed following these directions, and a strong non-stationarity was observed in the inline direction, as shown in Figure 4-21. As presented in these paragraphs, the linear model of coregionalization proposed to explain the data variability from the reservoir zone was composed by four structures. The first two structures C1 and C2 accounted for the short range, whereas the last ones, C3 and C4, accounted for the long range data variability. A zonal anisotropy was considered to model the non-stationary behavior of the amplitude variability when performing the simultaneous structural analyses of the twelve variograms and cross-variograms. The final parameters of the nested model are summarized in Table 4-12.

The choice of this linear model presents an operational advantage, as it reduces the time spent to simultaneously fit the $n(n-1)$ variogram and cross-variograms from n input variables. However, as the main directions of anisotropy were considered to be coincident with the inline and crossline directions, a combined effect of these two anisotropic structures at the intermediate directions should be observed, with the final variability being a sum of these combined effects. An inspection of the variogram maps extracted from the Senlac reservoir zone does not show a variability increase at these intermediate directions, as can be observed in Figure 4-19. These figures shown that the maximum variability directions are coincident with the inline and crossline directions, and all intermediate directions present variabilities smaller than or equal to those found in the inline and crossline directions.

In order to validate the subsequent structural modelling as presented in paragraph 4.3.3 regarding the decomposition and filtering by using the factorial cokriging technique, a new structural analysis approach was proposed. This approach considers the removal of this drift, or the non-stationarity part, of the computed variograms and crossvariograms of the inline direction.

To achieve this goal, the following steps were performed:

1. Defining the non-stationarity domain on the experimental variograms and crossvariograms in the inline direction;
2. Modeling the non-stationary behavior by deterministically adjusting a curve that best fits this part of the data variability, where an exponential model was considered;
3. Estimating the stationary variance, by extrapolating of the resulting curve up to the intersection with the vertical axis, allowing the estimation of the variance contribution of the non-stationary trend in the inline direction;

The non-stationary variance contribution is then removed from the inline experimental variograms and crossvariograms. After this step, all these new experimental variograms and crossvariograms are reinterpreted in terms of their structural components. During this phase, an equivalent structural interpretation approach as previously used was considered, where the main goal was to adjust the nested variograms/cross-variogram considering a number of structures as small as possible, as well as the less complex base variograms.

The experimental variograms and crossvariograms, with the corresponding modeled drifts are presented in Figure 4-26 and Figure 4-27, respectively. In these figures, the blue lines correspond to the modelled drift that was then removed from the experimental variograms and cross-variograms. It is noticeable that, in the AMP90 data, the stationary variance in the inline direction is of same order of magnitude from the one in the crossline direction, reaching a value close to 0.9×10^7 of variance. However, when evaluating the stationary variance for the AMP97 and AMP98 data, this value is approximately 17% smaller when compared to the crossline direction.

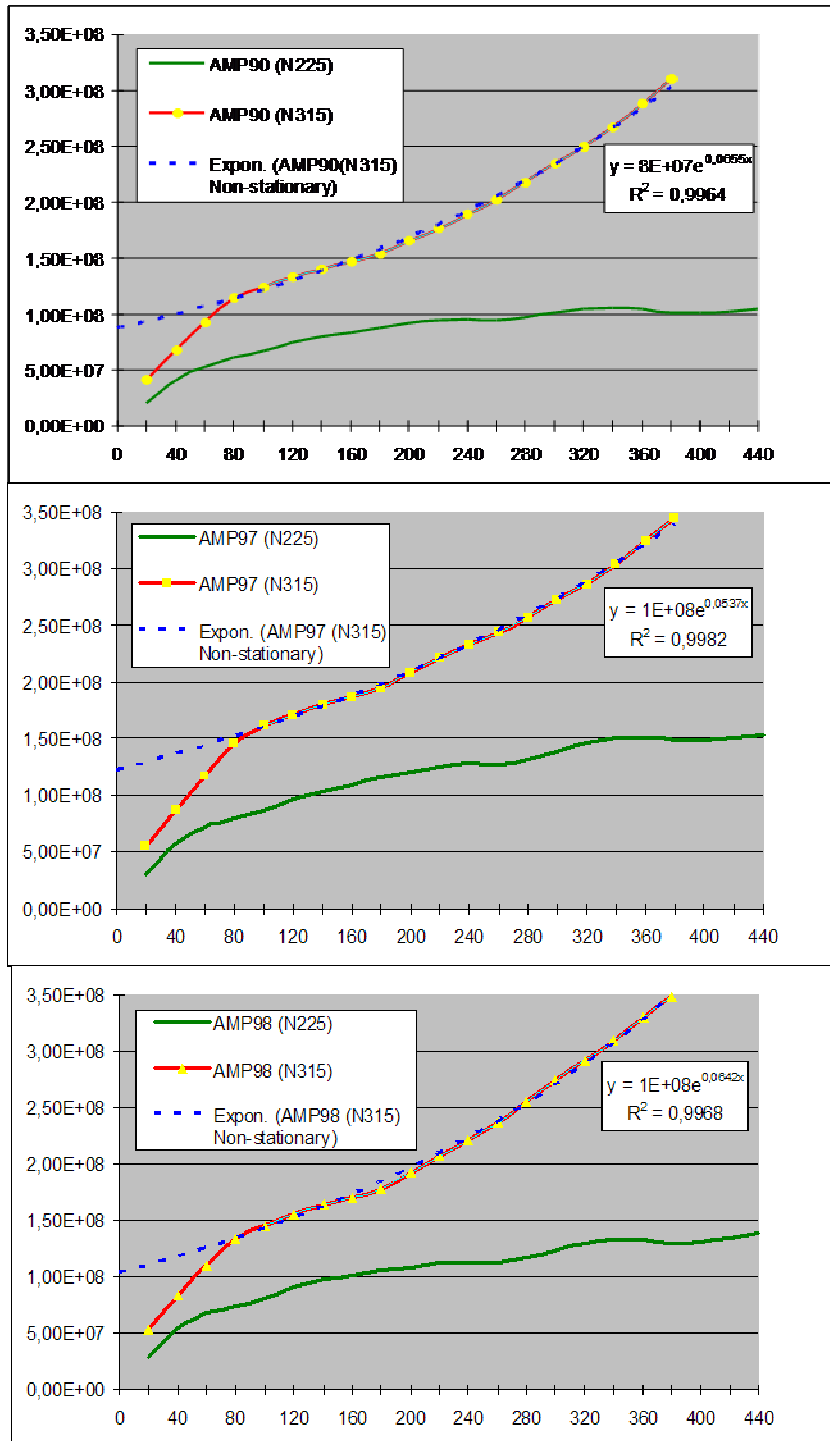


Figure 4-26 – Experimental variograms from Senlac Reservoir zone corresponding to AMP90, AMP97 and AMP98, from top to bottom, respectively. Red and green lines corresponding to the inline and crossline directions. The trend in the inline direction is modeled by an exponential function, corresponding to the blue line.

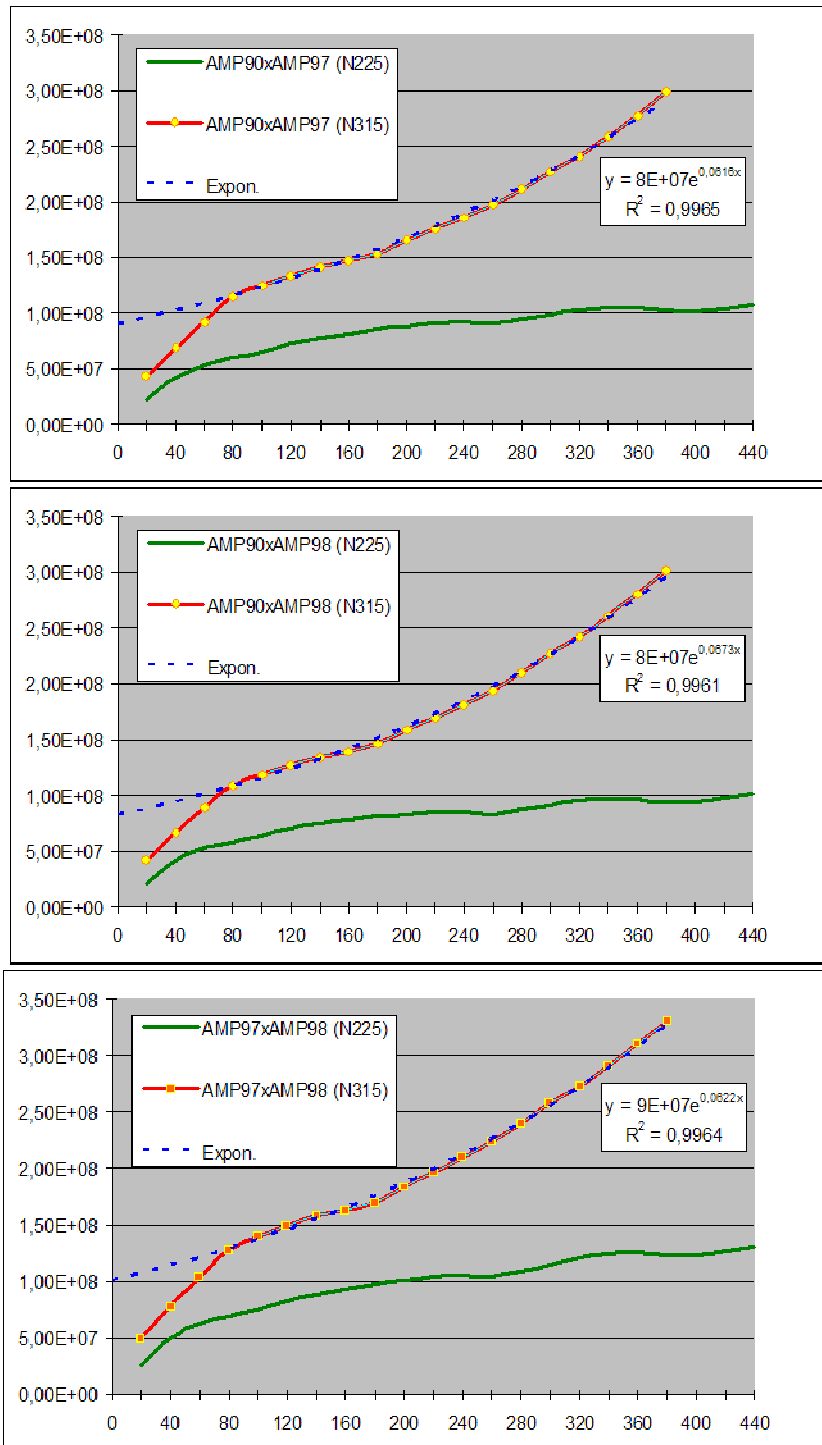


Figure 4-27 - Experimental cross-variograms from Senlac Reservoir zone corresponding to AMP90xAM97, AMP90xAMP98 and AMP97xAMP98, from top to bottom, respectively. Red and green lines corresponding to the inline and crossline directions. The trend in the inline direction is modeled by an exponential function, corresponding to the blue line.

The resulting variograms and cross-variograms, where the modelled drifts were removed, are shown in Figure 4-28. It is remarkable to notice that after this procedure, a

geometric anisotropy is observed instead. The resulting structures interpreted after removing the trend component are shown in Table 4-19. Comparing these results with those structures obtained in the previous work, as shown in Table x, one may notice that:

- Three structures (instead of four as in the previous analyses) were considered to model the data variability; and
- These three structures correspond to: one spherical short range; one exponential mid range, and a spherical long range, where the crossline direction corresponds to the higher continuity;

Table 4-19 – Reservoir zone nested variograms and cross-variograms fitting parameters after removing the inline non-stationarity.

Structure	Sill matrix B_p
$\Gamma_1^i(u)$ Spherical model <u>Practical range</u> a = 20 (315°) a = 50 (225°)	$B_1' = \begin{pmatrix} 0,04 & 0,04 & 0,04 \\ 0,04 & 0,05 & 0,07 \\ 0,04 & 0,07 & 0,11 \end{pmatrix}$
$\Gamma_2^i(u)$ Exponential model <u>Practical range</u> a = 100 (315°) a = 260 (225°)	$B_2' = \begin{pmatrix} 0,93 & 0,92 & 0,86 \\ 0,92 & 1,22 & 1,00 \\ 0,86 & 1,00 & 1,02 \end{pmatrix}$
$\Gamma_3^i(u)$ Spherical model <u>Practical range</u> a = 10000 (315°) a = 460 (225°)	$B_3' = \begin{pmatrix} 0,07 & 0,05 & 0,02 \\ 0,05 & 0,16 & 0,11 \\ 0,02 & 0,11 & 0,14 \end{pmatrix}$

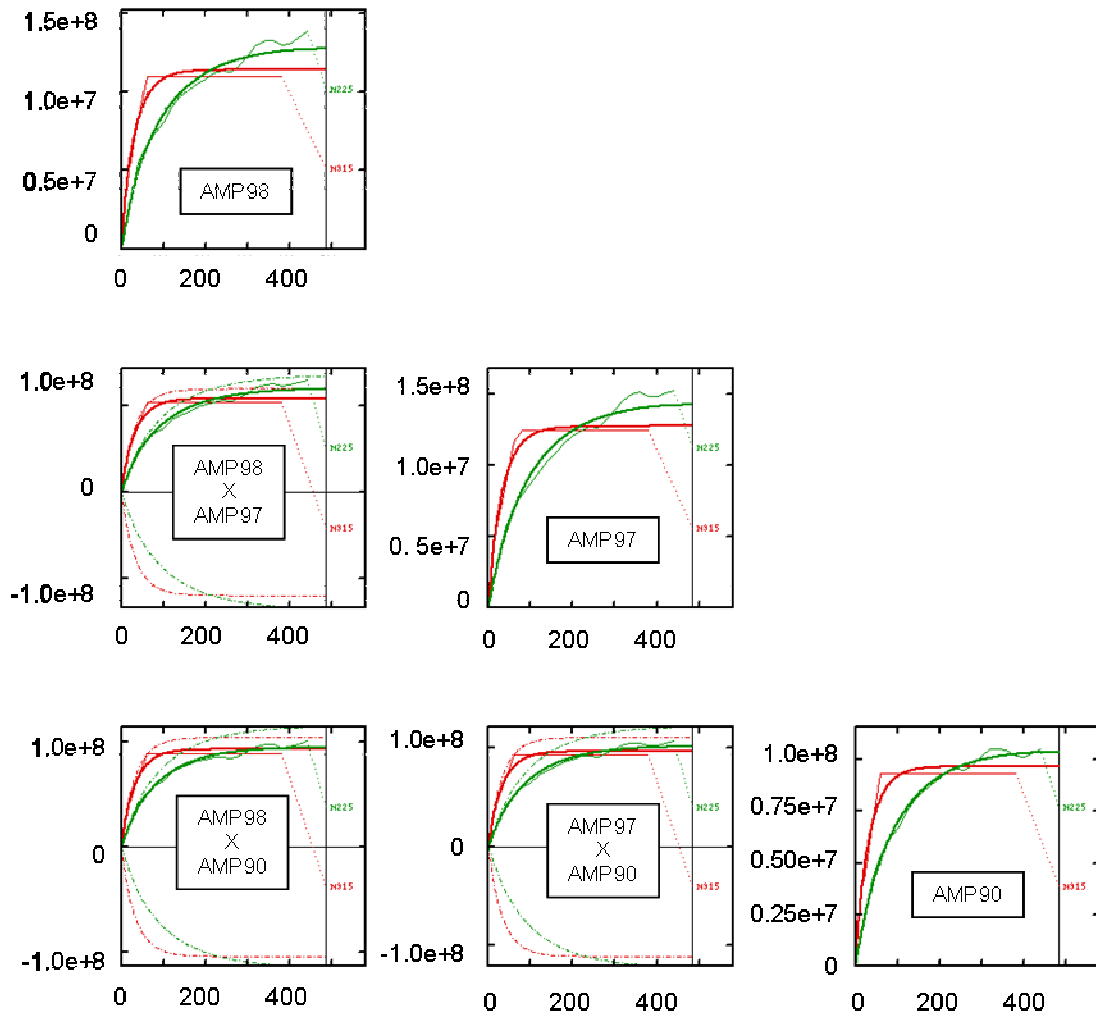


Figure 4-28 - Senlac Reservoir zone experimental variograms and cross-variograms (thin lines), and final nested modeled variograms and cross-variograms (thick lines) after removing the drift in the inline direction. Inline and crossline directions are indicated by red and green lines, respectively.

In Figure 4-29, two amplitude maps corresponding to the Senlac top reservoir are presented. In both cases, the short range structures were filtered by using the factorial cokriging filtering technique. The amplitude map on the left corresponds to the

case where the variograms and cross-variograms were modeled considering a zonal anisotropy to better adjust a drift in the inline direction, and both C1 and C2 short range structures were filtered. For the image on the right, the drift was removed and the short range structure C1 was filtered by the factorial cokriging.

These results show that a very strong similarity between these maps is observed, suggesting that no remarkable impact on the filtering of the small scale effects is observed due the presence of the drift, which validates the previous studies as presented in paragraphs 4.3 and 4.4.

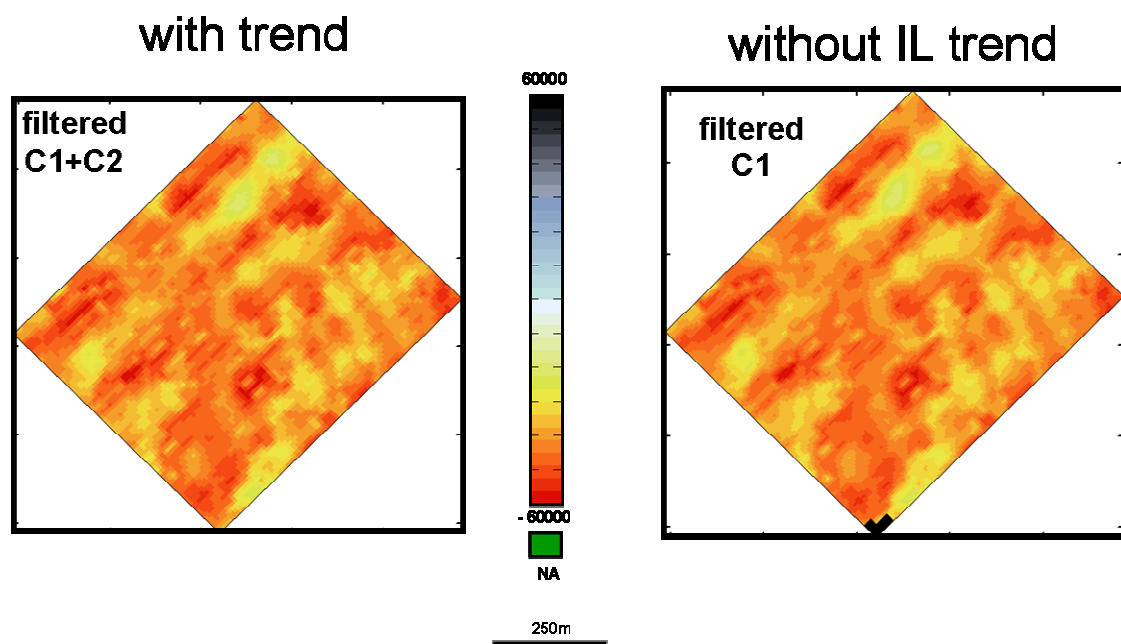


Figure 4-29 – Final amplitude maps corresponding to the Senlac reservoir top, from AMP90 dataset. On the left, filtered map before the inline trend removal (where short ranges structures C1 and C2 were filtered). On the right, the result of the filtering of the short range structure C1, after the trend removal.

4.4. Seismic Facies Analysis

Considering that two available datasets - the raw and the geostatistically filtered datasets - the objective of this chapter is to quantify the impacts of the filtering by using an interpretative method such as seismic facies classification analysis.

This technique aims to identify and group seismic traces with similar shape from a given population. It also addresses the problem of handling very large seismic volumes, with datasets composed of a multitude of seismic attributes that are relevant to be inspected in reservoir characterisation studies.

Depending on data availability and on the objectives of the study, two main approaches are considered: the unsupervised and the supervised classification techniques. The former does not take into account any external information from the population under study, whereas the supervised classification is performed by introducing external data to deliberately guide the classification. In this case study, the unsupervised seismic facies classification technique was used.

4.4.1. Description of the Methodology

The unsupervised seismic facies analyses approach, developed by the Lithoseismic Group of the Institut Français du Pétrole, is a classification technique that involves three main steps: (i) multivariate density function estimation; (ii) definition of the number of natural modes of the density function; and (iii) discriminant analyses to assign a class to each single trace from the observation space and its correspondent probability function of assignment (Fournier, 2004).

The seismic post-stack amplitude volumes from SENLAC, AMP90, AMP97 and AMP98, were filtered using the Factorial Kriging approach presented in Section 4.3.3, and the factors interpreted as noise from the components C0 and C1 were removed from the data. These filtered versions, as well as the raw data, have been used as the input to the seismic facies classification. In both cases, twelve (12) layers have been extracted from the time interval defined as the SENLAC Reservoir Zone and guided the decomposition of each trace into a 12-dimensional space. The classification has been done in this 12 dimensional space, where each point represents a trace of the seismic cubes.

Instead of performing an independent trace classification on each seismic cube separately, a simultaneous trace classification procedure was performed, in order to have the same classes for the three datasets, helping the facies distribution interpretation. With this approach, the three datasets (for raw and filtered cases) were considered simultaneously in the 12-dimensional space, as shown in Figure 4-30.

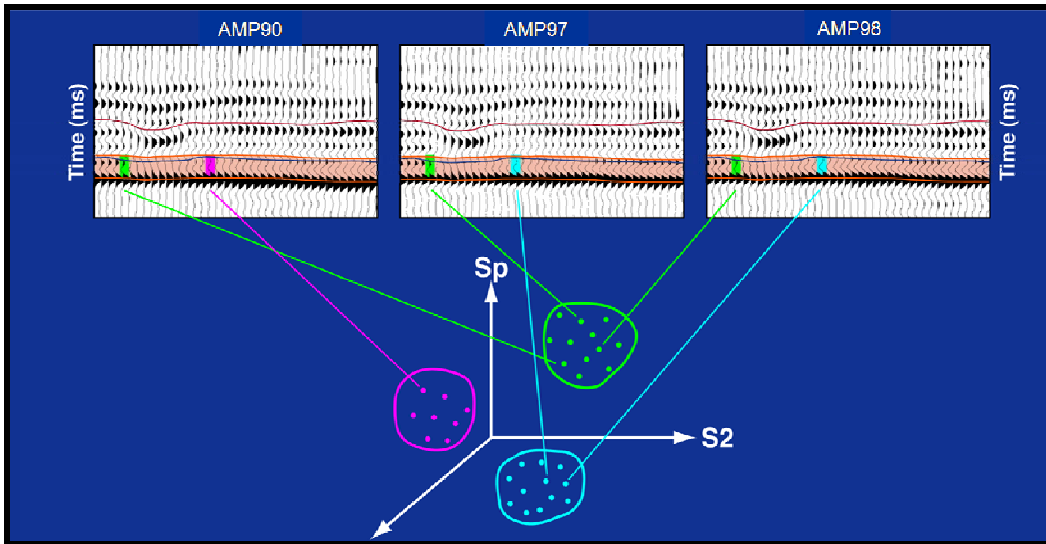


Figure 4-30 – Simultaneous trace classification scheme, using three seismic volumes (Lucet et al., 2001).

The following review is based on the developments found in Fournier (2004).

iii. Multivariate Density Function Estimation

Several statistical techniques are well adapted to perform the estimation of a multivariate density function, and they are grouped in hierarchical and non-hierarchical methods. As the main drawback of the hierarchical methods lies on handling large datasets - a common situation when interpreting seismic data volumes, particularly to time-lapse seismic - the non-hierarchical methods are more appropriate. Among the latter, the K-nearest neighbor (KNN) method presents several advantages.

The KNN method was developed by Wong and Lane (1983), and is applied by varying the values of K - the number of neighbors of each class or cluster - with each value of K yielding an estimate of the number of modal clusters to be used. If the estimated number of modal clusters is constant for a wide range of K values, there is strong evidence to support the existence of, at least, many modes in the population, meaning that a structuration exists within the data.

The multivariate density function can be written as

$$f(x) = \left(\frac{(K-1)}{n} \right) \left(\frac{1}{V(r_k, x)} \right) \quad (3.4)$$

where

$f(x)$ is the density function estimator on the point x ;

$x = (x_1, \dots, x_p)$ is the point of the p -dimensional space of variables;

n is the number of samples;

K is the number of neighbours considered;

$V(r_k, x)$ is the volume of the hypersphere defined by the radius r_k , taken from the point x to the k -nearest neighbour.

It should be noticed that the higher the K values, the higher the volume of the hypersphere and the smoother becomes the estimated density function, reducing the number of natural modes or facies. The main disadvantage of this method is the poor classification of those points that are located in the lower zones of the density function. This is why a two-step approach is used, where the denser zones create the learning classes and the discriminant analyses is used to assign the samples located in the less dense zones.

The analyses of the shape of the resulting curve is performed by plotting the estimated number of modes against K , giving a good insight as if a structuration exists, whereas the convergence of the curve for varying K values assures that a structuration was found, defining the number of classes corresponding to the constant K .

In this case study, these curves are shown in Figure 4-31 and Figure 4-32, plotted for the raw and the filtered data, respectively. It is clear that different convergence behaviours are achieved for the two different curves. In the first case, the choice of five and nine classes, corresponding to K values of 18 and 35, is straightforward. The filtered data curve stabilization, on the other hand, strongly

suggests a structure with five classes, for a K equal to 40, or even smaller number of classes for higher Ks. However, including a nine class group on the filtered data would allow a comparison with the raw data results.

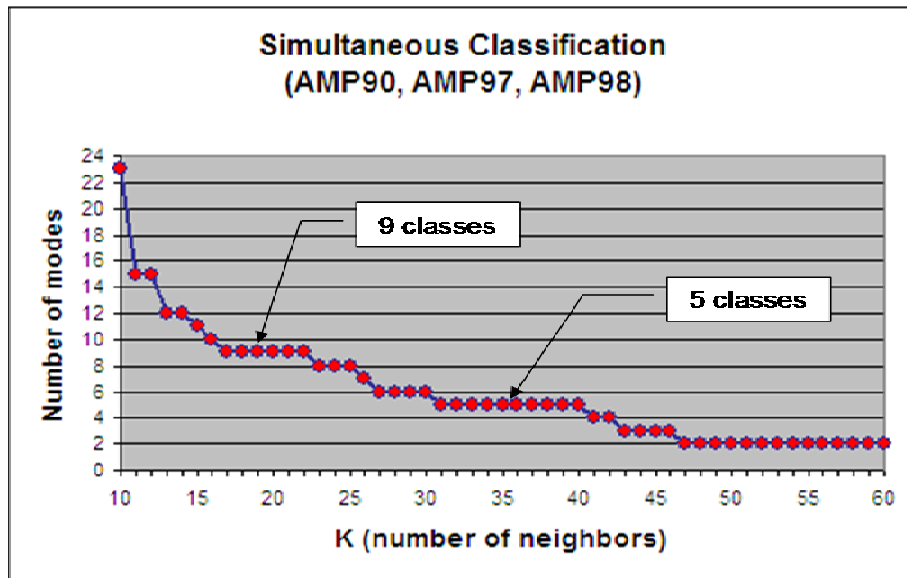


Figure 4-31 – Definition of the optimal number of modal classes for the raw data.

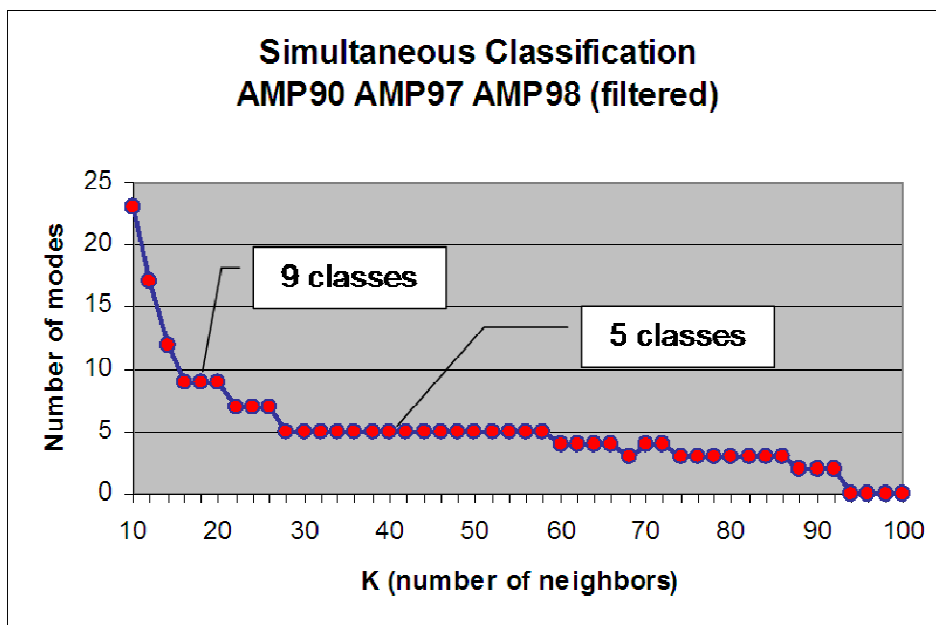


Figure 4-32 - Definition of the optimal number of modal classes for the filtered data.

iv. Learning Class Population definition

After defining the optimal number of clusters or classes naturally observed in the observation space by k-nearest neighbors clustering method, the next step is to select, from this initial dataset, the learning traces population. Learning traces may be regarded as an ensemble of objects that capture and synthesize the total variability of the observation space, in a multivariate sense - and will be an essential part of the following discriminant analyses classification.

The definition of the optimal number of learning traces per class is an important step. Usually, it is a trade-off between a number large enough to correctly describe the classes and small enough to let the discriminant analyses assign the samples located in the low density zones. Actually, the amount of learning traces should be high enough to enable a proper classification of the discriminant phase, and a total number of learning traces between 10 and 20% of the total amount of input traces is currently used as a rule-of-thumb.

In Figure 4-33, a graph showing the evolution of the number of traces with varying number of clusters (NCL) is presented. For a fixed number of K neighbors (in this case, $K = 32$), a KNN clustering over the whole observation space is iteratively performed, varying the number of clusters (NCL) from, for instance, 100 to 5,600, with a step of 100. In the first iteration, with $NCL=100$, most of the traces have been labeled as class 1, a smaller amount of traces as class 2, etc. As NCL increases, the traces clusters are progressively joined to a single, all-encompassing cluster that is formed at the class 99 column. The inspection of this graph yields a straightforward definition of the optimal number of traces – following the 10 to 20% rule – for each class, from 1 to 5, in this case. All these traces are then merged together to create the learning trace population, for each class.

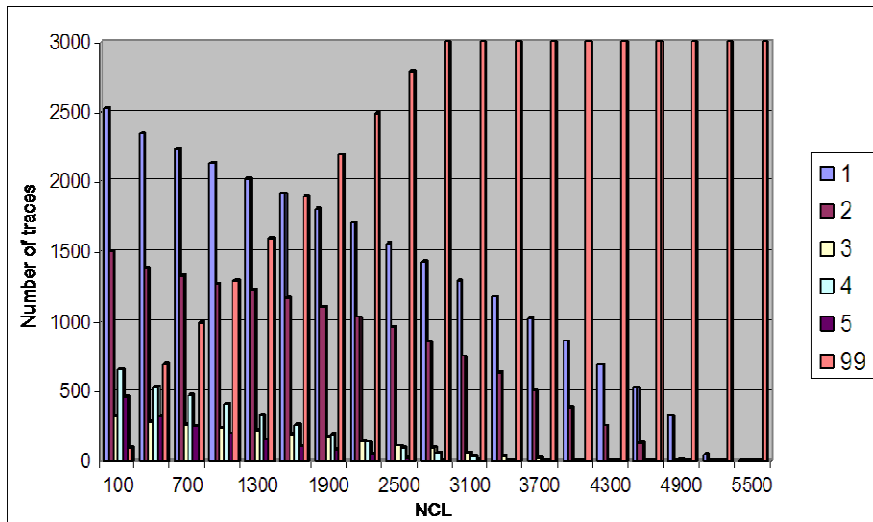


Figure 4-33 - Optimal number of learning traces is achieved by keeping constant $K = 32$ and analysing the evolution of the number of traces assigned to each class.

v. Discriminant Analysis

The KNN clustering technique is an efficient tool to perform a non-parametrical classification by investigating structures in the data, and to define the most representative traces for zones associated to peaks of the multivariate density function. However, it is less sensitive to label those traces that are placed in zones corresponding to a smaller density in the multivariate space. The discriminant analysis approach (Fischer, 1936) is more adapted to play this role.

The discriminant analysis in a Bayesian (or probabilistic) approach, addresses simultaneously two issues: (i) checks if the selected attributes are suitable to properly discriminate the learning classes; and (ii) determines the strategy for the trace assignment. As all hypotheses are computed, the trace is assigned to the class with the maximum probability of assignment. By using this approach, n probabilities of belonging to a class will be computed, and the highest probability selected.

The probability of assignment of a trace to a class is computed using the Bayes theorem, as follows:

$$p(C_i | x) = \frac{p(x | C_i) p(C_i)}{\sum_{j=1}^k p(x | C_j) p(C_j)} \quad (3.5)$$

where k is the number of learning classes, $p(x|C_i)$ is the conditional probability density function of a class C_i , and $p(C_i)$ is the *a priori* probability of the class C_i , or the weight of each class. These weights may be taken all identical and equal to $1/k$. The denominator of (3.5) is the non-conditional probability density function for the trace x .

The conditional probability density function $p(x|C_i)$ may be estimated assuming a Gaussian hypothesis. In this parametric estimation procedure, two approaches may be considered:

- the linear case, where the mean m_i and standard deviation σ_i values are constant for all classes, and the distributions of each class have the same covariance matrices; or
- the quadratic case, where a mean m_i and standard deviation σ_i values are assigned for each class, with a different covariance matrix for each class.

In the linear case, the surfaces separating the classes are defined by hyperplanes, whereas in the quadratic case, these surfaces are defined as hyperquadriques.

When no *a priori* hypothesis regarding the probability law is considered, the estimation is said to be non-parametric, and the probability density estimation is performed either by a kernel function or by the KNN technique. The non-parametric approaches usually demand a minimum amount of samples of the learning classes to ensure a proper statistical inference of the multivariate density function.

Usually, the three hypotheses are tested to define which one will provide a better discrimination of the learning classes. In the present study, these results show a quite high and similar response (> 0.9), and the non-parametric approach was selected.

4.4.2. Seismic Facies Classification Results

The seismic classification procedure has been performed using two different numbers of classes, five and nine. These values correspond to consistent flattenings of the K curve, for both raw and filtered datasets, as show in Figure 4-31 and Figure 4-32.

In the following maps, the horizontal wells submitted to the steam injection in the SAGD scheme are represented as black lines.

- **Results with 5 Seismic Facies**

The resulting facies maps considering 5 classes of seismic traces are presented in Figure 4-35, and it can be noticed that:

- i. **Regarding the seismic facies maps smoothness:**

- all seismic facies show a more continuous distribution on the filtered maps when compared to the raw data; for example, the occurrence of facies 2 (blue) in facies 5 (grey), as observed on all raw facies maps, is not seen in the filtered data;
- facies distribution changes the most in the southeast zone (facies 1 and 2): the AMP90 facies 1 map shows a smaller and sparser trace population in raw data, turning into a more dense trace population, with increased connectivity in the filtered data; the same comparison for AMP97 shows a reduction of facies 1 distribution in the filtered data, mainly in the south area; and comparing AMP98 maps, the filtered facies map is more homogenous than the raw data, with a reduction of facies 1 traces on the south and east areas, replaced by facies 2;
- the comparison of the probability of assignment maps for 5 classes shows a very slight improvement for filtered data, as shown in Figure 4-36. The probability of assignment was already quite high ($> 0,95$) for raw data, and could not be much improved by the geostatistical filtering process.

- ii. **Regarding the interpretation of AMP90 data (base survey):**

- a clear northeast-southwest trend of the facies distribution is observed on both raw and filtered data, and this distribution is in agreement with previous works conducted in the area (Dequirez et al., 1995);
- comparing these results to previous works of Dequirez et al. (1995), that considered a supervised approach resulting in 4 facies of reservoir quality (poor, intermediate, good and excellent, as shown in Figure 4-34), the facies 1 and 2

would represent excellent to intermediate reservoir quality; facies 3 and 5 intermediate quality; and facies 4 poor reservoir quality;

iii. **Regarding time-lapse effects:**

- two main regions are well characterized on both raw and filtered data, when comparing the time-lapse effect: the north-northwest area, comprising facies 3, 4 and 5 does not change with time; whereas a second region on the south area, where facies 1 and 2 are dominant, does change; it is important to notice that these zones correspond roughly to the reservoir quality zones described by Dequirez et al. (1995);
- comparing facies 1 and 2 on the filtered facies maps, it is clear that facies 1 replaces facies 2 from AMP90 to AMP97, on the center-east area. This effect (also observed in the raw data) could be related to the production effect;

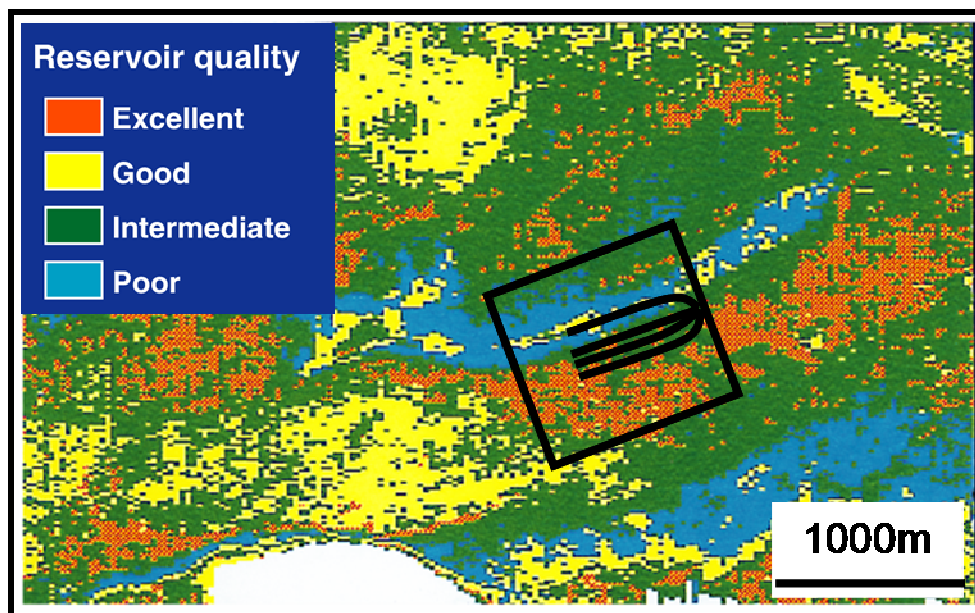


Figure 4-34 – Supervised facies classification (Dequirez et al., 1995), showing the 4 seismic facies related to reservoir quality. The black square corresponds to the present studied area, and the black lines to the horizontal well pairs.

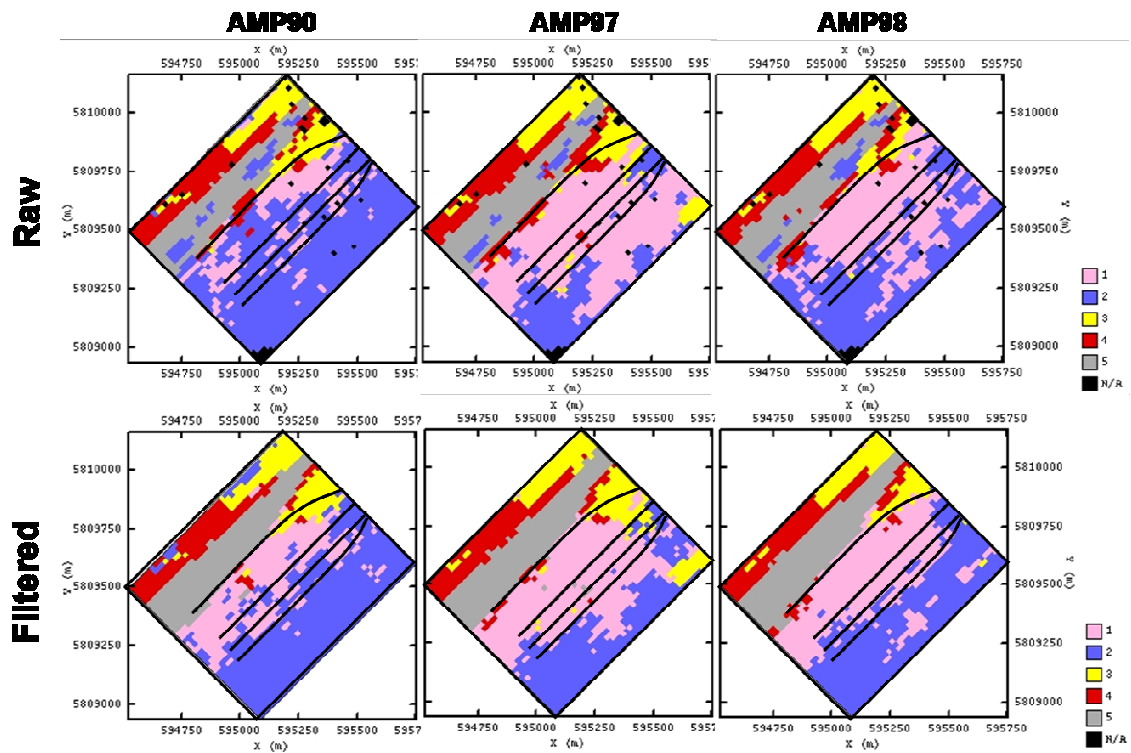


Figure 4-35- Resulting facies maps from Unsupervised Classification using 5 classes. Top row showing facies maps computed on the raw data, whereas bottom row on the filtered data.

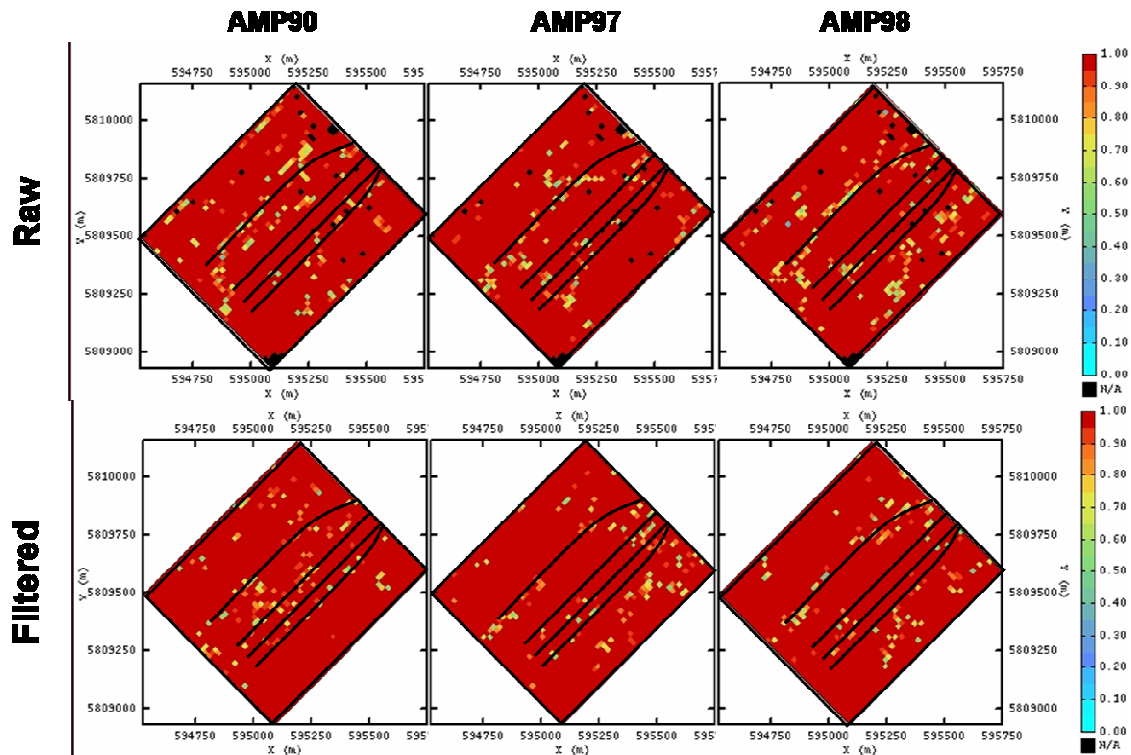


Figure 4-36 – Probability of assignment maps for 5 classes. Top row showing facies maps computed on the raw data, whereas bottom row on the filtered data.

- **Results for 9 Seismic Facies**

After increasing the number of classes from 5 to 9, it was noticed that the facies distribution becomes more complex for both raw and filtered volumes, as shown in Figure 4-37. The results are in agreement with the 5 classes classification as showed in the previous paragraph, and it can be noticed that:

- i. **Regarding the seismic facies map's smoothness:**

- As observed in the 5 classes maps, all seismic facies show a more continuous distribution on the filtered maps when compared to the raw data;
- Also as observed in the 5 classes maps, the northeast-southwest trend of the facies distribution is preserved on both raw and filtered data;
- the comparison of the probability of assignment maps for 9 classes shows a very slight improvement for filtered data, as shown in Figure 4-38. As mentioned earlier, the probability of assignment was already quite high ($> 0,95$) for raw data, and couldn't be much improved by a filtering process;

- ii. **Regarding the interpretation of AMP90 data (base survey):**

- No major differences are observed between the raw and filtered datasets;

- iii. **Regarding time-lapse effects:**

- The seismic facies classes substitutions, that could be associated to production or time-lapse effects, may be observed in both raw and filtered data (class 1 replacing class 5, at the center of the area, and classes 2 and 4 replacing class 6);
- Facies difference maps have been computed for both AMP90-AMP97 and AMP90-98 maps, and are shown in Figure 4-39 and Figure 4-40. These maps

help to better identify the areas where the most important changes took place, and also the zones with no detectable change (that are represented in white). In the southwest part of the area, it is interesting to notice that purple facies are more continuous in the southwest direction in the AMP90-AMP97 difference, and that these traces were replaced by white coloured points in the AMP90-AMP98. A possible production effect associated to these facies changes could be due to the production strategy of starting the steam injection at the bottom of the wells (southwest). Due to this strategy, at the beginning of the steam injection, the thermal effects would have been more conspicuous at the southeast zone than towards the northeast. The white colours in the same area for the difference of AMP90-AMP98 suggests that, at the AMP98 time, the seismic properties at this particular area have retrieved the initial AMP90 conditions.

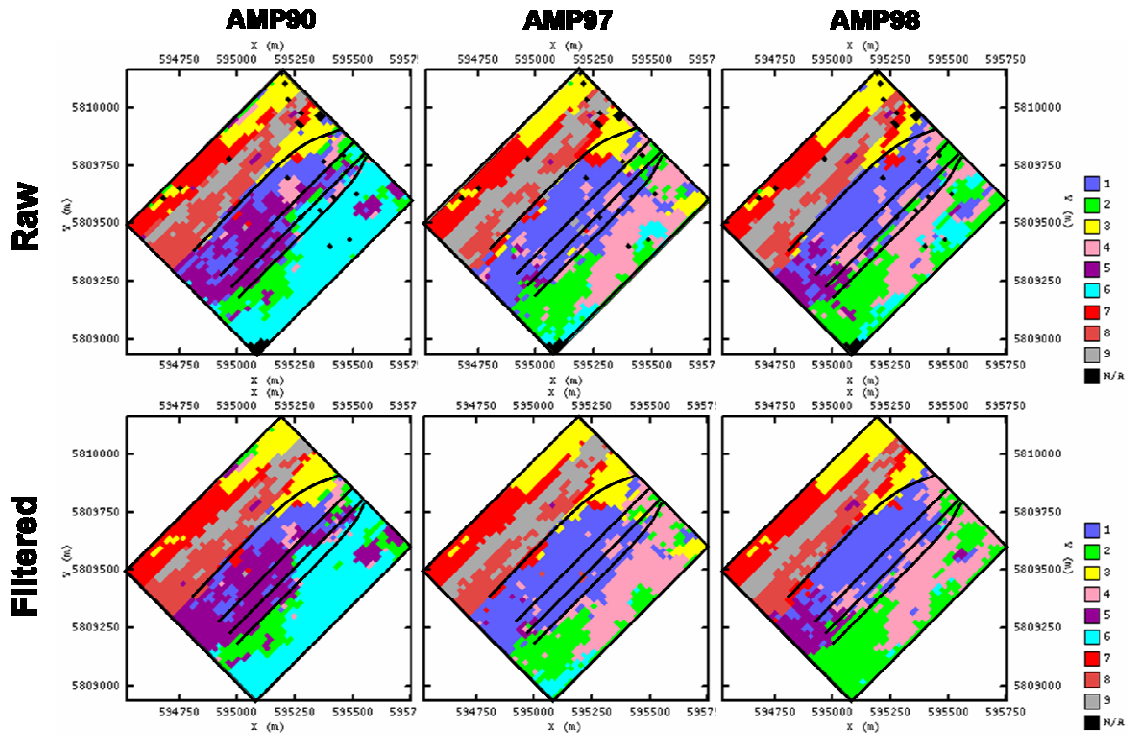


Figure 4-37 - Resulting facies maps from Unsupervised Classification using 9 classes. Top row showing facies maps computed on the raw data, whereas bottom row on the filtered data.

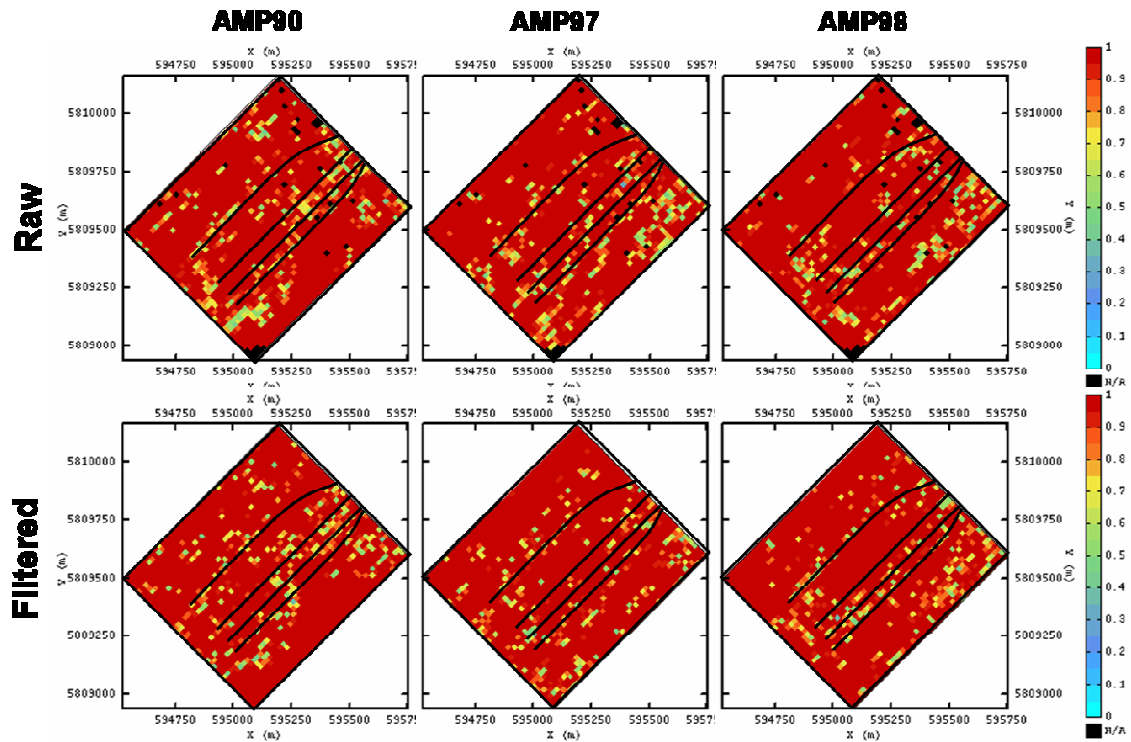


Figure 4-38– Probability of assignment maps for 9 classes. Top row showing facies maps computed on the raw data, whereas bottom row on the filtered data.

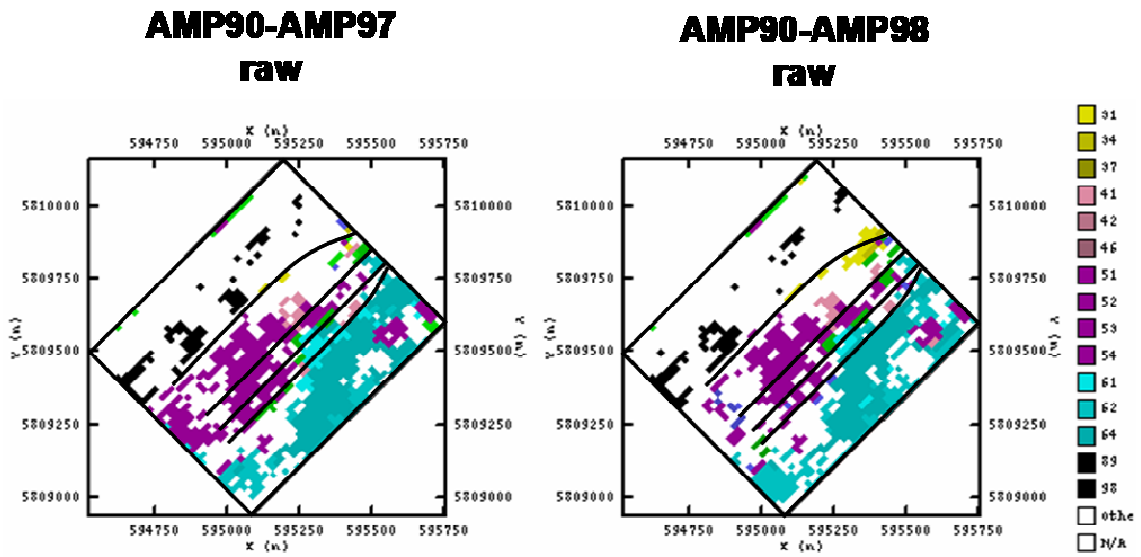


Figure 4-39 – Maps of class change (9 classes) from AMP90 to AMP97 (left) and from AMP90 to AMP98(right), for the raw datasets. White colors indicate no facies change.

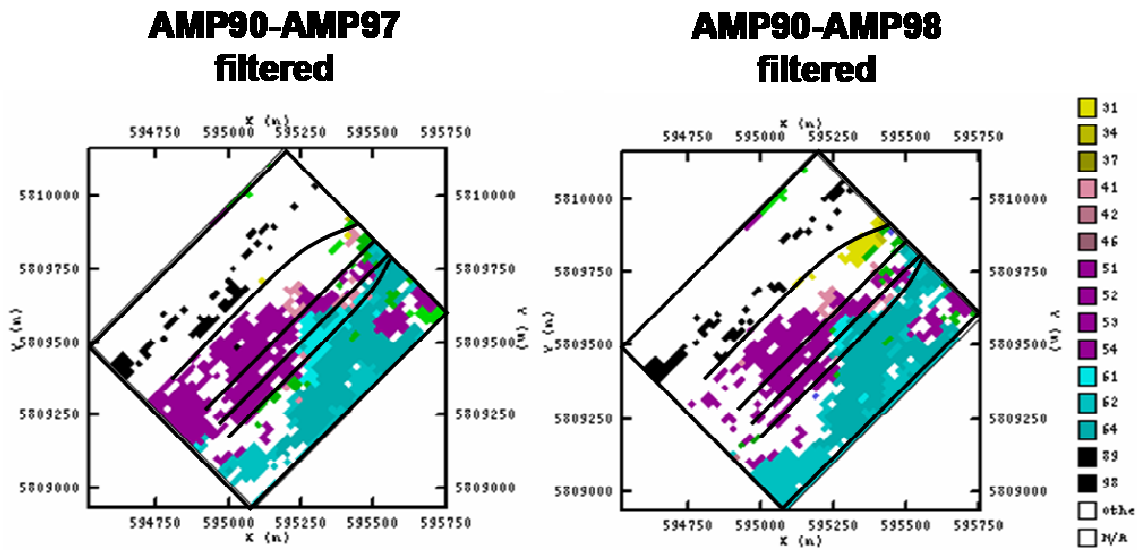


Figure 4-40 – Maps of class change (9 classes) from AMP90 to AMP97 (left) and from AMP90 to AMP98 (right), for the filtered datasets. White colors indicate no facies change.

4.4.3. Seismic Facies Analysis: Conclusions

The comparison of the resulting seismic facies classification maps showed that performing the unsupervised facies classification analyses over the geostatistically filtered datasets resulted in a more continuous behavior of the final facies maps. However, as the datasets were previously cross-equalized to minimize their discrepancies, no major changes were observed in the facies maps of the filtered data compared to the results on raw data. A small increase on the probability of class assignment was also observed, which reduces the interpretation uncertainty.

4.5. Modeling pore pressure effects on time-lapse seismic

The use of time-lapse or 4D seismic technology has grown exponentially in the last 10 years. It helped reservoir geoscientists and engineers to better manage their assets and to provide them reliable information in:

- identifying and mapping poorly drained or upswept zones;
- helping to better map the reservoir external geometry and internal architecture, by inferring possible compartmentalization;
- optimizing infill well locations, or even saving locations not optimally placed; and
- better managing the production/injection liquid rates.

During this early period, time-lapse seismic technology was applied in different oil provinces throughout the world, such as in the North Sea (El Ouair and Stronen, 2006) and in the Gulf of Mexico (GOM). Other areas experienced this new technology, such as in West Africa and in South America (Johann et al., 2006).

The experiences gathered particularly in the GOM in comparative studies with real time-lapse data have shown that: (i) time-lapse technology have often underestimated fluid effects; and (ii) pressure depletion effects could be measured directly by this approach, but request a higher accuracy regarding the seismic repeatability (Hartung et al., 2006).

4.5.1. Effects of steam injection on reservoir properties

Thermal processes, including the Steam Assisted Gravity Drainage (SAGD) schemes, are used to artificially enhance the oil recovery. These Enhanced Oil Recovery (EOR) methods are implemented by increasing the temperature of the reservoir system – the porous media and the fluids therein - by means of steam injection. This new temperature condition reduces oil viscosity, and thus increases liquid flow displacement from the injector to the producer wells. These thermal effects, however, are restricted to the well neighborhood. The region of influence of the temperature effect surrounding the steam injector wells is conventionally referred to as the *Steam Chamber*. One important task of most time-lapse projects conducted over heavy oilfields has been to deliver an estimate, as accurate as possible, of this steam-chamber geometry.

However, many other effects occur simultaneously to the temperature changes during the injection/production phase. These changes in reservoir properties involve factors such as: pore pressure, stress, fluid saturation state and material damage (Schmidt, 2005). As a consequence, seismic properties are affected in a non straightforward way, as a result of the reservoir properties changes due to production.

Effects associated to the presence of fluids and/or due to fluid substitution in porous media have a strong impact on seismic data interpretation. Actually, these effects characterize the physical changes occurring in the reservoir. Fluid effects on seismic wave propagating in porous media have been theoretically described by Gassmann (1951), who proposed the following equations to compute the compressional and shear wave components:

$$\rho V_p^2 = \underbrace{K_{dry} + \frac{4}{3}\mu_{dry}}_{dry\ rock} + \frac{\left(1 - \frac{K_{dry}}{K_{ma}}\right)^2}{\underbrace{\left(1 - \phi - \frac{K_{dry}}{K_{ma}}\right) \frac{1}{K_{ma}} + \frac{\phi}{K_{fl}}}_{fluid}} \quad (74)$$

and

$$\rho V_s^2 = \mu_{dry} \quad (75)$$

Where

V_p, V_s and ρ are the three elastic parameters corresponding respectively to the compressional and shear wave velocities and the density of the resulting composite media;

- ϕ is the porosity;
- K_{dry} is the dry-rock bulk modulus;
- μ_{dry} is the dry-rock shear modulus;
- K_{ma} is the bulk modulus of the matrix or grain material; and
- K_{fl} bulk modulus of the pore fluid.

The first term from Eq. (74) involves the dry-rock moduli, being only influenced by the rock frame, independently from fluid variations and properties. However, porosity changes, as those occurring in compacting reservoirs, will impose the computation of new elastic parameters. The second term in this equation involves not only the knowledge of the properties and types of the fluids present in the pore space, but also their volume fractions. The same is valid for the rock matrix modulus, and a few theoretical formulas were developed to compute the effective medium properties based on the knowledge of their constituents moduli, such as the Voigt, Reuss and Hill bounds (Mavko et al., 1998).

Equations (74) and (75) constitute the base of most of the analyses performed to evaluate the impact of replacing different types of fluids (and/or their saturations) on the oil reservoirs under production. As such, it is an important step of all feasibility studies supporting time-lapse decisions (Calvert, 2005). The use of the amplitude versus offset

(AVO) methodology, where seismic amplitudes of the reflected waves are evaluated as a function of the shot-receiver distance, has added even more value to the seismic data interpretation (Castagna and Swan, 1997; Hilterman, 2001). These techniques have also supported many successful time-lapse applications.

Compressional (V_p) and shear (V_s) wave velocities will depend much on reservoir properties changes. Particularly, the dependence of the compressional wave velocity on the temperature for different types of oil is a well know effect (Wang et al., 1990; Tosaya et al., 1987). The increase in temperature is followed by a reduction of the compressional and shear wave velocities, and, to a lesser extent, a reduction in the density (Schmitt, 2004). These changes, when observed in unconsolidated sandstones saturated with gas or brine, are usually small. However, in the presence of oil as the saturating fluid, and particularly of heavy oil in the reservoir, it promotes a rapid decrease of both compressional and shear wave velocities vs. temperature, as shown in Figure 4-41. In this experiment, a decrease of almost 15% was observed on both (V_p) and (V_s) as the temperature increased from 20°C to 177°C.

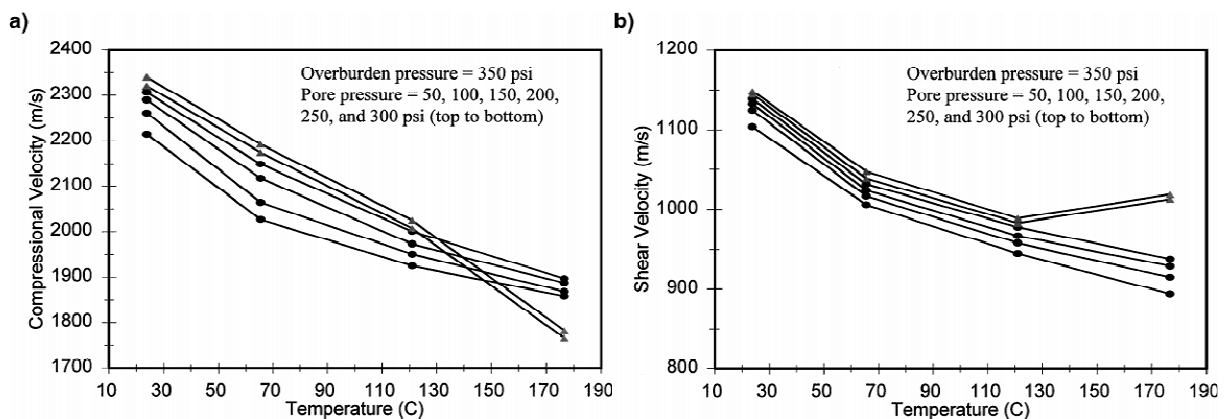


Figure 4-41 - Temperature effect on compressional and shear velocities in a heavy oil reservoir (after Wang, 2001).

Detecting pressure² effects using time-lapse seismic is still a challenging technological problem because the related measured signal is weak and, as a consequence, can frequently be obscured by acquisition noise, or even mixed with other

² In the International System (SI) unit, pressures are measured in *Pascal (Pa)*, which is the pressure produced when applying a force of 1 N (Newton) over an area of 1 m². At the sea level, the pressure exerted by the atmospheric column in the SI corresponds to 101,325 ($\approx 10^5$) Pa, being equivalent to the internationally-recognized standard atmosphere (atm).

reservoir effects (Landro and Kvam, 2002). Moreover, experimental data from laboratory measurements made in small core samples may not be representative of the *in situ* rock mechanical behavior at the seismic acquisition. Two main factors that play a crucial role are the sample size and the stress regime changes applied when it is extracted from the reservoir and during the coring procedure. Regarding this issue, Rasolofosaon and Zinszner (2003) presented results with a statistical comparison between velocity measurements made from core samples and from samples extracted from surface outcrops. These authors showed a systematic overestimation of the pressure effect when using core samples, confirming the hypothesis of damage effects.

Keeping in mind the above mentioned limitations, the theoretical dependence of the elastic parameters on the reservoir pressure is investigated and discussed in the following paragraph. In particular, the time-lapse seismic campaign data registered on the heavy oil Senlac reservoir, submitted to a Steam Assisted Gravity Drainage EOR scheme, will be carefully analyzed. In these datasets, the monitor seismic data surveys exhibit negative time-shifts in the reservoir interval, when compared to the base survey. This result is in disagreement with what is expected from theoretical models³. A comprehensive discussion on the effects of wave propagation in porous media can be found in Bourbié et al. (1997).

The first attempt to explain the negative time-shifts observed in the time-lapse data set can be found in Lucet and Fournier (2001). This work shows that the modelling results using the Gassmann equations for fluid substitution do not support the observed negative time-shift effects.

In order to better understand the effects of pressure on time-lapse response, a simple one-dimensional (1D) model was used. It is based on the Hertz-Mindlin equations (Mindlin, 1949) following the proposal of Landro and Kvam (2002). These equations describe the relationship between V_p and V_s as a function of the effective pressure. Next, a 1D convolution seismic modelling is used to obtain six different synthetic seismic traces. In this case, each seismic trace will correspond to one of the six different pore pressure scenarios.

³ Because of the increase in temperature when injecting steam, one expects a positive time shift.

4.5.2. Theory: Pressure effects

Basic concepts involving different types of pressure definitions used in the oil industry are presented in this paragraph. As noticed by Bruce and Bowers (2002), this terminology involves different disciplines and is used by various oil exploration and production experts, from reservoir engineering to rock-physicists, including geologists and drilling engineers. Therefore, a reminder of the precise definitions is given below. A comprehensive description of pressure origins and effects, particularly to those related to pore pressure estimation and dedicated to time-lapse seismic effects may be found in Kvam (2005).

The *confining pressure* corresponds to the pressure exerted by the weight of the rock column, including the fluid trapped in pore spaces, on an investigated point at a given depth. It is sometimes referred to as the *overburden* (also named *external* or *lithostatic*) *pressure* P_c and is defined by:

$$P_c = \int_{z_0}^z \rho(z) g dz \quad (76)$$

where z_0 is the reference depth, usually the sea level whose reference level pressure is equal to $p_0 = 105 \text{ Pa}$ ($\approx 1 \text{ atm}$); $\rho(z)$ is the medium density (in kg.m^{-3}), and g is the gravitational constant (9.81 m.s^{-2}). The confining pressure gradient varies in the subsurface as a function of the material density, and the value of 22.62 KPa/m (1 psi/ft) is considered as a gradient reference. Despite being usually referred to as a pressure, which means a scalar quantity, the term *confining stress* is more convenient, as this quantity represents a tensor. The confining stress is represented in Figure 4-42, by the green straight line.

Another important concept is the *pore pressure*, which is the pressure exerted by the fluids filling the pore spaces of a reservoir rock. In normal conditions, it represents the effect of the connected fluid column overlying the reservoir, or the *hydrostatic pressure*. Different terms are used in the petroleum industry to refer to the pore pressure, such as *formation pressure*, *reservoir pressure* or *pressure of liquids or fluids*.

The definition is the same as Eq. (76) in which $\rho(z)$ is now the *fluid density*. Normally pressured formations usually exhibit a pore pressure that is equal to the hydrostatic pressure of the pore water. This pressure tends to increase with depth according to the pressure gradient, as shown in Table 4-20.

Table 4-20 – Pressure gradients as a function of fluid type or density.

Fluid type	Gradient	
	psi/ft	KPa/m
Fresh water	0.43	9.8
Oil	0.25-0.40	5.70-9.11
Gas	0.1-0.2	2.28-4.56

The term *abnormal pressure* refers to those conditions where the pore pressure values deviate significantly from the normal pressure gradient. When pore pressure is below the hydrostatic pressure expected for a particular depth, the situation is referred to as *under-pressured*, or *subnormal* pressured zone or formation. The most current subnormal pressure condition is the one associated to depleted reservoirs, when the pressure reduction is directly linked to the hydrocarbon production. However, reservoir leakage due to seal or cap rock fracturing may also be a source of under pressure.

Overpressure zones are observed when the pore pressure is higher than the hydrostatic pressure computed for the given depth. The main causes usually associated to over pressured intervals are : (i) compaction disequilibrium, caused by high sedimentation rates and/or formation of seals, which will trap the water in the pore spaces causing the under compaction and reducing the contact between grains; this will become over pressurized after compaction due to overburden pressure; (ii) structural uplifting, displacing blocks from deeper and higher pressure zones to shallower depths, submitted to lower pressure conditions. Chemical processes occurring in the subsurface may also develop over pressured zones, such as those processes related to methane generation and to dehydration of clays (Barriol at al., 2005).

In Figure 4-42, a schematic illustration from a fictitious well is presented. In this image, the linear trends of the hydrostatic pressure and of the overburden stress define the range of pressures usually found when drilling a well.

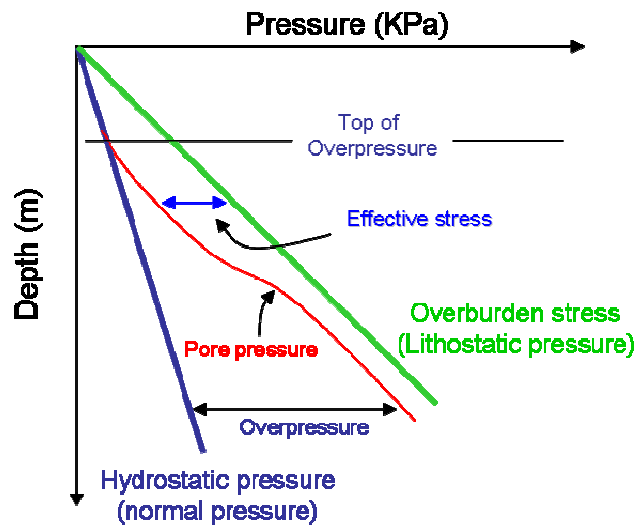


Figure 4-42 - Schematic representation of main pressure effects with depth (modified from Bruce and Bowers, 2002).

During the exploratory phase, an additional care must be taken regarding the identification of anomalous pressure zones, as it is crucial for safe and cost-effective drilling. With such information, important drilling parameters are defined, such as the density of the drilling fluids, or mud weights. A correct definition of the mud weights will minimize the risk of mud losses, or undesirable sticking of the drill pipes, which occurs due to reservoir under pressure. Additionally, pressure information is also important for assessing exploratory risk factors, including the migration of formation fluids, as well as for the characterization of the seal integrity (Chopra and Hoffman, 2006).

4.5.3. Pore pressure and confining pressure relationships: Differential and effective pressure

One of the first theories to describe the dependence of the velocity on pressure in unconsolidated sediments was proposed by Terzaghi (1943). Considering the confining and pore pressure concepts as previously described, and using a medium composed by unconsolidated rocks, this author suggested that the differential pressure be defined as follows:

$$P_{dif} = P_c - P_p \quad (77)$$

For consolidated rocks, Biot and Willis (1957) have shown that deformation depends on the *effective pressure* P_{eff} , or the difference between the confining P_c and *effective pressure coefficient* n times pore pressure P_p

$$P_{eff} = P_c - nP_p \quad (78)$$

Using saturated samples from Berea sandstone, Wyllie et al. (1958) showed the dependence of the compressional velocity with the differential pressure, and considered that coefficient n , that they referred to as *internal deformation coefficient*, to be equal to the unity.

After analyzing experimental results resulting from changing both confining and pore pressure data from saturated Berea sandstone samples, Christensen and Wang (1985) claimed that the *effective stress coefficient* should not be equal to one. They observed experimentally that changes in velocities resulting from changes in confining pressures were not exactly cancelled by the equivalent change in pore pressure, as predicted by Terzaghi. They associated this experimental response to the presence of high compressibility clay that lines grains and pores within the quartz framework of the Berea sandstone.

Rasolofosaon and Zinszner (2003) use indistinctly the effective and differential pressure concepts, and showed that bulk modulus for saturated porous rocks K_{sat} is almost insensitive to P_{eff} variation, and that most of the variation is due to shear modulus μ .

One may notice that Equations (77) and (78) differ only by the *effective pressure coefficient* n , which appears as a multiplicative factor of the pore pressure. This coefficient is known as *effective pressure coefficient* (Gurevich, 2004) or *coefficient of internal deformation* (Landro and Kvam, 2002). The definition of the value to be

associated to this coefficient has been a subject of intense debate, as previously showed. Recently, Gurevich (2004) provided a comprehensive discussion regarding the value associated to this coefficient, claiming that it should be equal to 1, under the following assumptions: (i) the homogeneity of the grain matrix; and (ii) validity of the linear elasticity hypothesis within the range of the considered stress and pressures. These theoretical results, where the coefficient is directly derived from the linear elasticity equations, are in agreement with the original work by Terzaghi (1944).

4.5.4. Predicting pressure effects with the Hertz model

At every location of the earth's subsurface, two different and complementary pressure fields, namely the confining or the overburden stress and the pore pressure, can be defined. These two pressure fields combine in a resulting pressure known as the differential pressure or effective pressure P_{eff} .

Hertz (1941) showed that the dependence of the velocity on differential pressure could be analytically derived, according to a power law. He considered this coefficient to be equal to 1/6 for compressional waves through a stack of identical spheres in elastic contact⁴. More details of the developments of the theory are presented in Annex B.

Bachrach et al. (2000) found strong discrepancies when comparing the V_p and V_s from experimental measurements to those predicted by the Hertz-Mindlin contact theory, for unconsolidated beach sediments. Their experimental data consists of a three-component surface seismic recorded over shallow unconsolidated beach sediments. At shallow depths, very low pressures are observed, smaller than 0.1 MPa, making this experiment an interesting analogue for over pressured reservoirs composed of soft unconsolidated sandstones. One of the conclusions was that both experimental V_p and V_s values were proportional to the pressure raised to the power of 1/6 as predicted by the Hertz-Mindlin theory, but their absolute values were less than half of those predicted. One possible source of discrepancies was regarded as associated with grain angularity.

⁴ Experimental values (Lucet, 1989) show that the Hertz coefficient for sandstones might be as high as 1/4.

Landro and Kvam (2002), using the Hertz-Mindlin model, suggested that the variation of the compressional velocities is function of a change in the effective pressure according to the following relationship :

$$\frac{\Delta V_P}{V_P^0} = \left(\frac{P_{eff}}{P_{eff}^0} \right)^{\frac{1}{6}} - 1 \quad (79)$$

And an equivalent formulation was proposed for the shear wave, as

$$\frac{\Delta V_S}{V_S^0} = \left(\frac{P_{eff}}{P_{eff}^0} \right)^{\frac{1}{6}} - 1 \quad (80)$$

where P_{eff}^0 is the effective pressure at the initial pressure conditions, P_{eff} is the effective pressure at any subsequent time, and the ΔV_P and ΔV_S are, respectively, the difference in the compressional and shear velocities at the equivalent times. This formulation is well adapted to evaluate the velocity variation on producing reservoirs.

4.5.5. Negative time-shifts and pore pressure: Modeling and results

A one dimensional seismic model was built to validate the achieved results from the 4D interpretation made on both monitors surveys in the Senlac heavy oil field. It aims at a better understanding of the possible physical factors that could explain the negative time-shifts observed In Figure 4-43.

This model was performed considering the velocity dependence on the effective pressure as proposed in the Hertz-Mindlin geomechanical model, and modified by Landro and Kvam (2002). In this case, the effective stress coefficient n was taken to unity. The one-dimensional seismic modelling was carried out using EasyTrace software.

In terms of initial reservoir parameters prior to the SAGD steam injection, the measured pore pressure in the reservoir was 5.2 MPa, as presented in Table 4-22

(Edmunds and Sugget, 1995). It is interesting to notice that this pore pressure value is below the hydrostatic pressure value expected at the corresponding reservoir depths (7.4Mpa at 730m). According to Hinkle and Batzle (2006), this under pressure condition may be an additional restriction to oil flow.

In Figure 4-43, five groups of traces, extracted from different spatial locations in the Senlac reservoir, are presented. Each trace group displays three different traces: a grey-to-black colour filled trace, corresponding to the S90 base survey; and blue and red non-filled wiggle traces corresponding, respectively, to the S97 and S98 monitor surveys. It can be noticed that both red (S97) and blue (S98) traces show a negative time-shift at the reservoir interval and below this interval reservoir. These differences reach a maximum value of approximately 3 (three) milliseconds when mapped over the bottom reservoir interval, and increase downwards, below the reservoir level.

It was also noticed that the seismic traces corresponding to the monitor campaign, S97, exhibit higher negative shifts than those from the S98 campaign, despite the fact that the maximum reservoir temperature had been reached at the time of the second monitor survey acquisition.

Table 4-21 – Senlac main reservoir properties (from Edmunds and Suggett, 1995).

Porosity	33%
Oil saturation	85%
Permeability	5-10 D
Viscosity (20°C)	15,000 mPa-s
Initial reservoir temperature	29°C
Oil gravity	13°API
Initial reservoir pressure (P_{pore})	5.2 MPa

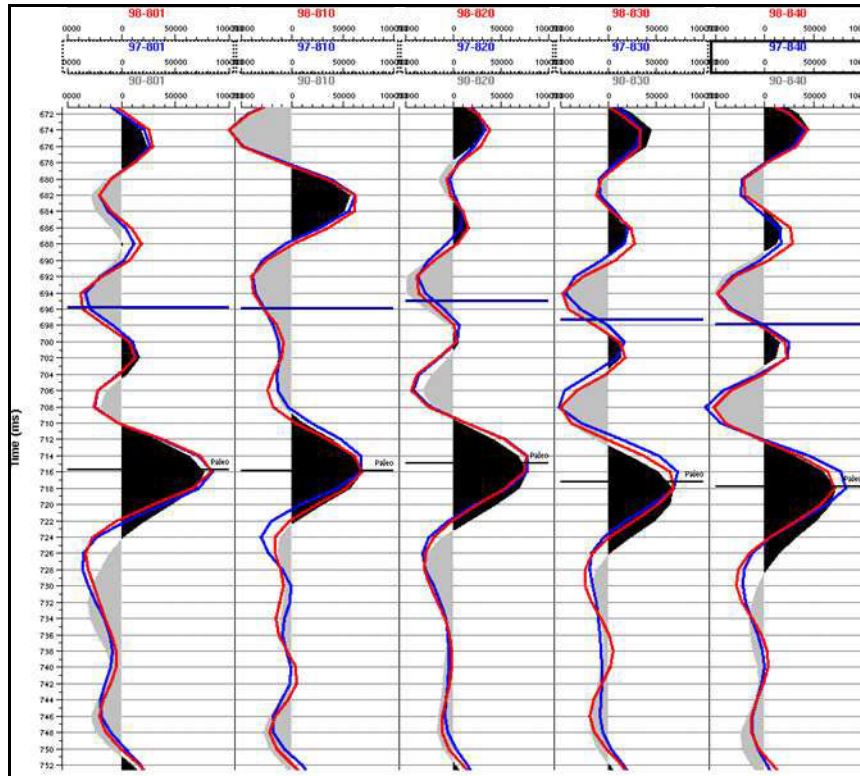


Figure 4-43 - Seismic traces taken from five different locations in the Senlac seismic survey, where the reservoir top and bottom are indicated by blue and black markers, respectively. Traces with grey-to-black colors represent the base surveys S90, whereas the blue and red traces represent the monitor surveys S97 and S98, respectively.

However, these time-shift differences observed when comparing the base and monitor surveys are not in agreement with the expected seismic response to an increment in the reservoir temperature. The classical models for heavy oils reservoirs submitted to steam injection imply in a reduction of the compressional and shear velocities, with a subsequent increase of the two-way-travel time at the reservoir level. In the Senlac case, an increment of the reservoir temperature, from the initial value of 29 °C, prior to the steam injection, to 240 °C, at the time when the second monitor seismic survey was shot in 1998, is observed (Li et al., 2001).

Considering the Well A displayed in Figure 4-44, and the reservoir parameters presented in Table 4-22 and Table 4-23, five different pore pressure scenarios were modeled to try to explain the observed seismic data.

In the following, the seismic modeling strategies and results are presented and discussed.

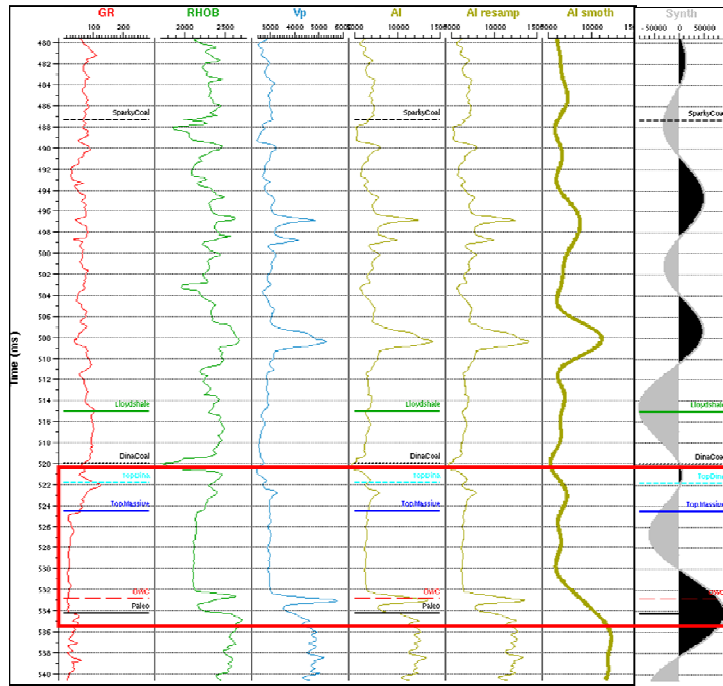


Figure 4-44 – Well A used as input to the pore pressure modeling. Logs registered prior to the start of the oil production. Rectangle in red corresponding to the reservoir limits, with top defined by the TopDina marker at approximately 522 ms, and the bottom defined by the geological marker Paleo at 534 ms.

Table 4-22 – Initial reservoir pressure conditions, before SAGD steam injection.

Initial reservoir conditions	
P_{pore}	5.2 MPa
P_{conf}	16.8 MPa
P_{eff}	11.6 MPa
n	1

Table 4-23 – Main parameters used in the seismic modeling of the pore pressure effects. ($P_{conf}=16.8$ MPa).

Scenarios	Modeled pressures (after injection)				
	S1	S2	S3	S4	S5
P_{pore} (Mpa)	1.20	3.20	7.20	9.20	11.20
ΔP_{pore} (Mpa)	-4 (-77%)	-2 (-38%)	2 (38%)	4 (77%)	6 (115%)
P_{eff} (Mpa)	15.60	13.60	9.60	7.60	5.60
Factor	1.05	1.03	0.97	0.93	0.89

4.5.6. Scenarios S1 and S2: Pore pressure reduction

In the first two scenarios, named S1 and S2, a reduction of the original reservoir pore pressure is assumed, corresponding to an under pressure regime. This reduction is in the order of 4 and 2 MPa, respectively, in comparison to the original reservoir pore pressure, equal to 5.2 MPa. These new conditions would correspond to, for instance, a depletion of the reservoir as a result of the oil production.

These new pressures represent, respectively, a reduction of 77 % and 38% from the initial pore pressure, as show in Table 4-23. According to the Hertz model, the corresponding compressional velocity increase must be of 5% and 3%, respectively. The traces resulting from the pressure modeling are displayed in Figure 4-45. In this figure, two sets of seismic traces are presented: on the left box, traces corresponding to the first two scenarios S1 and S2; and on the right, the remaining S3, S4 and S5 traces. The traces in black-grey colors represent the raw data.

The trace in red, S1, corresponding to the smallest final pore pressure among the five different considered scenarios, is in agreement with the original trace at least in the reservoir time interval. Very small negative time-shifts are observed in trace S1, mainly close to the reservoir bottom. These negative time-shifts increase downwards, reaching a maximum value of approximately 1 ms at 541 ms. In terms of amplitude differences, small contrasts were detected only locally in the reservoir interval, as observed at 527 ms.

Trace S2, in orange in Figure 4-45, represents the smallest negative pore pressure contrast. Almost no difference is identified when comparing this trace to the original one, for the whole time-interval investigated.

Another interesting point to investigate concerns the validity of the Hertz coefficient (equal to $1/6$ in all studied scenarios). However, some works showed that this coefficient may differ from the original value. Based on experimental measurements made on cores from sandstones and carbonates rocks under varying

differential or effective pressure, Rasolofosaon and Zinszner (2003) associate the higher experimental coefficient values to two factors. The first involves the mechanical damage of the core samples due to variations in stress during coring operations. The second one concerns the alteration of certain clay minerals, and that may also contribute to modify the mechanical properties of the rock sample

Assuming an uncertainty on the Hertz coefficient determination, the idea was to find out under which coefficients the negative time-shift values could be observed. To perform this analyze, the scenarios S1 and S2 were considered. In the S1 case, the velocity vs. pressure dependency is given by the following expression:

$$\frac{V_p^i}{V_p^0} = \left(\frac{P_{eff}^i}{P_{eff}^0} \right)^n \quad (81)$$

The ratio between the initial and final compressional velocities that would lead to a 2 ms time-shift in the reservoir interval was found to be equal to $\frac{V_p^i}{V_p^0} = 1.24$.

Considering the first scenario S1, and after simple calculations, the new Hertz coefficient computed is equal to 0.72 (or 1/1.38). Using the same approach, the coefficient was calculated for the second scenario S2 and is equal to it 0.54 (or 1/1.86).

Concluding remarks on scenarios S1 and S2

Despite the strong pore pressure reduction considered when modeling the scenario S1, corresponding to a reduction of 77 % of the original pore pressure, only second-order time-shifts were observed in the modeled traces. The corresponding compressional velocity increase imposed by these new pressure conditions in scenarios S1 and S2, according to the Hertz model, was of the order of 5% and 3%, respectively.

4.5.7. Scenarios S3 to S5: Pore pressure increase

The new pore pressures assumed for the S3, S4 and S5 scenarios correspond respectively, to increments of 38%, 77% and 115% of the original pore pressure, as

observed Table 4-23. These three scenarios model a hypothetical overpressure in the reservoir interval. Only subtle responses were observed in scenarios S1 and S2, in cases S3 to S5 important variations are imposed to the new seismic traces as a function of the new velocity contrasts.

The resulting velocity factors, as observed in Table 4-23, are all smaller than unity, and will result, in all cases, in a reduction of the original compressional velocity due to these new overpressure conditions. All results from S3, S4 and S5 seismic traces will present a pull-down effect as a response to these velocity contrasts, as it can be observed in Figure 4-45. These scenarios cannot be invoked to explain the observed downward shift from Senlac.

Concluding remarks on scenarios S3, S4 and S5

It was observed in S3 to S5 scenarios that an increase in the pore pressure, with the consequent reduction of the effective pressure, imposes a reduction of the compressional velocities as expected from the theoretical Hertz model. However, these responses do not explain the observed seismic data, where negative time-shifts were detected in the reservoir interval, as previously showed.

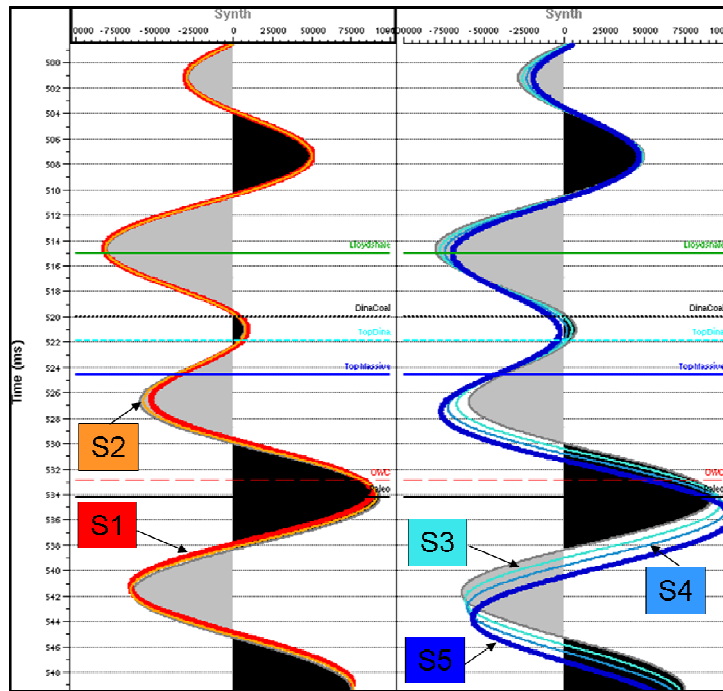


Figure 4-45 – Seismic traces resulting from pore pressure modeling. On the left, traces in red (S1) and orange (S2) corresponding to a pore pressure reduction (under pressure condition). On the right, traces S3 to S5 resulting from the over pressurization of the reservoir interval. The central trace on both sides corresponds to the raw trace.

4.5.8. Scenario S6: which pore pressure variation fits to the observed time-lapse measurements?

In the previous models, an increasing range of pore pressures - S1 to S5 models– was considered. The resulting effective pressure P_{eff} reductions, from 15.6 MPa to 5.6 MPa, as shown in Table 4-23, resulted in a range of reservoir velocities that did not explain the observed negative time-shifts as interpreted from the monitor surveys in the Senlac case study. Therefore, the proposed approach was to answer the question: if a negative time-shift of 2 ms is observed in the data, what would be the necessary pore pressure variation that would determine this time-shift?

In Table 4-24, the parameters assumed for the S6 scenario are presented, where the previous S2 model is included as a reference. This S6 new model shows a 22.5% increase in the compressional velocity at the reservoir interval, explaining the observed time-shift of the order of 2ms, as shown in Figure 4-46. From the Hertz formulation, this velocity variation is achieved at extremely low pore pressures only, and the results

indicating that a stiffer reservoir rock was traversed by the propagating waves during the monitor surveys. However, this observation is in contradiction with what one should expect from theory, if considering a steam injection mechanism.

It is known that:

One way to increase the compactness of the reservoir is to strengthen grain contacts by decreasing the reservoir pressure. However, pressure usually increases at injector wells, and decreases at the producers, as shown in scenarios S1 to S5;

As showed in scenario S6, the compressional velocity variation necessary to fit the observed negative time-shifts, considering the Hertz-Mindlin model, imposes a reservoir pressure decrease of approximately five times the initial reservoir pressure condition, which seems to be unrealistic;

Highly heavy viscous oil is replaced by a less viscous, less dense mixture of oil and water. As viscosity and density of substituted trapped fluids decrease after the steam injection, the velocity would have to be slower according to Gassmann's equation. Therefore, the time-shifts would have to be positive, the reverse of what is observed in the real Senlac case;

However, all the above remarks, including the Hertz-Mindlin model, are valid for a saturated consolidated material. It might be not the case for non consolidated sandstone saturated by heavy oil. One valid hypothesis to explain the increase of velocity during exploitation is that a non-consolidated sandstone saturated by heavy oil behaves as a non rigid material, but rather as a highly viscous body. In this case, the grains are not in elastic contact, but are rather floating in the liquid. Its seismic velocity is in fact lower than expected by applying directly the Hertz-Mindlin's model and the Gassmann's theory. After exploitation, the highly viscous fluid is substituted by a lesser viscous one, the reservoir pressure decreases and grains are no more floating in the liquid. Assuming that the grain edges could touch each other after the steam injection, the material would turn into a more classic rigid porous medium saturated with fluids. Under this condition, the seismic velocity will increase in the reservoir interval, leading

to negative time-shifts when comparing monitor and base surveys from the time-lapse seismic campaigns.

Aiming at comparing the results obtained with the Hertz-Mindlin model, the effective moduli of the reservoir medium was computed for two different saturation conditions: before and after steam injection. In this case, the reservoir was considered as a composite of three different phases, where the elastic parameters considered for each constituent are presented in Table 4-25. It was assumed that, prior to the steam injection, the oil saturation was equal to $S_o = 0,85$, being reduced to $S_o = 0,20$ at the time of the monitor surveys, due to the oil-to-water substitution. In this case, as the geometric details describing the different phases composing the rock are unknown, only the upper and lower bounds, defined as the Voigt (M_V) and Reuss (M_R) bounds were computed, as presented in Mavko et al. (1998), and using the following averaging equations

$$M_V = \sum_{i=1}^N f_i M_i \quad (82)$$

$$M_R = \sum_{i=1}^N \frac{f_i}{M_i} \quad (83)$$

$$M_{VRH} = \frac{M_V + M_R}{2} \quad (84)$$

Where f_i and M_i are, respectively, the volume fraction and the elastic modulus of the i th medium (or constituent) of the composite, and M_{VRH} is the arithmetic mean value of the Voigt and Reuss averages, known as the Hill bound.

Table 4-25 – Elastic properties of the components of the different phases of the Senlac data, with V_p in m/s, ρ in kg/m³ and $K + \frac{4}{3}\mu$ in Pa.

	V_p	ρ	API°	$K + \frac{4}{3}\mu$
Oil	1700.00	900.00	13	2.60×10^9
Water	1500.00	1000.00	10	2.25×10^9
Quartz	6000.00	2650.00	-	9.54×10^{10}

The input reservoir parameters considered to compute the effective moduli are:

- porosity: $\phi = 33\%$;
- initial oil saturation: $S_o^i = 0.85$;
- final oil saturation: $S_o^f = 0.20$

Table 4-26 – Theoretical bounds of the effective properties computed for the cases after and before steam injection.

	Before steam injection		After steam injection	
	V_p^0	$K + \frac{4}{3}\mu$	V_p^1	$K + \frac{4}{3}\mu$
Voigt (upper bound)	4571.00	4,34E+10	4528.00	4,30E+10
Reuss (lower bound)	3229.00	2,17E+10	3063.00	1,97E+10
Hill (average)	3900.00	3,16E+10	3796.00	3,02E+10

Two possible mechanisms are studied to fit to the observed velocities:

considering that the initial medium before injection is a tar-supported sandstone, the equivalent medium velocity that best describes this hypothesis is the one given by Reuss model (harmonic mean). In this case, the medium velocity is $V_p = 3229$ m/s, as shown in Table 4-26. Considering that the steam injection caused the heavy oil to be produced, then the new system becomes a grain-supported model, which is better described by the Voigt model (or Hill model). In this case, the velocity would increase to 4,528 m/s (or 3,796 m/s). All these values are still too high when compared to the measured ones. However, if the quartz velocity is reduced from 6000 m/s to 5000 m/s, then the resulting velocities for both states (before and after steam injection) fit with the real data

($V_p^0 = 3012\text{m/s}$ and $V_p^1 = 3858\text{m/s}$). A possible justification for lowering the matrix velocity could be the presence of clay minerals in addition to the quartz; and another hypothesis to consider is the reduction of the medium porosity, which would increase the final velocity. In this case, if the Hill model is used, the porosity should decrease from 33% to 9%, and the matrix velocity assumed to be 4100 m/s, for the velocities to fit with the observed data.

An equivalent mechanism as the first one described above was suggested by Dvorkin and Medina (2000). They proposed an effective-medium where, due to the very high porosity, the grains are suspended in a tar matrix, and do not represent a continuous load-bearing framework. Therefore, as the medium is heated and the oil produced, the reservoir will experience a porosity reduction as a response to the diminution of the heavy oil volumes. According to the authors, an abrupt increase of both V_p and V_s should be observed.

Schmidt (2004, 2005) noticed that, in some particular heavy oil reservoirs, those oil components corresponding to the heaviest fractions could act as a cementing agent. Analysis of photomicrography registered with scanning electron microscopes (SEM) allowed a better understanding of the role of the heavy oil, acting as cement which entirely coats the mineral grains and invades the grain contact zones, as shown in Figure 4-47 (a). In these cases, removing out this cement would modify the rock framework, and, therefore, its elastic properties. Within experimental conditions in laboratory, a simple way to remove this cement is washing the rock samples using solvents. In Figure 4-47 (b), a SEM image was recorded after washing out the same reservoir rock samples as in (a), taken from the SENLAC reservoir. These data corroborate the hypothesis that the cement bonding the grains is mainly composed by the heavy oil fractions. However, this hypothesis still assumes a grain supported medium, where the Hertz-Mindlin model of grain contacts is valid. In these cases, the cement imposes an increase of the compressional velocity.

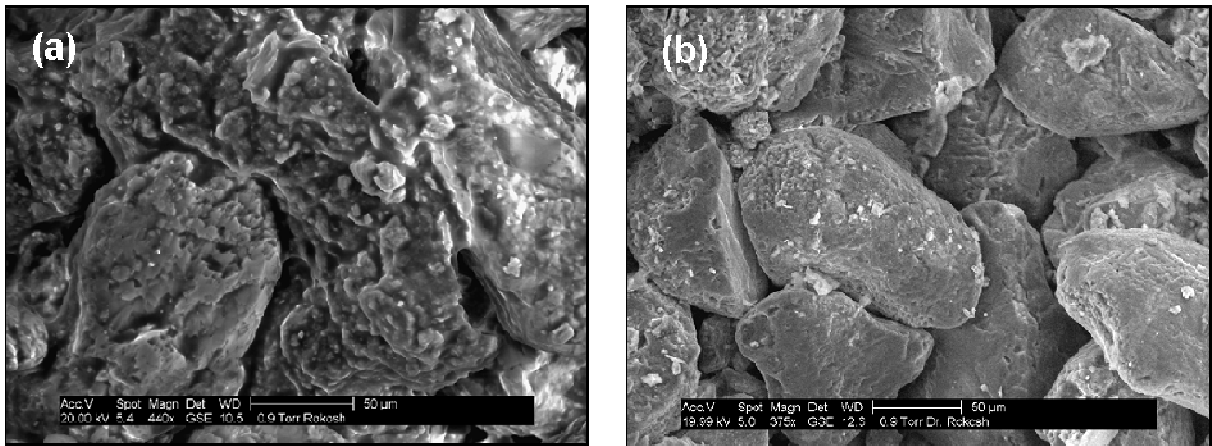


Figure 4-47 – Environmental scanning electron microscope (ESEM) photomicrography taken from one SENLAC heavy oilfield sample, before (a) and after (b) washing the sample by using solvents to remove the oil derived cement (extracted from Rokosh et al., 2004).

Hence, as heating heavy oil reservoirs through steam injection reduces the oil viscosity, one could also expect that those heavier fractions acting as cement would also be partially or completely removed. Therefore, an increase in the V_p velocities could be also expected as a consequence of the heating process, and could explain the negative time-shifts observed in the monitor seismic surveys from the SENLAC data.

A similar effect of velocity increase due to reservoir pressure increase in the context of steam injection was described by Lumley (1996) in the Duri field steam-flooding project, Indonesia. In this case, however, two different physical processes took place in the reservoir:

- close the steam injector wells, where the temperatures were kept very high due to the steam action (hot-steam saturated zones), a pull-down effect was observed, as a consequence of the reduced velocities due to the temperature effect; and
- around the hot-steam saturated zone, a high-pressure zone was identified due to the negative time-shifts (or pull-up effect) observed on the time-lapse monitor seismic data.

In the Duri Field case, the negative time-shifts were associated to a reservoir pressure increment. Following the steam injection into the reservoir, a transient high

pressure-front was formed. The gas out of the solution, as a result of the primary production, was reintroduced back into the solution due to the new pressure conditions. An increase in the reservoir compressional velocity was observed. However, this velocity effect particularly associated to the presence of gas is not expected to occur in the Senlac case, due to the distinct oil characteristics.

4.6. Conclusions

The analysis of the orthogonal factors computed through the FK methodology followed by the Unsupervised Facies Classification allowed the spatial interpretation of underlying structures that are hidden in the time-lapse seismic volumes, and are usually difficult to be identified when considering a conventional interpretation workflow. A by-product resulting from this analysis is the potential to perform a quality control on the time-lapse processing sequence, by investigating and comparing the variance of the structures in different time windows.

It was noticed that the orthogonal factors extracted by the FK on both the non-reservoir and reservoir zones of the Senlac dataset are quite similar in terms of spatial variability (range, anisotropy and number of components). However, the contribution (in %) of each FK factors are more contrasted in the Reservoir zone (100% or 0%) than in the Non-Reservoir zone; this could be explained by a more careful processing carried out in the Reservoir zone, introducing a stronger noise coherence between the time-lapse campaigns. Additionally, the contribution in terms of variance on each component AMP90, AMP97 and AMP98 is much higher in the reservoir zone, of one to two orders of magnitude.

Moreover, the correlation coefficients for large scale component C3 are more contrasted in the Reservoir zone. They are smaller (0.26) for AMP90xAMP97 and AMP90xAMP98, but higher (0.86) for AMP97xAMP98. This could be related to changes in the reservoir due to the steam injection in horizontal wells aligned with the cross line direction, indicating that changes in the reservoir would affect zones of similar extension and orientation as the C3 structures. These results show that FK seems

to be an efficient method to reveal common regional trends and time dependent zones from repeated seismic datasets.

The comparison of the results of the simultaneous seismic facies classification approach shows that the geostatistical filtering imposed a more continuous behavior of the mapped facies. The filtered seismic facies maps are in agreement with previous supervised seismic classification studies performed in the area. Regarding the number of facies classes, the use of a smaller number of classes – in this case, five classes – allowed an easier distinction of possible time-lapse effects when comparing the raw and filtered maps, even if more features can be observed in the nine classes maps, they are difficult to interpret.

The maps of probability of assignment into class showed minor improvements when comparing raw and filtered datasets. But even these small improvements could help reducing the time-lapse interpretation uncertainty.

The last part of this chapter concerns the investigation of the possible mechanisms that could lead to the observed negative time-shifts between base and monitor surveys.

First, the dependence of the compressional velocity on the reservoir pore pressure was investigated. These negative time-shifts are in disagreement with what is expected from theoretical models describing increasing temperature effects in heavy oil sands.

Aiming at providing a physical basis for these anomalous time-shift responses, a simple one-dimensional modeling, considering the velocity-pressure dependence, was conducted. The considered model was based on the Hertz-Mindlin (Mindlin, 1949) equations, following the proposal of Landro and Kvam (2002). Six different pore pressure scenarios were studied, where for five of these models - from S1 to S5 - the modeled pore pressures were considered to be in the normal pressure ranges. It should be noticed that the resulting modeled velocities did not explain the observed negative time-shifts, for none of the considered models. Additionally, it was observed that, to

reach this negative 2ms time-shift, an increase of 24% in the compressional velocities was necessary.

However, as described in the model S6, this velocity increase involved unrealistic pressure values, such as an effective pressure of 42 MPa in comparison to the initial pressure condition of 11.6 MPa, in the reservoir interval. Based on the Hertz-Mindlin contact theory, it seems that the observed negative time-shifts resulting from the different time-lapse seismic data from Senlac can not be properly explained by a pressure variation.

One valid hypothesis to explain the increase of velocity during exploitation is that non consolidated sandstones saturated by heavy oil do not behave like a rigid material, but rather like a mixture of grains and heavy oil. In this case, the grains are not in elastic contact, but are rather floating in the liquid. This hypothesis was tested using the effective medium theory, such as the Voigt, Reuss, and Hill models. The results showed that seismic velocity would increase in the reservoir interval, leading to negative time-shifts in agreement with the observations.

Another explored hypothesis was the porosity reduction as a consequence of the heavy oil production, that would also lead to an increase in the V_p velocity.

Chapter 5 - Marlim Case

The factorial cokriging filtering technique (see Chapter 3 - for theory) is applied to a time-lapse seismic dataset from the Marlim field in order to identify 4D effects due to reservoir exploitation. The Marlim field is a Brazilian deepwater heavy oil turbiditic field located in the Campos Basin along the Northern part of the Rio de Janeiro state, southeast to the Brazil's coast. Two time-lapse seismic campaigns were conducted in this field during 1997 and 2005, respectively. They aimed at better evaluating the water flooding injection scheme and recovery performances, as well as, at helping to locate new infill wells.

Previous feasibility studies conducted in the Marlim area and involving rock-physics and petro-elastic seismic modeling, demonstrated that the expected acoustic velocity variation due to the replacement of oil by water was in the order of magnitude of 7% (Oliveira et al., 2007). This velocity contrast is small and implies in a low 4D signature detectability in this area. In addition, operational obstacles in 2005 survey, such as offshore platforms, have limited the implementation of seismic monitoring acquisition tools in some areas of the field. So, the repeatability of the 4D seismic acquisition campaign held in 2005 is limited in these zones. The factorial cokriging technique was applied to (i) mitigate and filter the noise due to acquisition and (ii) better understand and discriminate the different 4D effects.

After an introduction on the geological and geophysical aspects of the studied area in paragraph 5.1, the adopted seismic interpretation methodology is presented. Special attention is given to the cross-equalization workflow applied to the base and to the monitor seismic vintages, which was implemented in a simultaneous processing approach to minimize the observed acquisition differences. Paragraph 5.2 shows that the 4D seismic signature can be improved by using additional geostatistical treatments which minimize the uncertainties on the seismic based reservoir estimates.

A seismic data subset was selected in the southern part of the field to perform the geostatistical analysis. Due to inherent difficulties to correlate time-series seismic data, the geostatistical processing methodology used in this work involves four different steps:

- (i) a flattening procedure for repositioning the amplitude seismic volumes using a regional stratigraphic marker as a reference;
- (ii) a statistical and geostatistical analysis performed along horizontal planes of each time-slice of the studied seismic volumes;
- (iii) a clustering procedure for regrouping the time-slices based on their spatial and structural characteristics; and
- (iv) a factorial cokriging analysis filtering step aimed at removing unwanted spatial structures associated to noise and non-related to the production.

The regrouping of the time-slices into classes, based on their structural or spatial behavior, was adopted to avoid possible non-stationary effects.

In the following, spatial variability description and analysis is performed by using the variogram and cross-variogram functions. As these tools are becoming more and more familiar in seismic processing procedures, it may be useful to remind the physical meaning of the semivariogram functions. The variogram function is computed as half of the average of the square differences of the seismic amplitude computed over a given spatial domain. From this point of view, one can think indeed in terms of energy distribution, which is by far a much more familiar concept among the geophysicist community.

5.1. Presentation of the Marlim field

5.1.1. Campos Basin overview

With a sedimentary area about 100,000 km², the Campos Basin is considered, to date, as the most important deepwater petroleum system of the Brazilian continental shelf in terms of oil production and reserves, and one of the biggest in the world (Weimer, 2004). Campos Basin is located between the north part of the Rio de Janeiro and the south of Espírito Santo states, and is limited by the Vitoria high to the north, and by the Cabo Frio high to the south, as shown in Figure 5-1.

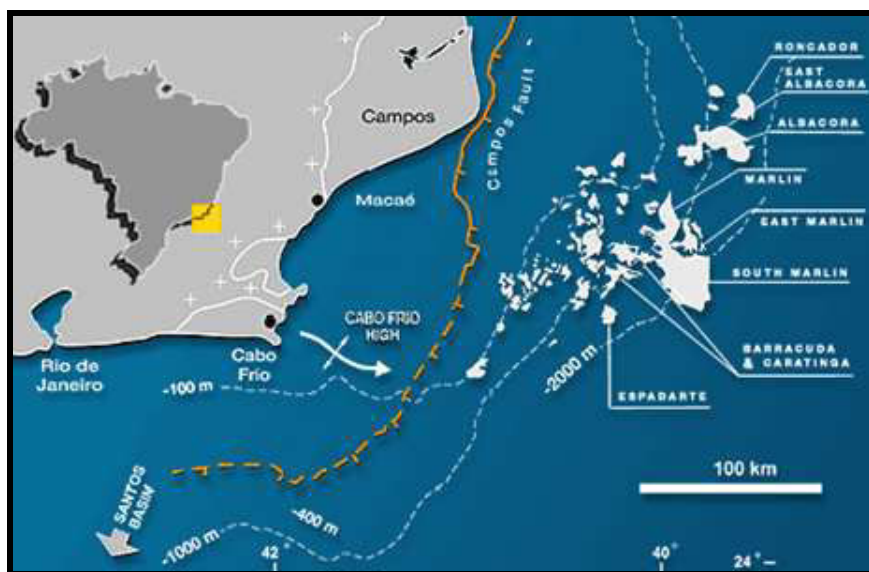


Figure 5-1 - Location map of the most important producing offshore oilfields from Campos Basin, operated by PETROBRAS.

Oil exploration in Campos Basin started in 1974 with the Garoupa field discovery, in a water depth of 120m. Three years later, the oil production started with the Enchova field, producing at that time 10,000 bpd. Until December 2007, more than 2200 oil and gas wells have been drilled in the Campos Basin, leading to an average annual production of 1,475 Mbd of oil and 19,874 Mm³pd of gas. This production corresponds, respectively, to 82% and 46% of the domestic PETROBRAS' oil and gas production (PETROBRAS, 2008).

5.1.2. Geological setting

The Marlim field was discovered by the RJS-219 exploratory well, drilled in 1985 at a water depth of 850 m. This well traversed a section of 70.0 m of unconsolidated turbiditic sandstones from the Oligocene/Miocene reservoir, saturated with 20° API oil. During the development phase of the field, additional fluid sampling showed that the oil gravity in the field varies from 18° to 21° API. The Marlim oil viscosity ranges from 4 and 8 cP, and the saturation pressure is 2.16 MPa (22.00 kgf/cm²), and below the original pressure, equal to 28.14 MPa (equivalent to 287.00 kgf/cm²). The rock characteristics are excellent and the sand is completely unconsolidated. The estimated volume of original oil in-place (STOIIP) is 1,020 million STD m³ (6,416 million STB). The field encompasses an area of 165 km², with water depths ranging from 600 to 1,100 m (Pinto et al., 2001).

The oil accumulation is classified as a combined stratigraphic-structural trap. The reservoir is limited to the west, north and south sides by a stratigraphic pinch-out, whereas a single fault, resulting from the halocinesis of the underlying evaporitic sequence, limits the Marlim reservoir to the east and northeast borders. This fault, which traverses the entire sedimentary column, from the rift sequence to almost the actual seafloor, acted as a conduit for primary oil migration from the rift mega-sequence to the oil bearing reservoirs from the Marine regressive megasequence, as shown in Figure 5-3.

Due to the systematic exploratory activity in the Campos Basin since the late 60's, a large amount of geological and geophysical database was gathered from this oil province, enabling a better comprehension of the geological evolution in the context of the eastern Brazilian margin. Six sedimentary mega-sequences were proposed to describe the stratigraphy, starting in the Late Jurassic up to the Recent (Bruhn, 1998; Bruhn, 2003), as follows: the Continental rift megasequence (R); the Transitional evaporitic megasequence (T); the Shallow carbonate megasequence (SC); the Marine Transgressive megasequence (MT); and the Marine Regressive megasequence (MR). The Oligocene/Miocene turbidite sandstones from the Marlim field reservoir form a part of the Marine regressive megasequence. All these sequences are represented in Figure 5-3.

As described in Bruhn (2003), the turbiditic lobes from Marlim Field form intra-slope accumulations, set in wide depressions developed in response to the eastward tilting of the basin. These structures, in turn, resulted from the downslope gliding of the underlying Aptian evaporites, as shown in Figure 5-3. A post-depositional erosional channel, 1 to 4 km wide, represents a remarkable geological feature that crosses the field from northwest to southeast. This channel was responsible for the erosion of almost 70m of the reservoir original thickness. Additionally, the main orientation of this channel, approximately Northwest-Southeast, suggests that the main dips of the paleo-slope topography did not considerably change when compared to the actual sea-bottom main dip direction. As described by Oliveira et al. (2007), two main sedimentary feeding zones of the Oligocene/Miocene turbidites are suggested in the field, as showed in Figure 5-4. These features, approximately coincident with the main dip direction, and by consequence, to the seismic acquisition inline direction, will demand an additional attention during the geostatistical analysis step.

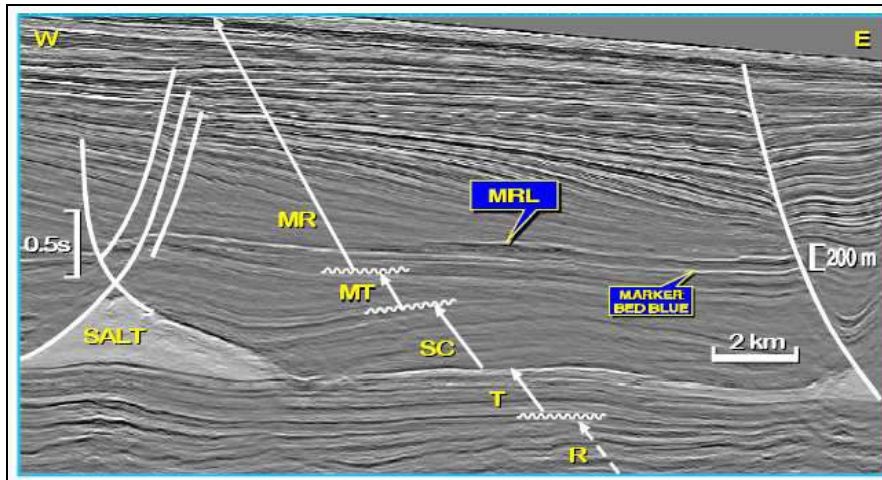


Figure 5-3 –Representative seismic section from Marlim Field, showing the most relevant sedimentary megasequences from the Campos Basin stratigraphy (from Bruhn, 1998). Seismic reflections that correspond to the reservoir and to the regional geological marker are indicated in the figure by MRL and Marker Bed Blue, respectively.

Concerning the oil production data, the first oil from Marlim Field was produced in 1991 from a non-permanent system, conceived to evaluate this initial oil production phase. Presently, an average oil production of 390,000 bpd (data from 2007) is maintained by eighty-one (81) producers. The peak of oil production, of 615,000 bpd, was reached in 2002. Water-flooding was considered the most feasible method for reservoir pressure maintenance and for increasing the recovery factor in Marlim Field. The availability of the sea-water, as well as favorable reservoir properties, such as good overall lateral continuity and small amount of gas, made the water-flooding the best drive choice in terms of secondary recovery mechanism. A total number of forty-four (44) injector wells were drilled in the field to guarantee the water injection program, started in 1994.

5.1.3. Seismic Acquisition Parameters

At the time of the Marlim field discovery, in 1985, only bi-dimensional (2D) seismic data were available. Since then, a set of three three-dimensional (3D) seismic

campaigns were shot over the field at different calendar times, thus representing different stages of the production life of the field.

The first 3D seismic campaign was shot in 1986, just after the field discovery. This seismic data was parameterized aiming at improving the external field geometry. The second seismic survey in Marlim Field has been shot in 1997, being designed not only to deliver a better description of external geometry of the reservoir limits, but also to better understand the internal architecture of this turbiditic sequence.

Covering an area of 1520 km², and encompassing the Marlim, the Marlim East and the Marlim South fields, the 2005 seismic survey was carried out with 13 permanent obstacles (production units, rigs, etc) and 40 temporary obstacles (Johann et al., 2006). The selected technology to fulfill the repeatability requirements for this monitor survey was the Q-Marine. This survey was primarily designed to monitor the fluid displacement in the reservoir as a response to the chosen enhanced oil recovery scheme, which is based on a water-flooding drive mechanism (Pinto et al., 2001; Shecaira et al., 2002). The areal limits of the seismic surveys registered in Marlim field are represented in Figure 5-4. In this figure, the external green box corresponds to the first 3D survey shot in the field, in 1986, just after the field discovery. The red box corresponds to the limits of the surveys shot in 1997 and 2005, which covered the same surface.

The new seismic acquisition survey parameters were defined taking into account a commitment between the new technologies and developments available in the seismic acquisition industry and the seismic repeatability requirements, considering the 1997 seismic data (Johann et al., 2006). Table 5-1 summarizes the most relevant seismic acquisition parameters adopted for the three seismic campaigns shot over the Marlim field.

Only the seismic datasets shot in 1997 and 2005 are considered in this work, and are referred to as S97 and S05 datasets, respectively. Despite the fact that S97 is the second seismic dataset shot in this field, it will be considered as the base survey, whereas the S05 will be referred as the monitor.

It is worth mentioning that the registered trace density has exponentially increased when comparing the three Marlim field surveys. The Q-survey, shot in 2005, is 9 times denser than the 1997 survey, and 64 times than the 1986 survey, which would potentially benefit the seismic data imaging.

Table 5-1 – Seismic acquisition parameters from seismic campaigns recorded in the Marlim field.

Year	1986	1997 (S97)	2005 (S05)
Objective	Exploration	Reservoir Characterization	Monitoring
Technology	Conventional	Conventional	Q-Marine ®
Area coverage	900 km ²	720 km ²	1,520 km ²
Number of streamers	1	6	10
Offsets near-far (m)	0-213-3,188	0-148-3,535.5	0-140-6,000
Number of channels/cable	120	288	1920
Shot interval (m)	25	25	18,5
Receiver interval (m)	25	12.5	3.125
Distance between cables (m)	75	50	50
Sampling rate (ms)	4	1	2
Cell size (m) inline x crossline directions	25 × 75	12.5 × 25	3.125 × 12.5
Inline direction (azimuth, in degrees)	90 (W-E)	123 (NW-SE)	123 (NW-SE)
Trace density (number of traces x 10³ /km²)	32	230	2,048

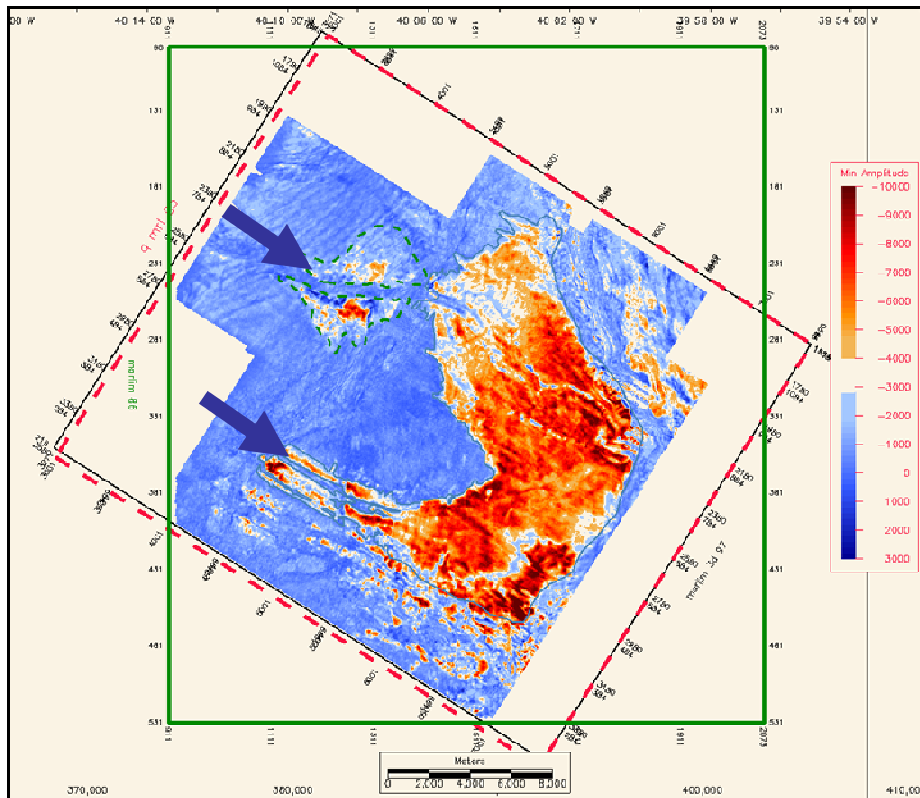


Figure 5-4- Amplitude map representing the Marlim reservoir with the external limits of the three seismic surveys.

5.1.4. Seismic processing issues

The Marlim field seismic datasets considered in this study consist of two sets of migrated angle-stacked data from the base S97 and from the monitor S05 seismic surveys. These surveys were processed following a cross-equalization methodology, in such a way that most of the discrepancies due to different acquisition schemes could potentially be attenuated. To achieve these goals, it was necessary to reprocess both the datasets, starting from the pre-stack phase, and the individual processing sequences applied to each survey, so that they can be kept as similar as possible.

One specific processing step, which is likely to impact on the final time-lapse analysis, is the post-stack local matching filter. As described by Nickel and Sonneland

(1999), this algorithm assumes that the monitor data is a displaced version of the base survey, also called the *reference cube*. The displacement estimation is performed using a multi-resolution gradient technique, assuming two main hypotheses (i) the amplitude of the displaced voxel remains constant; and (ii) the displacement does not vary significantly for a given neighborhood.

In the present study, this local matching filter, referred to as Non-rigid Matching filter (U.S. Patent 6574563) was applied to the migrated full-stack and to the partial angle-stack seismic volumes (comprising, thus, five stacks per vintage), followed a non-conventional approach. The filter was implemented as follows:

- Each of the five S05 stacks (one full-stack and four partial angle-stacks) was matched to the equivalent S97 angle-stack. After this step, all gathers from the monitor vintage were at the time of the corresponding base vintage ;
- Each angle-stack from the base survey S97 was matched to the S97 full-stack. Doing so, all S97 partial angle-gathers were displaced to the S97 full-stack times; and
- Applying the previous time shifts, computed for each S97 partial-stack, to the corresponding S05 partial-stacks.

Examples of the resulting time-shifts from the matching procedure applied to the full-stack S05 and S97 data are shown in Figure 5-5. In this figure, the four maps from (a) to (d), correspond to the following horizons: (a) W Marker; (b) MRL Top; (c) MRL Bottom; and (d) Blue Marker. Horizons (a) and (d) correspond to geological markers, situated above and below the reservoir interval, respectively. A crossline seismic section showing their relative position is displayed in Figure 5-8. Map (a) shows the time-shift values extracted from the topmost W Marker horizon that lays at approximately 800 ms above the reservoir time interval. In this map, only minor time-shifts are observed, with an average value close to zero. A homogenous distribution of these low valued time-shifts is observed, as indicated by the predominant green color. However, alignments of higher

time-shifts are observed in the south and north part of the map, occurring in stripes parallel to the inline direction, where it reaches the maximum absolute shift of 4 ms. These zones are coincident with those shown in Figure 5-9, and are associated to the presence of operational obstacles at the surface.

The three other maps from Figure 5-5, from (b), (c) and (d) show a very similar time-shift distribution. The observed average time-shift is small, close to 2ms – or half the 4 ms time-sampling interval. In average, the time-shift values are bigger than those observed in (a). In this interval, values as high as 12 ms, or 3 time-samples, are detected but very locally. These maximum values are surrounded by a zone of intermediate time-shifts values, displaying a clear orientation parallel to the inline direction. The spatial distribution of these anomalous time-shifted values structures are in close agreement with those areas of influence restricted seismic data quality due to the presence of platforms/other obstacles during the S05 seismic acquisition campaign.

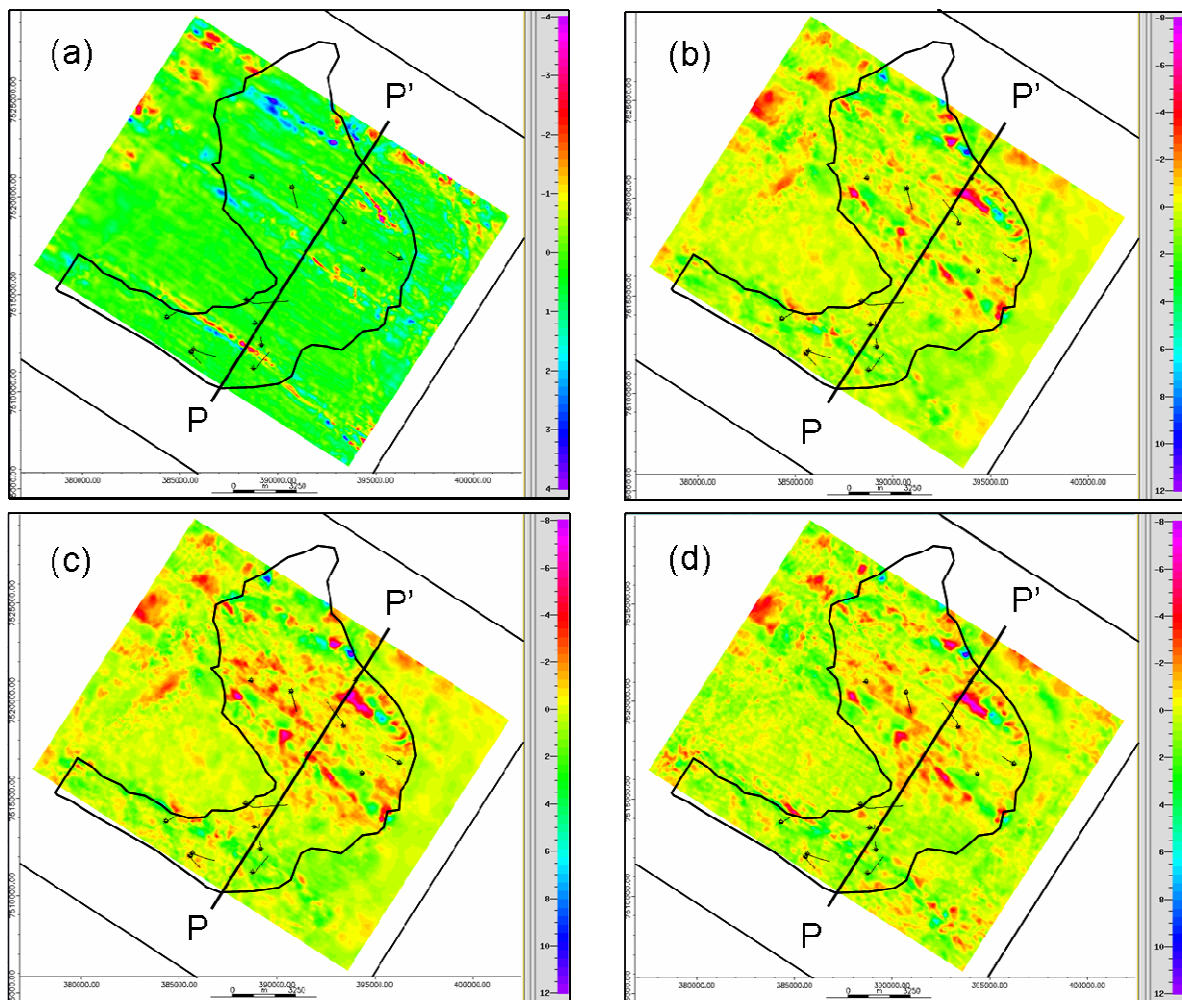


Figure 5-5 - Matching filter resulting time-shifts, extracted from crossline PP' as shown in Figure 5-8, for different horizons: (a) W Marker, above the reservoir; (b) MRL Top reservoir top; (c) MRL Bottom reservoir bottom; and (d) Blue Marker.

During all the steps of the cross-equalization seismic processing sequence applied, the original 2ms acquisition sampling interval was used. At the end, five angle-stacked migrated data from both base and monitor surveys are available, at a 4ms sampling rate, and comprising the following angle-stacks: full-stack ; 0° to 10° stacked data; 10° to 20° stacked data; 20° to 30° stacked data; and 30° to 40° stacked data. A scheme of the cross-equalization processing flow is presented in Figure 5-6.

A schematic view of the cell sizes before and after the cross-equalization processing is presented in Figure 5-7, where the inline direction coincides with the N123° direction.

The final bin sizes for the S05 and S97 dataset are eight and four times bigger, respectively, when compared to the original acquisition bins.

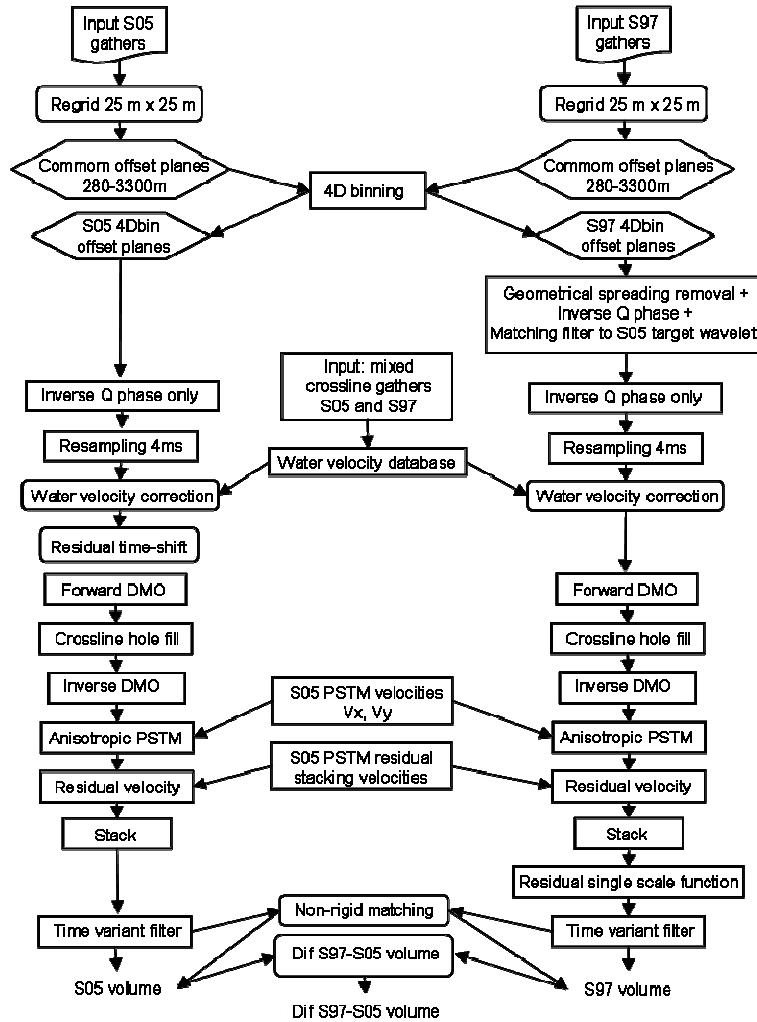


Figure 5-6 – Cross-equalization processing sequence applied to the S97 and S05 seismic datasets. (modified from PETROBRAS internal report, 2006).

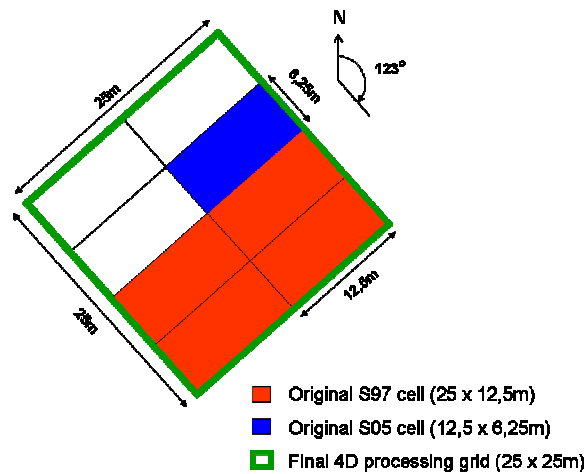


Figure 5-7 - Schematic representation of the seismic cell size before (red for S97 and blue for S97) and after the cross-equalization processing (green). In both S97 and S05 surveys the N123 direction coincides with the Inline direction.

5.1.5. Seismic Interpretation

A description of the seismic interpretation strategy is presented in this section, as well as the resulting amplitude maps used in all the present studies concerning the Marlim field.

Seismic Data Quality

The 3D seismic data from Marlim field have, in general, a good quality, as shown in Figure 5-8. A medium to high signal-to-noise ratio is observed, despite its low frequency content and the presence of strong multiple events associated to the water bottom reverberations. However, the presence of operational obstacles, such as rigs, platforms, etc, during the acquisition of the S05 monitor survey imposed a loss in seismic data quality in some areas of the field, which requested an additional processing effort to minimize these acquisition constraints.

Horizons definition

The S05 monitor seismic volume was the reference volume for the automatic picking procedure. The interpretation work resulted in 14 horizons that were picked on the cross-equalized datasets S05 and S97, named as: Seabottom (SB); W Marker (RM1); Marlim reservoir top (MRLTop); Marlim reservoir bottom (MRLBot); Blue marker top (RM2); Superior Cretaceous top (KS); and Salt top (ST). In Figure 5-8, cross-line 6005 from the S05 survey displays the previous listed horizons, from top to bottom, starting from the topmost SB horizon.

The horizons MRL Top and MRL Bottom correspond, respectively, to the reservoir top (green) and bottom (yellow). The other five horizons, which extend to an area much larger than the reservoir limits, were considered as these surfaces represent important geological or geophysical references in the Campos Basin, as well as due to their seismic character in terms of strength and continuity.

Regarding the non-reservoir horizons, two of them (SB and RM1), are located above the reservoir level, where no direct production effects are expected. However, the three horizons positioned below the reservoir (RM2, KS and ST), may present anomalous time-shift effects - pull-up and/or push-down - due to the reservoir response to the oil production, even if no fluid substitution or 4D effects are expected to occur at these intervals.

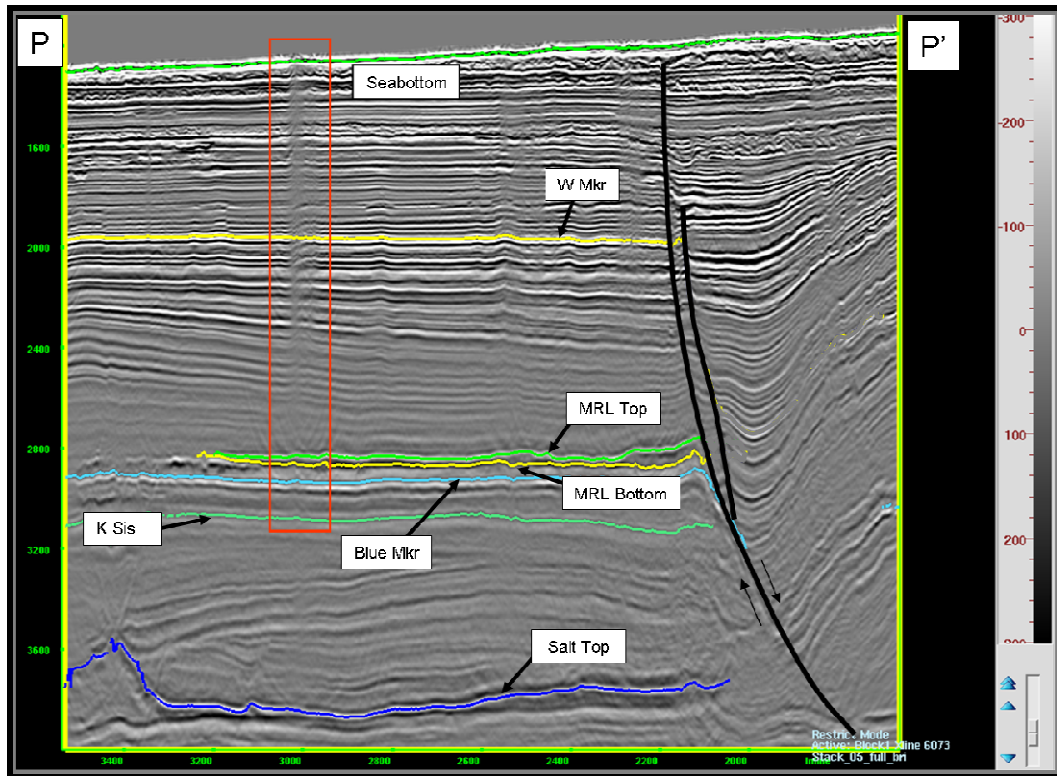


Figure 5-8 - Cross-line seismic section (XL 6073) extracted from the S05 volume, showing the interpreted horizons. In black, the segments of the main fault that limits the reservoir to the east and the northeast. Bad seismic quality zones due to the presence of obstacles represented by a red rectangle

Interpretation Methodology and results

The seismic interpretation phase was performed using the Paradigm[®] volumetric interpretation software. Depending on the observed seismic quality, different interpretation strategies were used, and both manual and automatic picking approaches were considered. In terms of automatic tracking approach, the application uses a waveform tracker that is based on a technology patented by TotalFinaElf. Traces in the vicinity of a given model trace – *seed traces* - are cross-correlated with this model trace, and accepted or rejected depending on a set of propagation criteria defined by the user. In this approach, acceptance means that the new trace actually became a model trace, and the propagation continues until all new traces are rejected. These propagation criteria are:

Type of event (pick, trough, or zero) to be mapped;

Time-window to proceed with cross-correlation, that may be symmetric or asymmetric regarding the seed position;

Threshold or minimum accepted correlation value.

The resulting interpreted maps will depend strongly on the seismic quality and on the interpretation strategy: the *seed number*, being small in areas with high signal/noise ratio, to a high number of traces in noisy areas. A strategy to interpret poor quality seismic data should involve the use of smaller investigation volumes, as well as extensive testing of all cross-correlation parameters prior to picking horizons. By performing these tests, it is possible to define the vertical time window that better reproduces the seismic character to be tracked, as well as the number of neighboring traces, where learning samples were selected according to the reservoir character response. Further details on the volumetric interpretation technique can be found in the Epos software manual (Epos Reference Manual, 2007).

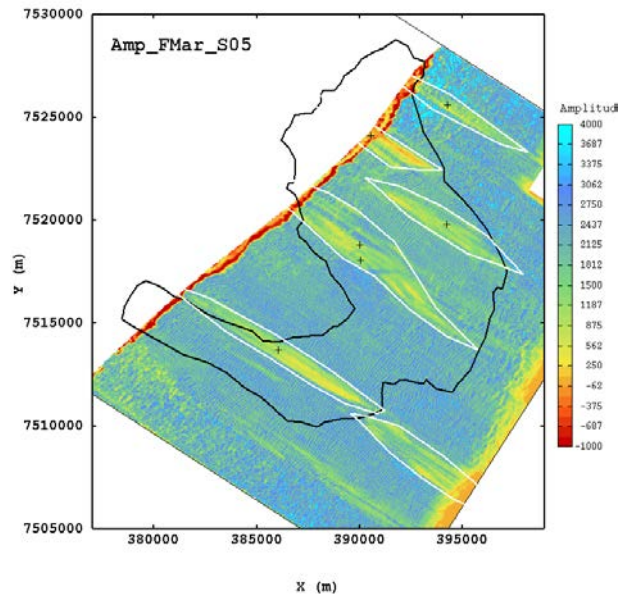


Figure 5-9 – Seabottom amplitude map, extracted from the S05 monitor survey. The white polygons represent the area of influence of the operational obstacles present at the time of the S05 acquisition campaign, and the impact on the final cross-equalized time-lapse data.

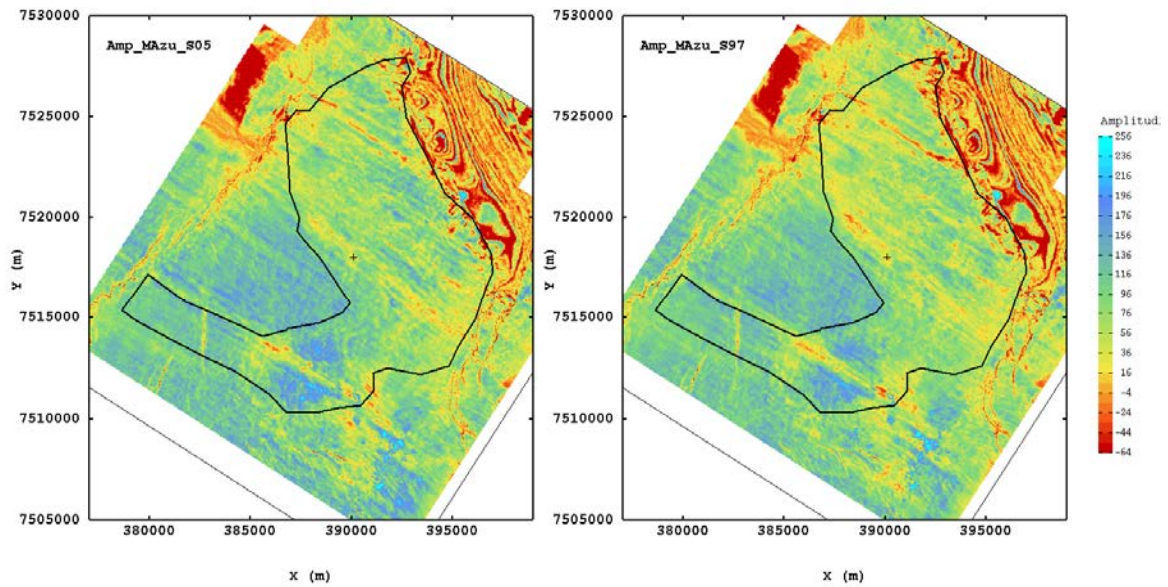


Figure 5-10 - Blue marker top reflector amplitude maps of the S05 monitor (left) and S97 base (right) surveys.

In Figure 5-10, the black polygon represents the Marlim reservoir limits. Seismically, the Blue marker is associated to a positive reflection coefficient, so most of the negative valued points are mainly due to acquisition artefacts.

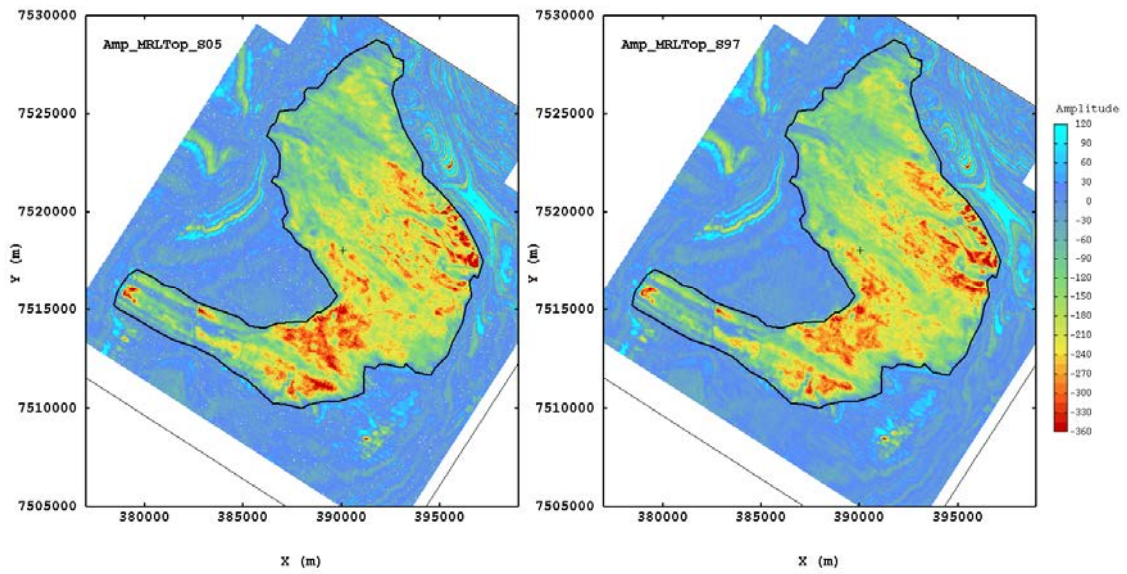


Figure 5-11 – Amplitude maps from Marlim top reflector, with S05 monitor survey data on the left and S97 base survey on the right. The black polygon represents the Marlim reservoir limits.

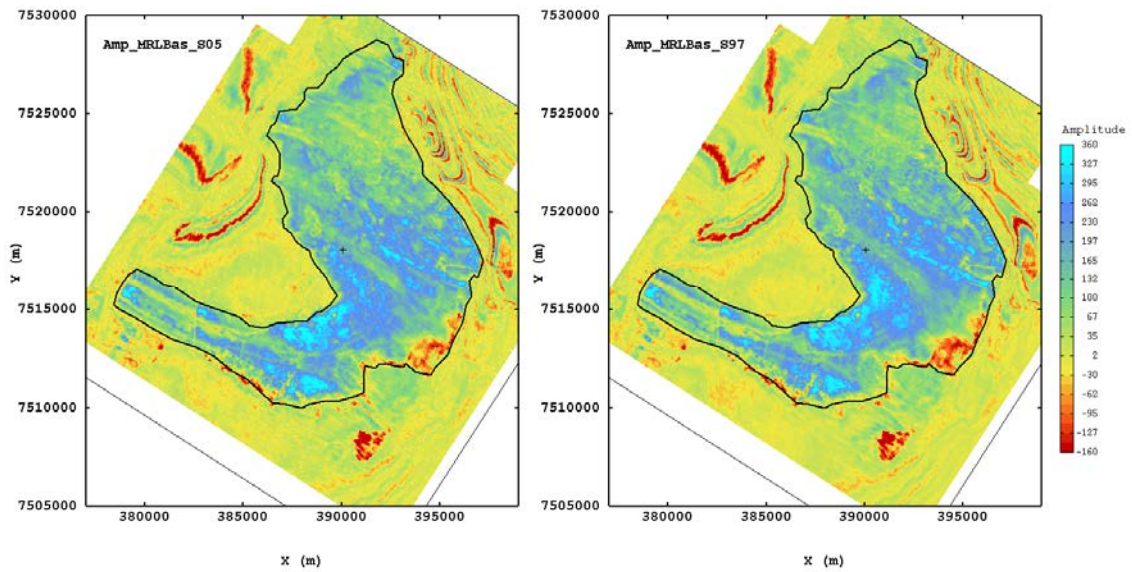


Figure 5-12 – Amplitude maps from Marlim bottom horizon, with S05 monitor (left) and S97 base (right) surveys.

Despite the overall similarity – which is strongly desirable when dealing with different seismic acquisitions vintages – differences in amplitude values are likely to be an amplitude response to the oil production.

5.2. Geostatistical Analysis

The multivariate factorial cokriging filtering technique, as presented in Chapter 3 - of this thesis, has been applied to the Marlim field, Campos Basin. The time-lapse study was carried out using two vintages, the base survey S97, shot in 1997 and the monitor, S05, in 2005. A detailed description of the acquisition and processing issues can be found in the previous sections of this chapter.

Even after a cautious cross-equalization processing sequence aimed at minimizing the discrepancies frequently associated to different seismic acquisition and processing parameters, the analysis of the reservoir and of the non-reservoir interval have showed that spatial structures exhibiting non-geological patterns were recognized on both volumes, and should be removed from the initial seismic data to enhance the 4D signature.

A subset of the seismic dataset in the south area of the field was selected to perform the geostatistical analysis. Due to inherent difficulties to correlate time-series variograms, the adopted geostatistical analysis strategy involved four different steps:

- (i) *repositioning* the amplitude seismic volumes using a regional stratigraphic marker as a reference for a flattening procedure;
- (ii) *performing* a statistical and geostatistical analysis, in the horizontal plane, on every time-slice of the considered flattened seismic volume;
- (iii) *regrouping* the slices based on their structural characteristics;
- (iv) *filtering* those unwanted spatial structures associated to noise and non-related to the production.

The regrouping of the time-slices into classes, based on their structural or variograms behavior was adopted to avoid possible non-stationary effects.

This study was carried out using a subset of the full-stack seismic data traces from two different campaigns acquired over the Marlim field, as previously described, the S05 and S97 datasets, and involved the following steps:

- a comprehensive *geostatistical analysis* using both the amplitude maps and the full-stack seismic cubes;
- the definition of the *main spatial structures* present in the data: a special attention will be devoted to the analyses of the "natural" spatial structures identified in the flattened amplitude maps, and the identification of potential physical processes that could explain these interpreted data;
- the application of the *Factorial Cokriging* technique;
- the *interpretation of the resulting factors* in terms of potential 4D effects, or to any other type of seismic event, such as noise, regardless of its origin (seismic acquisition or processing);
- the *filtering* of those unwanted factors;
- the *analysis* of the results.

5.2.1. Volumetric Analysis

Selection of sub-volume

The original seismic datasets from the Marlim field represented a huge volume of data to be processed, equivalent to hundreds of terabytes at the seismic pre-stack processing

step. In this study, we were interested on evaluating a methodology suitable to the time-lapse problem, but that could be applied over the entire reservoir, as well as to other equivalent reservoirs. Therefore, a representative sub-volume from the initial Marlim field volume was selected, which spatial and temporal limits are presented in Table 5-2.

Table 5-2 – Limits of the study area. In brackets, the original Marlim seismic dataset limits.

	Minimum	Maximum	total
Inline	2,701 (1,661)	3,231 (3,541)	266 (941)
Crossline	4,401 (2,957)	7,001 (7,477)	651 (1,131)
time (ms)	2,500 (0)	3,100 (6,000)	600 (6,000)

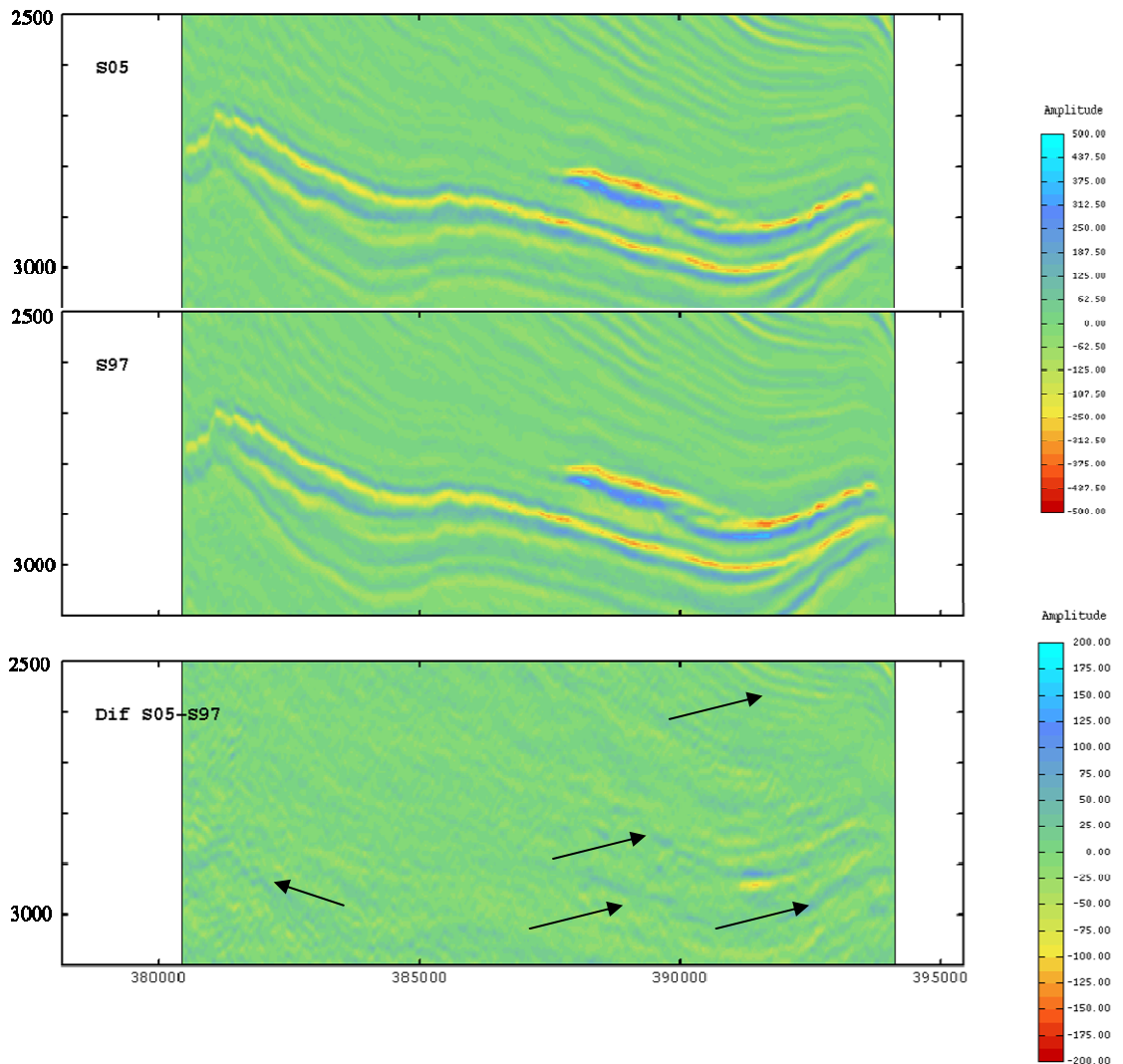


Figure 5-13 – Vertical seismic amplitude section from the inline direction. From top to bottom, S05 monitor survey, S97 base survey, and the difference DifS05-S97 (vertical scale in ms and horizontal in m). The difference amplitude section shows events exhibiting a spatial continuity due to the non-optimality repeatability conditions between base and monitor surveys.

A representative seismic amplitude inline was extracted from the seismic volumes S05, S97 and difference Dif S05-S97, as shown in Figure 5-13. Despite the remarkable similarity observed between the S05 and the S97 data, achieved after a careful cross-equalization processing sequence, one can easily detect numerous seismic events not directly associated with the oil production. These events, observed at the difference DifS05-S97 volume as indicated by the black arrows, may be recognized at various time levels. They exhibit a spatial continuity due to the non-optimality repeatability conditions between

the base S97 and the monitor S05 surveys, and maybe related both to the seismic acquisitions and to the processing.

Sub-volume quality control

An initial quality control of the selected sub-volume from the Marlim field involved a structural analysis to characterize its spatial variability. This analysis was performed in the original XYZ seismic grid, taking the horizontal inline-crossline planes at every time sample to compute a representative 3D variogram. The following parameters were considered:

- Horizontal lag distance: 50m, for both inline and crossline directions, equivalent to twice the original 25×25m seismic grid;
- Vertical lag: 8ms (TWT), equivalent to twice the time-sampling interval; and
- Maximum investigated distances: 8,000m and 3,250m, in the inline and crossline directions, respectively; and 300ms (TWT) in the time domain;

These distances correspond to half of the dimension of each axis X, Y and Z (T) of the investigated seismic volume. The variograms were grouped by inline, crossline and time direction. These computations also included the variograms of the variable S97_NW. This variable corresponds to the seismic dataset from S97 base survey campaign, where no warping matching filter to the S05 was applied, as shown in the seismic processing flow diagram from Figure 5-6. Comparison of the variograms from S97 and S97_NW shows that the applied matching filter procedure tends to decrease the total variance of the data.

The inline and crossline average variograms, showed in Figure 5-14 and Figure 5-15, were computed for the complete seismic sub volume. A strong similarity of the variogram functions are observed for the three investigated datasets, the S05, S97 and S97_NW, where the last one corresponds to the non-warped S97 dataset.

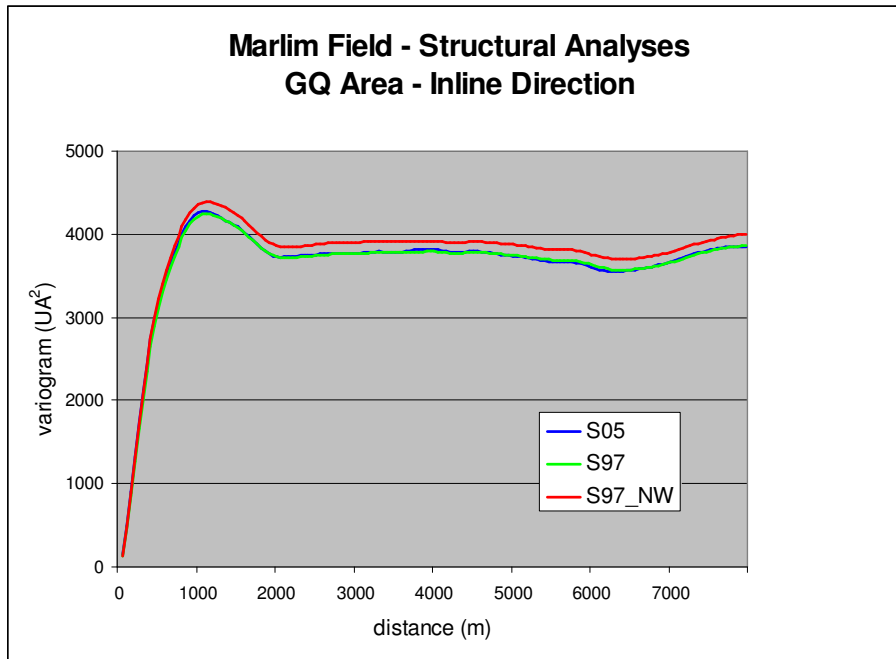


Figure 5-14 – Experimental variograms from Marlim field GQ area, showing the variability in the inline direction, coincident with the main dip direction. S05 and S97 surveys, corresponding to the blue and green lines, showing a similar behavior. S97_NW data (in red) where no matching filter was applied with higher variability.

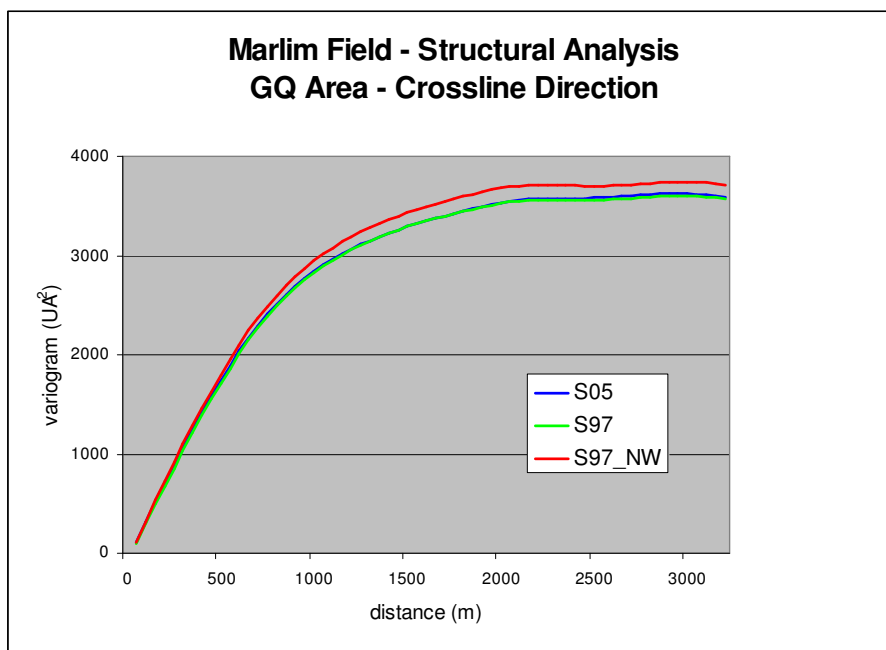


Figure 5-15 - Same as Figure 5-14, for the Crossline direction, and orthogonal to the main dip direction.

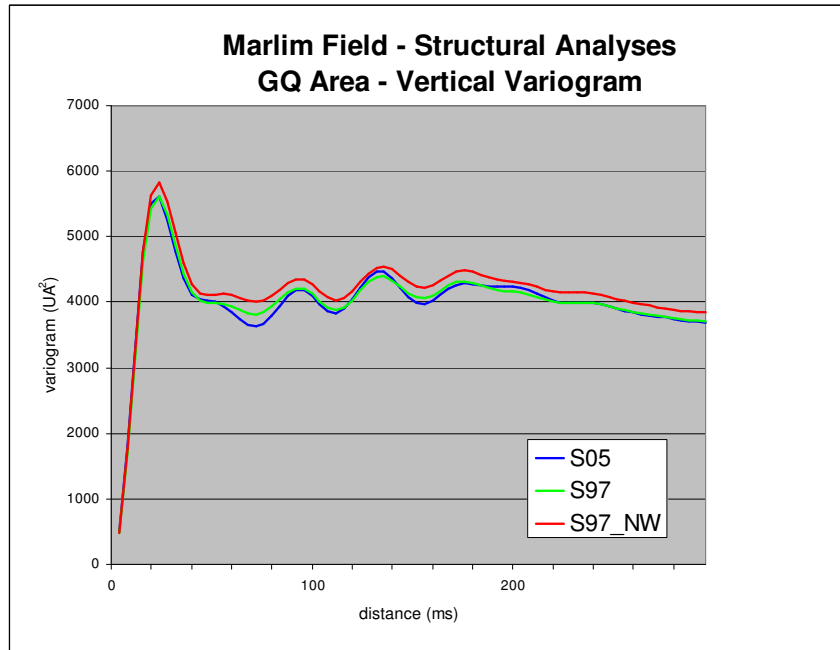


Figure 5-16 – Same as Figure 5-14, along the vertical direction (time axis).

Considering these variograms as representative of the studied sub-volume interval, it can be concluded that:

- the average inline and crossline variograms computed on the vintages S97 and S05 are identical for all inspected ranges;
- when analyzing only the short ranges, no differences are observed on the three groups of the computed variograms;
- the non-rigid matching filter applied to the S97 dataset tends to decrease the total amplitude variability by a factor of less than 5%, and mainly for the long ranges;

5.2.2. Flattening seismic volumes

Flattening a seismic volume using a reference horizon is a very useful interpretation procedure. By removing the structural component, it is possible to better understand depositional effects, lateral correlations between reservoir facies and to establish a pattern of the internal reservoir architecture.

Another advantage of using flattened volumes is to reduce the amount of data to be analyzed and/or processed, by suppressing the structural component. In the Marlim field, one important regional marker, known as Blue Marker (RM2) is suitable to be used as a flattening reference, as it represents a condensate zone that corresponds to a maximum flooding surface. In terms of lithology, this interval corresponds to a calcilutite, usually exhibiting a good seismic signature for both top and bottom interfaces.

In Figure 5-17, a representative seismic section of the studied time window is presented. This window is limited by the regional marker RM2 at the bottom, and by a shifted version of this horizon, referred to as RM2', at the top, thus defining a constant time window of 200ms surrounding the Marlim reservoir interval.

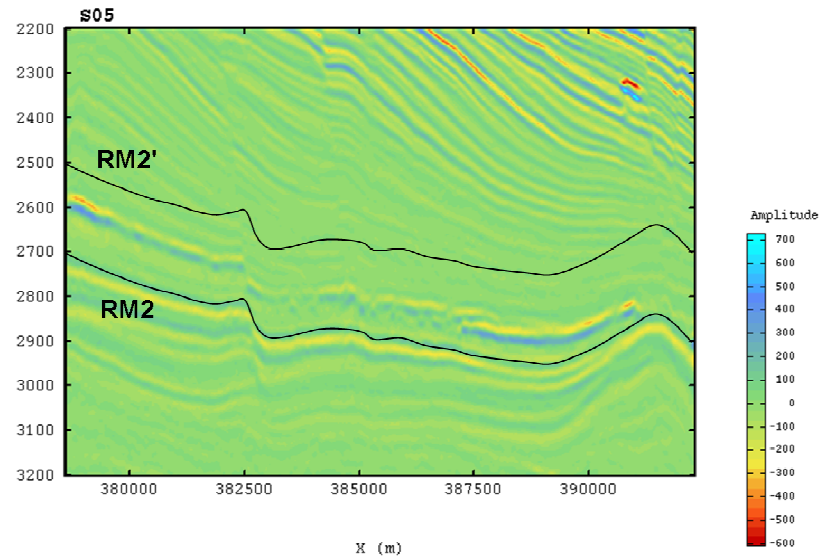


Figure 5-17 - Inline seismic section from the Marlim field. The RM2 and RM2' horizons represent the inferior and superior limits of the window of interest. Vertical and horizontal scales are in milliseconds (TWT) and meters, respectively.

The result of the flattening procedure is shown in Figure 5-18. The anomalous amplitude values in red and blue, correspond respectively, to the reservoir top and bottom. This procedure reduces the number of samples to be processed during the geostatistical analysis because the method can be applied on this restricted window compared to the initial 1000ms time window. Another technique frequently used could be to compute the variograms following isotime curves, as available in the gOcad software.

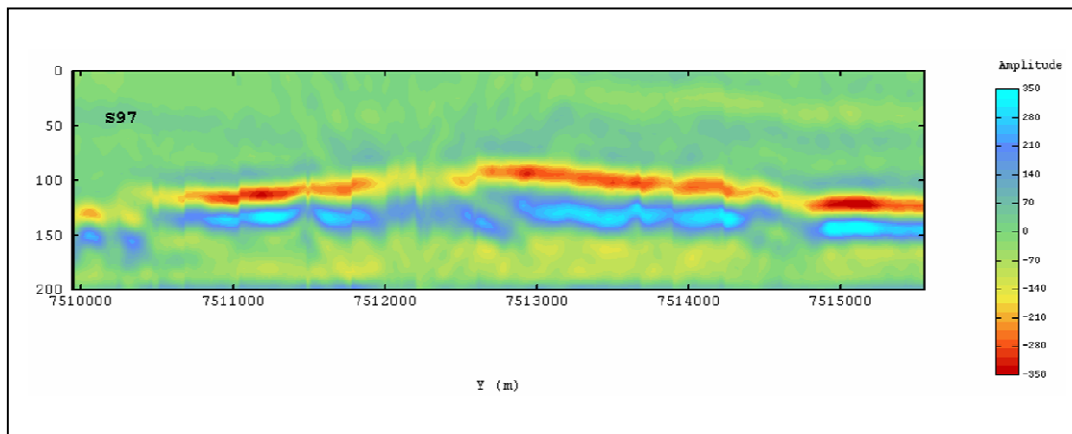


Figure 5-18 – Flattened amplitude seismic S05 survey section using the RM2 horizon as reference bottom (vertical time scale in milliseconds (TWT)).

Geologically, this 200ms interval of seismic data, starting from the Blue Marker, consists in a sequence of pelitic sedimentation from the initial phase of deposition of the thick regressive marine sequence, as shown in Figure 5-8 and Figure 5-19. This marine sequence, which sedimentation started at the Cretaceous, is still under deposition (Bruhn, 1998),

The choice of the Blue Marker as the flattening reference was a trade-off between a seismic horizon that could be identified and tracked over the entire area of interest and the one that would better explain, after flattening the data, the stratigraphy of the Marlim reservoir as close as possible at the time of the deposition, minimizing all post-depositional effects.

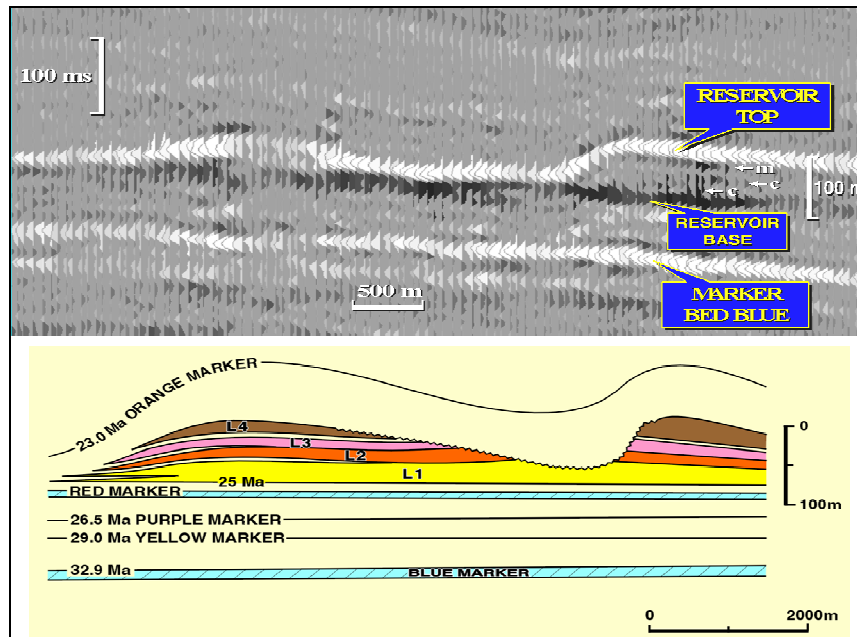


Figure 5-19 – Inline seismic profile (top) and the correspondent geological schematic section (bottom). The Blue Marker displays a good seismic signature, which is not observed in other important geological markers from the Campos Basin (from Bruhn, 1998).

The Blue marker is related to a geological phenomenon of regional extension, occurring widely in the Campos Basin. It is recognized on both seismic and well data, being characterized by low gamma-ray values, high resistivity and small transit-time values in sonic logs. Analyses of cores, well logs and lateral sampling suggest a calcareous origin. Biostratigraphic data showed that the deposition in this interval corresponds to the early times during the late Oligocene, in a superior to medium bathyal depths, and corresponds to the highest sea-level position during the Tertiary (Gamboa et al., 1986).

5.2.3. Statistical Analysis of the flattened data

A comprehensive statistical description of the all fifty time-slices, corresponding to the 200ms flattened window (with a time interval between slices of 4 ms) resulting from the adopted flattening procedure is presented in Table 5-3. The superior limit of the seismic

sub-volume is represented by time-slice 01 (TS01), whereas the bottom by the time-slice 50 (TS50). This bottommost slice corresponds to the Blue Marker regional horizon, and is represented by a strong positive amplitude value. The mean, standard deviation and variance values computed for each time-slice and for each vintage are shown in Table 5-3 , and are presented graphically in Figure 5-20 and Figure 5-21, thus representing the mean and variance traces. Analyses of these data show that:

- the mean seismic amplitude values over the 200ms flattened window are similar and comparable in terms of magnitude and sign when calculated on the S97 and S05 volumes, except in the first ten uppermost time-slices, where the amplitude values corresponding to the S05 data are, locally, five times more negative than those of S97;
- on the other time-slices, the mean seismic amplitudes are either greater or smaller when comparing the S97 and S05 campaigns, and the magnitude of the differences is of the order of 10%;
- the variance curves calculated on the entire 200ms window, covering all time-slices, show that the variability of the seismic amplitudes values of the S05 campaign is smaller than that of the S97 by an average factor of 11%, in the deeper part of the reservoir (from time-slices 29 to 44). However, it is greater than the S97 campaign values in the 20 to 29 time-slices interval by a factor of 7%. These differences can be attributed to either the seismic acquisition or/and to an exploitation effect of the reservoir.

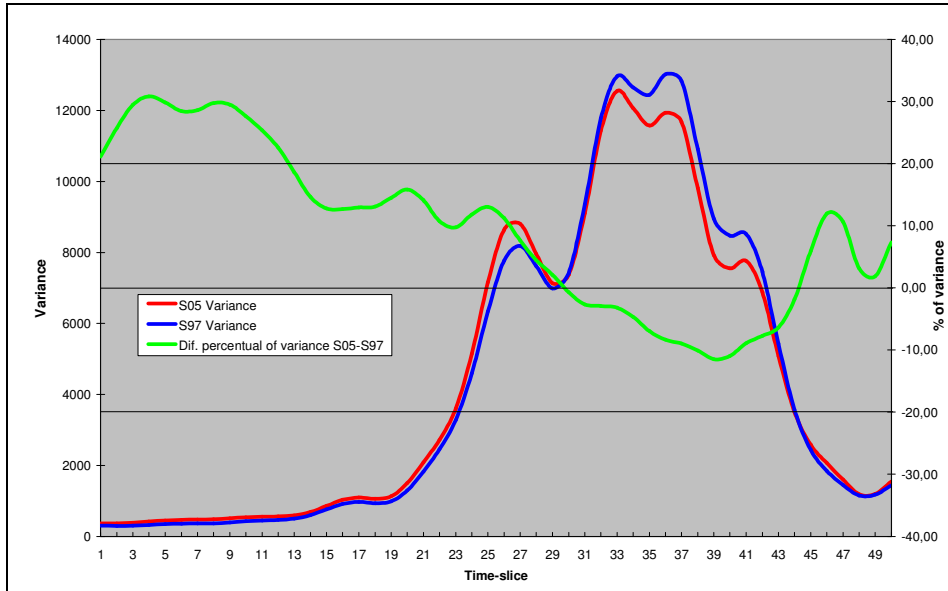


Figure 5-20 – Average variance values computed for each time-slice. Green curve represents the variance difference (%) relative to S97 data. S05 variance values are smaller than S97 only between time-slices TS30 and TS44.

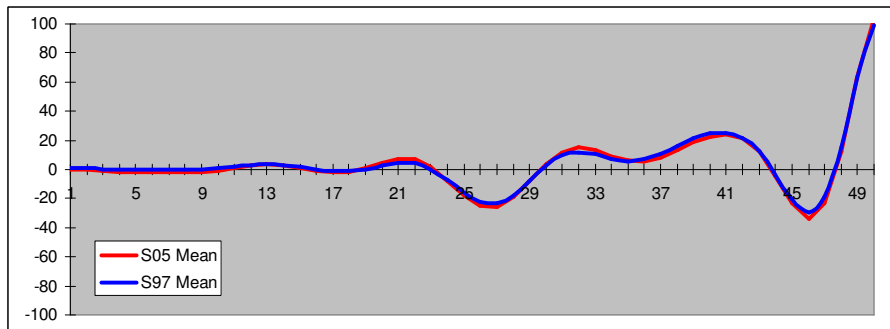


Figure 5-21 - Same as in Figure 5-20, for the mean amplitude values.

Table 5-3 - Statistical description of flattened time-slices.

Time-slice	S05			S97		
	Mean	Std. Dev.	Variance	Mean	Std. Dev.	Variance
1	0.3	19.16	367.2	0.93	17.41	303.16
2	-0.21	19.26	370.81	0.7	17.17	294.89
3	-0.85	19.67	386.76	0.29	17.28	298.72
4	-1.35	20.43	417.2	-0.1	17.86	318.84
5	-1.63	21.19	448.84	-0.32	18.59	345.59
6	-1.79	21.57	465.23	-0.37	19.03	362.11
7	-1.91	21.66	469.29	-0.31	19.1	364.85
8	-1.91	21.92	480.28	-0.11	19.24	370.1
9	-1.52	22.56	509.12	0.31	19.83	393.04
10	-0.52	23.3	542.88	1.05	20.62	425.23
11	1	23.67	560.15	2.02	21.14	446.77
12	2.5	23.77	564.79	2.9	21.46	460.73
13	3.27	24.36	593.35	3.26	22.36	500.14
14	2.82	26.22	687.6	2.81	24.49	599.74
15	1.23	29.26	856.39	1.58	27.55	759.25
16	-0.73	32.1	1 030.39	0	30.24	914.21
17	-1.96	33.12	1 096.68	-1.2	31.16	970.85
18	-1.45	32.54	1 059.01	-1.28	30.6	936.36
19	1.08	33.6	1 128.87	0.12	31.4	985.88
20	4.75	38.72	1 499.44	2.53	35.97	1 294.11
21	7.56	45.64	2 083.04	4.53	42.73	1 825.46
22	7.06	52.12	2 716.29	4.17	49.52	2 452.3
23	1.77	60.01	3 601.6	0.07	57.28	3 281.57
24	-7.65	71.73	5 145.51	-7.5	67.83	4 601.11
25	-18.14	84.6	7 157.24	-16.17	79.57	6 332.08
26	-25.32	92.96	8 641.94	-22.35	88.14	7 769.26
27	-25.8	93.84	8 806.13	-23.04	90.45	8 182.03
28	-19.16	89.21	7 957.71	-17.49	87.29	7 618.98
29	-7.98	84.46	7 132.9	-7.77	83.59	6 987.91
30	3.61	85.87	7 373.39	2.35	86.16	7 424.16
31	11.92	95.43	9 107.76	9.39	96.73	9 357.5
32	14.99	106.93	11 433.69	11.77	108.52	11 777.4
33	13.29	112.02	12 548.83	10.3	113.85	12 961.98
34	9.31	109.83	12 063.45	7.4	112.48	12 651.99
35	6.05	107.59	11 575.06	5.68	111.55	12 442.52
36	5.45	109.25	11 935.52	6.71	114.11	13 021.4
37	8.13	108.06	11 676.12	10.52	113.24	12 824.06
38	13.15	99.06	9 813.17	15.84	104.46	10 912.85
39	18.45	89.01	7 923.22	21.01	94.6	8 948.35
40	22.52	86.9	7 551.43	24.6	92.08	8 479.46
41	24.22	88.09	7 760.42	25.37	92.3	8 518.39
42	21.58	82.95	6 880.63	21.77	86.34	7 455.02
43	12.22	71.26	5 077.87	12.1	73.64	5 422.56
44	-4.33	59.14	3 497.94	-3.56	59.7	3 564.48
45	-23.38	50.79	2 580.03	-20.64	49.35	2 435.11
46	-34.05	45.48	2 068.42	-29.33	42.98	1 847.62
47	-23.59	40.02	1 601.6	-18.67	38.05	1 447.78
48	12.7	34.48	1 189.2	15.29	33.96	1 153.06
49	63.4	34.61	1 197.62	62.31	34.29	1 175.46
50	103.46	39.27	1 542.15	98.79	37.9	1 436.32

5.2.4. Grouping the amplitude time-slices

In order to reduce the amount of data to be processed in the geostatistical analysis and estimation phases, the 200 ms time window composed of 50 time-slices was split into seven time-slice groups. This classification was mainly based on the behavior of the first two moments, the mean amplitude value and the associated variance, computed for each time-slice and presented as an average value by amplitude slice.

A problem to be considered when performing an averaging as the one proposed to group the amplitude time-slices, concerns the vertical stationarity of the variables under study over the window of interest. By replacing each individual variogram by an average variogram computed for the whole group of time-slices, one must keep in mind the potential errors on the cokriging estimates that this methodology may impose. In this particular case, as the length of the time window of interest is comparable to the wavelet dimensions, these effects should be considerably reduced. One way to test this hypothesis is to compare the average experimental variogram of each group with the individual variograms computed for each time slice.

Assuming that the uppermost and bottommost limits are given by time-slice 01 (TS01) and time-slice 50 (TS50), the 200 ms thick interval was divided into seven of time-slices, as groups shown in Table 5-4.

Table 5-4 - Definition of time-slices groups.

Group	Top time-slice (TS) number	Bottom time-slice number	Thickness (ms)
G1	TS01	TS06	24
G2	TS07	TS12	24
G3	TS13	TS20	32
G4	TS21	TS28	32
G5	TS29	TS36	32
G6	TS37	TS44	32
G7	TS45	TS50	24

This grouping definition was also supported by qualitative criteria, such as the spatial pattern of amplitude anomalous values, which helped on defining, for instance, the external limits of occurrence of the Marlim reservoir. It is important to mention that, concerning this specific limit, it may differ from the actual reservoir limits, as it does only take into account the seismic data.

In the following paragraphs, a description of the main spatial characteristics observed at each group of amplitude time-slice maps is presented, including a statistical description based on the histograms computed for each considered variable, for each group. This description is deemed important not only for the comprehension of the amplitude map responses, but will be also a valuable tool during the geostatistical analysis phase, enabling a proper definition of the variograms and cross-variograms models for each group. As the classification is, as much as possible, based on a physical reasoning (characteristic dimensions of the expected effects), this step will help on the interpretation of the resulting factors computed during the multivariate factorial kriging.

The amplitude time-slice maps presented from Figure 5-22 to Figure 5-40, show, in the first and in the second rows, the topmost and the bottommost time-slice of each group,

respectively, exception made for Groups G4, G5, and G6, where an additional intermediate time-slice was also included for the sake of comprehension. At each row, three maps are presented: the leftmost map corresponding to the S05 seismic campaign; the map positioned at the center of the row, corresponding to the S97 vintage; and the rightmost map, computed as the difference between the S05 and S97 seismic volumes.

To enable the comparison between time-slices belonging to different groups, only two amplitude scales are displayed, where the first one accounts for very small amplitude values, as those found in the time-slices from TS1 to TS20. An additional amplitude scale was used to represent all remaining time-slices from TS21 to TS50, including higher positive and negative amplitude values compatible with those found in the reservoir intervals.

The reservoir limit is also displayed in all time-slice amplitude maps, and it corresponds to a black polygon. It is important to mention that this external reservoir limit does not coincide, in general, with each individual time-slice limit, at a particular time-slice.

Most of the seismic samples corresponding to the Marlim reservoir are represented by the amplitude time-slices from Groups G4 and G5, performing a total time interval of 64 ms. Therefore, seismic properties changes induced by the oil production mechanism are expected to be typically observed in these time intervals. For instance, when inspecting the time-slices with attribute difference Dif S05 – S97 from groups G4 and G5, particular shapes and geometries of the amplitude anomalies surrounding the wells are observed, frequently exhibiting circular geometry with maximum radius of approximately 255m. These effects, clearly associated to the well locations, result of the production mechanism, as observed in the following wells: 96D, 97D, 105D, 114D, 120D, and 144D (clearly observed from TS29 up to TS39).

When analyzing the seismic cross sections crossing these wells, the observed time-lapse effect is compatible with those modeled: in the reservoir zones submitted to injection, an overall decrease in the acoustic impedance is observed, due to the higher density and

velocity of the water replacing the heavy oil. This decrease in the impedance corresponds to a reduction of the reflectivity at the top and at the bottom horizons in the monitor survey when compared to the base survey. Therefore, the volume of amplitude differences $Dif\ S05 - S97$ should show positive amplitude values where water replaces oil ($Amp\ S05 < Amp\ S97$) at the top of the Marlim reservoir, and a negative difference at the bottom. In absolute amplitude values, the injected water will always impose a reduction of the amplitude value.

Group G1 (TS01-TS06)

The Group G1 interval corresponds to the uppermost portion of the 200ms time window, as shown in the inline seismic section from Table 5-4. Geologically, this interval corresponds to the sedimentary pelitic sequence that was deposited just after the Marlim turbiditic sandstones, and is mainly represented by shales and marls, as a part of the regressive marine megasequence as presented in paragraph 5.1.2.

In terms of spatial structures, and due to its geological/depositional characteristics, no particular structure is expected to be observed in this interval. Furthermore, assuming that the reservoir seal is preserved and by consequence, no fluid (oil or gas) flow from the underlying reservoir levels have occurred, one should not expect major acoustic contrasts as a result of the oil-production over these time-slices maps.

Analysis of the time-slices presented in Figure 5-22, reveal at least two main spatial features present on all time-slices from this interval. Firstly, a *low-frequency periodic event* is equally observed on both S05 and S97 datasets, corresponding roughly to the NNE-SSW direction, and almost orthogonal to the inline direction. This feature could be a response of discordant dipping reflections on this topmost interval, in comparison to the horizontal plane represented by the bottommost time-slice TS50 used as a reference to the flattening procedure, as described in paragraph 5.2.2.

The second identified structure corresponds to a *high-frequency feature*, oriented parallel to the inline direction and mainly observed on the central area of the time-slice maps from both S05 and S97 campaigns. This feature is more evident when analyzed in the

Dif S05-S97 difference amplitude time-slices, as shown in Figure 5-22. This effect, possibly associated to acquisition artifacts, shows higher variability in the crossline direction, exhibiting a periodic behavior with period varying from 260 to 330m.

The corresponding S05, S97 and Dif S05-S97 histograms exhibit normal distribution, symmetric, with one central mode corresponding to a mean value close to zero, as shown in Figure 5-23 and Figure 5-24. The variance computed for S05 data is 28% higher than the one from S97 data, and are equal to 410 and 320, respectively.

The quantile-quantile graphs presented in Figure 5-24 plot the original data distribution for S05, S97 and Diff S05-S97 in the vertical axis, against the equivalent theoretical Gaussian distributions in the horizontal axis, enabling check this fit. The interpretation is straightforward. The closer the distributions are from the first plotted bisector, the closer they are from a theoretical Gaussian distribution. In this case, one can observe a very good fit between the observed data and the equivalent models.

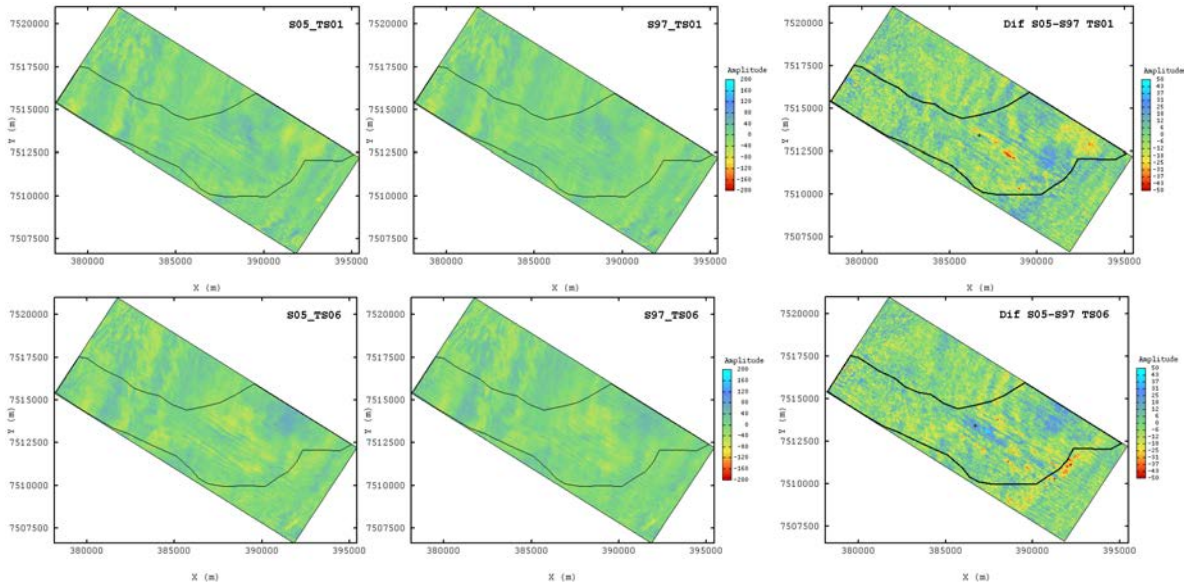


Figure 5-22 – Amplitude maps corresponding to the topmost (first row) and bottommost (second row) time slices from Group G1. From left to right, the three columns correspond to the S05, S97 and difference Dif S05-S97 datasets.

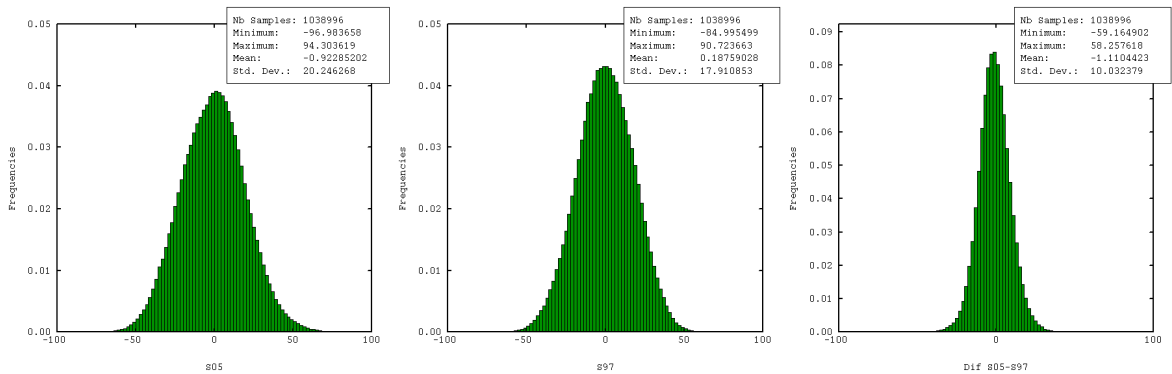


Figure 5-23 - Histograms corresponding to the S05, S97 and difference Dif S05-S97 data values distributions, for time slices Group G1. No major differences observed in terms of amplitude distribution when comparing the two vintage histograms, but a higher concentration of null values and smaller variance of S97 data.

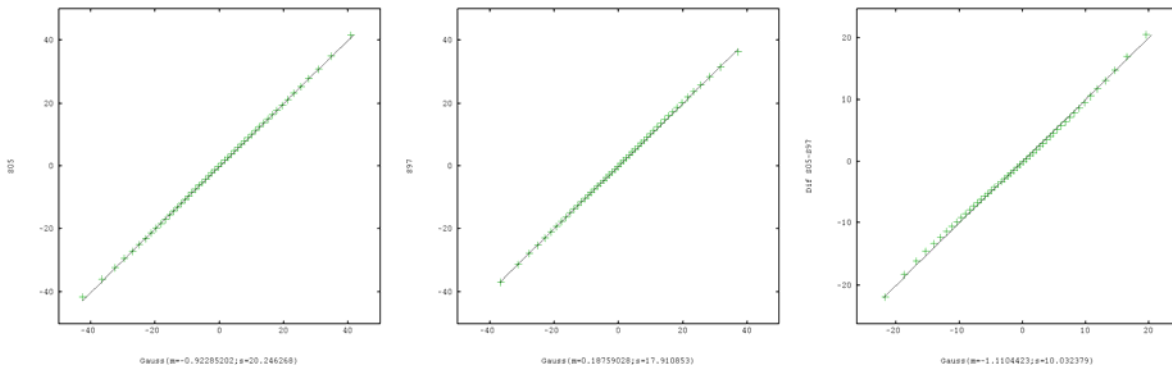


Figure 5-24 – Comparative quantile-quantile distribution plots for Group G1, corresponding to S05, S97 and DifS05-S97 data, from left to right.

Group G2 (TS07-TS12)

The time-slice amplitude maps corresponding to Group G2 cover a time window of 24ms and present a similar behavior in terms of amplitude distributions when compared to the Group G1. Two prevailing structures, with similar characteristics to those described in Group G1, are observed in this interval. Additionally, a few anomalous negative amplitude values, restricted to the eastern part of the bottommost time-slice maps, are also observed. These anomalous values point out the first samples corresponding to the underlying Marlim reservoir, as shown in the seismic section from Figure 5-25.

The difference maps show anomalous amplitude areas in the central part of the maps. These structures are spatially consistent on all observed time-slices, suggesting, as mentioned earlier, a possible noise related to the seismic acquisition campaign from S05 vintage.

Figure 5-26 shows the S05, S97 and Dif S05-S97 histograms, all exhibiting normal distribution, symmetric, with a central mode corresponding to mean value close to zero. As observed in the previous group, the variance associated to S05 data is 27% higher than the one of S97, and are equal to 524 and 411, respectively, with an overall increase of the variance. The quantile-quantile plots show a very good fit of each observed data distribution to the equivalent Gaussian.

Group G3 (TS13-TS20)

The seismic anomalies observed in the eastern area of the time-slice amplitude maps from Group G3 assume a more continuous spatial distribution at the bottommost slices, as show in Figure 5-28. These anomalous amplitude values, aligned almost parallel to the inline direction N122 degrees, are associated to sand-filled channels. Oliveira et al. (2007) described these elements as feeding channels from the southwestern sedimentary source of Marlim field.

Other linear events, already described in the previous Groups G1 and G2, and also oriented parallel or sub parallel to the inline direction, are easily identified in the middle

area of the time-slice amplitude maps. These events are potentially associated to the acquisition noise, as observed in Groups G1 and G2, are also present, showing the same spatial characteristics.

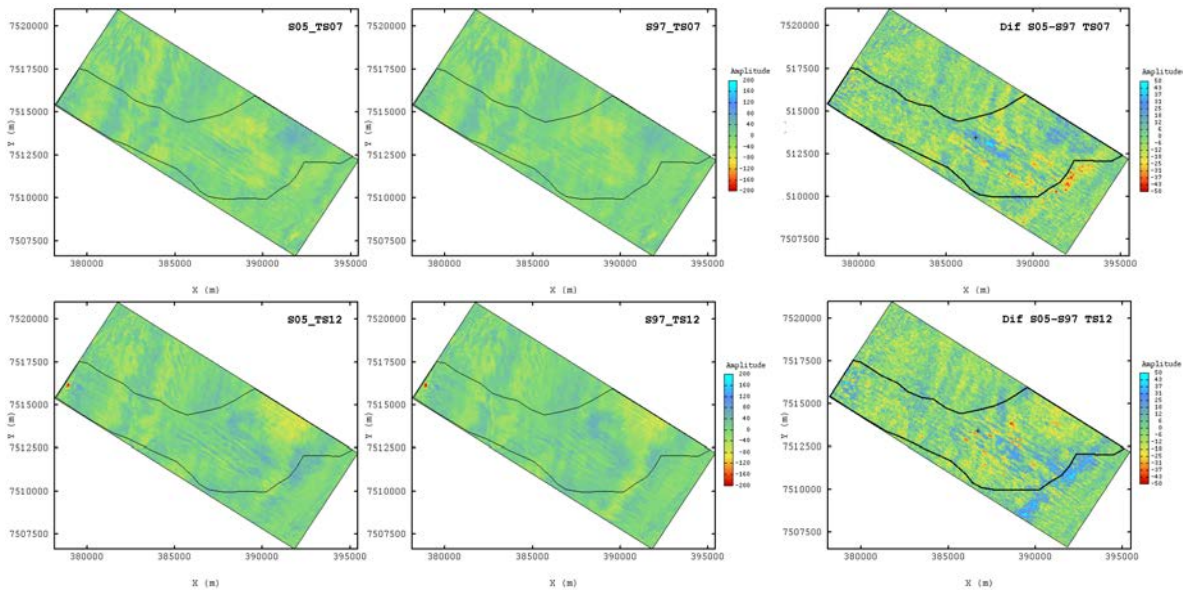


Figure 5-25 – Same as in Figure 5-22, for Group G2. Inline oriented spatial structures are predominant in the centre of the time-slices, and are more pronounced in the Dif S05-S97 data.

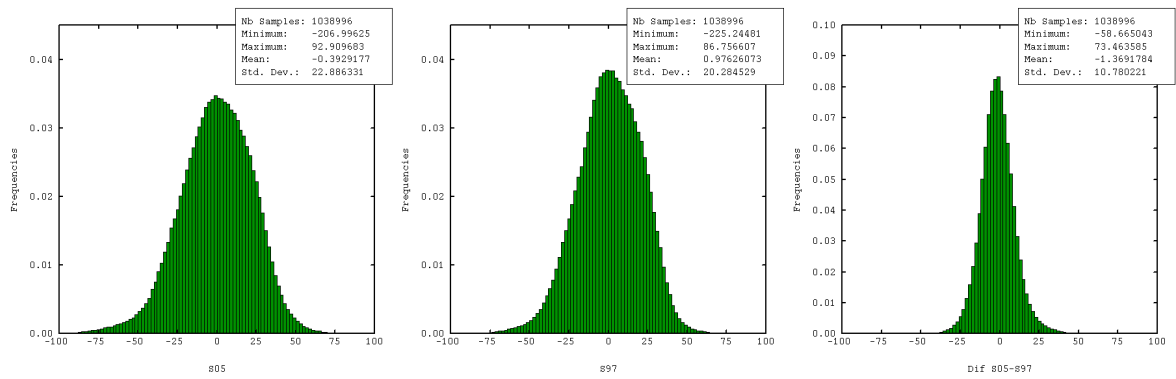


Figure 5-26 – Same as in Figure 5-23, for Group G2.

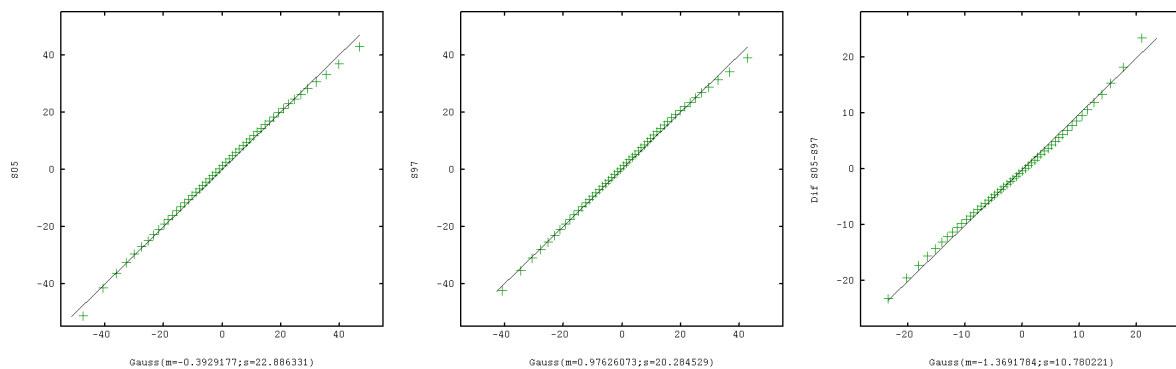


Figure 5-27 – Same as in Figure 5-24, for Group G2.

S05 and S97 data from Group G3 exhibit an experimental correlation coefficient of 0.93. Their distributions, as well as the one from the difference S05-S97, show a normal and symmetric distribution.

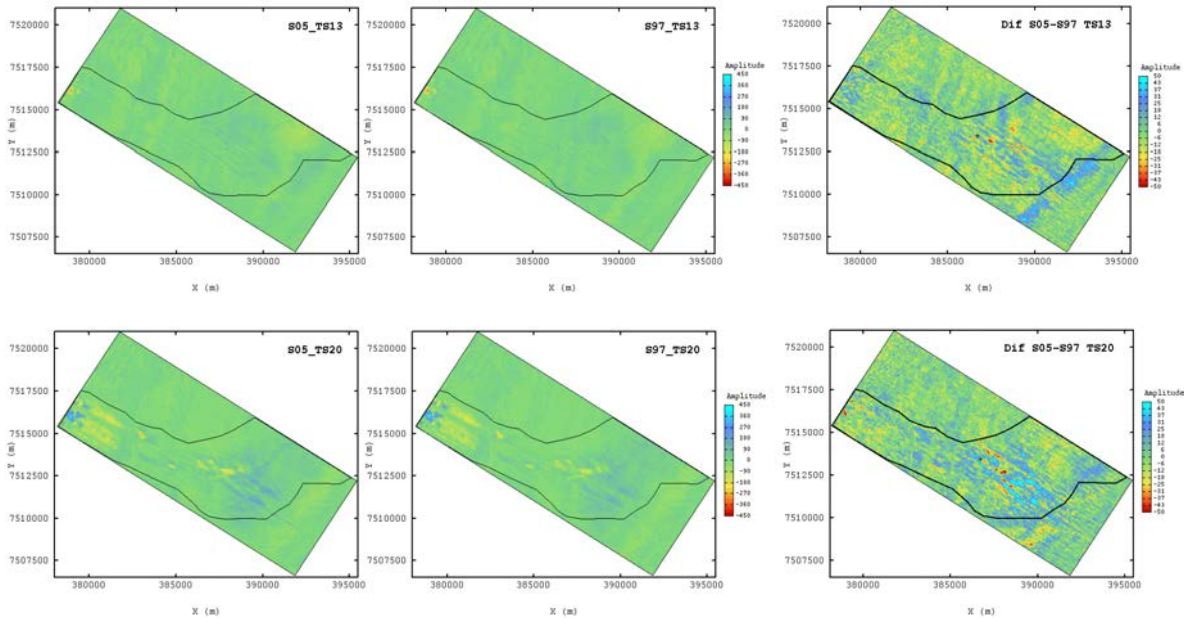


Figure 5-28 - Same as in Figure 5-22, for Group G3.

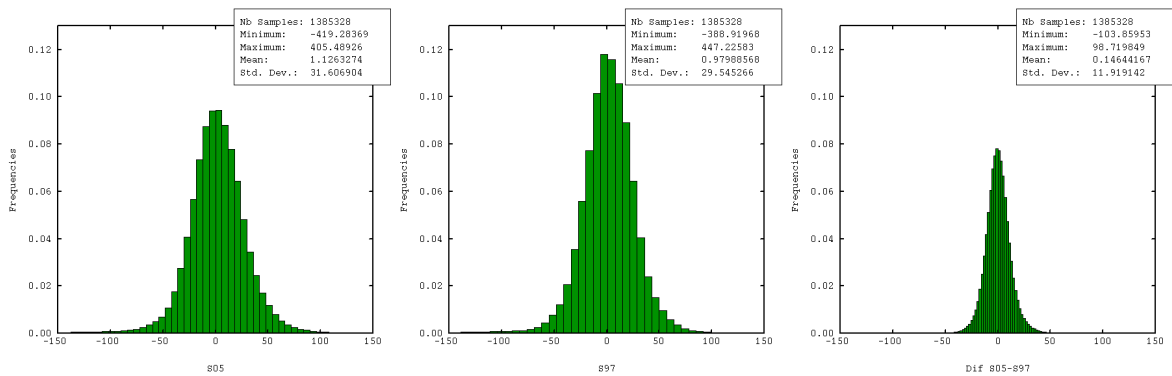


Figure 5-29 - Same as in Figure 5-23, for Group G3.

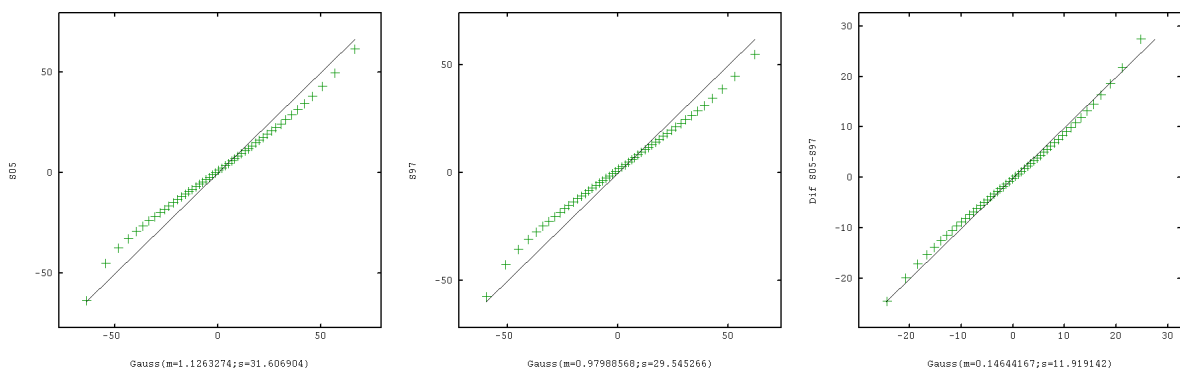


Figure 5-30 - Same as in Figure 5-24, for Group G3.

A closer inspection of the quantile-quantile plots (Figure 5-30) shows, however, that the tail behavior from both distributions depart from a Gaussian distribution. The variance of S05 data (999) is 14.4% higher than the S97 variance (873).

Group G4 (TS21-TS28)

In terms of seismic response, the Group G4 is mainly characterized by a sequence of time-slices showing contrasting values. Strong negative amplitude values which characterize the reservoir top anomalies are surrounded by background, close to zero amplitude values associated to the encasing non-reservoir rocks (Figure 5-31).

The reservoir external geometry is well explained by the seismic data on both vintages, and the remarkable feature observed on the time-slices from Group G4 strongly suggests a turbiditic lobe geometry spread in the central part of the maps. More than that,

the inflexion of the main depositional axis of this turbiditic lobe system, from NW-SE direction to the W-E direction, could also be inferred. This depositional lobe system is one of the two main turbiditic lobe systems recognized in the Marlim Field, as reported by Oliveira et al. (2007).

Figure 5-31 shows, at the rightmost column, the difference amplitude maps resulting from the subtraction of the S97 from S05 seismic volumes, and where mixing structures are observed. Two main zones of distinct amplitude values are identified: the first one, with a *widespread distribution* over the map, corresponds to small to null amplitude differences between S05 and S97 seismic data represented by the green areas; and a second zone, with *high negative amplitude* values represented by orange-to-red colors, showing elongated structures almost parallel to the inline direction. Few blue colored areas, corresponding to positive differences, are also observed.

Similar responses for S05 and S97 vintages are equally observed in the amplitude histograms (Figure 5-32), representing all seismic samples of all time-slices from Group G4. These histograms are characterized by highly negative asymmetric distribution, and this asymmetry is mainly due to the anomalous negative reservoir topmost samples. A single mode, coincident to zero amplitude value, is mainly linked to the background non-reservoir samples, as previously mentioned. Compared to the previous histograms from Groups G1, G2 and G3, all characterized by a normal and symmetric distributions, exhibiting a single mode close to zero average amplitude value, the group G4 histograms show a distinct behavior. The S05 campaign shows a variance 10.4% higher than the S97, respectively with 5,935 and 5,375, with a remarkable similarity between the two distributions, and high linear correlation coefficient equal to 0.99.

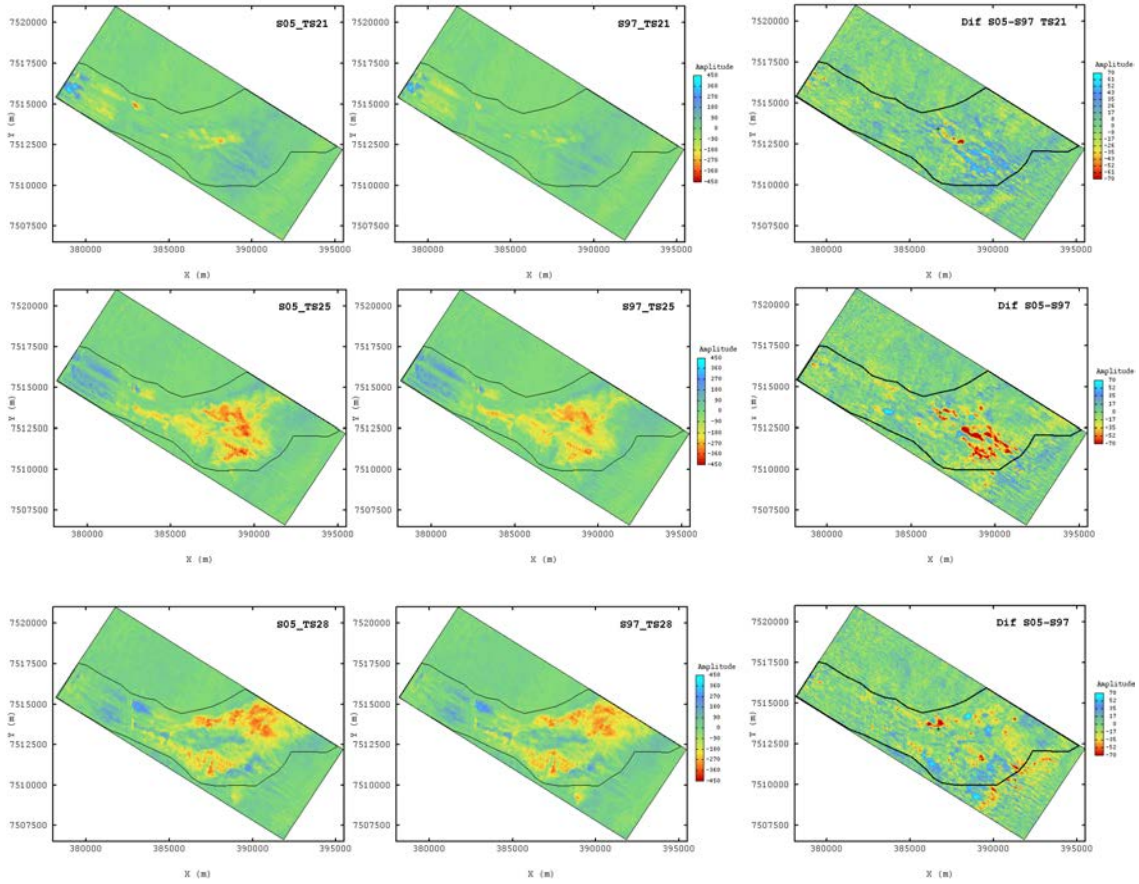


Figure 5-31 - Same as in Figure 5-22, for Group G4, including the intermediary TS25 time-slice amplitude maps.

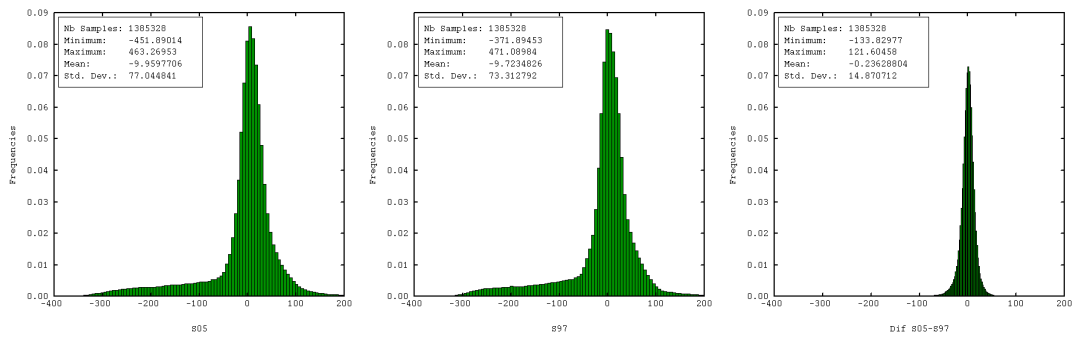


Figure 5-32 – Same as in Figure 5-23, for Group G4.

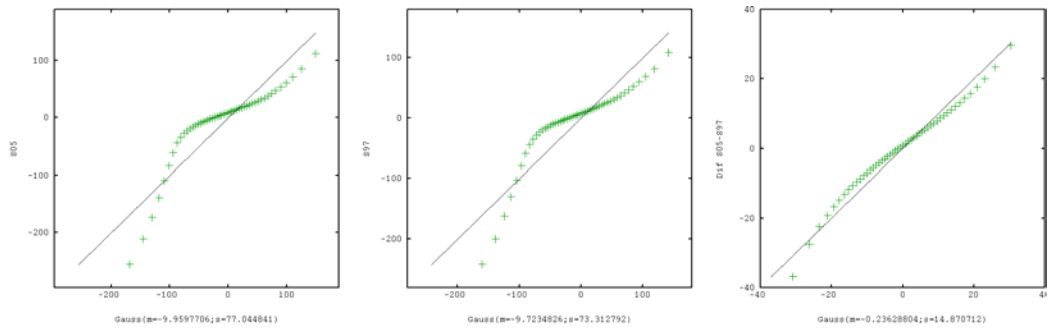


Figure 5-33 - Same as in Figure 5-24, for Group G4.

Group G5 (TS29-TS36)

The time-slices from Group G5 are most representative of the Marlim reservoir bottom zone, but also include anomalous amplitude values from the underlying Marlim South reservoir. In this interval, the most peculiar seismic amplitude responses and most likely to be associated to the oil production effects resulting from the replacement of oil by water, are expected to be observed.

Figure 5-34 shows three time-slices from this group: the topmost row corresponding to the first time-slice (TS29); the second row to an intermediate slice (TS33); and the bottommost row to the last time-slice (TS36) from this group. In the central area of the amplitude maps from S05 and S97, the blue colors, corresponding to the positive amplitude values, are dominant in the reservoir zone limited by the black polygon. The external reservoir geometry is clearly defined by the amplitude anomalies on both S05 and S97 maps, where the lobe geometry as observed in Group G4 is equally identified.

Considering these positive anomalous amplitude region from S05 and S97 maps, it is interesting to notice the conspicuous circular amplitude anomalies when observing the difference maps in the rightmost column in Figure 5-34. These structures, most of them representing negative amplitude differences values, coincides with the positioning of the injector wells, and are in agreement with the expected production-injection scheme for this zone (references and maps).

However, additional anomalous amplitude structures are equally observed in these maps, for instance, those alignments parallel to the inline direction and more pronounced in the southeast part of the amplitude maps. These linear structures show a similar behavior as those described for all groups' non-reservoir intervals, making its interpretation more uncertain. How to discriminate these spatial structures in terms of noise – as recognized outside the reservoir interval – to a time-lapse signature?

The histograms from S05 and S97, showing a similar behavior, are both symmetric, with normal distribution around the zero mean. The resulting difference histogram, shown in the left column of Figure 5-35, is equally symmetric, and the anomalous difference values as show in the amplitude difference maps, are immersed in the background values.

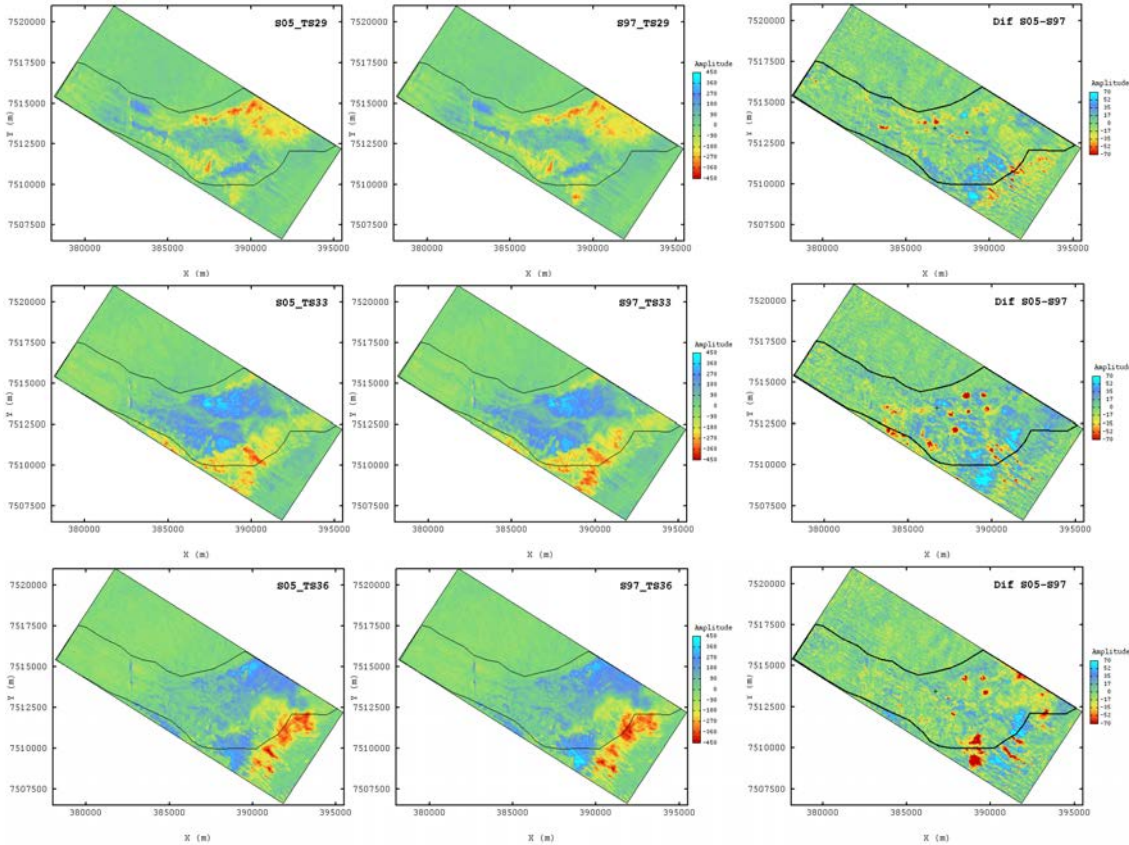


Figure 5-34 - Same as in Figure 5-31, for Group G5.

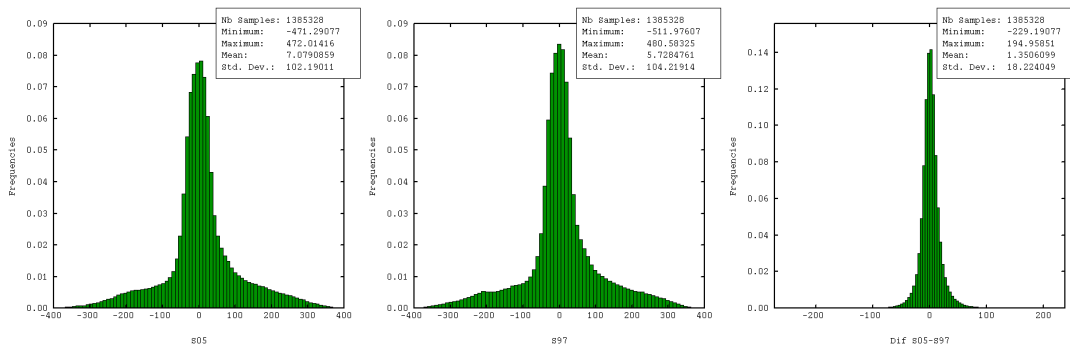


Figure 5-35 - Same as in Figure 5-23 for Group G5.

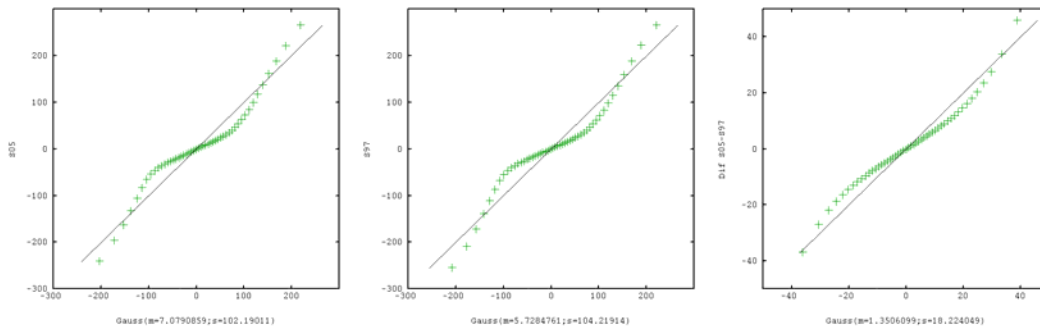


Figure 5-36 - Same as in Figure 5-24 for Group G5.

Group G6 (TS37-TS44)

The amplitude time-slices from Group G6 are mainly represented by the Marlim South reservoirs, as shown in Figure 5-37. In this figure, the first row shows the bottommost part of the Marlim reservoir, represented in the maps by the blue, or positive, amplitude values. The top of the Marlim South reservoir, represented by red or negative amplitude values, occurs mainly in the southeast part of the map. In the middle row, however, only positive anomalies and probably associated to the Marlim South reservoir base are observed. These anomalies disappear when inspecting the last time-slice at the bottom of Figure 5-37, as most of the samples from this slice lie outside the reservoir interval, where no anomalous amplitude values are expected.

The difference amplitude maps displayed in the right column of Figure 5-37 show an interesting pattern of spatial structures distribution. In general, the three maps show

predominance of zero, or close to zero, amplitude values, as indicated by green colors. Sparse anomalous zones are observed, preferentially in the east part of the area.

These anomalous values observed in the difference amplitude maps computed from the subtraction of vintages S05 and S97, could be split in two groups, as a function of the area distribution: i) punctual anomalies, exhibiting a circular geometry, and coincident to those anomalies already described in Group G5; ii) continuous anomalies, as observed in the first and middle difference maps with high negative amplitude difference values, in red. A careful analysis of these rather continuous anomalies shows a clear orientation parallel to the inline direction, as shown in the top and mid difference maps.

Distributions of the amplitude values show one-mode histograms for S05 and S97, and identically for the difference, as shown in Figure 5-38. Mean amplitude values are equal to 14.5 and 16 with variances equal to 7,600 and 8,346, for S05 and S97, respectively. The vintages histograms exhibit an asymmetrical distribution, positively skewed. Acquisition artifacts are still observed in this interval, representing differences between the S05 and S97 campaigns and oriented parallel to the inline direction can be observed.

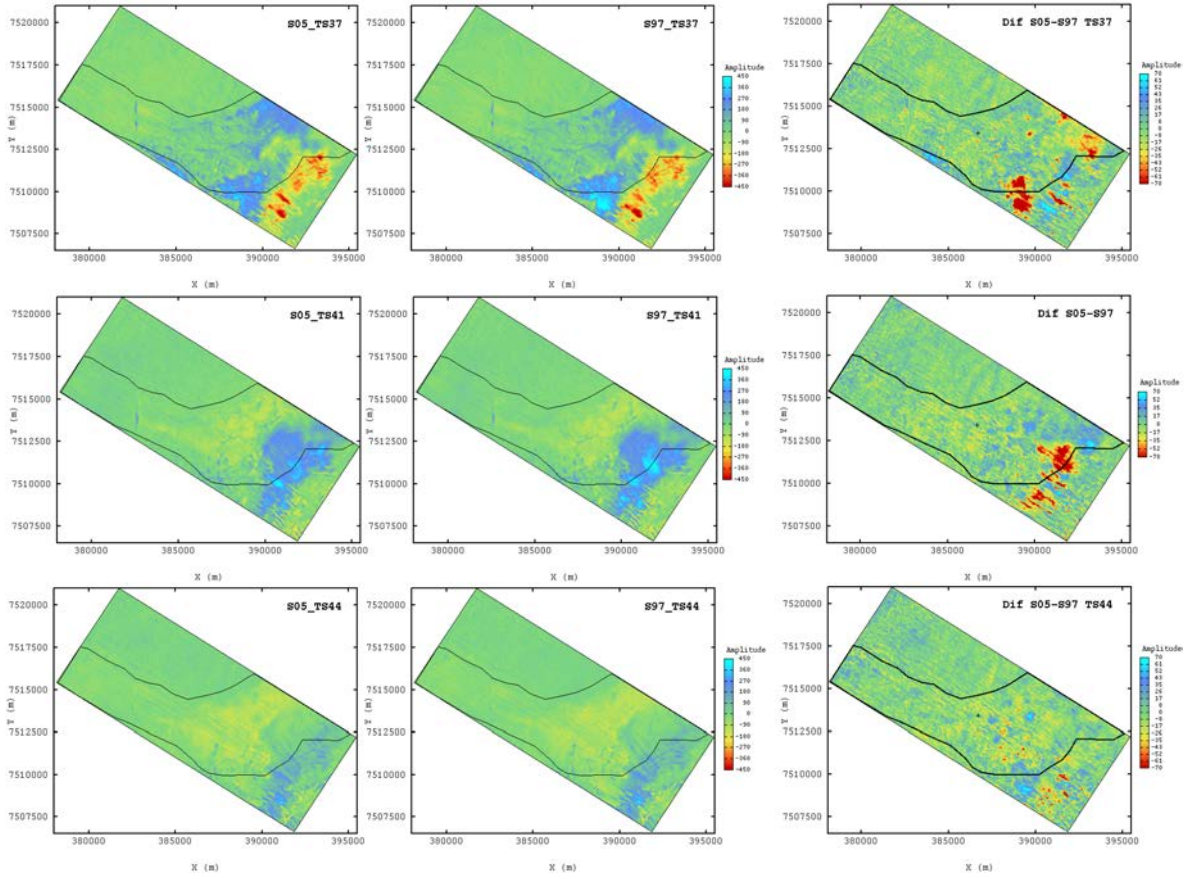


Figure 5-37 - Same as in Figure 5-31, for Group G6.

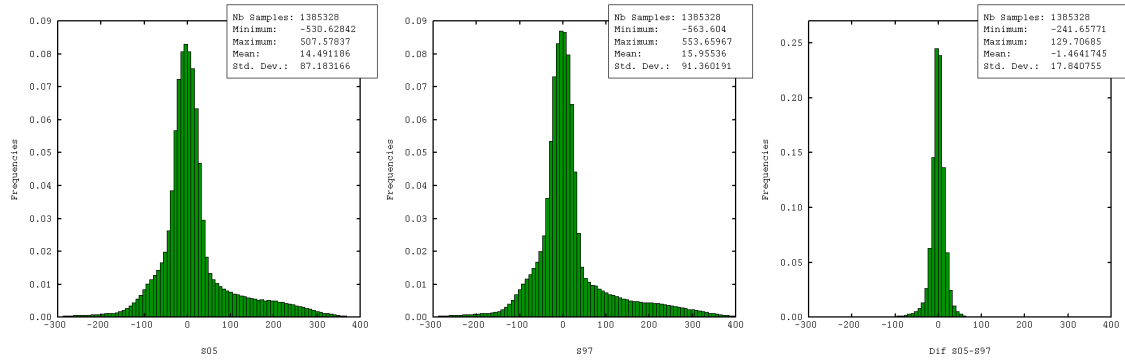


Figure 5-38 - Same as in Figure 5-23, for Group G6.

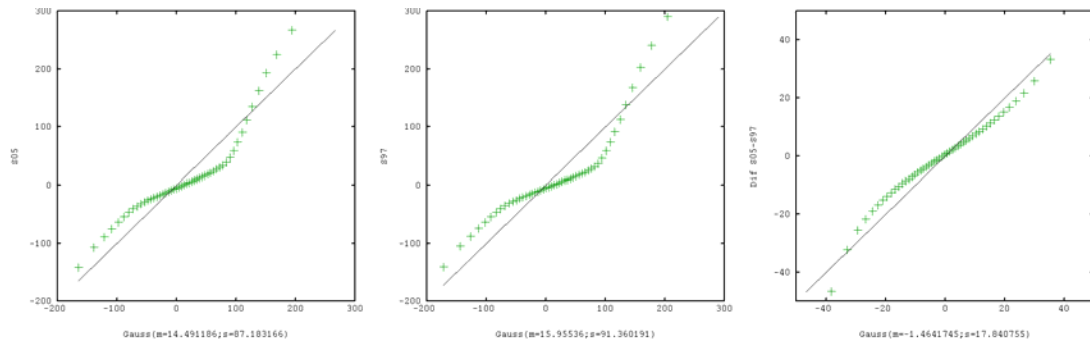


Figure 5-39 – Same as in Figure 5-24, for Group G6.

Group G7 (TS45-TS50)

Group G7 amplitude time-slices corresponds to the sedimentary sequence just below the reservoir intervals, from the bottom of the Marlim and Marlim South reservoirs up to the top of the Blue marker. As previously mentioned, this marker was considered as the reference horizon in the flattening procedure for the whole 200ms time window interval. The Blue Marker corresponds to the top of a sequence which deposition is associated to a maximum flooding surface. It has a constant thickness over the studied area (Rangel et al., 1994; Serin et al., 2005). Due to these characteristics, this marker is usually taken as a reference for most of stratigraphic studies performed in the Campos Basin area. As no spatial structures associated to depositional/geological processes are expected to be observed in this interval, these levels would be potential candidates to be considered as reference images for the interpretation.

Analyzing the S05 and S97 amplitude time-slices from Figure 5-40, one may notice contrasting amplitude values in the central area of the maps. These features that geographically correspond to the projection of the thicker Marlim reservoir areas into the bottommost layers could be interpreted as a "fingerprint" of the reservoir interval onto the underlying layers which was not properly attenuated during the seismic processing step. Additionally, the amplitude time-slices also present inline oriented structures probably related to different acquisition or processing parameters, and is interpreted as acquisition noise. A particular structure oriented North-south and occurring at the west side of the amplitude maps, corresponds to a discontinuity related to fault zone.

The difference amplitude maps shown in the right column, exhibit a very heterogeneous amplitude distribution, with two main spatial patterns: i) punctual anomalies observed at the topmost interval, similar to those previously described for groups G5 and not expected to be observed in these slices; ii) inline oriented structures, as previously described.

A prominent mode at zero amplitude value is observed in the histograms from Group G7, in Figure 5-41 , corresponding to the background amplitudes found in the

seismic trace interval from the Blue Marker up to the Marlim reservoir. The positive amplitude values, on the other hand, are mostly associated to the positive peak in the seismic trace associated to the top of the Blue Marker, as shown in Figure 5-8 and Figure 5-21.

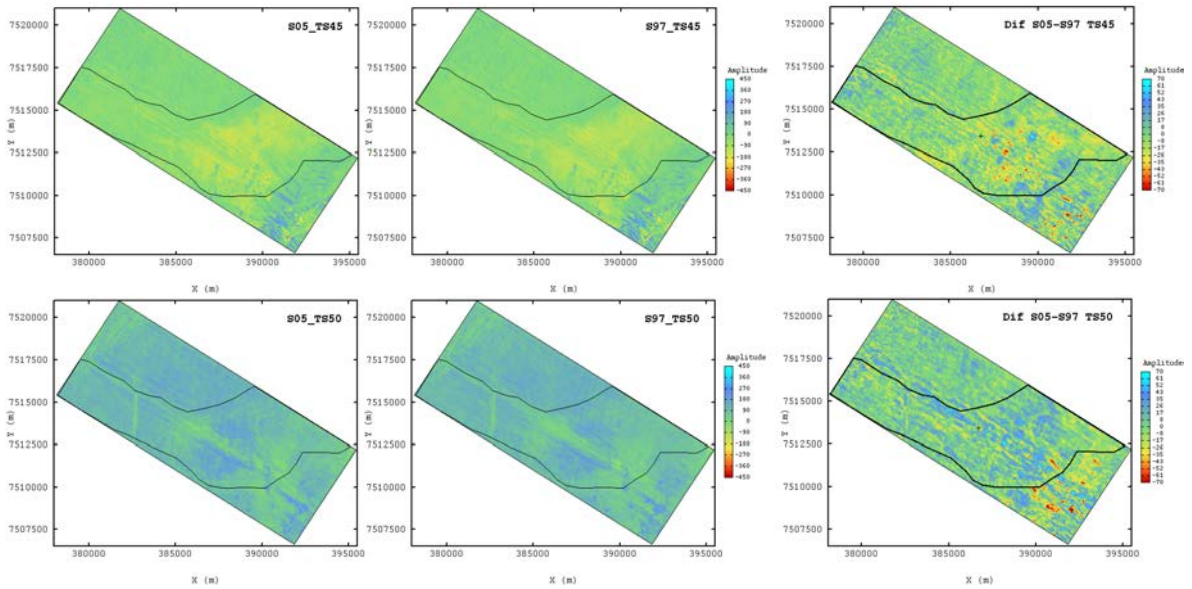


Figure 5-40- Same as in Figure 5-31, for Group G7. The bottommost time-slice (TS50) from G7 corresponds to the flattened Blue marker reference horizon.

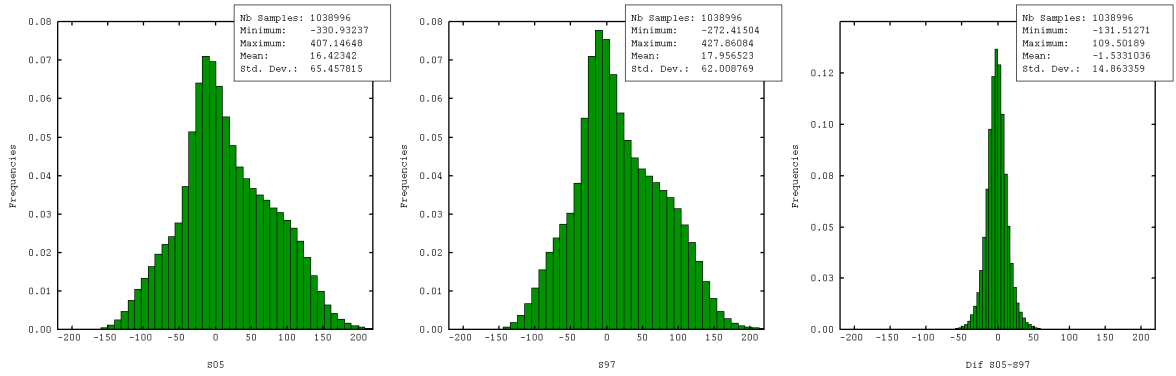


Figure 5-41 - Same as in Figure 5-24, for Group G7

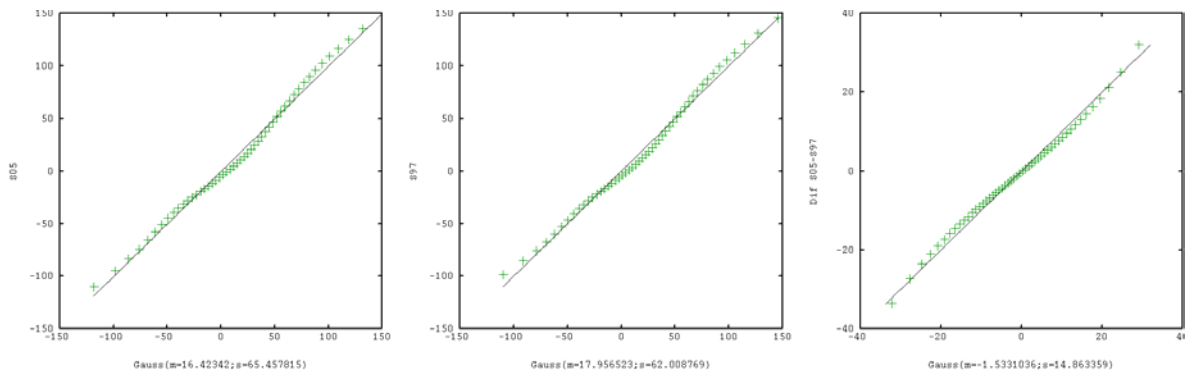


Figure 5-42 - Same as in Figure 5-23, for Group G7.

Discussion

Analyses of the statistical data from both groups of time-slices for each S05 and S97 vintages, and summarized in Table 5-5 and in Table 5-6, shows that:

- minimum, maximum and mean values show comparable values;
- compared to the S97 data, the S05 amplitude *a priori* variance shows a significant reduction in the reservoir interval, when compared to the non-reservoir intervals (this difference in variance is expressed in percentage and shown in brackets in Table 5-5);

Following these results, the linear correlation coefficient, as shown in the rightmost column of in Table 5-5, show smaller values for those groups that do not comprise reservoir layers, G1, G2, G3 and G7; whereas groups G4 to G6 show the higher coefficients, and equal to 0.98. These results concerning the *a priori* variance and correlation coefficient effects will be detailed in the next paragraphs. They are not easily explained, as these responses are reversed in comparison to what should be expected from a cross-equalized dataset.

Table 5-5 - Statistical data computed for each group of time-slice, for S05 seismic campaign.

Group	Count	Minimum	Maximum	Mean	Variance	Linear Correlation S05 x S97
G1	1 038 996	-96.98	94.30	-0.92	409.91 (27.8%)	0.87
G2	1 038 996	-207.00	92.91	-0.39	523.78 (27.3%)	0.88
G3	1 385 328	-419.28	405.49	1.13	999.00 (14.4%)	0.93
G4	1 385 328	-451.89	463.27	-9.96	5 935.91 (10.4%)	0.98
G5	1 385 328	-471.29	472.01	7.08	10,442.82 (-3.9%)	0.98
G6	1 385 328	-530.63	507.58	14.49	7,600.90 (-8.9%)	0.98
G7	1 038 996	-330.93	407.15	16.42	4,284.73 (11.4%)	0.97

Table 5-6 - Same as in Table 5-5, for the S97 campaign.

Group	Count	Minimum	Maximum	Mean	Variance
G1	1 038 996	-85.00	90.72	0.19	320.80
G2	1 038 996	-225.24	86.76	0.98	411.46
G3	1 385 328	-388.92	447.23	0.98	872.92
G4	1 385 328	-371.89	471.09	-9.72	5 374.77
G5	1 385 328	-511.98	480.58	5.73	10 861.63
G6	1 385 328	-563.60	553.66	15.96	8 346.68
G7	1 038 996	-272.42	427.86	17.96	3845.09

All histograms presented in the previous paragraphs were computed taking into account all time-slices corresponding to each group. These S05 and S97 histograms show a quite similar behavior, with most of them showing only one mode. A possible explanation for this behavior is due to the introduction of seismic traces that do not correspond to the reservoir window on the computation. Another feature also observed on almost all histograms is a higher frequency of null values on the S97 traces when compared to the S05.

5.2.5. Structural Analysis: Modelling the experimental variograms

A structural analysis was performed on each of the seven groups of time-slice amplitude data presented in the previous paragraph. This analysis aimed at characterizing the spatial structures present on both base S97 and monitor S05 surveys that should be filtered out, or pointed out in the following geostatistical estimation steps. The considered approach assumes a vertical stationarity of the amplitude data on each group of time-slices.

The basic geostatistical parameters, such as lag distance, number of lags, directions, etc, were kept constant for all the seven layers, and were defined as follows:

- lag distance: 50m, or twice the original 25x25m grid size;

- number of lags: 68, equivalent to 3400m, for both crossline and inline directions;

The experimental variograms and cross-variograms, computed for each variable, are represented in the following graphs as thin lines, whereas the modelled variograms, resulting from the structural analysis, are represented as thick lines. The red and green lines correspond, respectively, to the inline and crossline directions. For all variograms and cross-variograms, the horizontal scale represents the *range*, or distance of correlation, and is given in meters. The vertical variogram scales are represented by squared seismic amplitude unities. The observed spatial structures were classified as *short*, *medium* and *long range*, based on the following definition:

- *short range*: all spatial structures with dimensions up to 10 times the original cell size, or 250 m;
- *medium range*: for those spatial structures with ranges varying from 250 m to 1,500 m; and
- *long range*: for those spatial structures with ranges bigger than 1,500 m.

Group G1

This group represents the topmost sequence of time-slices, and is completely outside the reservoir time interval range. The interpretation of the experimental variograms and cross-variograms from S05 and S97 data resulted in a nested structure shown in Figure 5-43 and defined as a linear combination of five basic structures, as follows:

- a *short range spherical structure* C_1 , with a small correlation coefficient of 0.61, and a small contribution to the total variance, representing 19% of the total S05 variable and 16% of the S97's;

- a *medium range spherical structure* C_2 , with a high correlation coefficient equal to 0.91; and
- *three long range structures, from C_3 to C_5* , all them showing high correlation coefficients.

The experimental variograms from S05 and S97 vintages are quite superposed, as shown in Figure 5-43. A strong anisotropy is observed on both data, with periodic structures being identified only in the inline direction.

Small linear structural correlation coefficient as observed in the short scale range could be explained by (1) rescaling the original S05 and S97 cell sizes during the seismic processing phase, as show in Figure 5-7; and (2) poorer seismic imaging quality, and restricted to specific areas on the S05 data, probably due to seismic acquisition constraints imposed by operational obstacles, as can be noticed in Figure 5-2. The short and mid-range structures identified in the cross-variograms account for 12% and 20% of the total common variance in the inline directions, as shown in Table 5-7.

Table 5-7- Resulting modelling parameters from structural analysis of Group G1. In brackets, the percentage of the total variance explained by each structure, in the inline and in the crossline direction, respectively.

Structures		Ranges (m)		Sills			Correlation
		Inline	Crossline	S05	S97	S05×S97	
C ₁	Spherical	140	140	73 (19 / 15)	51 (16 / 14)	37 (12 / 10)	0.61
C ₂	Spherical	440	740	61 (16 / 13)	71 (23 / 20)	60 (20 / 17)	0.91
C ₃	Exponential	N/A	4 400	340 (- / 72)	240 (- / 66)	262 (- / 73)	0.92
C ₄	Cardinal sinus	2 800	N/A	70 (18 / -)	60 (19 / -)	64 (21 / -)	0.99
C ₅	Cardinal sinus	5 400	N/A	184 (47 / -)	131 (42 / -)	143 (47 / -)	0.92

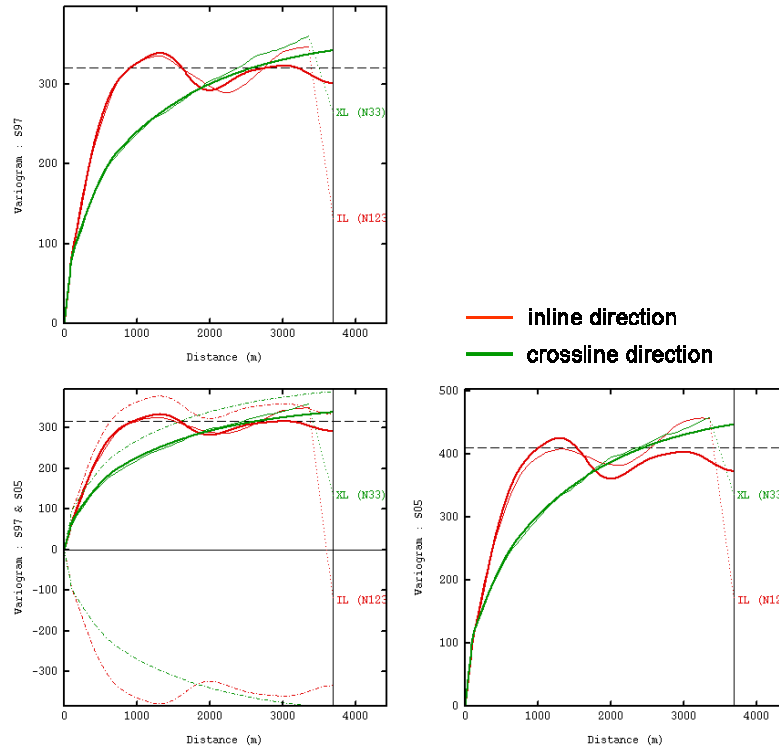


Figure 5-43 – Structural modelling results for Group G1, corresponding to time-slices TS01-TS06. Thin and thick lines correspond, respectively, to the experimental and theoretical variograms, whereas green and red colours to the crossline and inline directions, respectively.

Group G2

Compared to the previous Group G1, this interval presents a less pronounced *hole effect* in the inline direction, but an identical geometric anisotropy - the same sill is reached at different ranges, for different directions (Isaaks et Srivastava, 1989). Four structures were used to describe the data variability. The short scale structure shows identical range when compared to the previous group, equal to 140m, and similar correlation. One medium range structure was identified, and accounts for 21% of the cross-covariance. Two additional long range structures were considered: one exponential, that completely explains the variability in the inline direction, and one spherical, representing 64% of the total common variance, as can be observed in Table 5-8.

Table 5-8- Same as Table 5-7, for Group G2.

Structure		Ranges (m)		Sills			Correlation
		Inline	Crossline	S05	S97	S05×S97	
C ₁	Spherical	N/A	140	118 (- / 20)	86 (- / 20)	65 (- / 15)	0.65
C ₂	Spherical	N/A	1 250	102 (- / 17)	122 (- / 27)	96 (- / 21)	0.87
C ₃	Exponential	1850	N/A	583 (100 / -)	472 (100 / -)	458 (100 / -)	0.87
C ₄	Spherical	N/A	3 800	365 (- / 62)	230 (- / 52)	286 (- / 64)	0.99

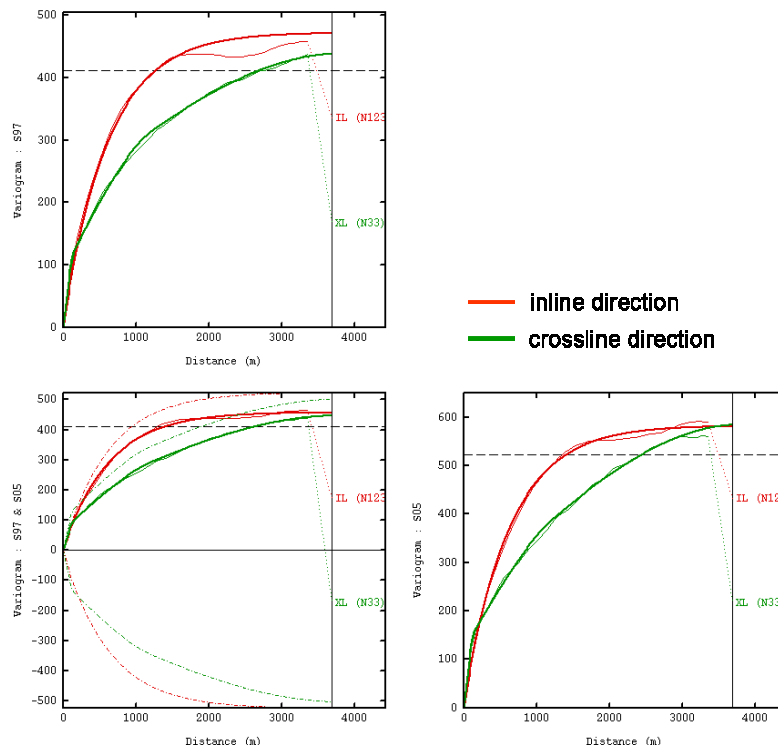


Figure 5-44 - Same as in Figure 5-43, for Group G2.

Group G3

Six basic structures were considered to adjust the theoretical variograms and cross-variograms from S05 and S97 for Group G3. As described for the previous Groups G1 and G2, a characteristic geometric anisotropic behaviour is also observed. When comparing the variograms from Group G1 to G3, one notices that the crossline direction shows a fairly constant behaviour in terms of spatial variability, reaching the sill value at long ranges. The

inline direction, however; shows a contrasting behaviour, becoming more continuous at deeper time-slices.

Comparing the variograms from the inline and crossline directions from Group G3, drawn, respectively, as red and green lines in Figure 5-45, one may notice that, concerning the short-range distances, the crossline direction is characterized by a higher variability. This effect could be explained by the spatial structures oriented parallel to the inline direction that were observed in these time-slices, as mentioned in section 5.2.4. However, a reversed behaviour is observed for the long range, where the higher variability coincides with the inline direction (red curves).

To fit the resulting experimental variograms, six basic structures were considered: one anisotropic short range C_1 ; one anisotropic mid-range C_2 ; and four long range structures, from C_3 to C_6 . Three of these long-range structures were necessary to model the amplitude variability behaviour along the crossline direction, where two cardinal sinus functions were combined to model the experimental variogram in this direction. However, the contribution of these periodic functions represents less than 10% of the total variance, as shown in Table 6.

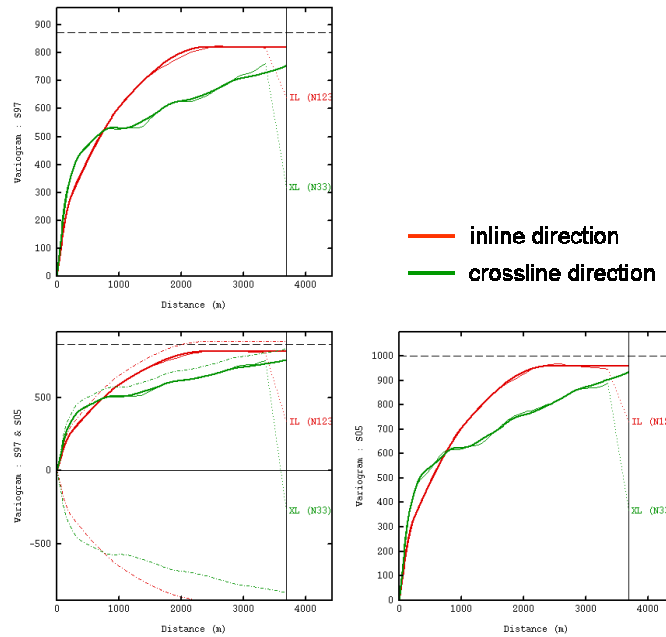


Figure 5-45 - Same as Figure 5-43, for Group G3.

Table 5-9 - Same as Table 5-8, for Group G3.

Structure		Ranges (m)		Sills			Correlation
		Inline	Crossline	S05	S97	S05xS97	
C ₁	Spherical	240	140	188 (20 / 18)	164 (20 / 20)	139 (17 / 17)	0.79
C ₂	Spherical	1 000	360	150 (15 / 15)	131 (16 / 16)	121 (15 / 15)	0.86
C ₃	Spherical	2 400	N/A	621 (65 / -)	526 (64 / -)	558 (68 / -)	0.98
C ₄	Cardinal sinus	N/A	1 600	59 (- / 6)	36 (- / 4)	45 (- / 5)	0.98
C ₅	Cardinal sinus	N/A	3 400	81 (- / 8)	92 (- / 11)	86 (- / 10)	1.00
C ₆	Spherical	N/A	5 600	540 (- / 53)	391 (- / 48)	435 (- / 53)	0.95

Group G4

The best fit of the experimental variograms and cross-variograms from Group G4 was achieved with a reduced number of basic structures, summing up to three. The first structure C₁, isotropic, with a range of 300m; and two other long-range structures were also

identified, one for each investigated direction. The correlation coefficient of the mid-range structure reaches 0.86, and is likely that this structure is associated to a common acquisition and/or processing noise for both S05 and S97 data rather than regarded as a production effect.

In the cross-line direction, a subtle hole-effect was observed, but was not considered in the final model due to its marginal contribution to the total variance. It is noticeable that the long-distance modeled ranges fit quite well with the turbiditic lobe dimensions geometry, as shown in Figure 5-47.

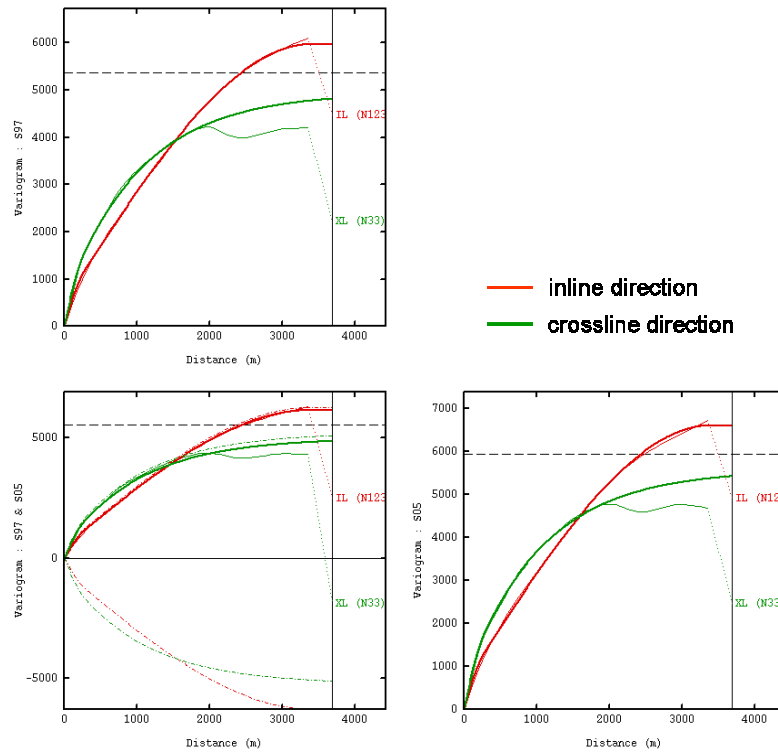


Figure 5-46 – Same as in Figure 5-43, for Group G4.

Table 5-10 – Same as Table 5-7, for Group G4.

Structure		Ranges (m)		Sills			Correlation
		Inline	Crossline	S05	S97	S05×S97	
C ₁	Spherical	300	300	559 (8 / 10)	495 (8 / 10)	455 (7 / 9)	0.86
C ₂	Spherical	3 400	N/A	6 044 (92 / -)	5 478 (92 / -)	5 714 (93 /)	0.99
C ₃	Exponential	N/A	3 100	5 000 (- / 90)	4 450 (- / 90)	4 550 (- / 91)	0.96

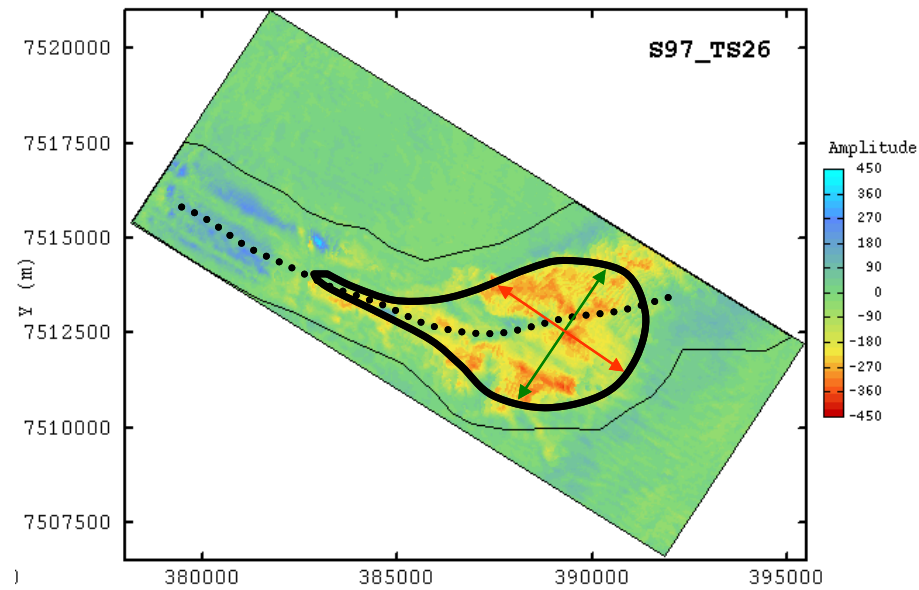


Figure 5-47 - Main characteristic dimensions of the turbiditic lobe geometry interpreted from time-slice TS26, G4, supporting the modelled structures of the variograms and cross-variograms. The thick black line suggesting the lobe system limits, as interpreted from the reservoir top anomalies. Dashed line indicates the main depositional axis.

Group G5

Following the same interpretation criteria as applied in the previous groups G3 and G4, three basic structures were modelled in this interval: an isotropic short-range and two long-range structures. A hole-effect is suggested in the inline direction, but due to its small contribution to the total variance, it was not considered.

The interpreted short-range structure shows a linear correlation coefficient of 0.8. This value, high if taken as the absolute value, is smaller than the one observed for the short-range structure in Group G4, equal to 0.86. This relative reduction of the correlation coefficient between S05 and S97 in this interval, at small scales, must be considered with care, and how it could be associated to the 4D effect.

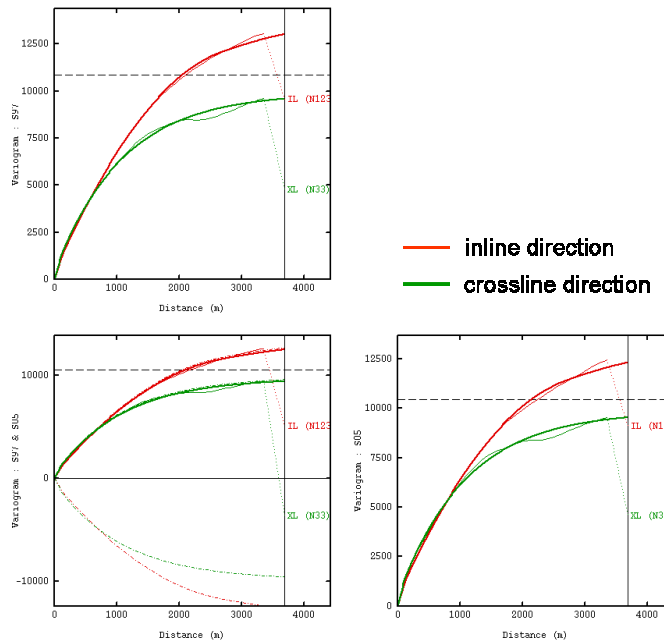


Figure 5-48 – Same as Figure 5-43 , for G5, corresponding to time-slices TS29-TS36.

Table 5-11 – Same as in Table 5-7, for Group G5.

Structure	Ranges (m)		Sills			Correlation
	Inline	Crossline	S05	S97	S05xS97	
C ₁ Spherical	140	140	368 (3 / 4)	290 (2 / 3)	260 (2 / 3)	0.80
C ₂ Spherical	2 600	N/A	3 800 (28 / -)	4 465 (31 / -)	4 097 (30 / -)	0.99
C ₃ Exponential	5 600	3 200	9 470 (69 / 96)	9 420 (67 / 97)	9 420 (68 / 97)	0.96

As observed in Group G4, a zonal anisotropy is also identified in this interval, and could be a response of the reservoir geometry, with a higher variability in the inline direction as show in the amplitude maps from Figure 5-34 and Figure 5-47.

Group G6

Most of the amplitude time-slices from this group do not sample the Marlim reservoir, but the underlying reservoir with similar acoustic properties, as already

mentioned in paragraph 0. This could be a possible explanation for the higher variability observed in the inline direction in comparison to the crossline.

Five spherical structures were used to model this nested variogram, as shown in Table 5-12.

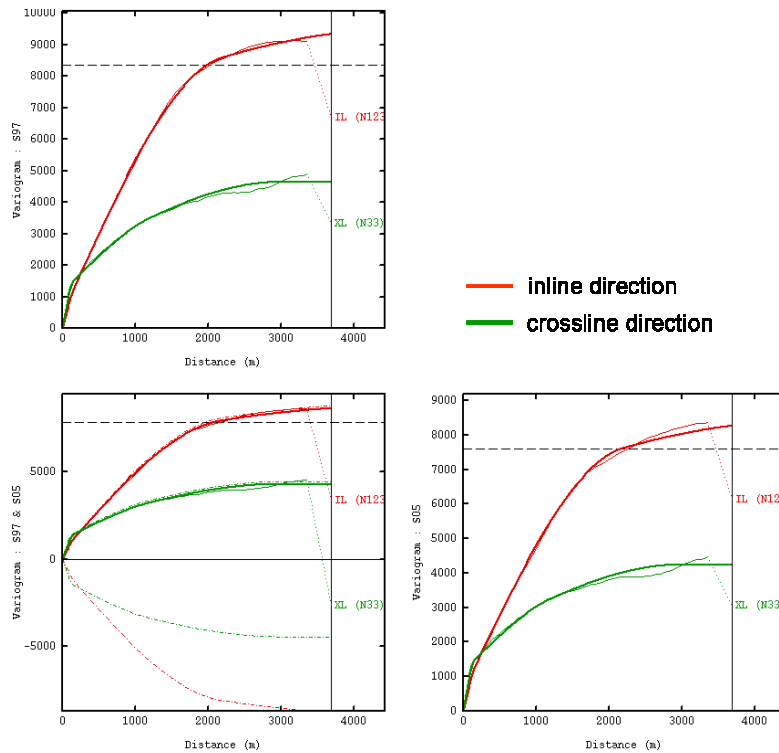


Figure 5-49 – Same as Figure 5-43 for Group G6.

Table 5-12 – Same as Table 5-7, for Group G6.

Structure		Ranges (m)		Sills			Correlation
		Inline	Crossline	S05	S97	S05xS97	
C ₁	Spherical	N/A	160.00	1 123 (- / 26)	1 118 (- / 24)	1 050 (- / 24)	0.94
C ₂	Spherical	180.00	N/A	508 (6 / -)	386 (4 / -)	387 (4 / -)	0.87
C ₃	Spherical	2 200.00	N/A	5 562 (66 / -)	6 418 (68 / -)	5 880 (67 / -)	0.98
C ₄	Spherical	N/A	1 200.00	814 (- / 19)	870 (- / 19)	772 (- / 18)	0.92
C ₅	Spherical	4 500.00	3 200.00	2 305 (28 / 54)	2 658 (28 / 57)	2 470 (28 / 58)	1.00

The first two structures, C_1 and C_2 , model the short range variability, exhibiting a high structural correlation coefficient, where C_1 structure has an important contribution to the total variance, equal to 26% and 24%, respectively for S05 and S97 data, in the crossline direction. The correlation coefficients of the mid and long range structures C_3 to C_5 are higher than 0.92, meaning that no remarkable differences between the two datasets can be identified at these spatial scales of variability.

The zonal anisotropy, as described in Group G5, is mainly due to reservoir geometry, showing contrasting amplitude values in the inline direction.

Group G7 Results

This interval corresponds to the bottommost group of time-slices, including the Blue Marker reference horizon, as described in paragraph 0. The variograms and the cross-variograms from S05 and S97 are similar, and a higher variability in the inline direction imposing a zonal anisotropy.

Five basic structures were used to describe the spatial variability of the data, including a nugget effect. The small-scale structure, with a high correlation coefficient and equal to 0.83, responds for 23% and 26% of the total S05 and S97 data variance in the inline direction, respectively. Additionally, one mid-range and two long-range structures were also identified, all them exhibiting high coefficients of correlation between S05 and S97, as shown in Table 5-7.

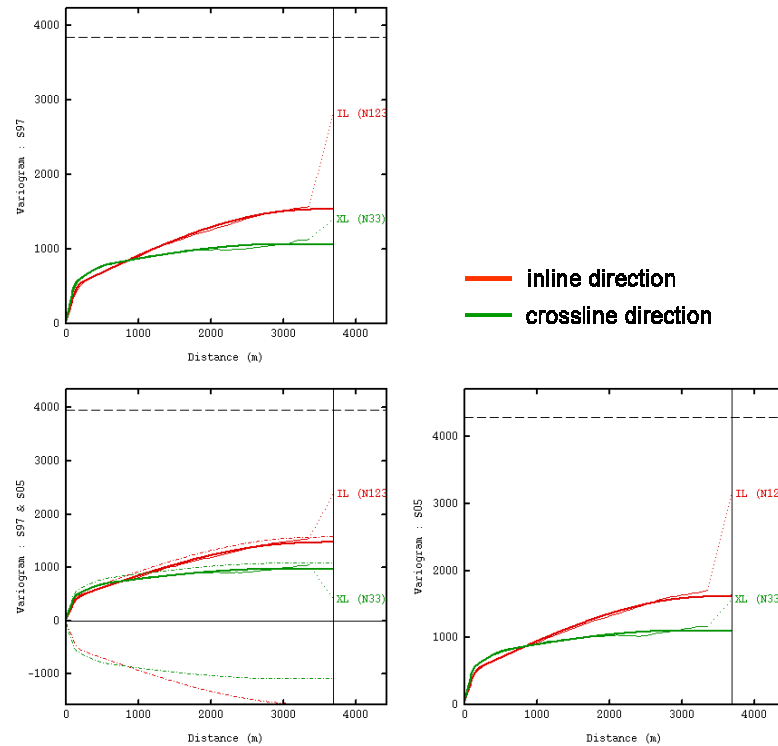


Figure 5-50 – Same as Figure 5-43, for G7.

Table 5-13 – Same as Table 5-7, for Group G7.

Structure		Ranges (m)		Sills			Correlation
		Inline	Crossline	S05	S97	S05xS97	
C ₀	Nugget			67 (4 / 6)	46 (3 / 4)	55 (4 / 6)	0.99
C ₁	Spherical	220	160	377 (23 / 34)	405 (26 / 38)	325 (22 / 33)	0.83
C ₃	Spherical	N/A	600	256 (- / 23)	238 (- / 22)	220 (- / 23)	0.89
C ₂	Spherical	3 200	N/A	778 (48 / -)	715 (46 / -)	725 (49 / -)	0.97
C ₄	Spherical	4 000	3 000	402 (25 / 36)	380 (25 / 36)	375 (25 / 38)	0.96

Summary and discussion of the Structural Analysis

The analysis of the variograms and cross-variograms from amplitude data extracted from time-lapse seismic volumes is quite challenging. Usually, time-lapse seismic datasets are processed aiming to minimize the discrepancies due to distinct acquisition parameters, resulting in quite similar volumes. Therefore, this similarity is achieved and imprinted in

the variograms, as observed in the previous paragraphs, where the variograms functions from the two investigated variables S05 and S97 showed similar responses.

In this study, a 200 ms time window extracted from a subset of seismic data from two seismic surveys, comprising the Marlim reservoir interval, was selected. This interval was subdivided into seven groups of amplitude time-slices, where groups G1 and G7 are the topmost and the bottommost groups, respectively.

The interpretation of the resulting variograms and cross-variograms for the first three Groups G1 to G3, showed a characteristic geometric anisotropy, with a less continuous behaviour in the inline direction. In the three groups containing the reservoir interval, Group G4 to G6, a zonal anisotropy was observed instead, with higher variance in the inline direction.

A summary of the most important remarks and conclusions of the implemented structural analysis over the flattened seismic data from S05 and S97 is presented.

- no Gaussian behaviour was detected on the modelled variograms and cross-variograms; suggesting that no remarkable trace averaging was introduced during the seismic processing phase;
- comparing the inline and crossline directions, the variograms from Groups G1 and G2 present a geometric anisotropy, with orthogonal directions reaching the same sill at different ranges. A possible explanation for this effect could be the more homogeneous amplitude values distribution on these time intervals, all lying above and outside the reservoir level. This homogeneity of the amplitude data distribution is confirmed by the normal histograms from Figure 5-23;
- on the other hand, the variograms and cross-variograms from Groups G4 to G6, that include the reservoir zones, show a zonal anisotropy, with higher variability in the inline direction. This anisotropic effect reaches its maximum expression on Group

G6, where the reservoir related amplitude anomalies are concentrated on the east part of the field, forming a thick stripe almost parallel to the crossline direction;

- a nugget effect was considered for a single interval, Group G7. Usually, the nugget effect is a high frequency structure, characterized by a discontinuity at the origin of the variogram. It is frequently associated to micro-scale effects and/or measurements or sampling errors (Sandjivy, 1984);
- the spherical model was the most frequent basic model used to adjust the experimental variograms and cross-variograms, followed by the exponential and by the cardinal sinus basic models; the introduction of the cardinal sinus base model enhanced the fitting of the nested variograms from Groups G1 and G4. However, on both cases, the hole effect did not represent a significant contribution in terms of variance;

The simplest nested structures were observed on those groups including the reservoir anomalies. The best fit was achieved with only 3 base structures on Groups G4 and G5, whereas Groups G1 and G7, which do not sample the reservoir, were fitted with 5 and 4 base structures, respectively;

A graphic representation of the basic structures used to model the spatial variability of S05 and S97 seismic datasets is shown in Figure 5-51 and Figure 5-52. In these graphs, the linear correlation coefficients are plotted as a function of the correspondent structure range, where the colour classification indicates to which time-slice group each structure belongs to. As a reminder, the linear spatial correlation coefficient is defined in Goovaerts (1997) as

$$\rho_{ij}^l = \frac{b_{ij}^l}{\sqrt{b_{ii}^l b_{jj}^l}} \quad (85)$$

And where b_{ij}^l are the sills of the variance-covariance matrix resulting from the modelling of the l spatial structures. Accordingly, each point in the graph represents a single spatial structure interpreted at each of the 7 time-slices groups, as described in paragraphs 5.2.5, for both inline and crossline directions. No mention to the type of the considered basic structure is given in these graphs.

Table 5-14 - Summary of all correlation coefficients for all time-slice Groups G1 to G7.

	G1	G2	G3	G4	G5	G6	G7
C_0							0.99
C_1	0.61	0.65	0.79	0.86	0.8	0.94	0.83
C_2	0.91	0.87	0.86	0.99	0.99	0.87	0.89
C_3	0.92	0.86	0.98	0.96	0.96	0.98	0.97
C_4	0.99	0.99	1			0.92	0.96
C_5	0.92		0.95			1	
C_6			0.98				

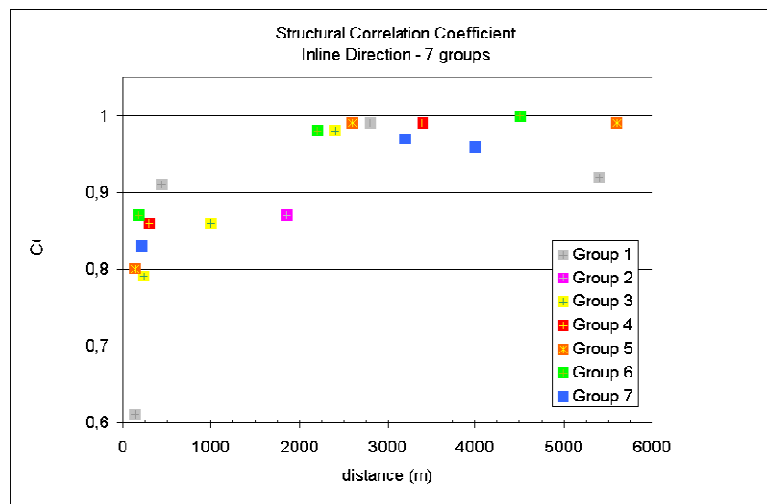


Figure 5-51 - Structural correlation coefficients computed for all spatial structures in the inline direction. Correlation coefficients are plotted as a function of the structure range.

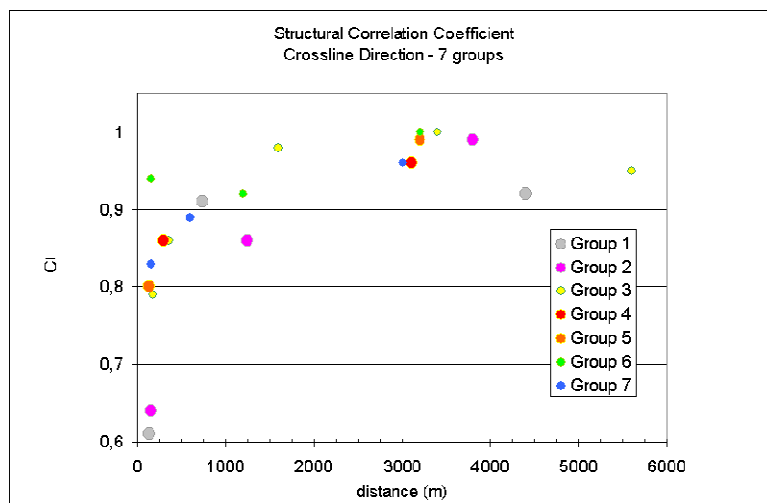


Figure 5-52 – The same as in Figure 5-51, for the crossline direction.

The points which range exceeds 3,400 m - the maximum variogram investigated distance - should be discarded, or analysed with care. These points, rather than belonging to the dataset sample population, are just a result of variogram modelling adjustment procedure. It is important to keep in mind that the main goal when performing such analysis is to explain the different scales of spatial variability, ideally by linking a plausible physical understanding of each of the interpreted structures. For instance, a spatial structure with a given range identified on all different time-slices groups should not, *a priori*, be associated to a production related effect, but rather to a (coherent) noise possibly associated to the seismic acquisition or processing. This event could equally affect many or even all the investigated time-slices. It is also reasonable to expect that, as the studied interval comprises a time window of 200ms, a few different geological scenarios were sampled and are represented by the analysed seismic time-slices. These different geological scenarios should be modelled and characterized by different spatial components depending on their relative time position.

Generally, a *high structural correlation* coefficient is assigned to a given spatial structure when it equally explains the common spatial variability of both input data, for that given scale. Otherwise, a *lower structural correlation coefficient* is observed. In this case, the given spatial structure better explains the variability associated with only one of the input variables.

Analysis of the graph from Figure 5-51, representing the structures interpreted in the inline direction, shows that:

- two main point clusters are observed, one for *short* and one for *long range* structures, respectively;
- the *short range* structures, with ranges $a < 250\text{m}$, show smaller correlations than the long ones, typically between 0.8 and 0.9 for the short and bigger than 0.9 for the long ranges;

- the *short range* structure from Group G1, representing the uppermost time-slices interval, shows the smallest coefficient, equal to 0.61. This group presents the same behaviour in the crossline direction, for this class of range;
- the *mid-range* structures ($250 < a < 1500$ m) are less representative than short and long ranges; only two samples from Groups G1 and G3 are identified;
- all *long range* spatial structures ($a > 1500$ m) exhibit very high correlation coefficients, almost close to one;

In the crossline direction from Figure 5-52, it was noticed that:

- *higher dispersion* of the correlation coefficients in the short range scales, when compared to the inline direction;
- *smaller dispersion* for the long-range structures, with a cluster of points with ranges varying from 3,000 to 3,400m, and correlations higher than 0.95, comprising groups G3 to G7;
- Groups 1 and 2 show *similar distributions*, suggesting that these spatial structures were equally sampled in both groups, with almost the same variogram and cross-variogram parameters over the investigated ranges;
- the same holds for Groups G4 and G5, where only short and long ranges were identified at these levels; and
- *mid-range* structures were sampled by different groups, which was not observed in the inline direction.

Discussion

High correlation coefficients observed between S05 and S97 data should correspond to spatial structures for which: (i) no changes are observed *before and after* exploitation; and (ii) the seismic acquisition noise was similar.

This is the case for the long-range structures identified in the inline direction for groups G1 to G7, except G2, considering the ranges between 2,000 and 3,400m; and for spatial structures interpreted in the groups G3 to G7, from 3,000 to 3,400m in the crossline direction. These long range structures potentially reflect the reservoir architecture and are not affected by the exploitation, or by conditions of the seismic data acquisition. These structures should be considered as seismic imprints of the *geological and sedimentary depositional structures*, the observed anisotropy having to be related to sediment infill directions and/or, in some parts of the reservoir, as turbidite channels.

On the contrary, small range structures identified in G1, in both inline and crossline directions, as well as in G2, in the crossline direction, are probably to be related to responses to specific seismic processing filters applied during the cross-equalization phase, such as re-meshing of the acquisition grid. These spatial structures should be considered as an *artefact*.

Groups G2 and G3 present both in inline and crossline directions, changes from S05 to S97 surveys indicated by smaller correlation coefficients at mid range scales, close to 1 km. These scales of spatial variability could be related to *reservoir changes due to production*.

In addition, structures observed on groups G3, G4, G5 and G7 which present changes, corresponding to correlation coefficients from 0.8 to 0.9 at spatial scales in the range of 250 to 500 m, in both inline and crossline directions, could be potentially related to both *acquisition or exploitation* effects.

The above suggested results show that processing raw seismic 3D cubes include geological, acquisition noise and 4D exploitation effects which can be of primary importance in some cases to better understand the architecture of a reservoir. However, in mature reservoir where the objective is to optimize to injection/production exploitation scheme, the underlying geological structures which are common in both acquisition seismic cubes might be a drawback and need to be moved or filter out. This is why the above methodology is applied on the 3D amplitude differences rather than on the raw amplitude cubes.

5.2.6. Factorial Cokriging Results

After characterizing the spatial structures identified during the structural analysis, and interpreted their main characteristics in terms of spatial distribution ranges and their possible meaning, the next proposed step is to filter out those structures clearly associated to noise.

The focus will be on the results obtained in Group G4, mainly characterized by a sequence of time-slices showing contrasting values: *strong negative* amplitude values, characteristic of the reservoir top anomalies, surrounded by background, close to zero amplitude values and associated to the encasing non-reservoir rocks, as observed in the time-slice amplitude maps from Figure 5-31.

The reservoir external geometry is well explained by the seismic data on both vintages, and the remarkable feature observed on the time-slices from Group G4, corresponds to the anomalous amplitude values associated to the Marlim reservoir top, which strongly suggests a turbiditic lobe geometry spread in the central part of the maps. Even the inflexion of the main depositional axis of this turbiditic lobe system, from NW-SE direction to the W-E direction, could also be inferred in the area. This depositional lobe system is known, being already reported by Oliveira et al. (2005).

5.2.7. Decomposing and filtering the short-range G4 structures

The spatial variability from S05 and S97 datasets was modelled by a nested structure as shown in Figure 5-46, and with structural parameters summarized in Table 5-10. The common short range C_1 spatial structure at 300 m interpreted as noise or artefact introduced by the acquisition scheme is remarkably observed in both S05 and S97 datasets. It was decided to remove this spatial component using factorial co-kriging analysis. Let remind that the sills of the short range structures are equal to 559, 495 and 455 for the S05, S97, and S05×S97 datasets, respectively.

The diagonalization of the sill correlation matrix from the C_1 spatial structure quantifies the variance explained by the two orthogonal factors. In this case, about 90% of the main spatial variability related to the short range C_1 structure is explained by factor F1, while factor F2 counts for only 10%. It is also important to keep in mind that this component responds for only 10 % of the total variance of the modelled nested structure.

A careful analysis of amplitude time-slices of the resulting factor F1 shows that:

- when compared to the original amplitude time-slices S05 and S97, this factor seems to reproduce the *high amplitude limits*, in agreement with the area of occurrence of the turbiditic lobe geometry;
- the observed features show a spatial distribution that *does not coincide* with inline or crossline directions;
- the fault trace that occurs at the SW part of the field, is well reproduced in the F1 map ;

F1 is, per construction, orthogonal to F2, so no linear correlation is observed, as shown in Figure 5-55. In addition, no spatial correlation is observed between F1 and the difference S05-S97 amplitude maps, which is confirmed by the very small linear

correlation coefficient ($\rho = 0.12$) computed between F1 and the difference map as shown in Figure 5-56. On the other hand, the factors F2 shows:

A high linear correlation coefficient ($\rho = 0,74$) with the difference S05-S97, as shown in the scatter diagram of Figure 5-56, Figure 5-53 and Figure 5-54;

Five geometrical spot structures observed in the west and (also on F1), identified as related to wells, are possibly linked to 4D effects due to exploitation

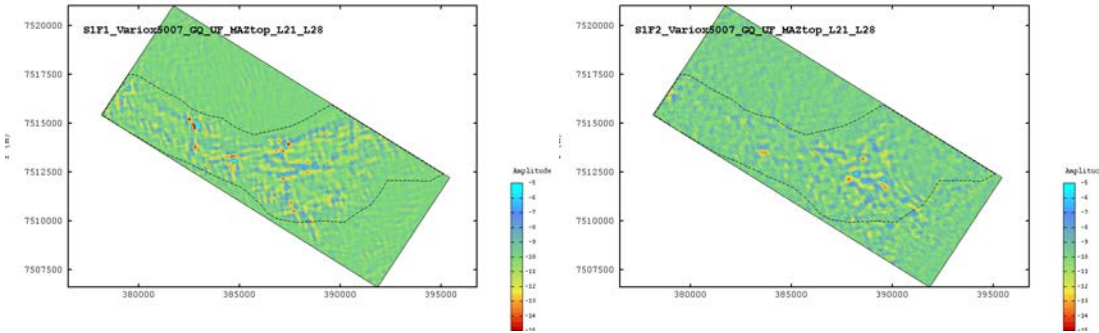


Figure 5-53 – TS26 time-slice amplitude values corresponding to orthogonal factors F1 (left) and F2 (right).

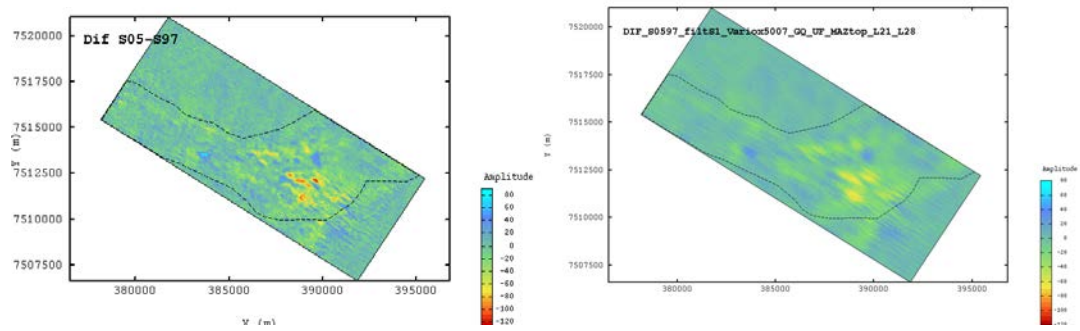


Figure 5-54 - Amplitude values for TS26 time-slice.

On the left side of Figure 5-54, the raw difference Dif S05-S97 and on the right, the difference DifS05-S97 after filtering the S1 component from both campaigns.

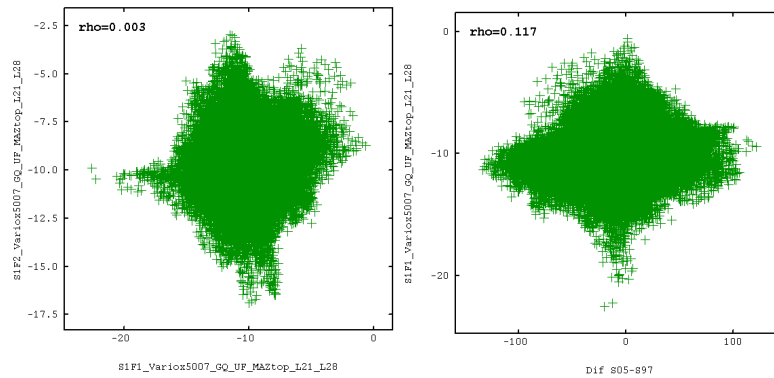


Figure 5-55 - Scatter diagram of factors F1 and F2 computed for all time-slices from group G4. No linear correlation is observed.

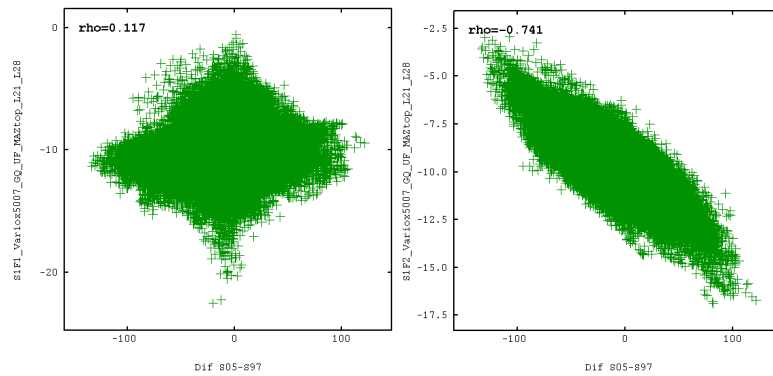


Figure 5-56 – Scatter plots of Factor 1 (left) and Factor 2 (right) and the difference Dif S05-S97. Scatter plots are computed for all time-slices from Group G4.

5.2.8. Results from time-slices clustering

Based on the analyses of the correlation coefficients presented in paragraph 5.2.4, as well as on a review of the time-slices maps and on the variogram behaviour analysis for each slice, a new grouping of time-slice was proposed, as follows:

- NG1 (from TS1 to TS12) corresponding to the *Non-reservoir zone*;
- NG2 (from TS13 to TS20): corresponding to a *channelling zone* of the main reservoir, mainly at the west most area;

- NG3 (from TS21 to TS36): *Marlim reservoir zone*.
- NG4 (from TS37 to TS43): bottommost slices of the Marlim reservoir, but mainly representative of the *South Marlim reservoir*, underneath Marlim reservoir;
- NG5 (from TS44 to TS50): *regional BM marker*, taken as the reference horizon for the flattening procedure.

Taking these new groups into account, the variograms and cross-variograms were recomputed, as well as the structural modelling for all new groups. The results are presented in the next section.

Table 5-15 – New time-slice clustering based on previous results, reducing to five the number of clusters.

Group	Top time-slice (TS) number	Bottom time-slice (TS) number	Thickness (ms)
NG1	TS01	TS12	48
NG2	TS13	TS20	32
NG3	TS21	TS36	64
NG4	TS37	TS44	32
NG5	TS45	TS50	24

Table 5-16 – Main statistical parameters for all time-slice groups.

Group	Minimum Amplitude Value S05 / S97	Maximum Amplitude Value S05/S97	Mean Amplitude S05/S97	Dispersion Variance of Amplitude S05/S97
NG1	-207 / -225	94 / 91	-1 / 1	467 / 366
NG2	-419 / -388	405 / 447	1 / 1	999 / 873
NG3	-471 / -511	472 / 480	-1 / -2	8 262 / 8178
NG4	-531 / -564	508 / 534	14 / 16	7 601 / 8347
NG5	-330 / -272	407 / 428	16 / 18	4 285 / 3845

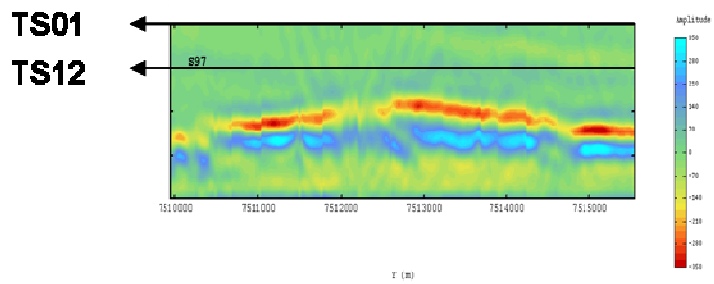


Figure 5-57 – Crossline seismic section from S97 survey showing the time-interval from TS01 to TS12, above the Marlim reservoir. The interval between time-slices corresponds to one sampling interval, or 4ms, vertical exaggeration of approximately 10 times.

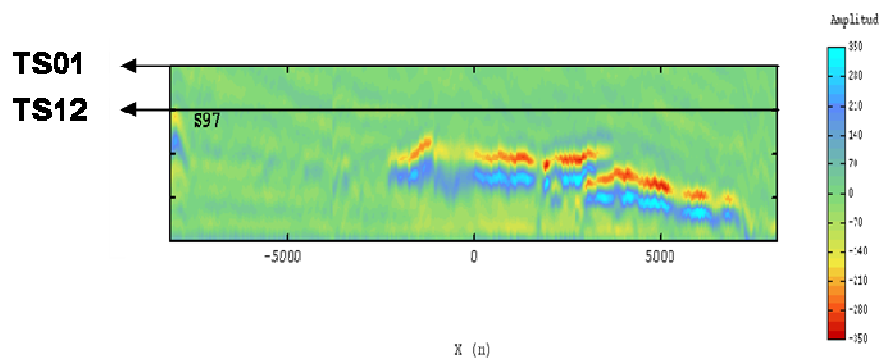


Figure 5-58 - Same as in Figure 41, for the inline direction. Vertical exaggeration of approximately 20 times.

NG1: Non-reservoir zone (TS01 to TS12)

This group includes all the first 12 time-slices (previously referred to as Group G1 and Group G2), and comprises the uppermost portion of the investigated subset of the Marlim seismic volume, as shown in Figure 5-57 and Figure 5-58.

Comparing the previous Group G2 structural modelling results with this new one, it is clear that the major contribution for the final modelled structural behaviour came from

the bottommost layers (TSL7 to TL12), as the number of nested variograms, the ranges and sills show a similar response.

When regrouping G1 and G2 into NG1, the periodicity along the inline direction is observed on almost all individual time-slice variograms as a hole-effect. This effect shows a periodicity of approximately 1.9 km, and presents a downward decreasing contribution to the total variance. This effect is much likely to be associated to contrasting dips observed on the uppermost part of the investigated volume in comparison to the dip of the regional marker used as the flattening reference, as shown in Figure 5-58. It was decided to do not consider this effect on the final theoretical model of the group.

A summary of the main parameters used to model the spatial variability in this zone is presented in

Table 5-17. Under the hypothesis of a linear model of correlogramization, as described in Chapter 3 - , four basic variograms were linearly combined to define a nested structure describing the spatial variability of the data. The inline direction is less continuous than the crossline, but both reach the same sill value characterizing a geometric anisotropy.

The first spatial structure, referred to as C1, maps the short scale variability, with range $a = 200$ m, and is only characterized in the crossline direction. The theoretical variogram was fitted using a spherical model, representing a contribution to the total variance of 23%, 22% and 17% for the S05, S97 and the cross-variogram S05xS97, respectively, as show in Table 5-17. The analysis of the sill matrix show that the variance contribution of this short scale setructure is similar for both monitor S05 and the base S97 data, but is less important for the commom variability. Additionally, a small correlation coefficient was observed, equal to 0.65. The dimension of this structure is close to those of the periodic features observed in the central area of Figure 5-59. This structure is probably associated to acquisition related noise and will be filtered out.

Structures C₂ and C₄, both spherical, with ranges equal to 1,250 m and 3,800 m, were combined to describe the medium-to-long scale variability in the crossline direction,

while a single exponential structure C_3 , with range $a = 1,480$ m, was used in the inline direction. In terms of correlation coefficient, higher values were observed on the structures C_2 and C_4 when compared to C_3 . These high correlation values indicate that these structures correspond to a common part that is equally well explained by both S05 and S97 vintages.

Table 5-17- Resulting modelling parameters from structural analysis of Group NG1. In brackets, the percentage of the total variance explained by each structure, in the inline and in the crossline direction, respectively.

Structure		Ranges (m)		Sills			Correlation
		Inline	Crossline	S05	S97	S05xS97	
C_1	Spherical	N/A	200	118 (-/23)	88 (-/22)	66 (-/17)	0.65
C_2	Spherical	N/A	1250	94 (-/18)	105 (-/26)	90 (-/23)	0.91
C_3	Exponential	1480	N/A	500 (100/-)	404 (100/-)	395 (100/-)	0.88
C_4	Spherical	N/A	3 800	310 (-/59)	205 (-/52)	244 (-/61)	0.97

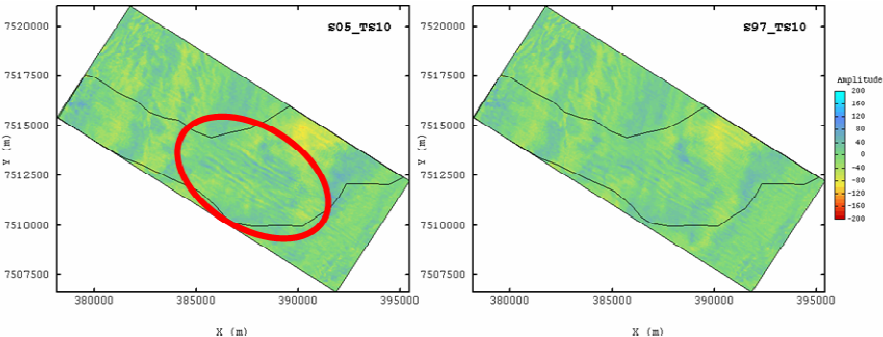


Figure 5-59 – TS10 time-slice, amplitude map of S05 (left) and S97 (right) surveys. The red circle points out the structure mapped as C_1 .

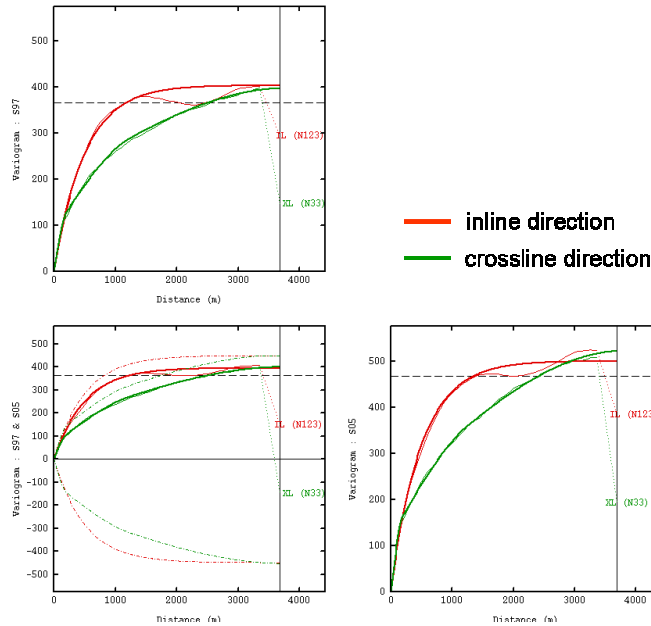


Figure 5-60 – Experimental (thin) and modelled (thick) cross-variograms computed on group NG1. Horizontal dashed line represent the dispersion variance, which is 28 % higher in S05 survey when compared to the S97 survey.

It was noticed that the monitor survey S05 shows a higher experimental dispersion variance when compared to the base survey ($\sigma_{S05}^2 = 467$ against $\sigma_{S97}^2 = 366$), as shown in Table 5-16. The interpretation of the two other long range structures is not straightforward, as no recognized geologic and/or seismic structure is directly associated to these dimensions. A possible explanation for these structures could be the dipping effect, as these layers are far away from the one taken as the reference for the flattening.

NG2: Thin reservoir channelized zone (TS13 to TS20)

Six basic structures were used to model the nested variograms and cross-variograms of the thin channelized reservoir zone, including one anisotropic short range C_1 , one anisotropic mid-range C_2 and four long range structures C_3 to C_6 . A geometrical anisotropic character is observed when comparing the inline and crossline directions, with a less continuous character exhibited in the inline direction.

Three of the long range structures were combined to model the amplitude variability behaviour along the crossline direction, comprising two cardinal sinus functions representing the periodic structures and one spherical function. However, the contribution of these periodic functions represents less than 10% of the total variance, as shown in Table Table 5-18.

In the inline direction, one mid range and one long range structures are necessary to explain the variability at these spatial scales. When comparing NG2 variograms to the NG1 ones, long ranges structures are observed in both S05 and S97 data with ranges of similar order of magnitude. These long ranges structures can be attributed to the sedimentary architecture of the reservoir, specifically to the flow of sediments and/or channelling, as observed in the west area. They are related mainly to geological structures rather than to acquisition or 4D effects, as the correlation coefficients are close to one. Similarly to the NG1 group, the smallest structure at 240 to 180m can be attributed to the acquisition related noise or more precisely to the process used to re-mesh the S05 and S97 campaigns at the same grid scale (correlation coefficient of 0.79). Finally, the median size structures (1000 x 360 m) with a correlation coefficient of 0.86 can be linked to possible channel structures observed in this central part of the reservoir.

Table 5-18 - Same as

Table 5-17, for group NG2.

Structure		Ranges (m)		Sills			Correlation
		Inline	Crossline	S05	S97	S05xS97	
C ₁	Spherical	240	180	188 (20/18)	164 (20/20)	139 (17/17)	0.79
C ₂	Spherical	1000	360	150 (16/15)	131 (16/16)	121 (15/15)	0.86
C ₃	Spherical	2400	N/A	621 (65/-)	526 (64/-)	558 (68/-)	0.98
C ₄	Cardinal sinus	N/A	1 600	59 (-/6)	36 (-/4)	45 (-/5)	0.98
C ₅	Cardinal sinus	N/A	3 400	81 (-/8)	92 (-/11)	86 (-/10)	1.00
C ₆	Spherical	N/A	5 600	540 (-/53)	391 (-/48)	435 (-/53)	0.95

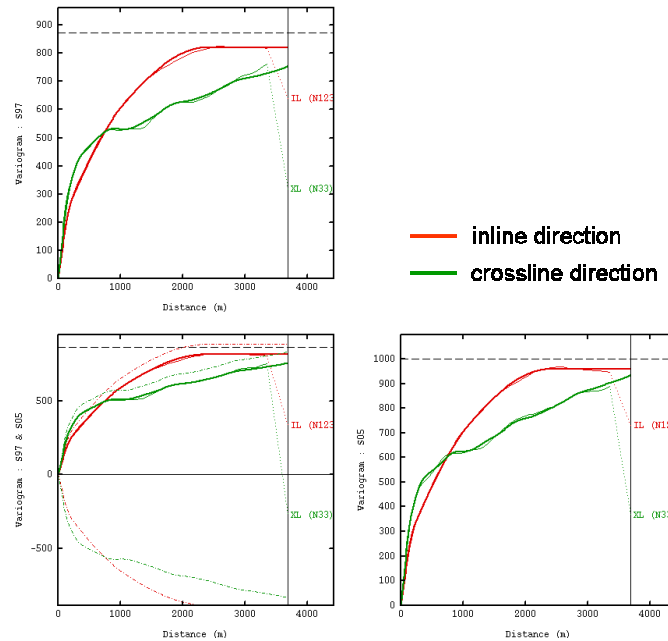


Figure 5-61 - Same as in Figure 5-60, for NG2.

NG3: Marlim reservoir zone (TS21 to TS36)

The main Marlim reservoir zone is mainly represented by group NG3, comprising 17 time-slices, from TS21 to TS36. It corresponds to a total thickness of 60ms (TWT), as shown in the crossline amplitude section from Figure 5-62, taken from the base S97 seismic vintage. The reservoir top is associated to a maximum negative amplitude value, in red, and the reservoir bottom as a positive seismic peak, in blue.

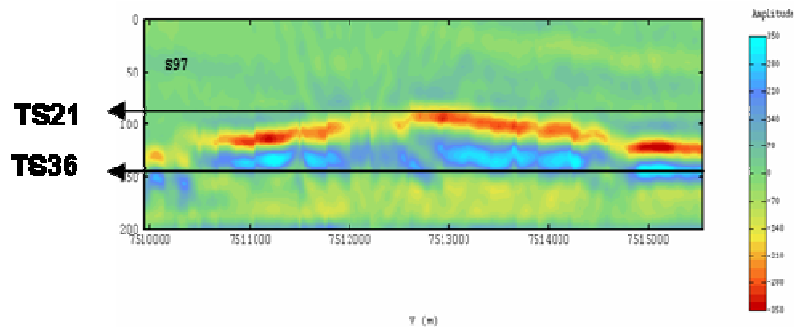


Figure 5-62 – Vertical crossline section from S97 survey showing the TS21 to TS36 time interval. This zone corresponds to the main Marlim reservoir zone. Vertical exaggeration of approximately 10 times and vertical time scale in ms (TWT).

The dispersion variance of both monitor S05 and base survey for this interval is of the same order of magnitude ($\sigma_{S05}^2 = 8178$ and $\sigma_{S97}^2 = 8261$). These high variance values could be a response to contrasting amplitude values between reservoir and non-reservoir zones, as it can be seen following the black line representing the time-slice TS21.

The structural analysis resulted in a quite good fitting, where three basic structures were considered to adjust the nested variograms, as shown in Figure 5-63. A small scale isotropic spherical structure with range $a = 155$ m, consistent with the previous interpretations, was identified. Its contribution to the total variance is small, and equal to 3% for S05 and 2% for S97, with a reduced linear correlation coefficient equal to 0.76.

The analysis of the constituting time-slices corresponding to this interval showed that two small scale effects could possibly be associated to the modelled small range structures:

the first one, associated to the *acquisition noise*, coincident with the inline direction and also identified on overlying time-slices corresponding to Groups G1 and 2;

anomalous amplitude values occurring parallel to the inline direction, mainly observed on the west area of the investigated sub-volumes, associated to channelized turbiditic reservoirs and mainly detected on the uppermost time-slices of this interval;

Two other long range basic structures were considered to model the experimental variograms: (a) a spherical structure, oriented parallel to the inline direction with a range at $a=3,250$ m and (b) a third structure, anisotropic, with ranges equal to 5,200m and 2 780m, in the inline and crossline directions, respectively, as shown in Figure 5-63 and Table 5-19.

Table 5-19 – Resulting structural modeling parameters for group NG3. In brackets, the variance contribution in the inline and crossline directions (in percentage).

Structure		Ranges (m)		Sills			Correlation
		Inline	Crossline	S05	S97	S05xS97	
C ₁	Spherical	155	155	280 (3/4)	235 (2/3)	195 (2/3)	0.76
C ₂	Spherical	3,250	N/A	3,168 (30/-)	3490 (33/-)	3305 (32/-)	0.99
C ₃	Exponential	5,200	2780	7,030 (67/96)	6,805 (65/97)	6,825 (66/97)	0.99

Comparing these results to the previous structural analysis, where the topmost and bottommost slices were divided into Groups G4 and G5, no major differences are observed. The number and type of base structures were kept the same.

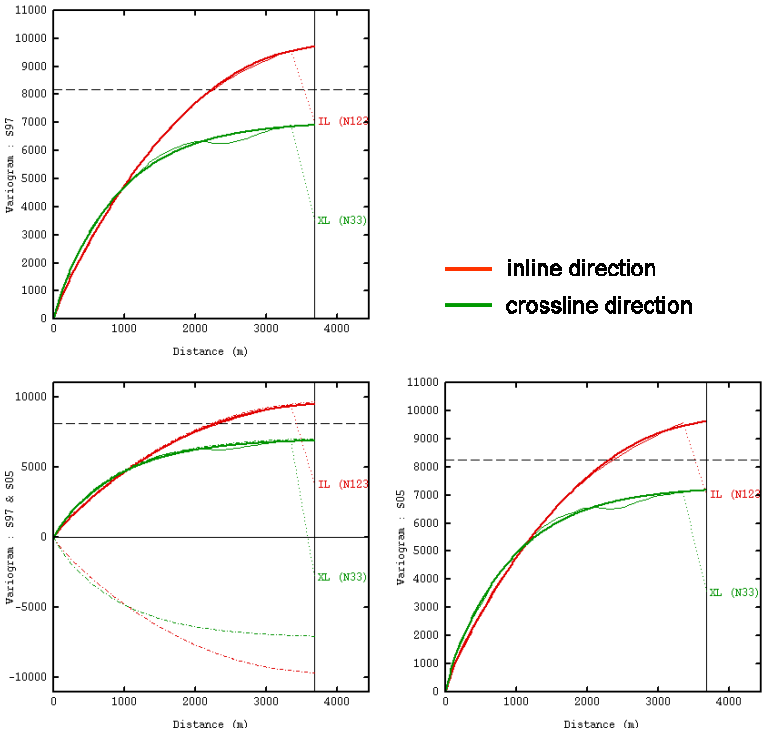


Figure 5-63 - Variograms of S97 (top) and S05 (bottom right) and cross-variogram S97xS05 (bottom left) for group NG3 (TS21-TS36) including all time-slices from the Marlim reservoir level.

NG4: Lower Marlim and Marlim South reservoirs (TS36-TS44)

The amplitude time-slices belonging to Group NG4 (TS37-TS44) sample the Marlim reservoir, but preferentially represent the underlying producing interval, known as the *Marlim South reservoir*. The hydraulic communication between these two producing zones is subject to discussion, and the time-lapse data is likely to be a useful tool to better describe and understand these issues. In terms of seismic response, the South Marlim reservoir exhibits similar acoustic properties when compared to the Marlim, despite its reduced thicknesses in this area.

The average variograms and cross-variograms of this group are presented in Figure 5-64. A pronounced zonal anisotropic behaviour is observed, where the inline direction exhibits almost twice of the variance of the crossline direction. This effect could be associated mainly to the reservoir external geometry, pinching out along the inline direction.

Comparing the dispersion variance observed on the monitor S05 with the S97 base survey for this interval, $\sigma_{S05}^2 = 7,601$ and $\sigma_{S97}^2 = 8,347$, one may notice that this group is the only interval from all analysed groups where the variance observed in the base survey S97 is higher than that from the monitor S05 survey, amounting to a total difference of 9% and considering the base survey as the reference. Possible causes are related to production effects at the bottommost layers from the Marlim reservoir, as expected, or an unexpected pronounced 4D effect on the South Marlim reservoir. This hypotheses assumes implicitly a strong connectivity between these two reservoirs. To clarify this aspect, further investigations must be implemented to improve seismic resolutions, as, for instance, by performing a pre-stack simultaneous inversion of this dataset.

Five spherical structures were considered to model these nested variograms, as shown in

Table 5-20. High correlation coefficients are observed for the interpreted spatial structures which mean that both variables are quite well explained, at these scales, by these structures.

It is interesting to notice the higher correlation coefficient observed for the short range structure C_1 , when compared to the same range structure interpreted in the previous Group NG3, from the Marlim reservoir. In this case, this short range structure plays a more important role in terms of variance contribution, as shown in

Table 5-20, and equal to 26 % and 24% for S05 and S07 surveys, respectively, in the crossline direction. These contributions are approximately 10 times bigger than those observed in the Marlim reservoir. Note also that its correlation is close to 0.95, so it appears as a permanent structure in both S05 and S97 campaigns, and it is difficult to attribute it to an exploitation effect. The small structure of 180 m observed only in the inline direction, with a contribution of 6% for S05 and a correlation coefficient of 0.87 is more likely to be associated to exploitation effects.

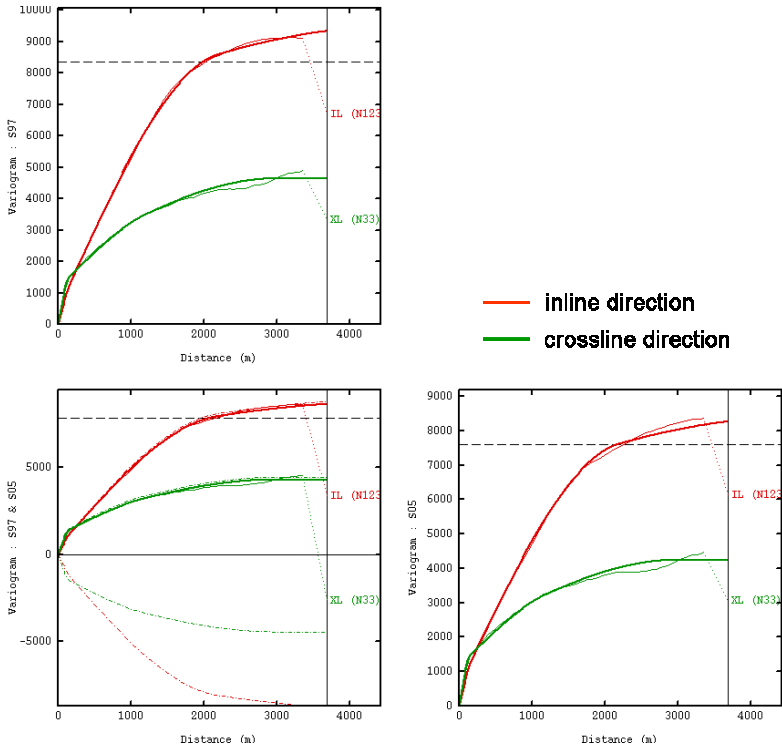


Figure 5-64 – Same as Figure 5-63, for group NG4.

Table 5-20 – Same as in

Table 5-17, for the Group NG4.

Structure		Ranges (m)		Sills			Correlation
		Inline	Crossline	S05	S97	S05xS97	
C ₁	Spherical	N/A	160	1 123 (-/26)	1 118 (-/24)	1 050 (-/24)	0.94
C ₂	Spherical	180	N/A	508 (6/-)	386 (4/-)	387 (4/-)	0.87
C ₃	Spherical	N/A	1200	814 (-/19)	870 (-/19)	772 (-/18)	0.92
C ₄	Spherical	2 200	N/A	5 562 (66/-)	6 418 (67/-)	5 880 (67/-)	0.98
C ₅	Spherical	4 500	3 200	2 305 (28/54)	2 658 (28 /57)	2 470 (28/58)	1.00

NG5: Regional BM marker (TS45-TS50)

This group represents the bottommost part of the analysed 200ms time interval, where the time-slice TS50 corresponds to the regional marker used as the flattening reference.

Experimental variograms for both surveys show similar behaviour, as shown in Figure 5-65, where five basic structures were considered to fit the nested experimental variograms. The short range behaviour of all variables suggested the inclusion of a nugget component, even with a small variance contribution of the order of 4%.

One short range structure was included with ranges equal to 220m and 160m, in the inline and crossline directions, respectively.

Table 5-21 – Same as in

Table 5-17, for the Group NG5.

Structure		Ranges (m)		Sills			Correlation
		Inline	Crossline	S05	S97	S05xS97	
C ₀	Nugget			67 (4/6)	46 (3/4)	55 (4/6)	0.99
C ₁	Spherical	220	160	377 (23/34)	405 (26/38)	325 (22/33)	0.83
C ₂	Spherical	N/A	600	256 (-/23)	238 (-/22)	220 (-/22)	0.89
C ₃	Spherical	3 200	N/A	778 (48/-)	715 (46/-)	725 (49/-)	0.97

C ₄	Spherical	4 000	3 000	402 (25/36)	380 (25/35)	375 (25/38)	0.96
----------------	-----------	-------	-------	-------------	-------------	-------------	------

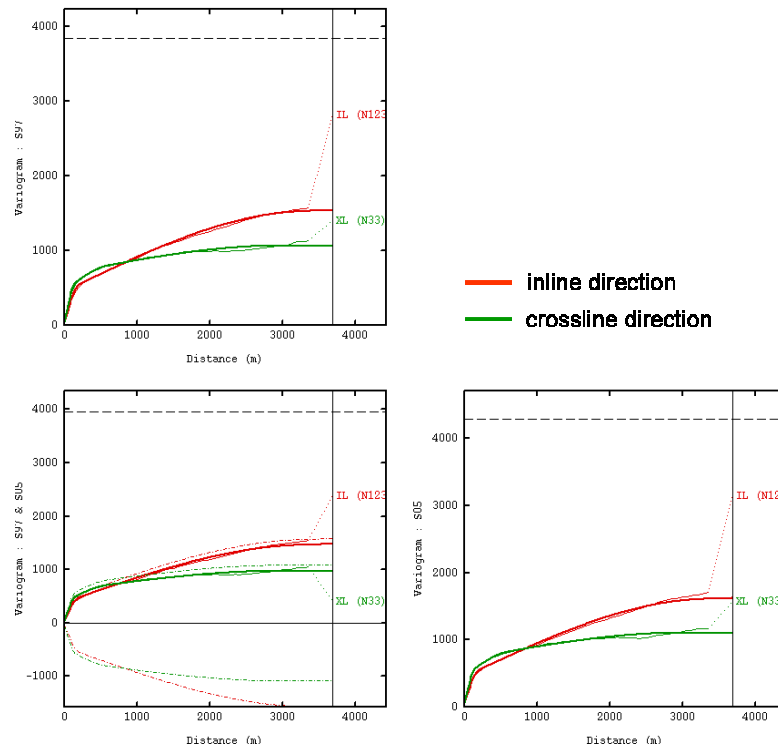


Figure 5-65 – Same as Figure 5-63, for group NG5.

These ranges are consistent with those identified on the previous group, but in group NG5 the variance contribution is more important, of the order of 20%, with a high linear correlation between the S05 and S97 campaigns. Three other spherical structures were included. One of mid range, oriented inline and with a linear correlation coefficient of 0.89, and two long structures that explains most of the data variability. A summary of the modeled variograms parameters is present in Table 5-21.

Summary of the Structural Analysis: groups NG1 to NG5

In terms of the spatial variability scales as identified and modelled in the five new groups of time-slices from NG1 to NG5 of the Marlim reservoir, and summarized in the graphs of Figure 5-66 and Figure 5-67, one could say that:

the shorter the ranges, the smaller are the correlation coefficients, and vice-versa, the longer the ranges, the higher are the correlation coefficients. Small correlation coefficients could be traduced in events that are not conjointly characterized on both surveys, and this could help on explaining the small correlations. In this case, these events are not only noise related, but also, and more important, those effects could also be associated to the oil production; another interesting point to be emphasized concerns the higher uncertainties to determine the short ranges during the structural analysis, in comparison to same identification for the long scale events;

important to say is the more contrasting correlation coefficients observed in the crossline direction, with higher dispersion per range interval when compared to the inline direction; and

comparing the short and long ranges, correlation coefficients are more contrasted in groups NG1 (grey colour), followed by NG3 (orange) and NG2 (yellow);

Comparing the results in terms of the observed directions, one can say that:

in the crossline direction, the long range structures, with ranges $a > 1,500\text{m}$, are grouped, forming a cluster with correlations of the order of 0.96 and distances varying from 2,750 up to 3,500m, approximately. These structures are probably associated to a common geological response;

in the NG2, NG3 and NG5 groups, a similar behaviour is observed when comparing inline and crossline, showing contrasted coefficients; the same in the inline direction;

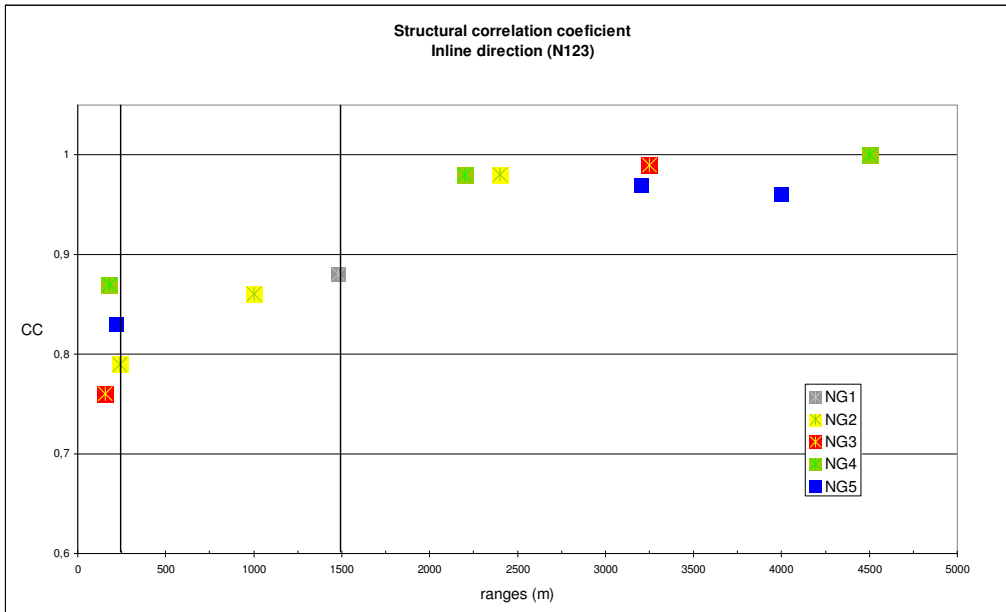


Figure 5-66 - Structural correlation coefficients computed for all spatial structures in the inline direction, plotted as a function of the structure range.

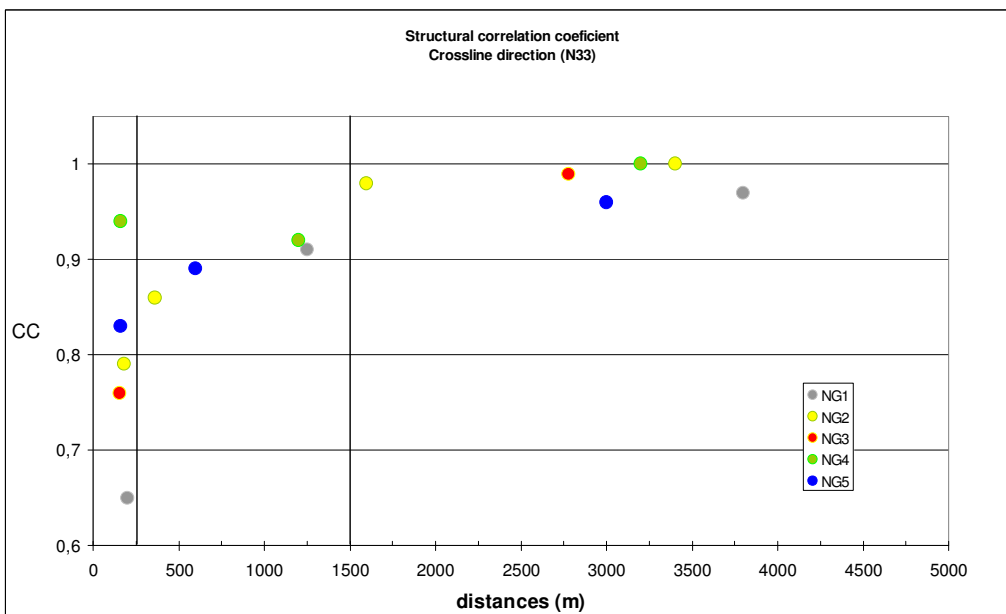


Figure 5-67 – Same as Figure 5-66, for the crossline direction.

5.2.9. Differences DifS05-S97

In the following, a summary of the main structures interpreted during the structural modelling of the variograms computed for the variable DifS05-S97, representing the difference volumes resulting from the subtraction of the seismic data S97 from the seismic data S05. These variograms were computed for each group as defined in section 5.2.8.

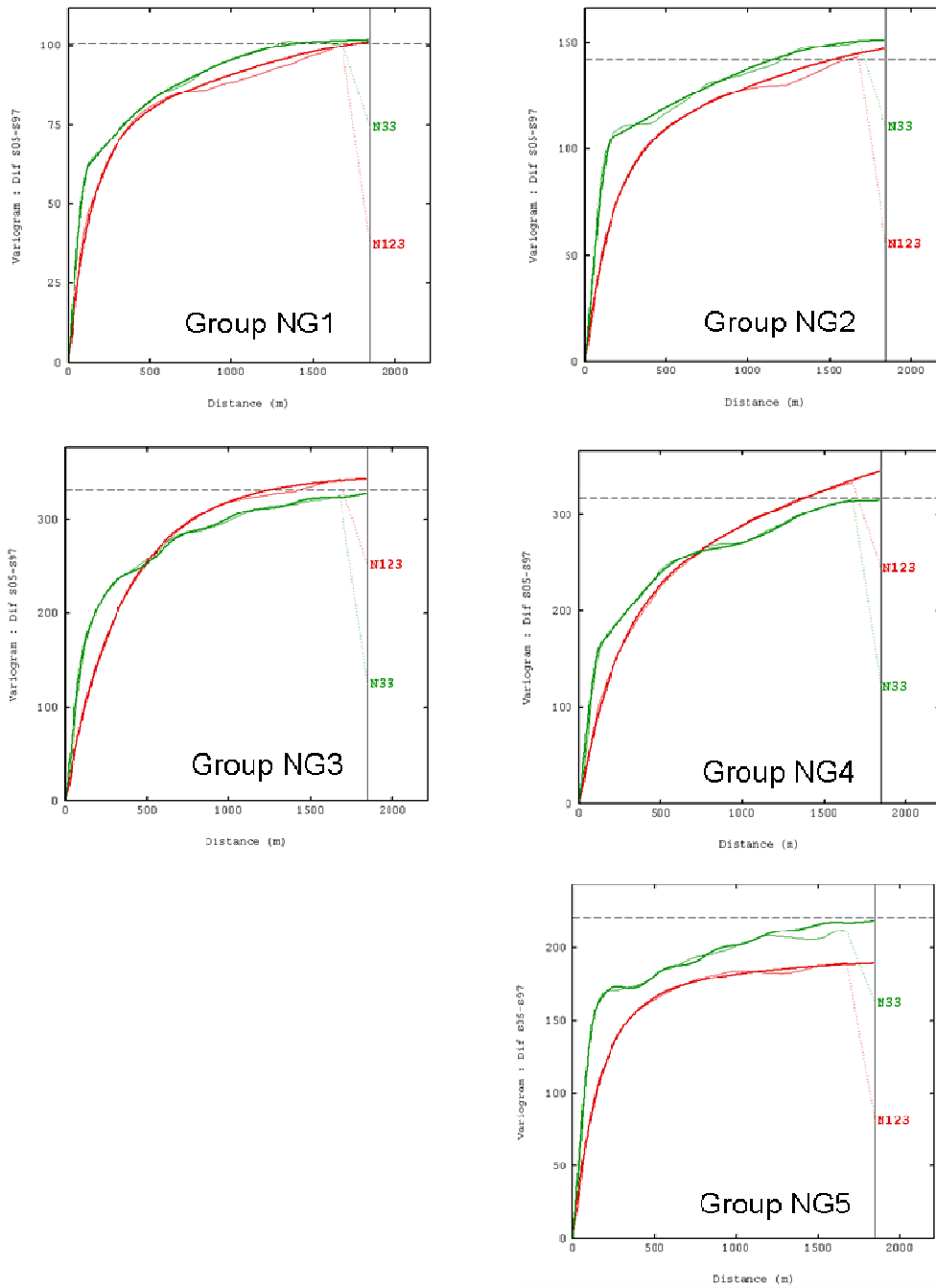


Figure 5-68 – Experimental (thin lines) and modeled (thick lines) variograms computed for the variable DifS05-S97, computed for each new group of time-slices from NG1 to NG5.

A summary of the structures and the main parameters used to model the experimental variograms from the DifS05-S97 data are presented in the following.

Table 4 -5-22 - Main structures identified on the volume of differences Dif_S05-S97. From top to bottom, parameters computed for all new groups of time-slices NG1 to NG5.

Structures from Group NG1		Ranges (m)		Sills
		Inline	Crossline	Dif S05xS97
C1	Spherical	-	130	54 (32)
C2	Exp	430	-	72 (42)
C3	Spherical	-	600	13 (8)
C4	Spherical	2300	1500	31 (18)
Structures from Group NG2		Ranges (m)		Sills
		Inline	Crossline	Dif S05xS97
C1	Spherical	-	167	98 (40)
C2	Exp	480	-	97 (39)
C3	Exp	2300	1800	53 (21)
Structures from Group NG3		Ranges (m)		Sills
		Inline	Crossline	Dif S05xS97
C1	Spherical	-	135	105 (30)
C2	Exp	500	-	126 (36)
C3	Spherical	-	1500	22 (6)
C4	Spherical	2300	1800	95 (27) (27)
Structure from Group NG4		Ranges (m)		Sills
		Inline	Crossline	Dif S05xS97
C1	Spherical	-	135	150 (21)
C2	Spherical	300	-	165 (24)
C3	Spherical	700	-	213 (31)
C4	Exp	-	2100	130 (19)
C5	Spherical	-	2850	40 (6) (25)
Structure from Group NG5		Ranges (m)		Sills
		Inline	Crossline	Dif S05xS97
C1	Spherical	-	143	133 (32)
C2	Spherical	450	-	150 (36)
C3	Spherical	-	1060	22 (5)
C4	Exp	-	1800	63 (15)
C5	Spherical	2200	-	43 (10) (30)

In terms of the relative contribution to the total variance observed for each structure range interval – short, medium and long, the main observed effects are:

a reduction of the relative contribution of the short range structures in the reservoir interval, reaching a minimum from 21 to 30%, in groups NG3 to NG4;

an increment of the mid range contribution from NG3 to NG4, where a maximum of 55% of this range contribution is observed, and it seems to be compensating the short range reduction;

an overall increase of the long range contribution, reaching its maximum range contribution, reaching a maximum of 36 in NG5;

Structures C1

These spatial structures, with ranges typically varying from 130 to 167m, were identified in all groups of time-slices from NG1 to NG5. It represents a periodic feature, where the maximum variability direction is orthogonal to the crossline direction. It was noticed that the contribution of this structure to the total variance was between 30 and 40%, from Groups NG1 to NG3 and in the group NG5. This contribution is reduced in Groups G3 and G4, where it reaches 21 to 30%.

Due to its vertical homogeneity, being observed in both reservoir and non-reservoir intervals, this short range structure is likely to be a response to acquisition noise.

Structures C2/C3

The medium scale structure, varying from 420 to 700m of range and mainly detected in the inline direction, is observed in all groups. In the non-reservoirs groups, NG1 to NG2 and NG5, the characteristic dimension varies from 430 to 480m. However, in the reservoir groups NG3 and NG4 it assumes bigger ranges, varying from 500 to 700 m.

Structure C3/C4/C5

The long range structures are vertically consistent from groups NG1 to NG4, with an important contribution to the total variance, ranging from 18 to 30%. The typical spatial scales are 2,300m in the inline direction and 1,500m in the crossline.

5.2.10. Comparing Low and High Noise Level Zones

An optimal geostatistical characterization in terms of spatial variability of a given dataset depends on several factors. One important decision in the structural analysis is the correct choice of the domain to be investigated, as well as the maximum representative distance to be sampled. The wider the investigated domain, the more complex becomes the interpretation of the resulting variograms and cross-variograms. The covariance function, or the variogram, plays a crucial role on all subsequent estimation steps, and a proper definition of these functions is mandatory.

In the previous paragraphs, it was shown that a few spatial structures being characterized in the structural analysis with small ranges could be, in some particular cases, directly identified in the amplitude maps, and associated to seismic acquisition artefacts. Often, these structures showed a reduced contribution to the total variance of the respective nested structure, and small correlation coefficients when comparing S05 and S97 datasets.

To better characterize and evaluate such small scale spatial features, it was proposed to reduce the investigated domain by selecting two smaller data subsets from the Marlim reservoir. The goal was to compare (i) the reservoir and the non-reservoir intervals, both in space and in time; and (ii) the zones of contrasting signal/noise ratios.

These new selected areas are indicated on Figure 5-69.

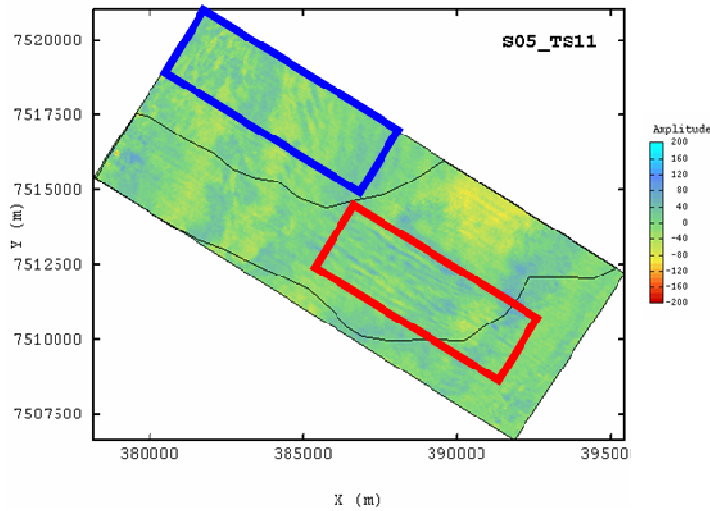


Figure 5-69 - Definition of the Noise Free (blue) and Noisy (red) areas. The black polygon represents the limits of the Marlim reservoir.

The northern zone, represented by the blue rectangle in the upper part of the map, points out the Noise Free Zone, and is completely outside the reservoir limits, which is indicated by the black polygon. The Noisy Area, on the other hand, is represented by the red rectangle in the central portion of the map, and rests inside the reservoir limits.

In the following paragraphs, some results of these analyses are presented, compared to the previous analyses and discussed. First, the results obtained from the Non-Reservoir interval, corresponding to the Group NG1 (TS01-TS12) will be introduced. Then, the same strategy is applied over the reservoir interval or Group NG3 (TS21-TS36). At the end, conclusions and suggestions for future works will be given.

The differences in the seismic signature response between the Noise free and Noisy areas are clearly observed by comparing the average amplitude and the variance traces for each area, as displayed in Figure 5-70 and Figure 5-71, respectively. In these figures, the five groups of time-slices are indicated from NG1 to NG5, where NG3 corresponds to the main Marlim reservoir interval. The green curves correspond to the difference between the variances $\sigma_{S05}^2 - \sigma_{S97}^2$, and are represented in percentage at the vertical scales on the right side of each graph.

The traces corresponding to the Noise free area are represented by smoothed curves, in which the average variance difference is approximately 8%, and never exceeds 20%. It is interesting to notice that in the whole interval the variance due to the monitor S05 data is greater than the base S97 survey.

In the Noisy area, despite the similar shape of the variance curves observed for both S05 and S97 surveys on the entire interval, important differences are observed just above the reservoir interval when compared to the Noise free area. Additionally, a negative linear trend is observed on the variance difference curve from the top to the bottom of the reservoir groups NG3 and NG4. This variance trend could be associated to the exploitation effects, as it represents an increase of the S05 amplitude differences on the top of the reservoir and a reduction on the bottom.

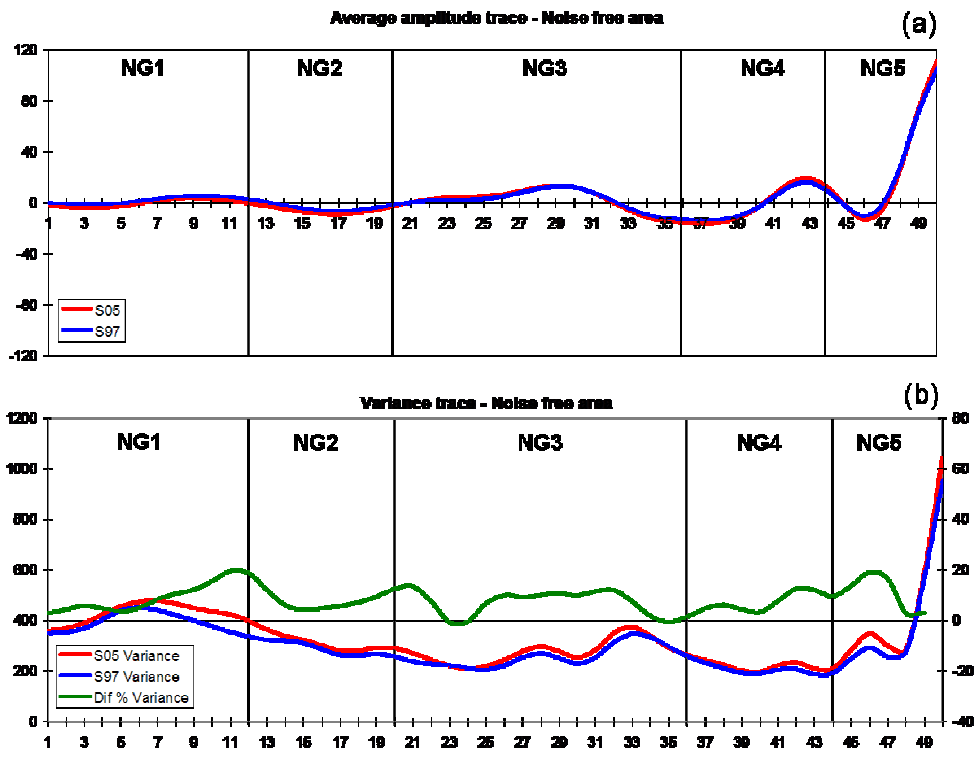


Figure 5-70 -Average amplitude (a) and variance (b) traces computed in Noise free area, where the horizontal axis corresponds to the time-slice numbering. Left vertical axis representing variance unities (squared amplitude values) and, on the right, difference of variance from S05 and S97 data, in percentage.

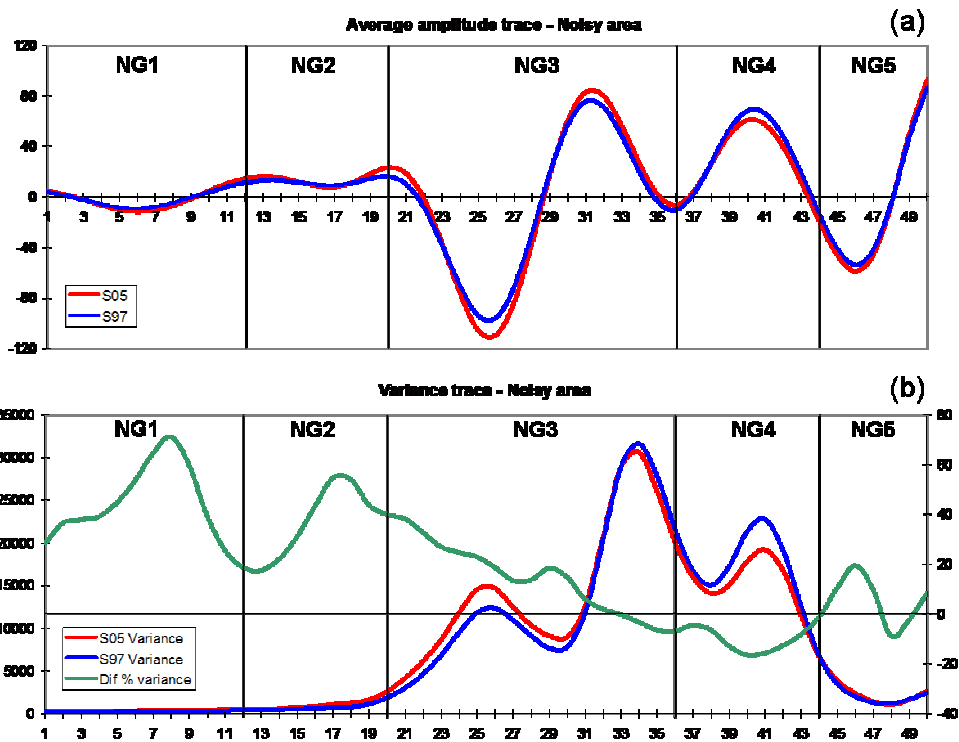


Figure 5-71 – The same as in Figure 5-70, computed in the noisy area.

Analyses of Noisy and Noise free Zones: The Non-Reservoir Interval

Compared to the previous structural analysis results as presented in item 5.2.8, these new zones represent a much smaller area, as shown in Figure 5-69. Due to its reduced dimensions, the parameters used to compute the variograms functions were redefined accordingly: (i) inline and crossline lags: 25m; and (ii) maximum investigated distance: 150 lags, or 3,750m, in the inline direction; and 40 lags, or 1,000m, in the crossline direction (these values were defined as half the dimensions of the studied area).

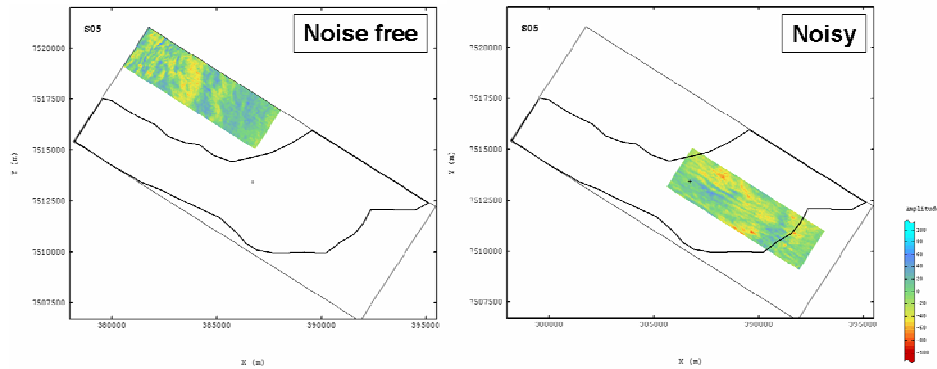


Figure 5-72 - Amplitude time-slices from TS06 representing the Non-Reservoir interval.

The experimental variograms and cross-variograms calculated on the Non-reservoir interval (Group NG1, time-slices TS01-TS12), for these two different zones are presented in Figure 5-73.

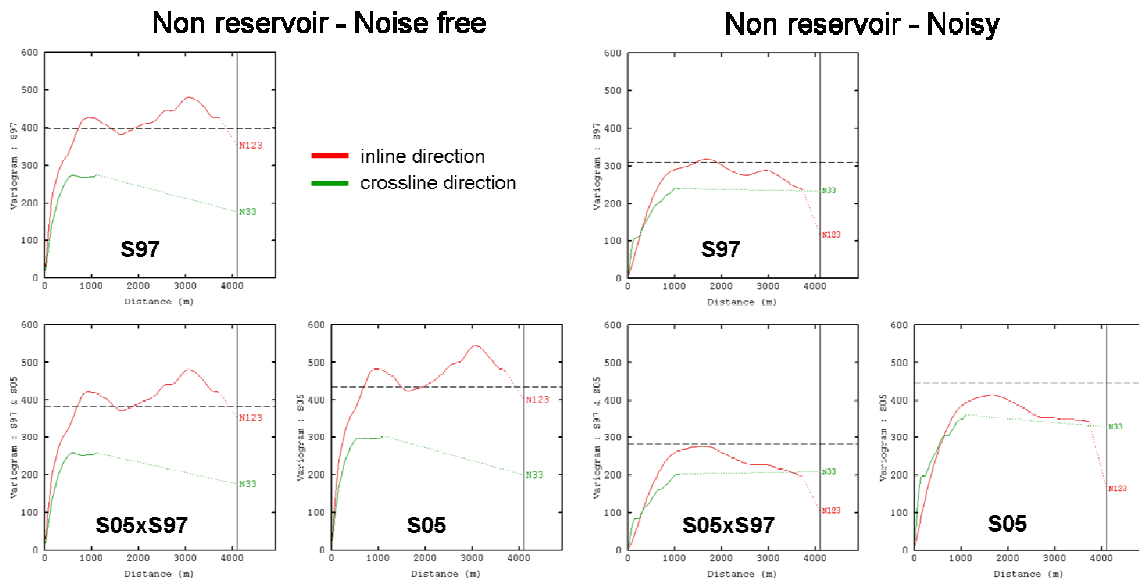


Figure 5-73 – Experimental variograms and cross-variograms for S97 and S05 datasets, corresponding to the Non-reservoir zone from group NG1 (TS01-TS12). Noise Free area data on the left, and the Noisy area on the right.

From these data, one can notice that:

- The variograms and cross-variograms from both Noise free and Noisy areas are more structured than those computed for the whole NG1 area, as presented in Figure 5-60;
- more contrasting *a priori* variance between the S05 and S97 campaigns is observed in the Noisy area ($\sigma_{S05}^2 = 450$ and $\sigma_{S97}^2 = 310$), than in Noise free area, where $\sigma_{S05}^2 = 430$ and $\sigma_{S97}^2 = 400$ (remember that, for the full area, higher but less contrasting *a priori* variance values were observed, $\sigma_{S05}^2 = 475$ and $\sigma_{S97}^2 = 375$);
- The geometric anisotropy observed in the original area, as previously described, becomes a more complex anisotropic pattern in both Noise free and Noisy areas;
- A well defined short range structure is observed in the Noisy area, mainly characterized in the crossline direction; and
- Periodic structure observed in the Noise free area, with $\lambda_1 \cong 1,000m$ and $\lambda_2 \cong 3,000m$;

A closer inspection on the spatial variability on both Noise free and Noisy areas is provided in Figure 5-74. In this figure, the variograms and cross-variograms of Figure 5-73 are redisplayed with the horizontal axis rescaled to focus on ranges smaller than 1500m. Table 5-23 summarizes the most important observations.

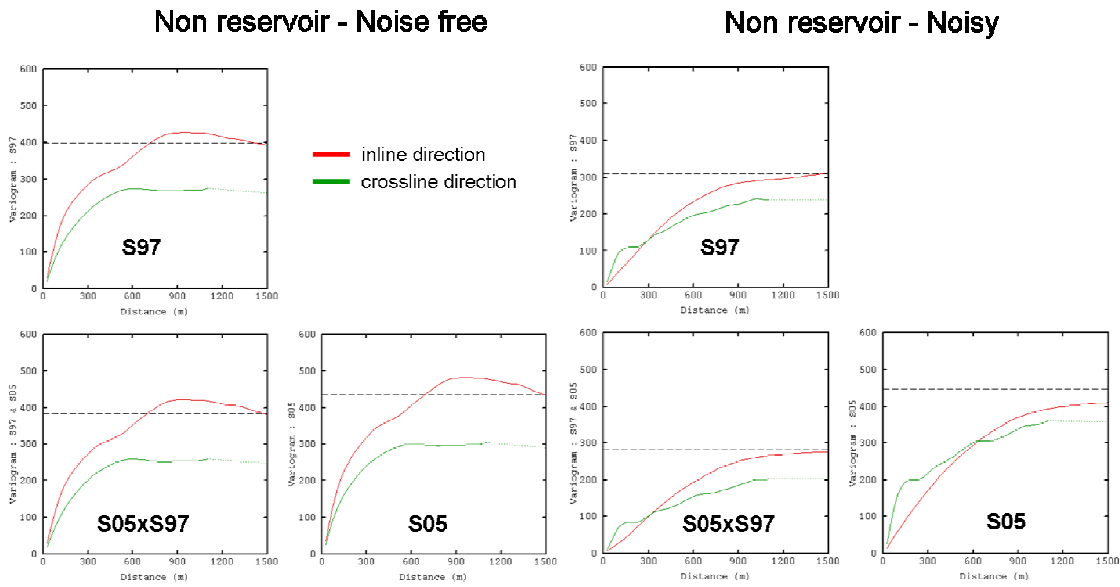


Figure 5-74 - Same variogram functions as in previous figure, highlighting the first 1,500m of range.

Table 5-23 – Summary of the spatial features for the Noise free and Noisy zones.

Noise Free area	Noisy area
Combined anisotropic effect;	Less obvious anisotropy;
Nested variogram in IL direction suggesting at least two structures;	More complex nested variogram in XL for short ranges;
IL direction more continuous than XL	IL direction more continuous than XL
IL direction with higher variability for all ranges	IL direction with higher variability for ranges $a > 600m$
No short range structure; both IL and XL reach the sill at mid-ranges;	XL exhibits a well defined short scale structure with $a = 150m$;
Very similar variograms for S05 and S97 surveys, for both inline and crossline directions.	S05 variogram showing higher variability; S05 is a scaled version of the S97.

In the following, our attention will be focused on the Noisy Area, and to better characterize the small scale structures. In Figure 5-75, the experimental and modelled

variograms and cross-variograms for the S97 and S05 variables are presented, with the resulting structural modelling parameters shown in Table 5-24.

Three basic structures were considered to describe the local variability of the Noisy Area: a *short range spherical structure*, only characterized in the crossline direction; and *two medium range structures*, being one spherical and another cubic. It is important to mention that this short range structure has been characterized in many previous structural interpretations, as shown, for instance, in Figure 5-51 and Figure 5-52, where all spatial structures mapped on the seven time-slices groups are displayed, as well as in Figure 5-66 and Figure 5-67, where the same analyses was performed on the regrouped data with 5 groups of amplitude time-slices.

Comparing the variance contribution of the short range structure as showed in Table 5-24, and also the very low correlation coefficient, equal to 0.53, with all those previous short range structures, it is interesting to notice how remarkable these values are. It is known that variogram rescaling does not affect the ordinary kriging weights or the ordinary kriging estimates, but affects the ordinary kriging variance (Isaaks and Srivastava, 1989). But how it impacts the factorial kriging results?

Inspecting the acquisition information and the cross-equalization processing sequence that have been applied to these surveys, one can better understand the small correlation coefficients and higher variance contributions associated to these small scale structures, as showed by the S05 data in comparison to S97, in Table 5-24. In the analysed interval - NG1, as show in Figure 5-57 and Figure 5-58 - no production or 4D related effects are expected to be registered on the seismic data, as this zone lies above the reservoir time interval.

During the S05 monitor seismic acquisition campaign, important operational constraints limited the seismic repeatability, and were mainly associated to: strong marine currents imposing strong seismic cable feathering; presence of operational obstacles (fixed platforms, rigs, FPSOs, etc), bad weather, etc. Aiming to minimize these effects on the final seismic data quality and to improve repeatability, alternative acquisition geometries such as

seismic undershooting, two-boat-shooting, and other non-conventional shooting techniques were considered (Johann et al., 2006). Concerning specifically the Noisy area, it is also important to recall that the operational obstacles that impacted the S05 acquisition campaign were not installed at the time the base survey S97 campaign was registered.

In terms of seismic processing, however, it was noticed that the implemented cross-equalization sequence succeeded on minimizing the acquisition discrepancies, as showed in section 5.1. Therefore, it seems that, originally, this spatial small scale structure is likely to belong to the monitor survey – as its contribution to the total variance is high, and equal to 38%. The contribution of this structure to the S97 data variance, equal to 29%, is still important, and could be explained as being "imported" to the S97 survey during the cross-equalization processing, as a response to the spectral (amplitude and phase) balancing as well as time-shift corrections to minimize the data discrepancies (Johann et al., 2006).

Table 5-24 – Resulting modelling parameters from structural analysis, NG1 in Noisy area.

Structure		Ranges (m)		Sills			Correlation
		Inline	Crossline	S05	S97	S05xS97	
C ₁	Spherical	NA	150	139 (- / 38)	71 (- / 29)	53 (- / 27)	0.53
C ₂	Spherical	1 200	1 200	230 (58 / 62)	178 (59/71)	145 (54 / 73)	0.72
C ₃	Cubic	1 100	NA	166 (42 / -)	126 (41/ -)	125 (46 / -)	0.86

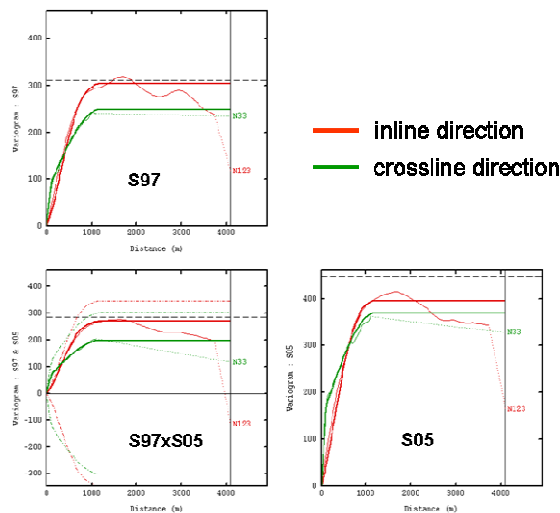


Figure 5-75 – Experimental (thin) and theoretical (thick) variograms and cross-variograms for group NG1 (TS01-TS12) corresponding to the Noisy area.

In order to emphasize the different variogram responses obtained when analysing the original area and the smaller Noisy area, a comparison between the variograms and cross-variograms from S97 and S05 datasets, computed for group NG1 (TS01-TS12) is presented in Figure 5-76. The same calculation parameters were considered, but for different areas. On the left side of the figure, the regional variograms and cross-variogram, and, on the right, the local variograms and cross-variogram considering only the Noisy Area.

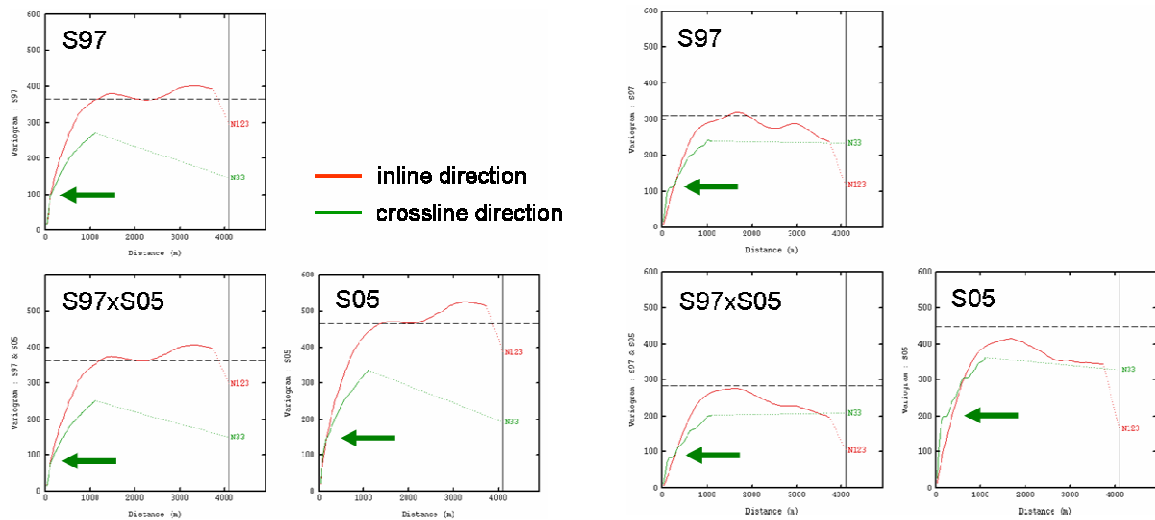


Figure 5-76 - Cross-variograms for S05 and S97, corresponding to group NG1 (TS01-TS12). These variograms and cross-variograms were computed with the same parameters, but considering different areas. On the left, data corresponding to the original area, whereas on the right it corresponds to the Noise Area.

Considering the original area as shown on the left in Figure 5-76, the crossline direction (N33) variograms show a transitory behaviour whereas in the inline direction the sill is reached at approximately 1,200m. However, a much more conspicuous feature is the small scale structure captured by the crossline variograms on the Noisy area as showed in right side of Figure 5-76, and indicated by a green arrow. At approximately the same ranges, these structures are also suggested in the regional variograms, but showing a much more smoothed characteristic. During the fitting step of the variograms, this smoothness of the variogram curves is traduced in a much more uncertain decomposition of these nested structures.

Results from Factorial cokriging Analysis on Noisy Area

In the following, the results obtained from the decomposition and factorial cokriging filter of the structures associated to the noise will be presented. These results were achieved using the following parameters:

- basic structures: as defined in Table 5-24 and Table 5-25 (non-reservoir and reservoir intervals, respectively);
- search ellipsoid: 1, 725m (inline) and 150m (crossline);
- minimum number of samples: 8;
- number of sector: 4;
- optimum number of samples per sector: 15;

In Figure 5-77 and Figure 5-78, the results from the implementation of the factorial cokriging in the Noisy area are presented. In this case, the time-slice TS11, corresponding to the first group NG1 above the reservoir interval, is shown. The first figure compares the raw S05 monitor data, on the left, and the same data after filtering the C1 structure, whereas the second figure shows the same, now for data S97. The improvement of the data quality after filtering the C1 structure is considerable, for both datasets. Additionally, it must be noticed that most of the data features were preserved after the filtering process, including all the medium to large scale structures.

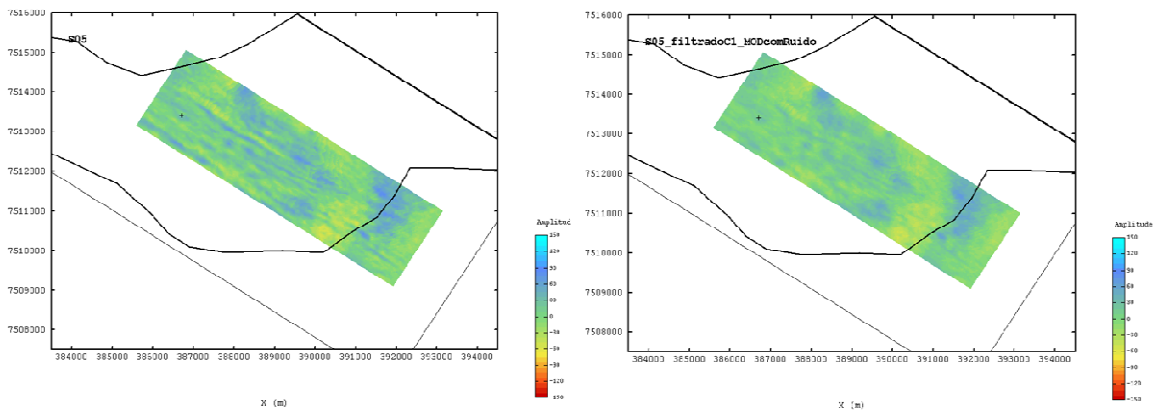


Figure 5-77 – Results after filtering the short range C1 structure of variable S05 from time-slice TS11 of group NG1. Raw data on the left and filtered on the right, with black polygon corresponding to the interpreted reservoir limits.

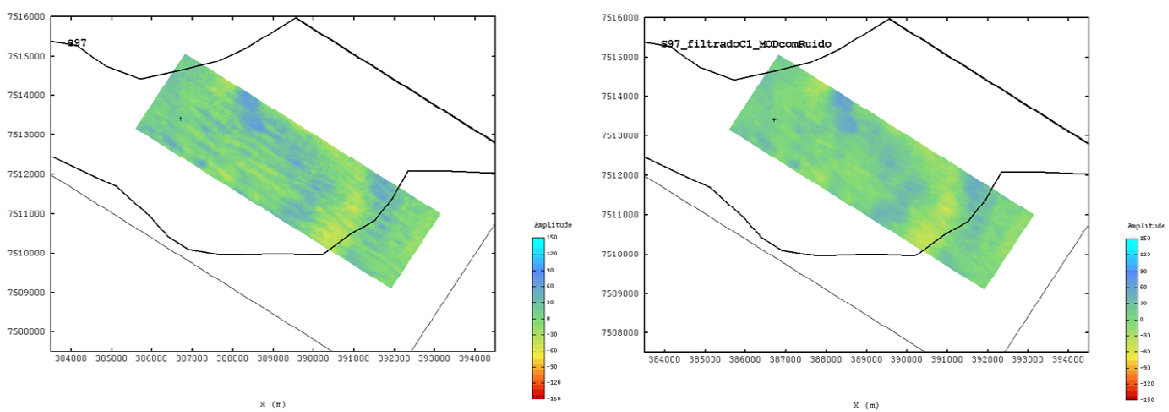


Figure 5-78 – Same as in Figure 5-77 Figure 5-77, for the S97 data.

Structural Analyses for Noisy and Noise free Zones: The Reservoir Interval

The same approach used in the Non-Reservoir interval was applied to the reservoir level. First, an attempt to adjust the variograms using the same parameters as presented in section 0, when the Group NG3 was fitted. However, no possible adjustment was achieved. A new model was proposed, and four structures were then considered, as showed in Table 5-25. The short range spherical structure identified in this zone possesses the same dimension as the one identified in the "Noisy" area, outside the reservoir zone, but shows an isotropic behaviour, which was not the case in the previous example.

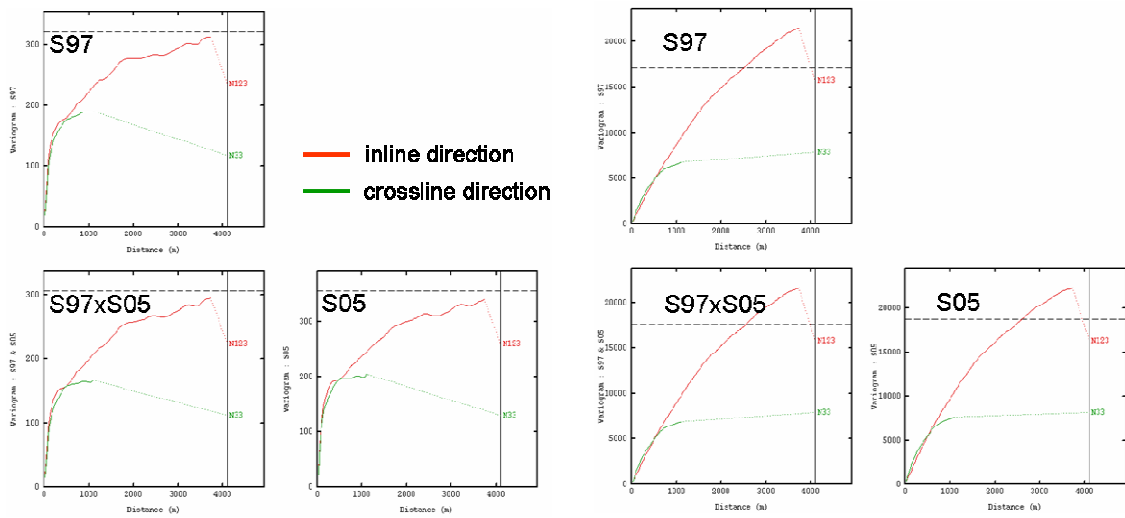


Figure 5-79 - Experimental variograms and cross-variograms for S97xS05 corresponding to group NG3(TS21-TS36), in the Marlim reservoir zone. Identical calculation parameters were used. Noise Free area graphs displayed on the left, while for the Noisy Area on the right.

Table 5-25 – Resulting modelling parameters from structural analysis of the Noise Free area.

Structure		Ranges (m)		Sills			Correlation
		Inline	Crossline	S05	S97	S05xS97	
C ₁	Spherical	150	150	80 (25)	65 (22)	50 (18)	0.69
C ₂	Exp	450	550	80 (25)	84 (28)	78 (28)	0.95
C ₃	Spherical	1500	700	40 (12)	36 (12)	35 (12)	0.92
C ₄	Spherical	3600	3600	126 (39)	116 (39)	118 (42)	0.97

As shown in Table 5-25, the isotropic spherical short range structure was assumed to be an effect of noise due to acquisition. In Figure 5-80 and Figure 5-81, the data before and after filtering the short scale structure are presented. The periodic noise in the crossline was efficiently attenuated in the filtered image, preserving the other scales of variability present in the data.

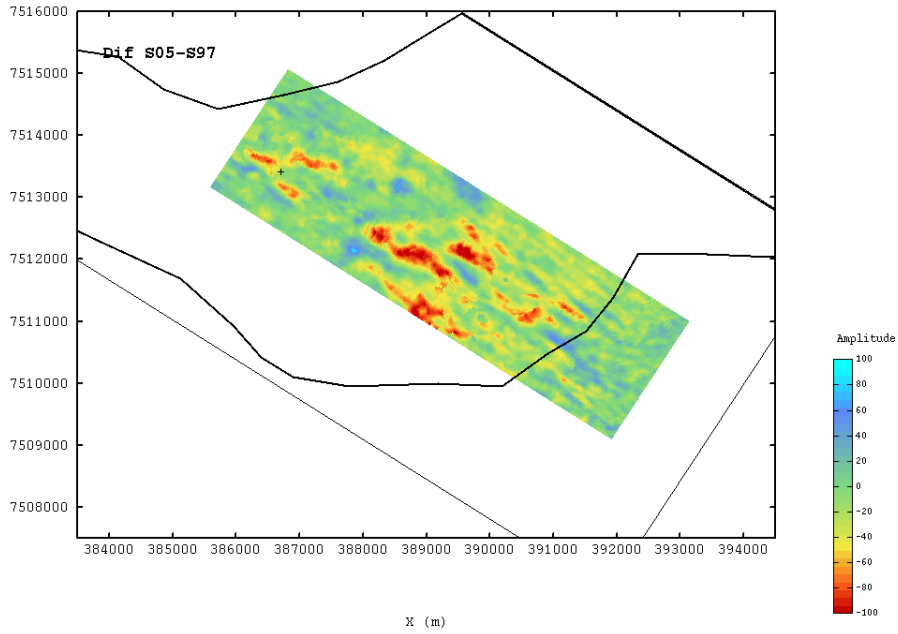


Figure 5-80 – Amplitude map corresponding to time-slice 26 (TS26), from Marlim reservoir interval NG3. The map corresponds to the difference of raw data.

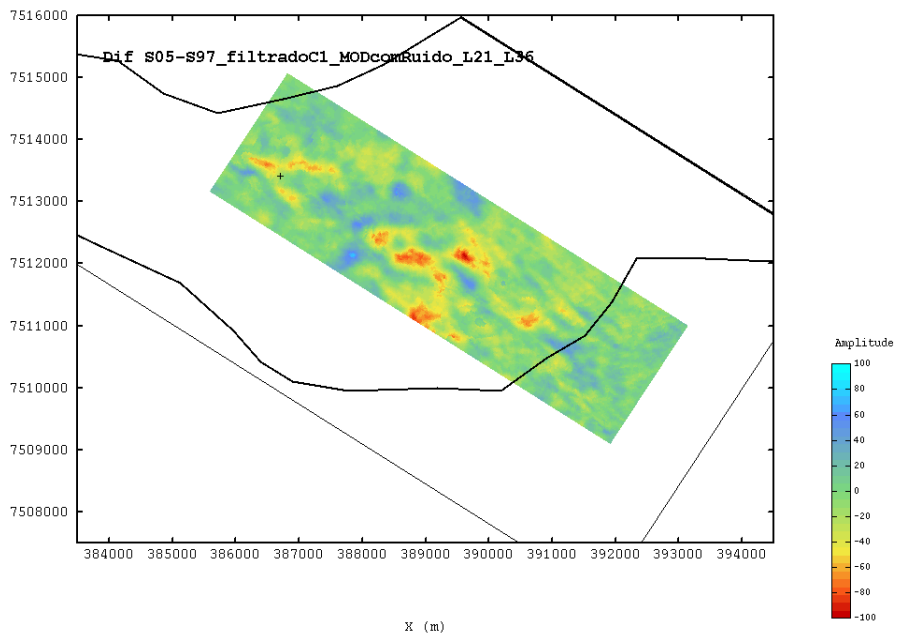


Figure 5-81 – As in Figure 5-81, but corresponding to the difference of the data S05 and S97 after filtering the short scale structure C1.

5.3. Conclusions

The proposed methodology of interpretation and filtering seismic data by using geostatistical techniques, particularly the multivariate factorial cokriging technique, was successfully applied in an offshore Brazilian turbiditic field located in the Marlim Field, Campos Basin, offshore Brazil. The results obtained so far showed that this methodology helped on improving the time-lapse signature, affording a better comprehension and characterization of the spatial structures that interact at different spatial scales, resulting in a complex data.

The multivariate factorial cokriging methodology relies on the principle that the variograms $\gamma_1, \dots, \gamma_p$ (or the covariance function) of a regionalized variable Z_1, \dots, Z_n can be decomposed into a linear combination of a set of independent components, or orthogonal functions, that could explain, at different scales, the variability model observed in the variograms or the covariance. In the time-lapse domain, the resulting orthogonal functions may be interpreted as a response to the common geology; the common noise or to the time-lapse response due to the exploitation of the reservoir.

Even assuming that the seismic volumes resulting from a time-lapse experiment have been properly and conveniently processed to minimize the discrepancies resulting from different seismic acquisition and processing technologies and conditions, it was noticed that an important part of the seismic data variability is associated to structures non-related to the production, or to any the particular geological/geophysical structure of the reservoir under analysis. Prior to applying any kind of filtering technique, these structures must be correctly characterized in terms of spatial distribution.

To achieve these goals, a geostatistical analysis approach was suggested and implemented, considering five main steps:

- first, the time-lapse seismic datasets are repositioned by using a regional stratigraphic marker as a reference for a flattening procedure;
- secondly, a statistical and geostatistical analysis is performed in the horizontal plane, on every time-slice of the investigated seismic volume. The attribute slices are gathered into cluster of similar spatial structural characteristics;
- third, and based on the previous analysis, these sub volumes resulting from the grouping of time-slices are analyzed in terms of their structural behavior, by modeling the experimental variograms and cross-variograms;
- fourth, and based on the structural analysis and on additional geological and geophysical data, those structures interpreted to be not related to the geology or to the production mechanism are filtered from the data by the multivariate factorial cokriging approach;
- fifth, the filtered data are interpreted and incorporated into the reservoir model.

One of the important steps of the proposed methodology refers to the decision of the considered co-regionalization model. This step involves the interpretation of $N_v(N_v + 1)$ variograms and cross-variograms, where N_v is the number of variables under consideration. By adjusting a proper covariance function and choosing an adequate neighbourhood, it was possible to filter out those structures interpreted to be associated to seismic acquisition noise, and simultaneously preserve the time-lapse signal. In this work, a 2,5D covariance model was considered. A point for future research is the proper definition of a three-dimensional covariance or variogram function, representative of the selected geological unity undergoing the production/exploitation effects, as well as from the encasing rocks where no time-lapse effects are expected.

Lastly, a new methodology based on the filtering of the difference seismic amplitude cube rather on the raw data was suggested. This last procedure gives better result

as long range spatial structures commonly recorded in the various vintage datasets, usually related to sedimentary imprints or geological structures, are eliminated. Only the acquisition noise or the investigated 4D effects are preserved, as reported in previous work by Calvert (2005). This Factorial cokriging filter approach is therefore recommended in practical time lapse studies as an efficient analyses and filtering tool, despite the additional interpretative work required to its implementation.

Chapter 6 - General conclusions and Future Work

Time-lapse seismic monitoring technology is becoming a conventional tool for monitoring and management hydrocarbon reservoirs. The physical principle supporting this technology is simple, and is based on the recording of repeated seismic surveys over a hydrocarbon producing field at different calendar times. The hydrocarbon production determines changes in the reservoir properties due to fluid saturation, pressure, or temperature variations that could potentially be registered on the repeated seismic surveys.

This technology aims to provide qualitative and quantitative information to improve the reservoir description in terms of both static and dynamic properties during hydrocarbon production. Tracking the actual pathways of the fluids injected into the reservoir from the injector to the producer wells, and quantifying the total amount of upswept oil zones, helps with (i) redefining reservoir management strategies that includes the positioning of well locations in infill programs, (ii) saving planned wells to be drilled in swept zones, and (iii) balancing injection and production rates.

In this thesis, a brief introduction of some important geostatistical concepts and techniques and formulations were presented and discussed, with the main focus on the Factorial Kriging (FK) technique and its applications.

A comparison of the Factorial Kriging technique with other conventional techniques, such as the Single Value Decomposition (SVD) and the Spectral Analysis, is presented. These tools are usually applied in the conventional seismic processing workflow to perform spatial data analysis and filtering, but both have limited impact when evaluating the variability as a scale-dependent phenomena. In the first case, it was show that the SVD operates only on the variance-covariance matrix of the available data, and that the resulting eigenimages are only independent at zero lag distances. The Spectral Analysis applications, on the other side, operates directly on the frequency domain, typically by implementations

of the Fourier transforms. These applications are not constrained by any spatial structure, and performs a brute filtering.

One shortcoming of the Factorial Kriging technique – and of all estimation techniques applications based on the variogram - is the strong dependence on an arbitrary and subjective variogram interpretation, usually referred to as the structural analyses. The decomposition of the random function in a set of independent basic variogram functions is strongly dependent on the interpreters' choice. As described in the text, some authors have explored the uncertainties associated to the variogram estimation parameters. If this decomposition is based solely on the sample covariance, then it is an artifact of the model rather than a proof of the physical significance of the resulting orthogonal factors (Deutsch & Journel, 1998). Some approaches are based on the automatic extraction of the "common-part" provided by the experimental cross-covariance or cross-variogram, as the automatic extraction technique proposed by Coleou (2005). This author suggests that this robust common part extraction may bypass this characteristic, considered as a drawback of the Factorial Kriging technique. In this work, we will explore the possibility of adapting those models of covariance or variograms used in the FK to better characterize the underlying spatial structures from time-lapse seismic datasets.

The analysis of the orthogonal factors computed through the FK methodology followed by the Unsupervised Facies Classification allowed the spatial interpretation of underlying structures that are hidden in the time-lapse seismic volumes, and are usually difficult to be identified when considering a conventional interpretation workflow. A by-product resulting from this analysis is the potential to perform a quality control on the time-lapse processing sequence, by investigating and comparing the variance of the structures in different time windows.

It was noticed that the orthogonal factors extracted by the FK on both the non-reservoir and reservoir zones of the Senlac dataset are quite similar in terms of spatial variability (range, anisotropy and number of components). However, the contribution (in %) of each FK factors are more contrasted in the Reservoir zone (100% or 0%) than in the

Non-Reservoir zone; this could be explained by a more careful processing carried out in the Reservoir zone, introducing a stronger noise coherence between the time-lapse campaigns. Additionally, the contribution in terms of variance on each component AMP90, AMP97 and AMP98 is much higher in the reservoir zone, of one to two orders of magnitude.

Moreover, the correlation coefficients for large scale component C3 are more contrasted in the Reservoir zone. They are smaller (0.26) for AMP90xAMP97 and AMP90xAMP98, but higher (0.86) for AMP97xAMP98. This could be related to changes in the reservoir due to the steam injection in horizontal wells aligned with the cross line direction, indicating that changes in the reservoir would affect zones of similar extension and orientation as the C3 structures. These results show that FK seems to be an efficient method to reveal common regional trends and time dependent zones from repeated seismic datasets.

The comparison of the results of the simultaneous seismic facies classification approach shows that the geostatistical filtering imposed a more continuous behaviour of the mapped facies. The filtered seismic facies maps are in agreement with previous supervised seismic classification studies performed in the area. Regarding the number of facies classes, the use of a smaller number of classes – in this case, five classes – allowed an easier distinction of possible time-lapse effects when comparing the raw and filtered maps, even if more features can be observed in the nine classes' maps, they are difficult to interpret.

The maps of probability of assignment into class showed minor improvements when comparing raw and filtered datasets. But even these small improvements could help reducing the time-lapse interpretation uncertainty.

The last part of this chapter concerns the investigation of the possible mechanisms that could lead to the observed negative time-shifts between base and monitor surveys. First, the dependence of the compressional velocity on the reservoir pore pressure was investigated. These negative time-shifts are in disagreement with what is expected from theoretical models describing increasing temperature effects in heavy oil sands.

Aiming at providing a physical basis for these anomalous time-shift responses, a simple one-dimensional modelling, considering the velocity-pressure dependence, was conducted. The considered model was based on the Hertz-Mindlin (Mindlin, 1949) equations, following the proposal of Landro and Kvam (2002). Six different pore pressure scenarios were studied, where for five of these models - from S1 to S5 - the modelled pore pressures were considered to be in the normal pressure ranges. It should be noticed that the resulting modelled velocities did not explain the observed negative time-shifts, for none of the considered models. Additionally, it was observed that, to reach this negative 2ms time-shift, an increase of 24% in the compressional velocities was necessary.

However, as described in the model S6, this velocity increase involved unrealistic pressure values, such as an effective pressure of 42 MPa in comparison to the initial pressure condition of 11.6 MPa, in the reservoir interval. Based on the Hertz-Mindlin contact theory, it seems that the observed negative time-shifts resulting from the different time-lapse seismic data from Senlac can not be properly explained by a pressure variation.

One valid hypothesis to explain the increase of velocity during exploitation is that non consolidated sandstones saturated by heavy oil do not behave like a rigid material, but rather like a mixture of grains and heavy oil. In this case, the grains are not in elastic contact, but are rather floating in the liquid. This hypothesis was tested using the effective medium theory, such as the Voigt, Reuss, and Hill models. The results showed that seismic velocity would increase in the reservoir interval, leading to negative time-shifts in agreement with the observations.

Another explored hypothesis was the porosity reduction as a consequence of the heavy oil production, that would also lead to an increase in the V_p velocity.

The last part of this work involved another real case application. In this case, the proposed methodology of interpretation and filtering seismic data by using geostatistical techniques, particularly the multivariate factorial cokriging technique, was successfully applied in an offshore Brazilian turbiditic field located in the Marlim Field, Campos Basin,

offshore Brazil. The results obtained so far showed that this methodology helped on improving the time-lapse signature, affording a better comprehension and characterization of the spatial structures that interact at different spatial scales, resulting in a complex data.

The multivariate factorial cokriging methodology relies on the principle that the variograms (or the covariance function) of a regionalized variable can be decomposed into a linear combination of a set of independent components, or orthogonal functions, that could explain, at different scales, the variability model observed in the variograms or the covariance. In the time-lapse domain, the resulting orthogonal functions may be interpreted as a response to the common geology; the common noise or to the time-lapse response due to the exploitation of the reservoir.

Even assuming that the seismic volumes resulting from a time-lapse experiment have been properly and conveniently processed to minimize the discrepancies resulting from different seismic acquisition and processing technologies and conditions, it was noticed that an important part of the seismic data variability is associated to structures non-related to the production, or to any the particular geological/geophysical structure of the reservoir under analysis. Prior to applying any kind of filtering technique, these structures must be correctly characterized in terms of spatial distribution.

To achieve these goals, a geostatistical analysis approach was suggested and implemented, considering five main steps:

- (i) first, the time-lapse seismic datasets are repositioned by using a regional stratigraphic marker as a reference for a flattening procedure;
- (ii) secondly, a statistical and geostatistical analysis is performed in the horizontal plane, on every time-slice of the investigated seismic volume. The attribute slices are gathered into cluster of similar spatial structural characteristics;
- (iii) third, and based on the previous analysis, these sub volumes resulting from the grouping of time-slices are analyzed in terms of their structural behavior, by modeling the experimental variograms and cross-variograms;

(iv) fourth, and based on the structural analysis and on additional geological and geophysical data, those structures interpreted to be not related to the geology or to the production mechanism are filtered from the data by the multivariate factorial cokriging approach;

(v) fifth, the filtered data are interpreted and incorporated into the reservoir model.

One of the important steps of the proposed methodology refers to the decision of the considered co-regionalization model. This step involves the interpretation of variograms and cross-variograms, where n is the number of variables under consideration. By adjusting a proper covariance function and choosing an adequate neighbourhood, it was possible to filter out those structures interpreted to be associated to seismic acquisition noise, and simultaneously preserve the time-lapse signal. In this work, a 2,5D covariance model was considered. A point for future research is the proper definition of a three-dimensional covariance or variogram function, representative of the selected geological unity undergoing the production/exploitation effects, as well as from the encasing rocks where no time-lapse effects are expected.

Lastly, a new methodology based on the filtering of the difference seismic amplitude cube rather on the raw data was suggested. This last procedure gives better result as long range spatial structures commonly recorded in the various vintage datasets, usually related to sedimentary imprints or geological structures, are eliminated. Only the acquisition noise or the investigated 4D effects are preserved, as reported in previous work by Calvert (2005).

6.1. Future work and perspectives

The interpretation of time-lapse seismic data is a subject with a wide range of possible research activities. The following activities of this research work may involve:

- A point for future research is the proper definition of a three-dimensional covariance or variogram function, representative of the selected geological unity undergoing

the production/exploitation effects, as well as from the encasing rocks, where no time-lapse effects are expected.

- From the previous point, performing the Factorial cokriging in a full three-dimensional context will probably improve the final factors estimations;
- Incorporate more well data, petrophysical and/or additional reservoir information to better characterize those spatial structures that responds for the geology;
- Improve the proposed methodology in such a way it can be used to check the building of the petro-acoustical models during time-lapse feasibility studies, as different sources of data are used during this step, taken from different supports.

Bibliographic References

Arnaud, M., Emery, X., Fouquer, C., Brouwers, M., Fortier, M., 2001. L'Analyse Krigéante pour le Classement d'Observations Spatiales et Multivariées. *Rev. Statistique Appliquée*, XLIX (2), p.45-67.

Avseth, P., Mukerji, T., and Mavko, G., 2006. *Quantitative seismic interpretation: applying rock physics tools to reduce interpretation risk*. Cambridge University Press, 359pp.

Bachrach, R., Dvorkin, J., and Nur, A., 2000. Seismic velocities and Poisson's ratio of shallow unconsolidated sands. *Geophysics*, 65, 559-564.

Bourgault, G., 1994, Robustness of noise filtering by kriging analysis: *Mathematical Geology*, v. 26, no. 6, p. 733–752.

Bruhn, C. H. L., 1998. Deep-water reservoirs from the eastern Brazilian rift and passive-margin basins. Course No. 6, AAPG International Conference and Exhibition, Rio de Janeiro.

Bruhn, C. H. L., Gomes, J.A.T., Del Lucchese Jr., C., Johann, P.R.S., 2003. Campos Basin: reservoir characterization and management – historical overview and future changes. 2003 Offshore Technology Conference, Houston.

Barriol, Y., Glaser, K.S., Pop, J., Bartman, B., Corbiell, R., Eriksen, K.O., Laastad, H., Laidlaw, J., Marin, Y., Morrison, K., Sayers, C.M., Romero, M.T., Volokitin, Y., 2005. The pressures of drilling and production. *Oilfield Review*, 17, No. 3, 22-41.

Bergbauer, S., Mukerji, T., and Hennings, P., 2003. Improving curvature analysis of deformed horizons using scale-dependent filtering techniques. *AAPG Bulletin*, 87, 8, 1255-1272.

Biot, M.A. and Willis, D. G., 1957. The elastic coefficients of the theory of consolidation. *J. Appl. Mech.*, 594-601.

Bourbié, T., Coussy, O., and Zinszner, B., 1987. *Acoustics of Porous Media*. Gulf Publishing Co., Houston, 334p.

Bowers, G., 2002. Detecting high overpressure. *The Leading Edge*, 21, 174-177.

Bruce, B. and Bowers, G., 2002. Pore pressure terminology. *The Leading Edge*, 21, 170-173.

Calvert, R., 2005. Insights and methods for 4D reservoir monitoring and characterization. *EAGE/SEG Distinguish Instructor Short Course*, No. 8, 219p.

Calvert, R., 2005. 4D technology: Where are we, and where are we going? *Geophysical Prospecting*, 53 (2), 161-171.

Castagna, J., and Swan, H., 1997. Principles of AVO crossplotting. *The Leading Edge*, 21, 170-173.

Chiles, J.P., Delfiner, P., 1999. *Geostatistics: modeling spatial uncertainty*. Willey series in Probability and Statistics. John Willey & Sons, 703pp.

Choppra, S. and Hoffman, A. R., 2006. Velocity determination for pore pressure prediction. *The Leading Edge*, 25, 1502-1515.

Christensen, N. I., and Wang, H.F., 1985. The influence of pore pressure and confining pressure on dynamic elastic properties of Berea sandstone. *Geophysics*, 50, 2, 207-213.

Coléou, T., 2001. On the use of seismic velocities in model building for depth-conversion. 63rd EAGE Conf., Amsterdam, The Netherlands.

Coléou, T., Hoerber, H., and Lecerf, D., 2002. Multivariate geostatistical filtering of time-lapse seismic data for an improved 4d signature. Expanded Abstracts, 72nd Ann. Intern. Mtg., Soc. Expl. Geophys., Expanded Abstracts, p.1662-1665.

Coléou, T., 2002, Time-lapse filtering and improved repeatability with automatic factorial co-kriging (AFACK), 64th EAGE Conference, Florence, Italy.

Coléou, T., 2005. US PATENT number 2005/0209895.

Dequirez, P.Y., Fournier, F., Blanchet, C., Feuchtwanger T. and Torriero, D., 1995, Integrated stratigraphic and lithologic interpretation of the East-Senlac heavy oil pool. 65th Ann. Intern. Mtg., Soc. Expl. Geophys., Expanded Abstracts, p.104-107.

Deutsch, C., & Journel, A., 1998, GSLIB Geostatistical Software Library and User's Guide. Oxford University Press, New York. 369p.

Epos Reference Manual, 2007.

Dubrulle, O., 2003, Geostatistics for Seismic Data Integration in Earth Models. SEG & EAGE Distinguished Instructor Short Course, no 6.

Dusseault, M., 2002, CHOPS Cold Heavy Oil Production in Oil sands, in www.energy.gov.ab.ca/Oilsands/1189.asp, consulted in 10/12/2005.

Dvorkin, J. and Medina, A., 2000. Elastic-wave velocity changes in compacting heavy oil sands. In: XXV European Geophysical Society, Geophysical Research Abstracts, 2000, v.2.

Edmunds, N.R., and Suggett, J.C., 1995. Design of a commercial SAGD heavy oil project. Paper SPE 30277: SPE International Heavy Oil Symposium. Calgary. 19-21 June, 1995.

Eiken, O., Haugen, G. U., Schonewille, M. and Duijndam, A., 2003, A proven method for acquiring highly repeatable towed streamer seismic data. Geophysics, 68 (4), p.1303-1309.

El Ouair, Y. and Stronen, L.K., 2006. Value creation from 4D seismic at the Gullfaks Field: achievements and new challenges. In: 76th SEG Ann. Internat. Mtg., Soc. Expl. Geophys., Expanded Abstracts, pp. 3250-3254.

EnCana homepage www.encana.com, consulted in 12/10/2005.

Fournier, F., 2004, Interprétation orientée réservoir des attributs sismiques : une contribution à la lithosismique, Mémoire d'habilitation à diriger des recherches, spécialité Géosciences, Institut National Polytechnique de Lorraine, 223 p.

Freire, S.L.M., Ulrych, T.J., 1988. Application of singular value decomposition to vertical seismic profiling. *Geophysics*, 53, 6, 778-785.

Galli, A., Gerdil-Neuillet, F. and Dadou, C., 1984. Factorial kriging analysis: a substitute to spectral analysis of magnetic data. In: Verly, G., Davis, M., Journel, A.G., & Maréchal, A. (eds), *Geostatistics for Natural Resources Characterization, Part 1*. Raidal Publishing Company, 1984, p. 543-557.

Gambôa, L.A.P., Esteves, F., Shimabukuro, S., Carminatti, M., Peres, W. 1986. Evidências de variações do nível do mar durante o Oligoceno e suas implicações faciológicas. In: XXXIV Congresso Brasileiro de Geologia, 1986, São Paulo. *Anais do XXXIV Congresso Brasileiro de Geologia*, 1986. v.1, p. 8-22.

Gassmann, F., 1951. Elastic waves through a packing of spheres. *Geophysics*, 16, 673-685.

Goovaerts, P., 1997, *Geostatistics for Natural Resources Evaluation*. Oxford Univesrity Press, New York.

Goovaerts, P., 1998, Geostatistical tools for characterizing the spatial variability of microbiological and physico-chemical soil properties. In: *Biol. Fertil. Soils*, Springer-Verlag, v.27, 4, p.315-334.

Gurevich, B., 2004. A simple derivation of the effective stress coefficient for seismic velocities in porous rocks. *Geophysics*, 69, 393-397.

Hartung, M.M. and Koster, J.K., 2006. Time-lapse seismic monitoring in the Gulf of Mexico – 10 years of experience. In: 68th EAGE Conference & Exhibition, Extended Abstracts.

Hilterman, F., 2001. Seismic amplitude interpretation. EAGE/SEG Distinguish Instructor Short Course, No. 4, 235p.

Hinkle, A. and Batzle, M., 2006. Heavy oils: A worldwide overview. *The Leading Edge*, 25, 742-749.

Isaaks, E. and Srivastava, R.M., 1989. *An Introduction to Applied Geostatistics*. Oxford University Press, New York.

Johann, P.R.S., Thedy, E.A., Gomes, F.A., and Schinelli, M.C., 2006. 4D Seismic in Brazil: Experiences in Reservoir Monitoring. Presented at: SPE Offshore Technology Conference, Houston, 1–4 May.

Jugla, F., Rapin, M., Legeron, S., Magneron, C. and Livingstone, L., 2004. Improving 4D Repeatability using 3D Factorial Kriging. 66th EAGE Conf. Paris, France

Kvam, O., 2005. Pore pressure estimation from single and repeated seismic datasets. PhD Thesis. Norwegian University of Science and Technology.

Landro, M. and Kvam, O., 2002, Pore pressure estimation: what can we learn from 4D?. *CSEG Recorder*, 82-87.

Lecerf, D. and Coleou, T., 2002. Application of the Automatic Factorial Co-Kriging Method. 64th EAGE Conf. Florence, Italy.

Li, G., Purdue, G., Weber, S. and Couzens, R., 2001. Effective processing of nonrepeatable 4-D seismic data to monitor heavy oil SAGD steam flood at East Senlac, Saskatchewan, Canada. *The Leading Edge*, 20, p.54-62.

Lucet, N., 1989. Vitesse et atténuation des ondes élastiques soniques et ultrasoniques dans les roches sous pression de confinement. Thèse de Doctorat. Université de Paris VI.

Lucet, N. and Fournier, F., 2001, 4D seismic interpretation through seismic facies analyses, 71st Ann. Intern. Mtg., Soc. Expl. Geophys., Expanded Abstracts, p.1640-1643.

Lumley, D.E., 1996. 4-D seismic monitoring of an active steamflood. AAPG/SEPM Annual Meeting Abstracts, 5, 87.

Lumley, D. E., 1995, 4-D seismic monitoring of an active steamflood, 65th Ann. Intern. Mtg., Soc. Expl. Geophys., Expanded Abstracts, p.203-206.

Nivlet, P., Fournier, F., and Royer, J.J., 2001, A new methodology to account for uncertainties in 4-D seismic interpretation, 71st Ann. Intern. Mtg., Soc. Expl. Geophys., Expanded Abstracts, p.1644-1647.

Ma, Y.Z. and Royer, J. J., 1988, Local geostatistical filtering: Application to remote sensing. *Geomathematics and geostatistics analysis applied to space and time dependent data. Sci. de la Terre, Sér. Inf. Géol.*, 27, 17- 36.

Ma, Y.Z., & Royer, J.J., 1987, Le Comportement des Ponderateurs en Analyse Krigeante. Comparaison avec les Filtrés Classiques Utilizees en Traitement d'Images. *Sci. de la Terre, Inf. Geol.*, v.28, p.175-194.

Magesan, M., Depagne, S., Nixon, K., Regel, B., Opich J., Rogers, G., and Hudson T., 2005, Seismic processing for time-lapse study: Genesis Field, Gulf of Mexico. *The Leading Edge*, 24, 364-373.

Mari, J.L. , 2006. Seismic wave separation by SVD and F-K combined filters. Presented at: ISCCSP Conference, Marrakech, February 2006.

Matheron, G., 1982, Pour une Analyse Krigéante des Données Régionalisées. Report N-732, CG, Paris School of Mines, Fontainebleau, France.

Mavko, G., Mukerji, T., and Dvorkin, J., 1998. The rock physics handbook: Tools for Seismic Analysis in Porous Media. Cambridge, New York, Melbourne: Cambridge University Press., 329 pp.

Mindlin, R.D., 1949. Compliance of elastic bodies in contact. J. Appl. Mech., 16, 259-268.

Mundim, E.C., 1999, Avaliação da Krigagem fatorial na filtragem de atributos sísmicos: um filtro geoestatístico aplicado à caracterização de reservatórios. MSc Thesis, Universidade Estadual de Campinas. Brasil.

Mundim, E.C., Johann, P. and Remacre, A., 1999, Factorial kriging analysis: geostatistical filtering applied to reservoir characterization. The Leading Edge, 18, p.787-788.

Nickel, M. & Sonneland, L., 1999. Non-Rigid Matching of migrated time-lapse seismic. 69th Annual International Meeting of the Society of Exploration Geophysicists, p. 872-875.

Oliveira, R.M., Bampi, D., Sansonowski, R.C., Ribeiro Junior, N.M.S., Johann, P.R.S., Santos, M.S., and Ferreira, D.M., 2007. Marlim Field: Incorporating 4D Seismics in the Geological Model and Applications in Reservoir Management Decisions. Paper SPE 108062. SPE Latin American and Caribbean Petroleum Engineering Conference, Buenos Aires.

Oliver, M.A., Webster, R., and Slocum, K. 2000, Filtering SPOT imagery by kriging analysis. International Journal of Remote Sensing, vol. 21, no. 4, p.735-752.

PETROBRAS homepage www.petrobras.com.br , consulted in January 2008..

Pinto, A.C.C., Guedes, S., Bruhn, C.H.L., Gomes, J.A.T., Sá, A.N., Fagundes Netto, J.R., 2001. Marlim complex development: a reservoir engineering overview. Paper SPE 69438 presented at the 2001 SPE Latin American and Caribbean Petroleum Engineering Conference. Buenos Aires. 25–28 March. 2001.

Rangel, H.D., et al., 1994. Bacia de Campos. Boletim de Geociências da Petrobras, Rio de Janeiro, v. 8, n. 1, p. 203-217, jan./mar. 1994.

Rasolofosaon, P. and Zinszner, B., 2003. Petro-acoustic Characterization of Reservoir Rocks For Seismic Monitoring Studies: Laboratory Measurement of Hertz and Gassmann Parameters. In: Oil & Gas Science and Technology – Éditions Technip, Rev. IFP, 58, 6, 615-635.

Rokosh, D. and Schmitt, D., 2004. Laboratory rock physical and geological analyses of a ‘SAGD’ Mannville heavy oil reservoir, Senlac, West-central Saskatchewan; in Summary of Investigations 2004, Volume 1, Saskatchewan Geological Survey, Sask. Industry Resources, Misc. Rep. 2004-4.1, CD-ROM, Paper A-13, 9p.

Sandjivy, L., and Galli, A., 1984, Analyse krigéante et analyse spectrale. Sci. de la Terre, Sér. Inf. Géol., 21, 115-124.

Sandjivy, L., 1984. The Factorial Kriging Analysis of regionalized data: Its application to geochemical prospecting. Geostatistics for Natural Resources Characterization: Reidel, Dordrecht, Holland, 559–572.

Sandjivy, L., 1987, Analyse Krigéante des Données de Prospection Géochimique. PhD Thesis, Ecole des Mines de Paris, France, 166p.

Saporta, G., 1990. Probabilités, Analyse des Données et Statistique. Editions Technip. Paris.

Shecaira, F.S., Branco, C.C.M., Souza, A.L.S., Pinto, A.C.C., Holleben, C. R.C., Johann, P.R.S., 2002. IOR: The Brazilian perspective. Paper SPE 75170 presented at the 2001 SPE/DOE Improved Oil Recovery Symposium. Tulsa. 13–17 April 2002.

Solow, A. R., 1984. The analysis of second-order stationary processes. Time-series analysis, spectral analysis, harmonic analysis and geostatistics. *Geostatistics for Natural Resources Characterization*, Reidel, Dordrecht, Holland, 559–572.

Schmitt, D.R., 2004. Oil sands and geophysics. *CSEG Recorder*, 29 (11), 5-11.

Schmitt, D.R., 2005. Rock-physics and time-lapse monitoring of heavy-oil reservoirs. *SPE International Thermal Operations and Heavy Oil Symposium*, Calgary, November 2005.

Tosaya, C.A., Nur, A.M., Vo-Thanh, D., and Da Prat, G., 1987. Laboratory seismic methods for remote monitoring of thermal EOR. *SPE (Society of Petroleum Engineers) Reserv. Eng.*, Vol. 2, Issue 2, 235-242.

Voutay, O., 2003. *Mise au Point d'Attributs Sismiques pour l'Interpretation AVO et 4D des Réservoirs Pétrolier par l'Analyse en Composantes Generalisée*. PhD Thesis, INPL-Nancy.

Wackernagel, H., 1995. *Multivariate Statistics: an Introduction with applications*. Springer-Verlag, 256p.

Wang, Z., Nur, A.M. and Batzle, M.L., 1990. Acoustic velocities in petroleum oils. *Journal of Petroleum Technology*, 42, 2, 928-930.

Wang, Z., 2001. Y2K Tutorial: Fundamentals of Rock-physics. *Geophysics*, 66, 2, 398-412.

Weimer, P., 2004. *Petroleum Systems of Deep-water Settings*. 2004 EAGE/SEG Distinguished Instructor Short Course.

Zhang, Y., and Schmitt, D. R., 2004, A Case Study: QC Analysis of Time-lapse Seismic Monitoring in a Heavy Oil Reservoir, pp. 4 – CDROM, Can. Soc. Exploration Geophysicists Annual Meeting, Calgary, May 2004.

Annex A

Technical paper *Improving 4d Seismic Data Interpretation using Geostatistical Filtering*, authors Carlos Eduardo Abreu, Nathalie Lucet and Philippe Nivlet (Institut Français du Pétrole) and Jean-Jacques Royer (CNRS-CRPG), presented at the 9th International Congress of the Brazilian Geophysical Society held in Salvador, Brazil, 11-14 September 2005.

Improving 4D Seismic Data Interpretation using Geostatistical Filtering

Carlos Eduardo Abreu, Nathalie Lucet and Philippe Nivlet, Institut Français du Pétrole
Jean-Jacques Royer, CNRS-CRPG

Copyright 2005, SBGf - Sociedade Brasileira de Geofísica

This paper was prepared for presentation at the 9th International Congress of the Brazilian Geophysical Society held in Salvador, Brazil, 11-14 September 2005.

Contents of this paper were reviewed by the Technical Committee of the 9th International Congress of the Brazilian Geophysical Society. Ideas and concepts of the text are authors' responsibility and do not necessarily represent any position of the SBGf, its officers or members. Electronic reproduction or storage of any part of this paper for commercial purposes without the written consent of the Brazilian Geophysical Society is prohibited.

Abstract

4D Seismic is becoming a conventional tool for hydrocarbon reservoirs monitoring and management, especially for heavy oil bearing fields (Calvert, 2005). In this case, 4D, or time-lapse seismic, can be used to detect important reservoir properties variations imposed by thermal enhanced oil recovery processes.

This work aims at identifying remaining noise, invariant common features and time-dependent variations in oil reservoirs from post-stack amplitude time-lapse data. It involves a geostatistical multivariate technique called factorial co-kriging, an extension of the factorial kriging (FK) technique proposed by Matheron (1982). It is based on the decomposition of spatial correlations to identify redundant structures at various scales. Three seismic surveys, with different acquisition parameters, were acquired at the same site in different calendar times to monitor the progress of injected steam fronts into a heavy-oil reservoir. These seismic volumes were then carefully processed to minimize their discrepancies. Factorial co-kriging revealed possible common geological structures, 4D effects and remaining noise, and it seems to be an efficient method for extracting common regional trends from several repeated seismic datasets.

Introduction

Despite of recent technological improvements during the last years, repeatability is still a major issue for 4D seismic surveys. Much has to be done in terms of acquisition, processing and interpretation in order to provide reservoir geoscientists and engineers with reliable information from subtle 4D seismic effects. During exploitation, fluid content, pressure and/or temperature vary with time at the reservoir level due to production. Theoretically, these changes in the subsurface could be potentially detected by 4D seismic surveys. Assuming that the reservoir is the only geological formation submitted to physical properties changes, repeated seismic surveys should be a helpful tool to map the evolution of an exploited reservoir over time.

However, in the real world, non-related to reservoir factors, such as seismic acquisition, processing and even interpretation artifacts, may compromise the ultimate goal of a 4D study, increasing the associated uncertainties of the final quantitative interpretation in terms of pressure and fluid variations at the reservoir level. These artifacts, which are not related to the production and are assumed to be noise, can be detected even for highly repeatable seismic experiments (Eiken *et al.*, 2003).

Due to distinct acquisition designs and technologies, weather conditions, water velocities, etc, the simultaneous processing of 4D seismic datasets requires an additional effort in terms of phase, amplitude and frequency equalization, and processing schemes to minimize non-repeatability using cross-equalization techniques (Li *et al.*, 2001; Magesan *et al.*, 2005). In practice, however, even cross-equalized datasets may show artifacts that may potentially compromise the final 4D quantitative interpretation.

Geostatistical techniques may be conveniently adapted to analyze and filter 4D seismic data. A factorial kriging approach has been proposed to address the analysis and filtering issues of 4D seismic datasets. Assuming a second-order stationary process, it is possible to discriminate different structures on nested cross-variograms computed over the non-reservoir zones that are assumed not to be impacted by production, and to interpret these structures either as noise or as geological structures. These techniques have been successfully applied in the petroleum industry (Jugla *et al.*, 2004; Coléou, 2002; Lecerf and Coléou, 2002; Mundim *et al.*, 1999; and Piazza, 1999), and also in some other geoscience areas (Ma and Royer, 1988; Sandjivy, 1987; and Sandjivy and Galli, 1984).

This work combines several repeated seismic datasets to identify remaining noise, invariant common features and variations over time using a factorial co-kriging approach. Three cross-equalized seismic vintages from a Canadian heavy-oil reservoir, submitted to steam-assisted gravity drainage (SAGD) process, were studied. The first step included an exploratory data analysis to define which stationary models should be considered. A second step involved variograms and cross-variograms fitting, followed by multivariate factorial co-kriging. These steps aimed at investigating structures that could or could not be linked to a plausible geological model, and address those ones clearly associated to noise. This methodology was firstly applied in a seismic window outside the reservoir, minimizing the production related artifacts, and then over the reservoir level.

Dataset description

The studied area comprises a shallow heavy-oil reservoir located close to the Alberta-Saskatchewan fields, Canada. The producing reservoir corresponds to unconsolidated fluvial channels of the Lower Cretaceous Dina Formation, with an average thickness of 15m and good average permo-porosity (5-10 D and 33%, respectively), where a SAGD scheme was employed to enhance the production of the 13%API and 5000cp @ RC oil (Dequirez *et al.*, 1995; Li *et al.*, 2001).

A time-lapse study was performed, using three cross-equalized seismic vintages shot in 1990, 1997 and 1998 (referred to as S90, S97 and S98 in the followings). The base survey, S90, was shot before the start of production, while the S97 and S98 surveys were shot, respectively, 18 and 24 months after starting the steam injection, to monitor the evolution of the steam chamber in the reservoir. It is worth to mention the highly potential sources of non-repeatability observed in the acquisition parameters of these surveys: varying inline direction, sampling rates, source types and parameters, receiver and shot arrays, bin size, etc, as showed in Figure 1.

The three datasets were then cross-equalized to minimize their discrepancies. A grid rotation was performed over the S90 data to match the S97 and S98 grids, with a final post-stack bin size of 20x20m. This final bin size dimension was a multiple of the original S97 and S98 survey ones, but not of the S90's. A detailed description of the cross-equalization processing sequence can be found in Li *et al.* (2001).

Factorial Kriging and proposed methodology

Factorial Kriging relies on the principle that a regionalized variable (RV) $Z(x)$ can be decomposed into a linear combination of independent orthogonal components $Z_i(x)$, that explain the variability observed in variograms at various scales,

$$Z(x) = \sum \lambda_i Z_i(x) \quad (1)$$

FK is based on the property that the sum of component variograms is equal to the global variogram of the RV (nested structures). The total variability observed in the global variogram γ (or covariance function C) is hence decomposed into a sum of elementary variability C_i or γ_i , associated to various scales

$$C = \sum_i C_i$$

(2)

4D seismic applications are more concerned with regionalized vectors than regionalized variables, the components of which refer to each seismic vintage. In such a case, factorial co-kriging can be applied. The variability decomposition can be written as

$$C = \sum_j C_j$$

(3)

where C is a square matrix of variograms/covariograms models between each survey and C_j is a square matrix for each component.

More than using factorial co-kriging as a filtering technique, this work aims at developing an interpretative and quantitative methodology for repeated seismic surveys. In particular, it focuses on assessing spatial joint variability of the 4D seismic datasets and assigning these spatial structures to time invariant and non-invariant phenomena.

The working sub-volumes were defined by a) regional markers on the non-reservoir zone; b) top and bottom markers on the reservoir zone according to the well calibration study (Lucet and Fournier, 2001). Figure 2 shows a comprehensive interpretation over the volumes, where several horizons were mapped using volumetric based algorithms.

The proposed methodology for this work involves:

- computation of the experimental variograms and cross-variograms of amplitudes over the three datasets, firstly calculated on the non-reservoir zone (with no production-related effects) and then, on the reservoir level;
- variogram and cross-variogram fitting by a comprehensive co-regionalization intrinsic nested model;
- factorial co-kriging to filter the components and interpretation of the factors response. These factors corresponds to a principal component analysis (PCA) decomposition of each variographic component of the three seismic vintages.

Preliminary results

The study was conducted using a horizon-guided window, for both non-reservoir and reservoir zones. In Figure 2, a seismic inline section shows the main characteristics of the area, where very gentle dips are observed. The selected non-

reservoir and reservoir zones have an average two-way-time thickness of 100ms and 20ms, respectively. A visual inspection of the three cross-equalized inlines (and even of the whole volume) shows that only weak differences can be observed.

The amplitude distribution over the non-reservoir and reservoir level is shown in Figures 3 and 4, respectively, and it can be noticed that:

- a) the amplitude distribution behavior for S97 and S98 are similar, but differ from the S90 survey, for both non-reservoir and reservoir levels, probably due to the closer acquisition geometry used in the S97 and S98 surveys; and to the grid rotation and rebinning imposed to S90 data;
- b) the amplitude values are closer to a normal distribution in the non-reservoir level, as shown by the Q-Q plots. The three distributions are asymmetric, positively skewed, showing a uni-modal behavior, as should be expected for zero-phased seismic data;
- c) a bimodal distribution characterizes the amplitudes over the reservoir level, explained by the shorter window length. In this level, an overall amplitude dimming with the elapsed-time can be observed. This effect maybe related to non-repeatability, as stated in (a), but should also be due to acoustic properties variations induced by reservoir exploitation. The discrimination between these effects is the main goal of this research work.

Variogram maps are useful tools to inspect the spatial variability and determine the main directions of anisotropy. The horizontal variogram maps from the non-reservoir and for the reservoir zones are presented in Figures 5 and 6. They represent the average of the 2D variograms computed along several stratigraphic slices, in such a way that structural effects are not considered. The lag used for computation is 20m, following the final bin size after cross-equalization. To avoid data sampling reduction and variograms misinterpretations, a maximum distance of half the inline and cross line dimensions were chosen, which represents approximately 20 lags. The variogram maps over the non-reservoir zone show an anisotropic behavior, with main continuity directions following both inline and cross line directions. A more complex response is observed in S97 variogram map, showing a medium to long range behavior oriented to N15, bisecting the inline-cross line orientation. Variogram maps over the reservoir show similar anisotropic behavior in terms of ranges, but present a greater variability (by one to two orders of magnitude) for both small and long range spatial structures.

From these variogram and cross-variogram maps, it was possible to model the variograms of each seismic vintage and the associated cross-variograms, for both non-reservoir and reservoir zones. Tables I and II show the main parameters used in this interpretation phase, where four structures were adjusted.

Discussions

The first two structures C0 and C1, with smaller ranges (10x40 and 50x120m, respectively) and NE-SW anisotropy mainly along inline direction, account for noise both in reservoir and non reservoir zones, as shown in Figures 7 and 8. They are probably related to the bin resizing and regridding effects of the S90 vintage performed during the cross-equalization. Matrices C0 and C1 reflect the spatial correlation coefficients between vintages at small scales (less than 120m). On the non-reservoir zone, they are slightly smaller for S97xS98 (C0=0.68, C1=0.67) than for S90x97 (C0=0.80, C1=0.73) and S90xS98 (C0=0.78, C1=0.71), respectively, as shown in the third part of Table I. When performing the same analysis on the reservoir zone, these coefficients are quite similar and close to 1. A possible explanation for this behavior is that a stronger filtering effort was applied over the reservoir level to improve the noise filtering.

Structures C2 and C3, on the other side, reflect medium to large range and reveal the redundant geological response contained in the seismic datasets and/or the exploitation effect. For structure C2, higher correlation values were observed. A possible cause for this is that, even with different sources, the acquisition geometries of both S97 and S98 – quite similar – played a very important role on the imaging of the most important geological features.

Conclusions

It is remarkable that the factors extracted by the FK on both the non-reservoir and reservoir zones are quite similar in terms of spatial variability (range, anisotropy and number of components). However, the contribution (in %) of each FK factors are more contrasted in the reservoir (100% or 0%) than in the non reservoir zone, indicating a time-lapse amplitude effect in this level. In addition, the contribution in terms of variance on each component S90, S97 and S98 is much higher in the reservoir zone (one to two orders of magnitude). Moreover, the correlation coefficients for large scale C₃ are more contrasting in the reservoir zone. They are small (0.26) for S90xS97 and S90xS98, but higher (0.86) for S97xS98. This could be related to changes in the reservoir due to the steam injection in horizontal wells aligned along the cross line direction. This would indicate that changes in the reservoir would affect zones of similar extend

and orientation as the C₃ structures. These preliminary results show that FK seems to be an efficient method to reveal common regional trends and time dependent zones from repeated seismic datasets.

Acknowledgments

The authors thank their colleagues from the Direction Géophysique of IFP for valuable discussions, suggestions and contributions. They are also deeply thankful to PETROBRAS for sponsoring this research work and to Encana Corporation for permission to show these results.

References

Calvert, R., 2005, 4D technology: where are we, and where are we going? *Geophysical Prospecting*, 53 (2), 161-171.

Coléou, T., 2002, Time-lapse filtering and improved repeatability with automatic factorial co-kriging (AFACK). 64th EAGE Conf. Florence, Italy.

Dequirez, P.Y., Fournier, F., Blanchet, C., Feuchtwanger T. and Torriero, D., 1995, Integrated stratigraphic and lithologic interpretation of the East-Senlac heavy oil pool. Expanded Abstracts, 65th Annual Int. SEG Meeting, 104-107.

Eiken, O., Haugen, G. U., Schonewille, M. and Duijndam, A., 2003, A proven method for acquiring highly repeatable towed streamer seismic data. *Geophysics*, 68 (4), 1303-1309.

Jugla, F., Rapin, M., Legeron, S., Magneron, C. and Livingstone, L., 2004, Improving 4D Repeatability using 3D Factorial Kriging. 66th EAGE Conf. Paris, France.

Lecerf, D. and Coleou, T., 2002, Application of the Automatic Factorial Co-Kriging Method. 64th EAGE Conf.. Florence, Italy.

Li, G., Purdue, G., Weber, S. and Couzens, R., 2001, Effective processing of nonrepeatable 4-D seismic data to monitor heavy oil SAGD steam flood at East Senlac, Saskatchewan, Canada. *The Leading Edge*, 20, 54-62.

Lucet, N. and Fournier, F., 2001, 4D seismic interpretation through seismic facies analyses. 71th SEG Abstracts, San Antonio, Texas.

Nivlet, P., Fournier, F., and Royer, J.J., 2001, A new methodology to account for uncertainties in 4-D seismic interpretation. 71th SEG Abstracts, San Antonio, Texas, 1644-1647

Ma, Z. and Royer, J. J., 1988, Local geostatistical filtering: Application to remote sensing. *Geomathematics and geostatistics analysis applied to space and time dependent data. Sci. de la Terre, Sér. Inf. Géol.*, 27, 17-36.

Magesan, M., Depagne, S., Nixon, K., Regel, B., Opich J., Rogers, G., and Hudson T., 2005, Seismic processing for time-lapse study: Genesis Field, Gulf of Mexico. *The Leading Edge*, 24, 364-373.

Matheron, G., 1982, Pour une analyse krigéante des données régionalisées. Report N-732, CG, Paris School of Mines, Fontainebleau, France.

Mundim, E.C., Johann, P. and Remacre, A., 1999, Factorial kriging analysis: geostatistical filtering applied to reservoir characterization. *The Leading Edge*, 18, 787-788.

Sandjiv, L., 1987, Analyse krigéante des données de prospection géochimique. PhD Thesis, Ecole des Mines de Paris, France, 166p.

Sandjiv, L., and Galli, A., 1984, Analyse krigéante et analyse spectrale. *Sci. de la Terre, Sér. Inf. Géol.*, 21, 115-124.

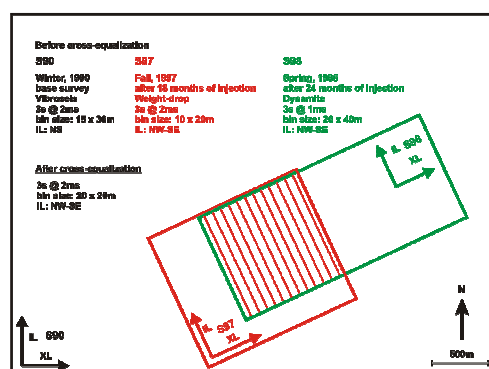


Figure 1 – Seismic acquisition map and main parameters of the S90, S97 and S98 surveys. The studied area is represented by dashed lines.

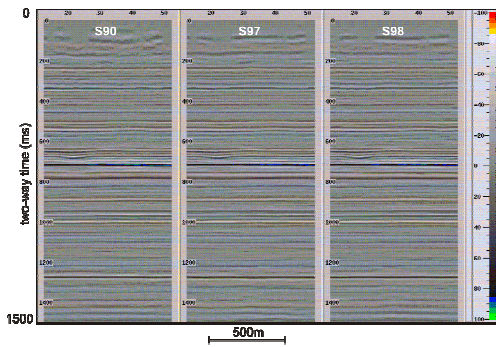


Figure 2 - Inline sections from S90, S97 and S98 (from left to right), where only weak differences can be observed.

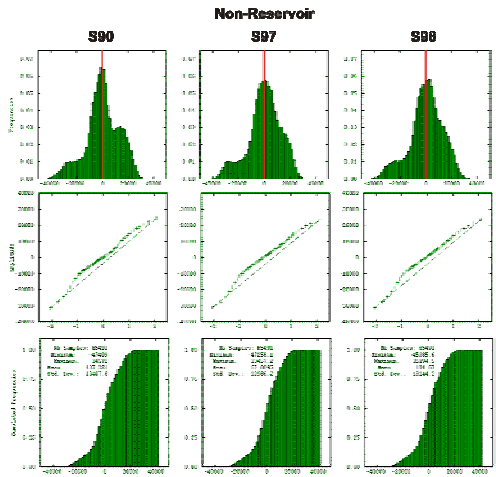


Figure 3 - Statistical characterization of amplitudes for S90, S97 and S98 (from left to right) of the non-reservoir zone.

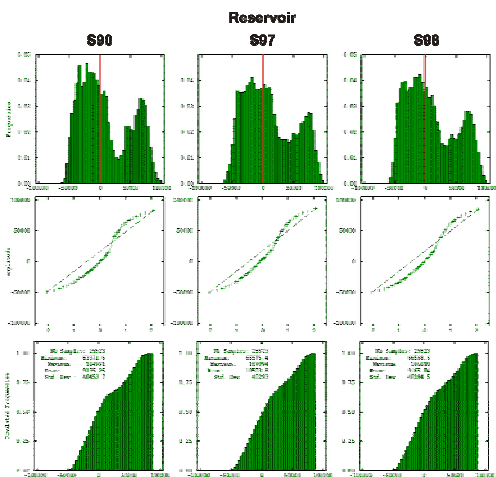


Figure 4 - Statistical characterization of amplitudes for S90, S97 and S98 (from left to right) of the reservoir zone.

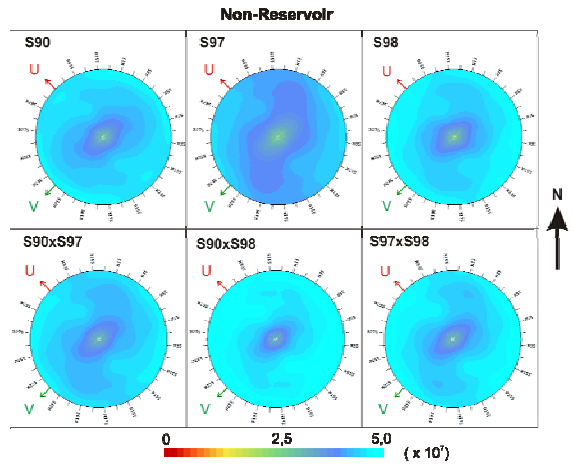
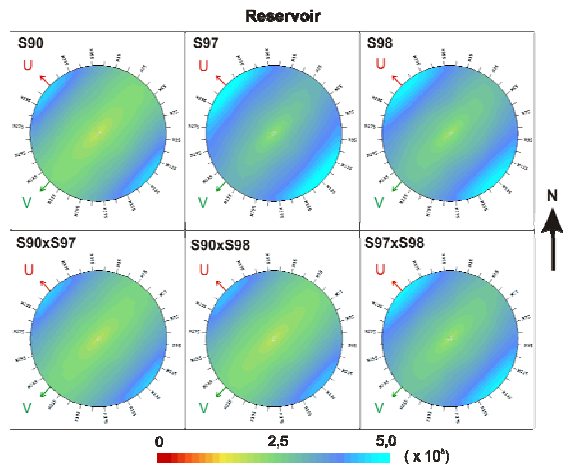


Figure 5 - Variogram and crossvariogram maps for the non-reservoir zone. The inline and crossline directions coincides with the U (red arrow) and V (green arrow) vectors, respectively.



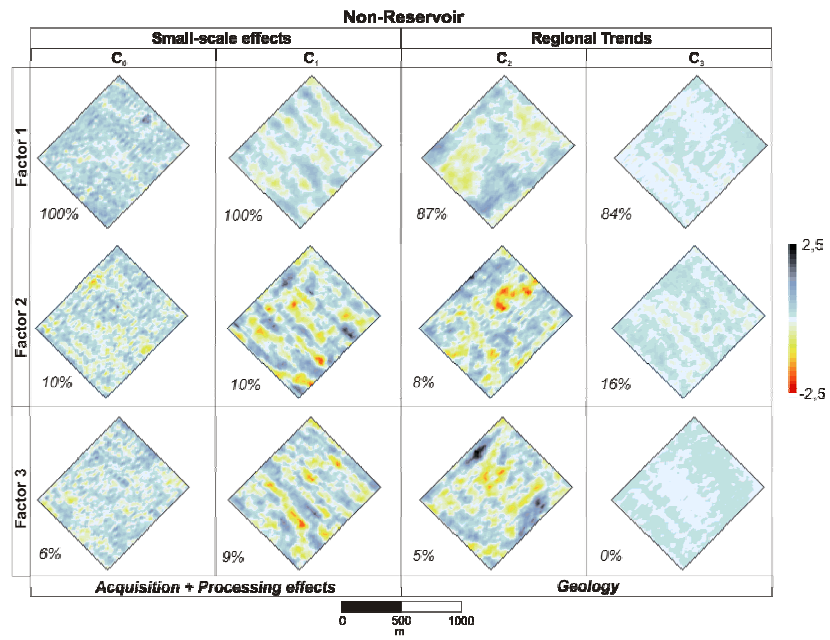


Figure 6 –The same for Figure 5, for the reservoir zone. Notice the higher variability when compared to the non-reservoir zone.

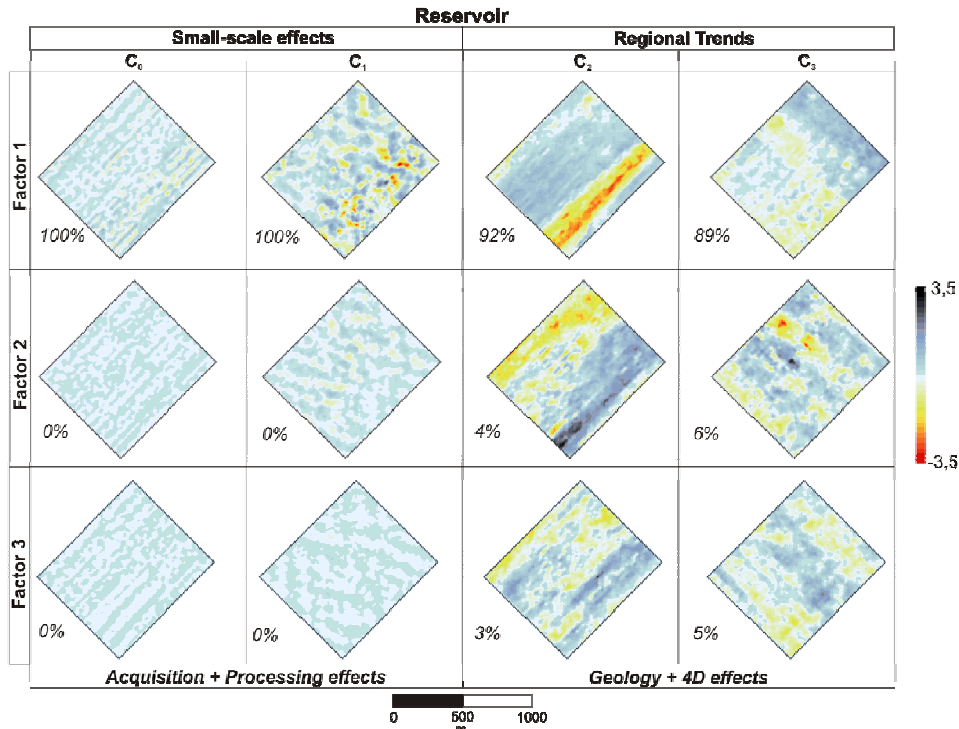


Figure 7 - Factorial co-kriging resulting factors for the non-reservoir zone. Small scale structures C_0 and C_1 were interpreted as gridding effects, while medium to longer scale structures C_2 and C_3 are related to the geology (Numbers indicate the contribution (in %) of each factor to the total variance).

Non - Reservoir									
Structure		Ranges (m)		Sills (in 10^6)			Correlations		
		U Inline	V Cross line	S90	S97	S98	S90xS97	S90xS98	S97xS98
C_0	Spherical	10	40	4.7	3.8	3.6	0.78	0.80	0.68
C_1	Spherical	190	70	7.4	5.5	7.1	0.71	0.73	0.67
C_2	Exponential	220	480	19.6	21.1	21	0.77	0.80	0.86
C_3	Spherical zonal	-	2500	3.2	7.7	14.1	0.68	0.98	0.60

Table I – Horizontal variogram fitting parameters for the non-reservoir zone. Variograms ranges are represented in m, and sills in squared amplitude units. The U and V directions correspond to the inline and cross line directions, respectively.

Figure 8 – Same as in Figure 7, for the bottom reservoir zone. Small scale structures C_0 and C_1 were interpreted as gridding effects, while medium to longer scale structures C_2 and C_3 , are related to the geology and 4D effects due to oil production. Numbers indicate the contribution (in %) of each factor to the total variance.

Reservoir									
Structure		Ranges (m)		Sills (in 10^6)			Correlations		
		U Inline	V Cross line	S90	S97	S98	S90xS97	S90xS98	S97xS98
C_0	Spherical	10	-	0.44	0.90	1.15	1.00	1.00	1.00
C_1	Spherical	120	50	1.09	1.74	1.73	1.00	1.00	1.00
C_2	Exponential zonal	240	-	14.90	18.20	16.00	0.88	0.87	0.91
C_3	Exponential zonal	-	250	77.00	9.70	8.88	0.26	0.26	0.86

Table II – Horizontal variogram fitting parameters for the reservoir zone. Notice that variogram sills are of one to two orders of magnitude larger than in the non-reservoir zone both for small and regional scale structures. Contrasted correlation coefficients for large scale C_3 (low for S90xS97 and S90xS98, high for S97xS98, respectively) could be related to changes in the reservoir due to the steam injection.

Annex B

THE HERTZ-MINDLIN MODEL

Few theoretical models were developed to describe the dependency of elastic and bulk modulus on pressure. These models usually consider small strains, and one of the limitations is that they consider ideal grains, which are supposed to be identical elastic spherical grains. Unfortunately, this hypothesis is barely satisfied in usual petroleum reservoir rocks.

Hence, these models estimate the effective bulk and shear modulus of a random dense pack of identical spheres for a given porosity and confining pressure. Mavko et al. (1998) use the term hydrostatic confining pressure to describe the stress field acting on each grain. It was noticed that the pressure terminology is not that clear, and trying to clarify the concepts and terms used, we will follow the nomenclature proposed by Gurevich (2004).

The following developments concerning the Hertz model are based on Mavko et al. (1998). Assuming a normal compression of two identical spheres as show in Figure 0-1, the radius of the contact area a between the two spheres and the normal displacement δ are given by

$$\begin{aligned} a &= \sqrt[3]{\frac{3FR}{8G}(1-\nu)} \\ \delta &= \frac{a^2}{R} \end{aligned} \tag{86}$$

where G and ν are the shear modulus and Poisson's ratio of the grain solid material, respectively.

If a hydrostatic confining pressure P is applied to this packing of random identical spheres, then the confining force acting between two grains are

$$F = \frac{4\pi R^2 P}{C(1-\phi)} \quad (87)$$

where C is the number of contacts per grain, also known as coordination number, and ϕ is the porosity. Then the radius a may be rewritten as

$$a = R \sqrt[3]{\frac{3\pi(1-\nu)}{2C(1-\phi)G} P} \quad (88)$$

and the normal stiffness is

$$S_n = \frac{4Ga}{1-\nu} \quad (89)$$

and the effective bulk modulus of a dry random identical sphere packing is given by

$$K_{eff} = \sqrt[3]{\frac{C^2(1-\phi)^2 G^2}{18\pi^2(1-\nu)^2} P} \quad (90)$$

The Mindlin model shows that if the spheres are first pressed together and a tangential force is applied afterwards, the shear and the normal stiffness are given by

$$\begin{aligned} S_\tau &= \frac{8aG}{2-\nu} \\ S_n &= \frac{4aG}{1-\nu} \end{aligned} \quad (91)$$

where ν and G are the Poisson ratio and the shear modulus of the solid grains, respectively.

The effective shear modulus of a dry random identical sphere packing is then given by

$$G_{eff} = \frac{5-4\nu}{5(2-\nu)} \sqrt[3]{\frac{3C^2(1-\phi)^2 G^2}{2\pi^2(1-\nu)^2} P} \quad (92)$$

The effective bulk and shear modulus using both Hertz and Mindlin developments is referred to as the Hertz-Mindlin geo-mechanical model. It is used to describe the properties of a dry dense random pack of identical spherical grains subject to a hydrostatic pressure P . In these formulations, no slip at the contact between the spheres is assumed. Despite considering this to be a second-order effect, Avseth et al. (2005) refers to this assumption as one possible explanations to the observed overpredictions when one applies the Hertz-Mindlin model to unconsolidated sands.

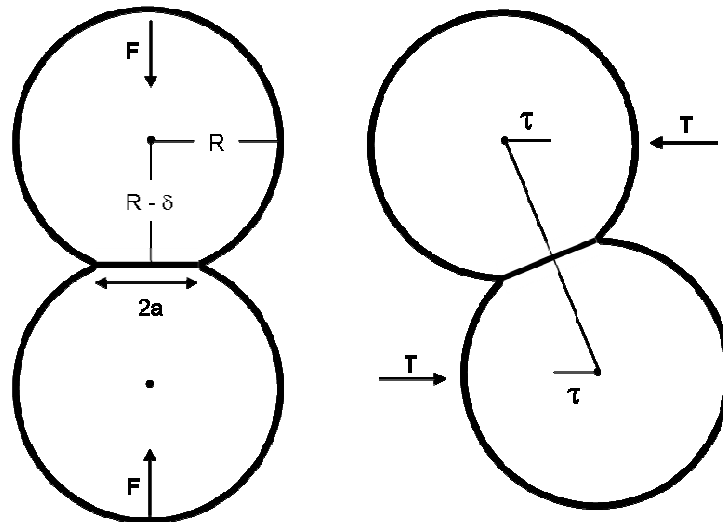


Figure 0-1 - Model of packing of spheres submitted to normal and tangential forces F and T (from Mavko et al., 1998).

Following the works of Zimmerman (1991), where he considered a non-porous material submitted to a pressure P with no temperature variation, the compressibility parameter, usually represented by C (or K , or β) relates the pressure exerted over a material and the consequent volume variation in the form

$$C = \frac{-1}{V^i} \frac{dV}{dP} \quad (93)$$

where V is the volume of the material at the time i prior to deformation, and P is the pressure.

The compressibility will be a positive number if a compressive stress is applied over a body and reduces its volume resulting in a negative volumetric variation. This volumetric variation can be written as

$$\begin{aligned} d\varepsilon &= \frac{dV}{V^i} \\ &= -C dP \end{aligned} \quad (94)$$

All the above expressions are valid for non-porous materials.

Annex C

In this section, an usefull representation of data variability know as variogram map is introduced, and examples computed from the interpreted horizons from the Marlim field, as described in Chapter 4.3, are presented.

The variogram map is a representation of the variogram or the cross-variogram in all investigated directions. In this approach, a circle is used to represent a given grid, and all distance and angles of every par of points are referred to the center of the circle. So, every point inside the circle will be represented by three coordinates:

- the distance or radius a , that corresponds to a given distance or lag between two points in the space;
- the angle defined between a given point and, for instance, the north direction; and
- the variance associated to that given point, usually represented in colour scales.

These maps are conventionally used as auxiliary tools on the initial phase of data analysis, and helps on highlighting possible anisotropies that are present in the data. After analyzing these maps and defining the directions of maximum data variability, the variograms and cross-variograms computation will be referred to these new directions. In the following, the variograms maps computed for three main interpreted horizon from Marlim Field are presented. The parameters used to compute the variogram maps are as follows: (a) lag distance: 50m; and (b) number of lags:100.

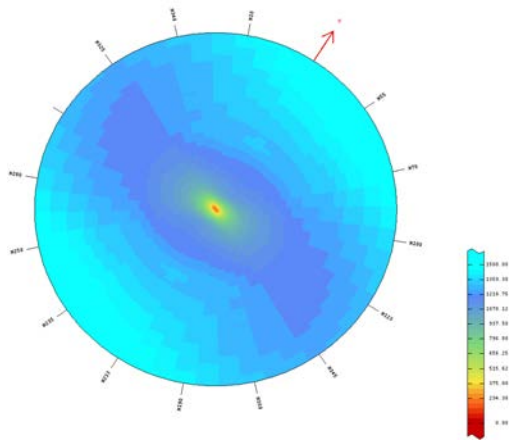


Figure C-1 – Variogram map computed for the Blue marker amplitude map horizon taken from S05 monitor survey.

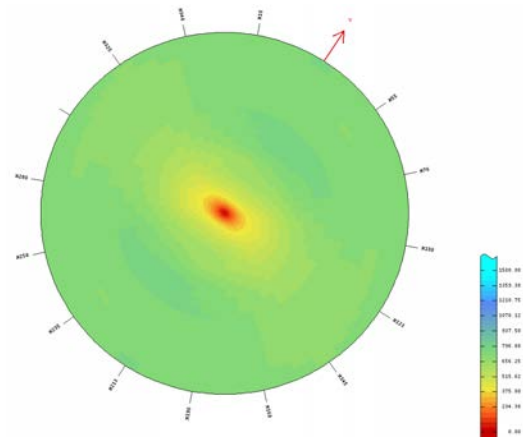


Figure C-2 – Cross-variogram map computed for the Blue marker amplitude map horizon, considering both the S05 monitor survey and S97 base survey.

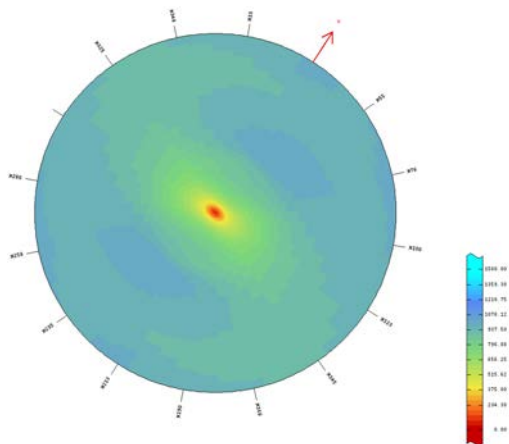


Figure C-3 - Variogram map computed for the Blue marker amplitude map horizon taken from S97 base survey.

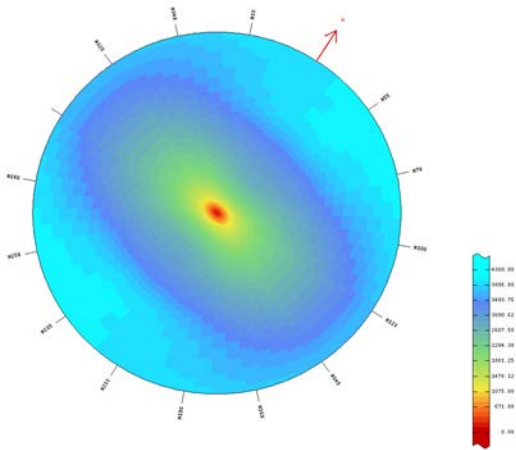


Figure C-4 - Variogram map computed for MRL Top horizon amplitude map horizon taken from S05 monitor survey.

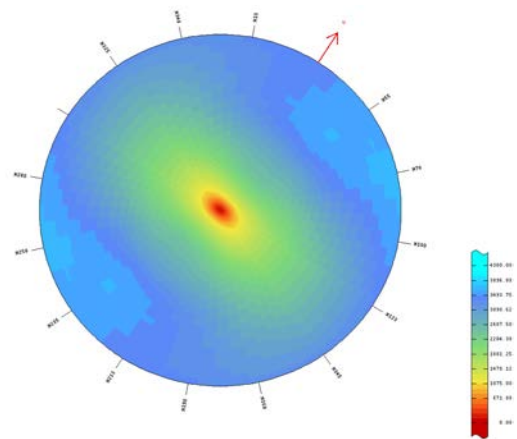


Figure C-5 - Cross-variogram map computed for MRL Top amplitude map horizon, considering both the S05 monitor survey and S97 base survey.

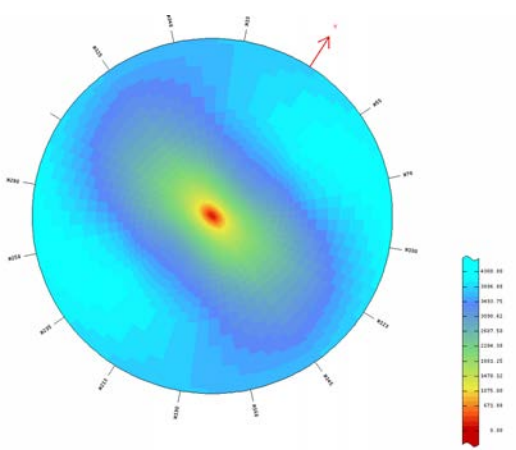


Figure C-6 - Variogram map computed for the MRL Top amplitude map horizon taken from S97 base survey.

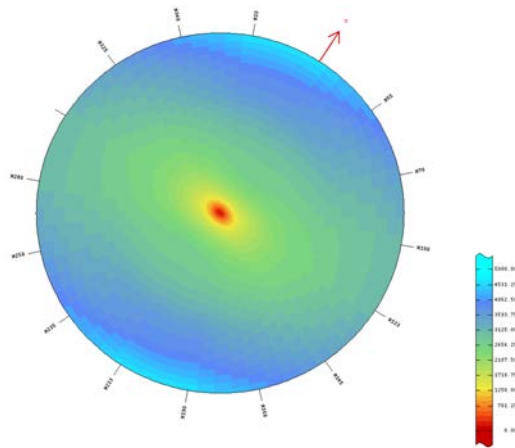


Figure C-7 - Variogram map computed for MRL Bottom horizon amplitude map horizon taken from S05 monitor survey.

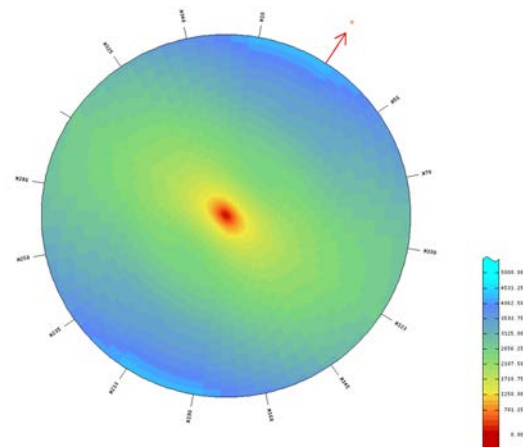


Figure C-8 – Cross-variogram map computed for MRL Bottom horizon amplitude map horizon taken from S05 monitor and S97 base survey.

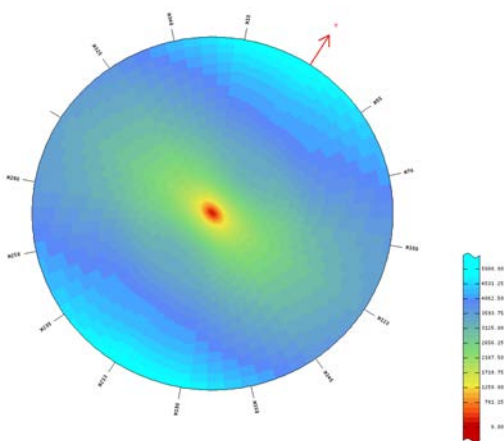


Figure C-9 - Variogram map computed for the MRL Bottom amplitude map horizon taken from S97 base survey.

Résumé

L'objectif de la thèse est de développer une méthodologie permettant d'obtenir une interprétation quantitative des données de sismique répétée (sismique 4D). Une étape essentielle consiste à évaluer la répétitivité des données, puis à filtrer les bruits indésirables, qui peuvent masquer ou détériorer la signature 4D. Une méthodologie basée sur des outils géostatistiques a été développée. Deux fenêtres temporelles des cubes sismiques étudiés sont choisies, l'une au-dessus du réservoir - où aucun effet 4D n'est attendu - et l'autre incluant le réservoir. Une analyse statistique et variographique conduite sur ces différentes fenêtres permet de proposer une décomposition des variogrammes en structures communes ou indépendantes, qui sont ensuite interprétées en termes de bruit, de signature géologique ou 4D. Les structures interprétées comme indépendantes de la géologie ou de la production sont ensuite filtrées à l'aide de la technique du krigeage factoriel proposée par Matheron en 1982.

La méthodologie a été testée sur deux cas réels. Le premier concerne un champ d'huiles lourdes canadien, sur lequel trois campagnes sismiques ont été enregistrées, avant et pendant la production obtenue à l'aide d'injection de vapeur. Le bruit interprété comme tel sur les 3 campagnes a été filtré à l'aide la méthode décrite plus haut ; une analyse en termes de faciès sismiques non supervisée a ensuite été conduite sur les données brutes et filtrées afin d'évaluer l'intérêt du filtrage. Finalement, une interprétation des décalages en temps observés entre campagnes a été proposée. Le deuxième cas réel concerne un champ turbiditique profond dans l'offshore du Brésil, sur lequel deux campagnes sismiques 3D ont été acquises, avant et après le début de la production obtenue par injection d'eau. Le bruit présent sur les deux campagnes a été filtré à l'aide de la technique du krigeage factoriel, et la qualité de ce filtrage a pu être évaluée par comparaison avec d'autres techniques couramment utilisées.

Abstract

This thesis research aims at investigating seismic interpretation methodologies and techniques that will help on better characterizing time-lapse, or 4D, seismic signatures. These techniques and methodologies are used to evaluate the time-lapse repeatability and then to filter out undesirable artefacts that are non-related to the production, while enhancing the 4D signature. To achieve these goals, a methodology based on geostatistical tools, was developed. Typically, at least two time-interval windows are considered: one above and the other comprising the reservoir of interest. A statistical and variographic analysis, conducted on both windows and on all surveys, leads to an interpretation step where common or independent structures – in the variographic sense- can be pointed out. The structures interpreted as not related to the geology or to the production mechanism are filtered from the data by a multivariate factorial cokriging technique, based on the concept of Kriging Analysis developed by Matheron in 1982. Two real case time-lapse studies were used to test the methodology. The first case is a Canadian onshore heavy oil reservoir submitted to steam injection, where three different time-lapse surveys were shot to monitor the steam-chamber evolution. The noise present in the three surveys was first filtered using the technique described above; next, an unsupervised seismic facies analysis was conducted on both raw and filtered data in order to evaluate the effectiveness of the filtering technique, and finally an interpretation, in terms of reservoir properties changes, of the time-shift observed between the campaigns was proposed. In the second case, the seismic data was acquired on a deepwater turbiditic oilfield from Brazil at two different times of reservoir life, before and after production and water injection. The two seismic surveys were filtered using the factorial kriging technique; the quality of the filtering was, in this case, evaluated by comparison with more common techniques.

Centre de Recherches Péetrographiques et Géochimiques
Laboratoire d'Infographie et d'Analyse des données
Rue du Doven Marcel Roubault – 54500 Vandoeuvre

AUTORISATION DE SOUTENANCE DE THESE
DU DOCTORAT DE L'INSTITUT NATIONAL
POLYTECHNIQUE DE LORRAINE

o0o

VU LES RAPPORTS ETABLIS PAR :

**Monsieur Richard SINGING-LARSEN, Professeur, Norwegian University of Science and
Technology, Trondheim, Norway**

Monsieur Jean-Paul CHILÈS, Professeur, ENSMP, Fontainebleau

Le Président de l'Institut National Polytechnique de Lorraine, autorise :

Monsieur BORGES DE SALLES ABREU Carlos Eduardo

NANCY BRABOIS
2, AVENUE DE LA
FORET-DE-HAYE
BOITE POSTALE 3
F - 5 4 5 0 1
VANDŒUVRE CEDEX

à soutenir devant un jury de l'INSTITUT NATIONAL POLYTECHNIQUE DE LORRAINE,
une thèse intitulée :

**"Méthodologies d'Interprétation par Analyse krigeante des données sismiques 4D
réservoir. Applications aux huiles lourdes de Senlac (Canada) et au champ Marlim
(Brésil)"**

en vue de l'obtention du titre de :

DOCTEUR DE L'INSTITUT NATIONAL POLYTECHNIQUE DE LORRAINE

Spécialité : « Géosciences »

Fait à Vandoeuvre, le 25 février 2008

Le Président de l'I.N.P.L.,

F. LAURENT

